Development of New Magnesium Alloys for High Temperature Applications

Doctoral Thesis

(Dissertation)

to be awarded the degree of

Doctor of Engineering (Dr.-Ing.)

submitted by

Dipl.-Ing. Tarek Abu Leil

from

Bethlehem

approved by the Faculty of Natural and Materials Sciences,

Clausthal University of Technology

Date of oral examination

13.11.2009

Chairperson of the Board of Examiners

Prof. Dr. rer. nat. A. Wolter

Chief Reviewer

Prof. Dr. R. Schmid-Fetzer

Reviewer

Prof. Dr. K. U. Kainer

Statement

I hereby declare that this research work is the best knowledge and belief original except as acknowledged in the text. In addition, it has not been submitted for any other institution.

Acknowledgment

First, I would like to thank my advisor Prof. Dr. K. U. Kainer for his patience, encouragement and guidance during my research work. My special thanks also go to Prof. Dr. R. Schmid-Fetzer, who agreed to be the chief reviewer of my thesis and for his support.

Special thanks to Dr. N. Hort for his valuable comments, suggestions and for his careful guidance in bringing this work to realization. I have really enjoyed the time together with all my colleagues at GKSS research centre. I would like to thank all of the staff members and the students of the Magnesium Innovation Centre “MagIC” for their great work environment and interesting discussions on many subjects; in particular, I would like to thank:

Dr. H. Dieringa for his valuable time in guiding me to do the creep tests,

Dr. C. Blawert for his guidance and assistance in corrosion tests,

Dr. Y. Huang for his guidance and assistance in the XRD measurements,

Dr. J. Bohlen for his guidance and assistance in mechanical tests,

Dr. M. Oehring for his valuable time in guiding me to do DSC tests and for his helpful discussions.

Many thanks for the technical and support staff: Mr. Punssen and Mr. Meister for providing assistance in doing the casting and Mr. Kree and Mr. Wiese for extensive assistance in doing light optical- and scanning electron microscopy.

During this research, I met some people whom I need to thank for their excellent and rewarding cooperation and for their support; I would like to thank Prof. Dr. K. Rao from City University of Hong Kong. I am deeply grateful to him. In addition, I would like to thank Dr. Y. Jirásková as well as Dr. J. Buršík from Institute of Physics of Materials, Academy of Science of the Czech Republic. Furthermore, I would like to thank all scientists whom I met during my stay in India (Indian Institute of Science, Bangalore), or while attending conferences in Germany, Switzerland, and in the USA.

I would like to extend my warm thanks to all members of my family, to my parents, brothers and sisters in Jerusalem for supporting me in everything during my study in Germany. Their support is so overwhelming that I cannot mention it in one page… Finally, I am forever grateful to my wife, Mona for her great patience, understanding, and help that gave me the strength to finish my work. This thesis would not have been possible without her support. I dedicate this work to my son Omar and my daughter Dania…

Abstract

The main target for automobile producers nowadays is the prerequisite to reduce the weight of vehicle components and consequently decreasing the output of environmentally harmful substances. Magnesium is the lightest of all commonly used metals and is therefore very attractive for automobile industry. Several studies were undertaken in order to develop new magnesium alloys particularly in powertrain applications. As a result, various Mg-alloys were recently introduced to replace competitive lightweight materials. However, there is still a need to increase the quantity and variety of both cast and wrought Mg-alloys.

The aim of this study is to develop new high temperature creep resistant Mg-alloys based on Mg-Sn system with calcium (Ca) as a ternary alloying element. The series of the selected alloys Mg-Sn-Ca (TX-alloys) contain Sn and Ca in the ranges of 2-6 wt.-% and 0-3 wt.-%, respectively. They should exhibit better creep properties than the mostly used AZ91D-alloy and the high temperature creep resistant AE42-alloy. Therefore, AZ91D- and AE42-alloys supplied by Hydro were also cast as benchmark for this purpose.

The microstructure of the selected alloys was examined using common microscopy equipments: light optical- (LM), scanning electron- (SEM) with energy dispersive X-ray facility as well as the transmission electron microscopy (TEM) and x-ray diffraction (XRD) technique. The alloys were also measured using both thermal analysis methods, namely DTA and DSC. Their results were analyzed and then were compared to thermodynamic calculated data. The corrosion behavior of the mentioned alloys was studied using both corrosion methods, namely salt spray tests and potentio-dynamic measurements. Furthermore, research was undertaken on their mechanical properties, including tensile, compression, hardness, and creep tests. All of the selected alloys were investigated in the as-cast condition.

The results on the microstructure indicate that all of the TX-alloys have at least two phases, namely α-Mg and $Ca_{2-x}Mg_xSn$. Furthermore, binary phases either Mg_2Sn or Mg_2Ca can also be formed in the investigated alloys dependent on the ratio of Sn:Ca (in wt.-%). These ratios with their related phases are divided in to the following three major groups:

- ~ 3:1: ternary $Ca_{2-x}Mg_xSn$ phase,
- < 3:1: ternary $Ca_{2-x}Mg_xSn$ and binary Mg_2Ca,
- > 3:1: ternary $Ca_{2-x}Mg_xSn$ and binary Mg_2Sn.

In addition, a participation of a development of ternary Mg-Sn-Ca phase diagram was raised after DTA and DSC measurements. The results of creep investigations show that a number of TX-alloys, which have a Sn:Ca ratio below 3:1 (in particular less than 2:1) exhibit better creep properties than cast AZ91D-alloy and even better than AE42-alloy. On the other hand, the corrosion behavior and mechanical properties of these alloys need further improvement. Finally, the results of this work, in particular creep results, indicated that some of TX-alloys can be used in automobile industry and thus a contribution will help to develop new class of Al-free Mg-alloys. This development will enable to expand the use of Mg-alloys in elevated temperature applications.

List of symbols and abbreviations

A	Cross sectional area of specimen
Abbr.	Abbreviation
Approx.	Approximately
Ar	Argon gas
AC	As cast
ASTM	American Society for Testing and Materials
ATS	American Testing System
BSE	Back scattered electrons
CO_2	Carbon Dioxide
CYS	Compressive yield strength
DSC	Differential scanning calorimetry
DTA	Differential thermal analysis
E	Young’s modulus
EDX	Energy dispersive X-ray spectroscopy
F	Faraday’s constant
FC	Furnace cooling
HCP	Hexagonal close packed
HPDC	High-pressure die-casting
I_{corr}	Current corrosion
LM	Light optical microscopy
M	Matrix
MagIC	Magnesium Innovation Centre
MM	Misch metal
P	Particle
r	Corrosion rate
RE	Rare earth metals
Rem.	Remainder
SEM	Scanning electron microscopy

TEM	Transmission electron microscopy
T_m	Melting temperature
TYS	Tensile yield strength
UCS	Ultimate compression strength
UTS	Ultimate tensile strength
V	Volt
XRD	X-Ray diffraction
W	Weight loss of specimen in mg
wt.-%	Weight percent
z	Number of electron
σ	Stress
ρ	Density of specimen

Table of Content

1 Introduction

Magnesium and its alloys are rapidly gaining more acceptances in various applications, such as in the automotive, aerospace and electronic industries. They serve as an alternative substitution to aluminum alloys and steel due to their attractive technical and environmental properties [1-10]. Their major advantages are:

- Lightest structural material,
- Higher strength-to-weight ratio,
- Good castability,
- Good machinability,
- Acceptable weldability under controlled atmosphere,
- Recyclable and thus fewer raw resources are consumed.

However, the use of magnesium and its alloys is still restricted, due to the following drawbacks:

- Low elastic modulus,
- Limited cold workability and toughness,
- Restricted high strength and creep resistance at high temperature,
- Poor corrosion resistance (in some applications).

The most significant and economically competitive used magnesium alloys are based on the magnesium-aluminum system, such as AZ91 (Mg-Al-Zn) and AM50/60 (Mg-Al-Mn) [4,8]. They offer good die-castability, reasonable room-temperature strength or ductility, and even good corrosion resistance [11]. However, the mentioned alloys are unsuitable for power-train applications due to their poor mechanical properties at elevated temperatures [12-14].

In the last two decades, a significant rapid growth in the enhancement and development of magnesium alloys has been reviewed [15-20]. The current increase is driven by the introduction of a number of environmental legislations started by the Kyoto protocol. They recommend automobile producers to use additional quantities of magnesium alloy components. The target of this recommendation is to reduce the weight of vehicles, which leads to considerable decreasing of fuel consumption and thus reducing CO_2-emission [21-25]. Furthermore, the development of casting technology of magnesium alloys and the improvement of corrosion resistance by reducing the impurities generates additional interest in magnesium [4]. As a result, several studies and research were carried out in order to develop new magnesium alloys with high-temperature properties better than the AZ- and AM- series alloys. The major companies of the automotive industry are technically and commercially significantly involved in the development and application of new Mg-alloys [26].

Some of the new modified magnesium alloys are based on the mentioned alloys sytems AZ and AM [27] as well as the AS (Mg-Al-Si) [28-30], AE (Mg-Al-RE) [31-35], AX (Mg-Al-Ca) [36-39], MRI (Mg-Al-Ca-Sr) [40-44], and AJ (Mg-Al-Sr) [45-52]. Most of them can only partially meet the required properties. Alloys, such as Mg-Al-Ca, Mg-Al-Ca-RE, and Mg-Al-RE alloys also suffer from poor diecastability [36]; others such as, Mg-Al-Ca-RE or Mg-Al-Ca-Sr-RE have disadvantages in terms of insignificant performance improvements. In addition, Mg-alloys containing RE are expensive alloys due to the presence of rare earth metals.

Recently, Noranda Inc. Technology Center and Avisma successfully developed high-temperature creep resistant AJ62- and AS31-alloys, respectively. Currently, BMW is using the AJ62x-alloy to produce the world's first composite six-cylinder-aluminum-magnesium-crankcase [45-52] and Daimler is applying die cast AS31-alloy to fabricate seven speed automatic transmission housing (7G-TRONIC) [28-30].

In spite of the mentioned developed alloys, a development of an inexpensive new high temperature creep resistant Mg-alloys with good castability will increase the quantity and variety of Mg-alloys. In this study, extensive experimental work has been carried out to examine the Al-free Mg-alloys based on Mg-Sn-Ca-alloys. The selected Mg-Sn-Ca alloys system with various compositions was preferred, due to the achievable of the following summarized reasons:

- The high solid solubility of tin (14.48 wt.-%),
- Sn also has a reputation of castability improvement,
- Sn addition proves to be beneficial in providing corrosion resistance,
- Low density of Ca of 1.55 gcm^{-3},
- Ca can improve the creep resistance of Mg-alloys,
- The high melting points of the precipitates of Mg_2Sn (T_m = 770°C), and Mg_2Ca (T_m = 715°C) as well as the thermally stable CaMaSn phase
- Their inexpensive price compared to other alloying elements, in particular rare earth elements.

2 Literature review

2.1 Pure magnesium

Magnesium is the sixth most abundant element in the earth's crust and even the third most dissolved abundant element in seawater [53-54]. In general, Mg is never found free in nature. It can be obtained from various minerals. Some of the most nature occurring minerals include magnesite (28.80 wt.-%), serpentine (26.3 wt.-%), dolomite (13.00 wt.-%), bischofite (11.96 wt.-%), and carnallite (8.75 wt.-%). It attains an average of 0.13 wt.-% in seawater but with 4.20 wt.-% in Dead Sea [4]. The English chemist Sir H. Davy achieved the first isolation of magnesium metal approx. 200 years ago [5]. However, the initial commercial production of Mg goes back to the German scientist R. Bunsen in 1852. Nowadays, magnesium can be produced by two basic commercial process technologies, namely the electrolytic and the thermal (Pidgeon) process [55-57].

Table (1): Properties of magnesium in comparison to aluminum (Al), titanium (Ti), and iron (Fe).

Property	Units	Mg	Al	Ti	Fe
Atomic number		12	13	22	26
Atomic radius	**[nm]**	0.145	0.118	0.176	0.156
Atomic weight	**[g mol^{-1}]**	24.30	26.98	47.87	55.85
Density at RT	**[g cm^{-3}]**	1.74	2.70	4.51	7.87
Melting point	**[°C]**	650.00	660.00	1668.00	1538.00
Boiling point	**[°C]**	1090.00	2519.00	3287.00	2861.00
Thermal conductivity at RT	**[W m^{-1} K^{-1}]**	160.00	235.00	22.00	80.00
Specific heat at 20°C	**[J kg^{-1}K^{-1}]**	1025.00	904.00	520.00	449.00
E-Modulus	**[GPa]**	45.00	70.00	116.00	210.00
Strength	**[MPa]**	90.00	98.00	150.00	275.00
Specific strength	**[m x10^{6}]**	52.00	36.00	33.26	35.00

The properties of magnesium are highly attractive due to its low density compared to other common structural metals. Its density is only two-third of Al, two-fifth of Ti, and even one quarter of the weight of Fe. In addition, magnesium is better than other metals, such as Al or Fe in terms of heat dissipation and heat transfer due to its high thermal conductivity of 160 W/mK. It also has a higher specific heat value of 1025 J/kgK than Al, Ti, and Fe. Its machinability, turning, milling, and drilling processes are the easiest compared to other metals [2].

The elastic modulus of magnesium alloys is relatively low at approx. 45 GPa, compared to approx. 70 GPa, 116 GPa, and 210 GPa for aluminum, titanium, and steel, respectively. Furthermore, its tensile and yield strength is relatively low as well. However, its specific strength (strength/density) is higher compared to other metals. The most essential properties of pure Mg in comparison to Al, Ti and Fe are listed in Table (1) [16].

2.2 Magnesium alloys

Pure magnesium itself is too soft for use in most industrial applications [2]. Its properties, like creep resistance, strength, or ductility can be improved after the addition of alloying elements. Their application is however dependent on the required performance [42]. Aluminum (Al), calcium (Ca), manganese (Mn), rare-earths (RE), silicon (Si), strontium (Sr), tin (Sn), and zinc (Zn) are all examples of currently used alloying elements.

2.2.1 Designation

The method of codification used to designate magnesium alloy castings is identified by a system established by the American Society for Testing and Materials (ASTM) B275 [58]. It gives an idea of the chemical composition of an alloy, with the first two letters representing the major alloying elements followed by their respective weight percentage rounded off to whole numbers of these constituents. They are followed by a serial letter at the end (A, B, C, D and E) which designates the stage of development or degree of purity of the alloy. The ASTM B296 includes a coding system for the temper designation of magnesium alloys. Some of them are as fabricated (F), solution heat-treated (T4) and solution heat-treated and artificially aged (T6). Table (2) presents a review of the letters that designate Mg-alloying elements. However, it can be seen that calcium is not classified in the ASTM system. In some publications, Ca was tentatively designated as C because copper was not a significant alloying element in magnesium alloys [59]. However, after the development of the copper containing secondary alloys ACZ912 [60], calcium was subsequently designated as X [61]. This designation will also be given in this work.

Examples of the designations are AZ91D- and AE42-alloy, which contain aluminum as a major alloying element. While AZ91D contains zinc as a ternary alloying element and the letter “D” represents the fourth stage of its development, AE42-alloy contains rare earth elements as a ternary one. Both of

AZ91D- and AE42-alloys were investigated in this study and thus their chemical compositions are given in the experimental procedures in section (3.1).

Table (2): Code letters for designation system from ASTM of Mg-alloys, (*) excluded Ca: X.

Letter	Element	Letter	Element	Letter	Element
A	Aluminum	K	Zirconium	R	Chromium
B	Bismuth	L	Lithium	S	Silicon
C	Copper	M	Manganese	T	Tin
D	Cadmium	N	Nickel	W	Yttrium
E	Rare Earths	P	Lead	Z	Zinc
H	Thorium	Q	Silver	(*)X	Calcium

2.2.2 Mg-alloys based on Mg-Al alloy system

Currently, magnesium alloys have found use in many various commercial applications [62-63]. The mostly applied processes for the fabrication of these alloys are high-pressure die-casting (HPDC) besides the permanent mould, and sand casting [64-67]. The HPDC alloys exhibit a better quality of microstructure than the permanent mold cast alloys. They generally demonstrate a high potential for structural applications, due to their improved mechanical properties compared to cast components. Permanent mold cast and sand casting are used for alloys that show restricted castability like the Al-free magnesium alloys.

The development of Mg-alloys depends on the required properties of a desired component [91]. It can be divided into three main areas:

- High yield strength for structural parts,
- High ductility and energy absorption for safety parts,
- Creep resistance for elevated temperature components.

The most common commercial Mg-alloys currently used are based on Mg-Al system, such as AZ or AM series alloys. Recently, several studies were conducted in order to develop new magnesium alloys with an optimal combination of creep and corrosion resistance. Several Mg-Al alloys, such as AZ, AM, AS, AE, AX, and AJ are given in Table (3) showing their major and ternary alloing elements.

Table (3): Most common Mg-Al based alloys system.

Alloys	
Mg-Al based system	**Abbreviation**
Mg-Al-Zn	AZ
Mg-Al-Mn	AM
Mg-Al-Si	AS
Mg-Al-RE	AE
Mg-Al-Ca	AX, MRI
Mg-Al-Sr	AJ

Mg-Al-Zn alloys system (AZ-alloys)

The currently most widely used AZ91D-alloy represents the typical Mg-alloy. It is a high strength alloy at room temperature, which offers a good combination of excellent die castability, salt-spray corrosion resistance and good strength [92]. The high-pressure die-casting alloy AZ91D is used in automobile parts, such as in transmission castings, brake pedal assemblies, clutch housings, and roof frame assemblies [4].

Mg-Al-Mn alloys system (AM-alloys)

The ductility of AM-alloys, such as AM50 and AM60 is improved compared to AZ91-alloy due to the reduction of the amount of Al and thus the decreasing of the volume fraction of the β-$Mg_{17}Al_{12}$ phase [13,93]. The AZ and AM based alloys are limited to low temperature applications where they are known to lose their creep resistance at temperatures above 120 °C [12-14,66]. The high ductility AM-alloys are suitable for some automobile components where greater ductility is required. Examples of AM-alloys (AM50/60) applications include braces, steering wheel armatures, instrument panels, and seat frames [8].

Mg-Al-Si alloy system (AS-alloys)

The AS-alloys, like AS21 and AS41 have been reported as alternative alloys for elevated temperature applications [94]. Due to the presence of the stable Mg_2Si phase, considerable improvements can be obtained in the Mg-Al-Si alloys [95]. The most considerable application of magnesium in the automobile industry was after Volkswagen started to use AS41-alloy to produce the air-cooled engine in the Beetle cars seven decades ago [8,10,26,50,93,94]. However, when a higher performance was required for the new water-cooled engine the fabrication of magnesium engine was ceased [8]. Hydro Magnesium announced the development of a creep resistant die cast magnesium alloy named AS21X, which is based on AS21-alloy. Only corrosion resistance improvement was achieved due to a small addition of rare earth misch-metal (MM) combined with a reduced level of Mn. The other drawbacks of AS21-alloy like lower yield strength and inadequate castability for complex parts remained unchanged for the new alloy. The new seven speed automatic transmission housing die cast (7G-TRONIC) (AS31-alloy) was produced by Daimler in order to acquire a compromise between castability and creep resistance [26].

Mg-Al-RE alloy system (AE-alloys)

The well-known AE42-alloy offers small improvement in creep and corrosion resistance as well. The favorable properties of AE-alloys have been reported by Foerster in the 1970’s [96,97] and by several publications [28, 31-33]. Bakke et al. [33] mentioned that the addition of RE elements to some magnesium alloys might also enhance the ductility and strength. This improvement is due to the formation of $Al_{11}RE_3$ phase, which replaced the weak β-$Mg_{17}Al_{12}$ phase [31,98]. However, the mentioned properties deteriorate rapidly when the temperature exceeds 150 °C [99]. This deterioration occurs due to the formation of the undesired β-$Mg_{17}Al_{12}$ phase that can be formed from the unstable $Al_{11}RE_3$ phase [37,92-101]. Unfortunately, this alloy also has poor castability compared to AZ91D or AM50/60 alloy and thus its use is still restricted. General Motors presented a Corvette Z06 engine cradle as an example of a temperature-exposed load bearing chassis part [102]. The interest in the AE-alloys was renewed and a new die casting alloy AE44 was developed by Hydro [35]. The new alloy offers excellent castability and mechanical properties besides recycling qualities. However, the mentioned alloy is uneconomical due to the use of RE elements in the fabrication of this alloy [28,99]. This initiated a search for replacing the RE metals by an inexpensive one. Therefore, calcium additions became more common in the development of economically creep resistant magnesium alloys [96,103].

Mg-Al-Ca alloy system (AX-alloys)

The Mg-Al-Ca alloys, such as the newly developed AX51 showed a creep resistance at 150 °C similar to the AE42 with a corrosion resistance like the AZ91D-alloy [37,38]. Nissan has also exhibit improved creep strength which exceeds the AE42-alloy [15]. A combination of Al-RE and Al-Ca phases were detected in the Mg-Al-Ca-RE alloys and thus this alloy has a better creep resistance than AE42-alloy [39]. Later, Honda developed a new alloy for application in oil pans for hybrid vehicles. The ACM522 alloy was based on AM50 alloy with the addition of misch-metal and calcium [27]. It was reported that this alloy exhibits creep strength in the ranges of 120°C-200°C similar to that of aluminum alloy A380. However, the mentioned alloy has a low ductility that can restrict its applications.

Mg-Al-Ca alloy system (MRI-alloys)

Volkswagen AG and Dead Sea Magnesium developed new alloys by adding Sr and other alloying elements to the Mg-Al-Ca alloy [40-44]. The codenamed MRI-alloys such as MRI153 and MRI230 alloys exhibit elevated temperature performance at 150 °C and 180°C, respectively. In addition, MRI153-alloy represents good die castability similar to AZ91-alloy. This alloy is successfully used in Volkswagen cast gearbox and clutch housing.

Mg-Al-Sr alloy system (AJ-alloys)

The introduction of Sr in Mg-Al alloys leads to the formation of additional high temperature phases like Al_2Sr, Al_4Sr, and $Mg_{13}Al_3Sr$ [37]. Its addition also decreases the aluminum content in solid solution and thus reduces the fraction of the thermally instable β-$Mg_{17}Al_{12}$ phase. The mentioned phases generally improve the creep performance while they do not affect other significant properties like tensile strength, elongation, and castability at elevated temperatures [45]. The first generation of Mg-Al-Sr was based on the AM50-alloy with addition of 1.7-2.0 % Sr. The developed AJ52-alloy shows good castability when the correct process parameters are used and exhibits good creep resistance in the temperature range of 150 ºC-175 ºC. This alloy was used to fabricate the first gearbox housing. Later, a new AJ62-alloy with 6 % aluminum and 2 % strontium was also developed [45-46,48]. The newly developed AJ62x offers even more advantages. It exhibits superior creep performance, high ductility (AJ62Lx-alloy), very good die-castability and excellent corrosion resistance [45,49]. The development of AJ-alloys was reported in investigations by Noranda Inc. Technology Center [45-47,50].

2.3 Phase diagrams

Mg-alloys can be described by the chemical composition and by the presence of their phases as well. This can be illustrated in the form of phase diagrams, which only show the equilibrium condition for binary and ternary systems. However, they do not provide information concerning the physical shape or dispersion of the phases that might emerge in non-equilibrium processing.

In this study, the investigated Mg-alloys contain Sn as a major alloying element and Ca as a ternary one. Therefore, this section will only explicitly explain both of the alloying elements of Sn, Ca, and their related phase diagrams.

2.3.1 Mg-Sn Phase diagram

Sn addition to Mg was studied in the beginning of the 20th century [68-71] and was later reported by Hansen et al. [72]. They pointed out the presence of Mg_2Sn compound in the Mg-Sn system. Investigations on the liquidus curves of the Mg-Sn system Sn additions were also reinvestigated by Steiner et al. [73] and by Nayek et al. [74,75]. Furthermore, Ellmer et al. [76] examined only the liquidus on the Sn-rich Mg-Sn alloys. Nayeb-Hashemi and Clark [77] reported later the binary Mg-Sn phase diagram. Fries [78] calculated the phase diagram and Kozlov et al. [79] indicated a correction in the thermodynamic data.

Various phases have been obtained in the Mg-Sn phase diagram. These phases are the liquid, hcp-(Mg), bct-αSn, diamond-βSn, and the Mg_2Sn phase. Figure (1) illustrates the Mg-Sn phase diagram according to Nayeb-Hashemi and Clark showing the high solubility of Sn of 3.35 at.-% (14.48 wt.-%) in solid magnesium at 561.2 °C. The large solubility of Sn drops sharply to 0.45 wt.-% at 200°C. Figure (2) presents the Mg-Sn phase diagram according to Fries showing slightly different value with a solid solubility of Sn in magnesium observed at 563 °C. According to the same author, the experiment study determined that there is a small amount of solubility of Sn in (Mg) nevertheless there was no observation of solubility of Mg in βSn. In this system, there are two eutectic reactions: the first one is L ↔ (Mg) + Mg_2Sn at 563 °C on Mg-rich side. This temperature is 2.8 °C higher than the one presented in Figure (1)). The second eutectic is L ↔ βSn + Mg_2Sn at 204 °C on the Sn-rich side (at a temperature 0.5 °C higher than in Figure (1)). The high melting temperature of Mg_2Sn phase is 774 °C as calculated by Fries, Figure (2), which is with 3.5 °C more than the one mentioned by Nayeb-Hashemi and Clark [77] in Figure (1)).

In addition, the low melting point of Sn (232°C) makes it very simple to alloy. It dissolves in liquid magnesium with an exothermic reaction due to a small negative enthalpy. Comparison between the values of the two phase diagrams are listed in Table (4).

Table (4): Comparison of observed phases and eutectic temperature of Mg-Sn phase diagram according to Nayeb-Hashemi and Clark as well as Fries.

	Nayeb-Hashemi and Clark [77]	Fries [78]
Max. solid solubility	3.35 at.-% or 14.48 wt.-%	
T_m of Mg_2Sn / °C	770.5	774.0
First eutectic / °C	561.2	563.0
Second eutectic / °C	203.5	204.0

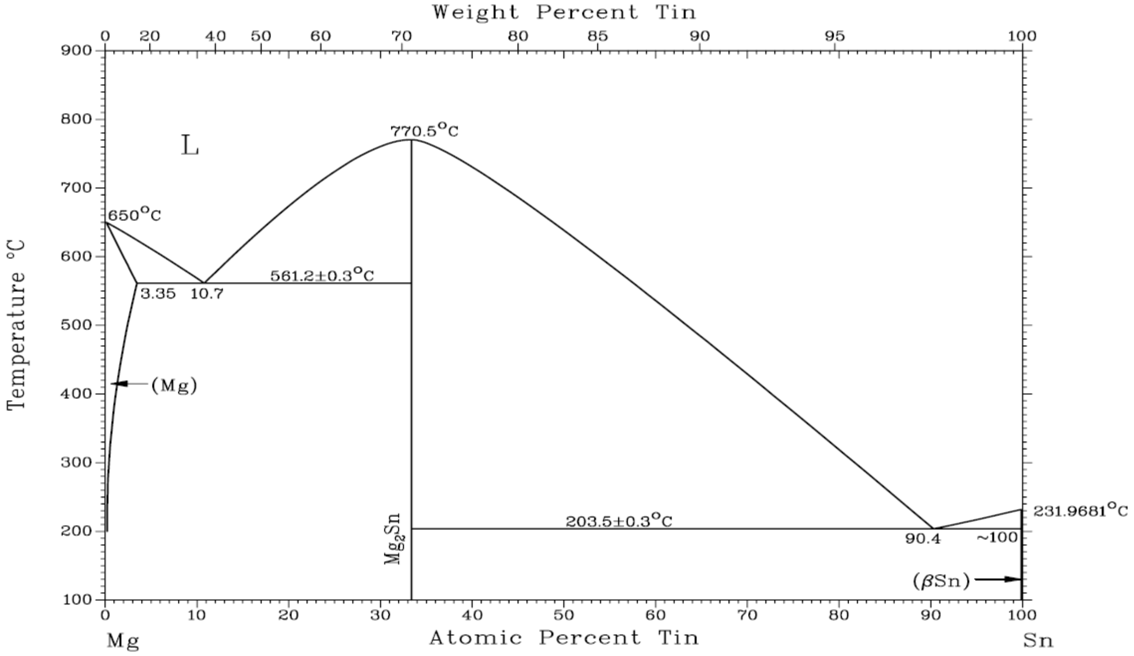

Figure (1): Mg-Sn phase diagram reported by Nayeb-Hashemi and Clark [77].

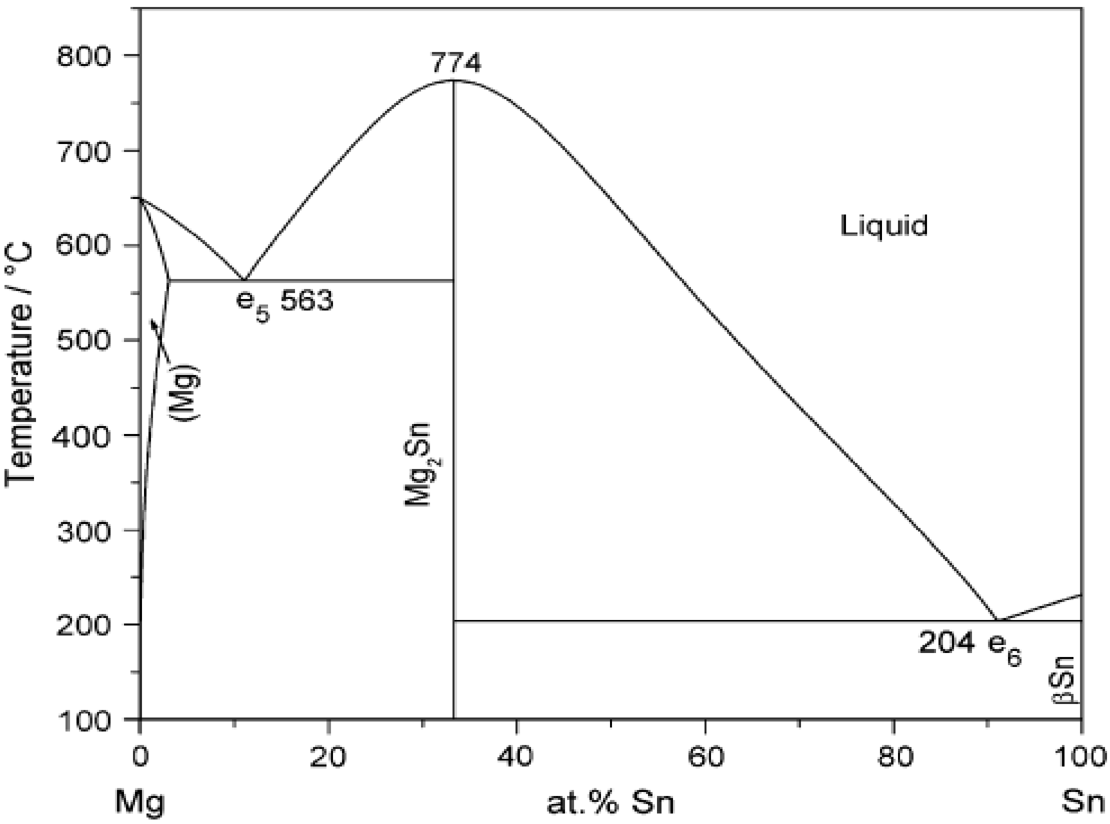

Figure (2): Mg-Sn phase diagram calculated from the data given by Fries [78, 79].

2.3.2 Mg-Ca Phase diagram

The solubility of Ca in Mg was investigated long ago [80-84]. The Mg-Ca phase diagram, which is illustrated in Figure (3) was reported by Nayeb-Hashemi and Clark [77]. The thermodynamic modeling of the Mg-Ca system has been newly mentioned in [85-86]. The calculated Mg-Ca phase diagram is presented in Figure (4) showing the five phases, liquid, hcp-(Mg), fcc-αCa, bcc-βCa, and Mg_2Ca. Ca has a low solubility in Mg of 0.82 at.-% (1.34 wt.-%) at 516.5°C [77]. There are three variant reactions: the first one is on the magnesium-rich side, namely L ↔ (Mg) + Mg_2Ca at 516.5 °C according to Nayeb-Hashemi and Clark [77] and with 517 °C reported by [85,86]. The second reaction is on the calcium-rich side L ↔ βCa + Mg_2Ca at 445 °C (446 °C). The third one is congruent melting of Mg_2Ca compound L ↔ Mg_2Ca at 715 °C (710 °C).

Table (5) presents the differences between literature review of Nayeb-Hashemi and Clark [77] and the results obtained by Kozlov et al. [79].

Table (5): Comparison of observed phases and eutectic temperature of Mg-Ca phase diagram

	Nayeb-Hashemi and Clark [77]	Kozlov et al. [79].
Max. solid solubility	0.82 at.-% or 1.34 wt.-%	
T_m of Mg_2Ca / °C	715.0	710.0
First eutectic / °C	516.5	517.0
Second eutectic / °C	445.0	446.0

Calcium proves to be a very interesting alloying element due to its low density of 1.55 gcm^{-3}. The addition of Ca becomes more common in the development of new economically high temperature creep resistant Mg-alloys. It was reported that the creep resistance of Mg-Al alloys could be improved due to the formation of the mentioned Mg_2Ca phase. The addition of calcium can also refine the microstructure of Mg-alloys and thus the mechanical properties can be improved [87].

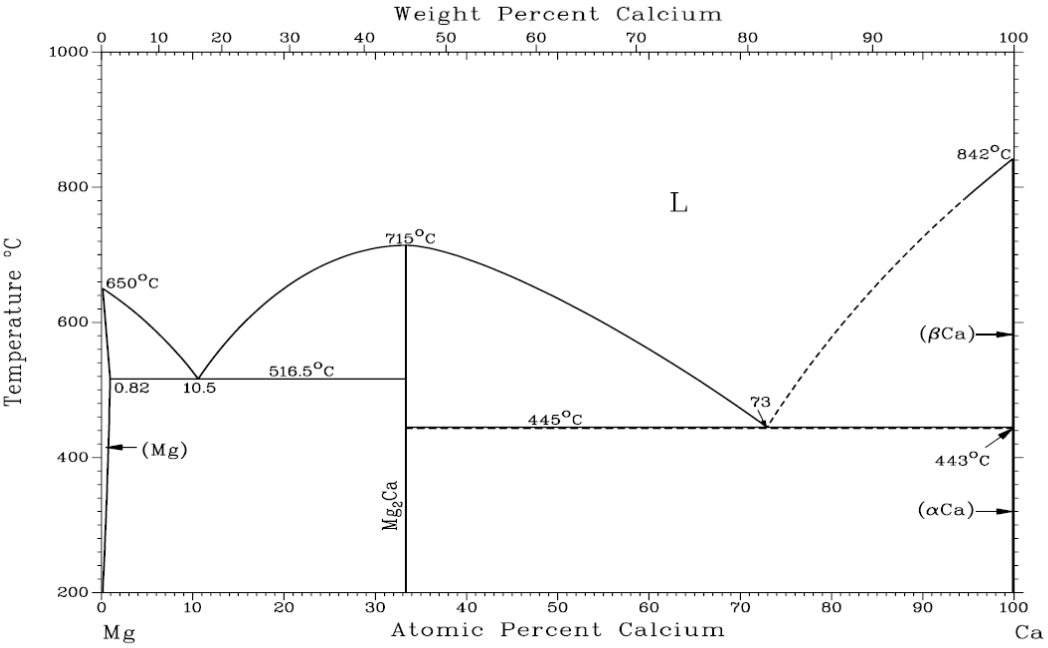

Figure (3): Mg-Ca phase diagram [77].

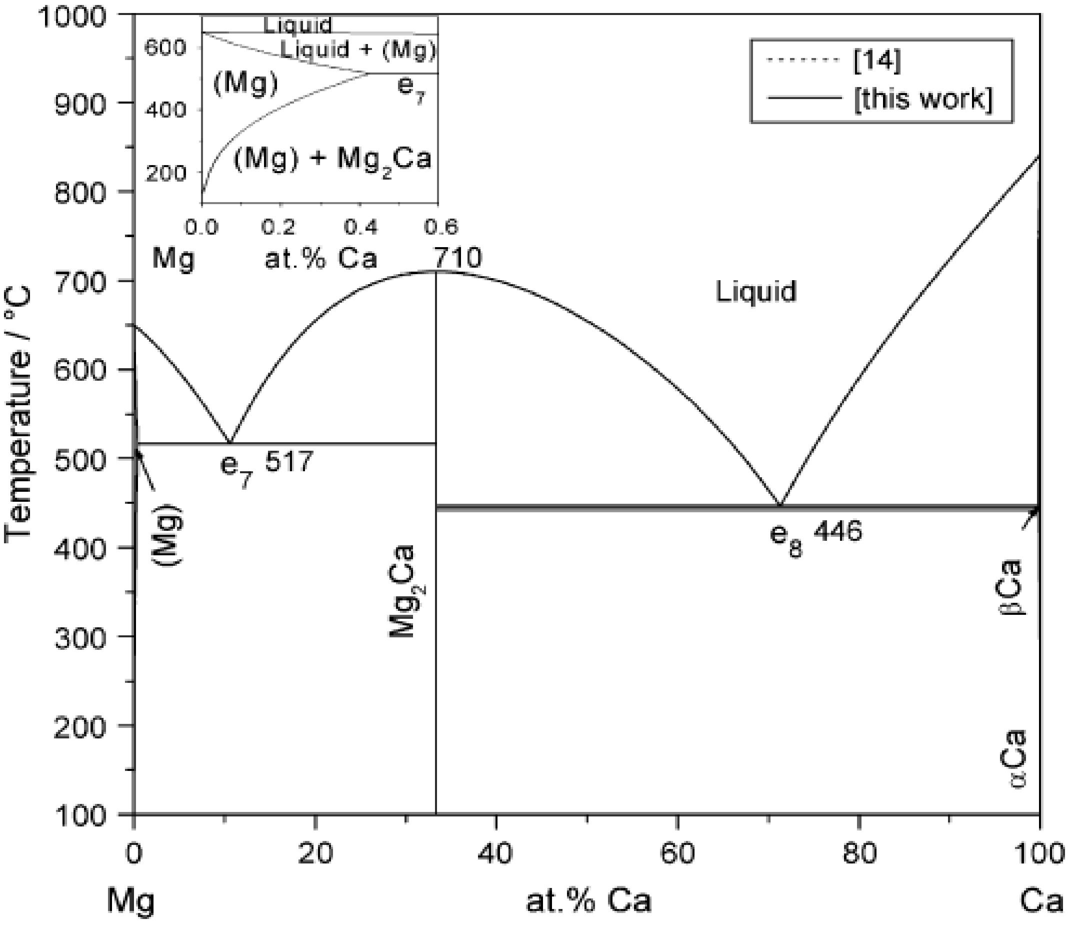

Figure (4): Mg-Ca phase diagram at.-% and wt.-% [79].

2.3.3 Ca-Sn Phase diagram

The phase diagram of Ca-Sn was reported by W. Hume-Rothery [70] long ago. Figure (5) shows the binary phase diagram of Ca-Sn according to Nayeb-Hashemi and Clark [77]. The thermodynamic modeling based on a combination of key experimental work and Calphad-technique involving also first-principle output of Ca-Sn system reported by Ohno et al. [88] is illustrated in Figure (6). It can be seen that three compounds, Ca_2Sn, CaSn and $CaSn_3$ melt congruently, while the other four compounds (Ca_5Sn_3, Ca_3Sn_{23}, Ca_7Sn_6 and $Ca_{31}Sn_{20}$) melt through peritectic reactions.

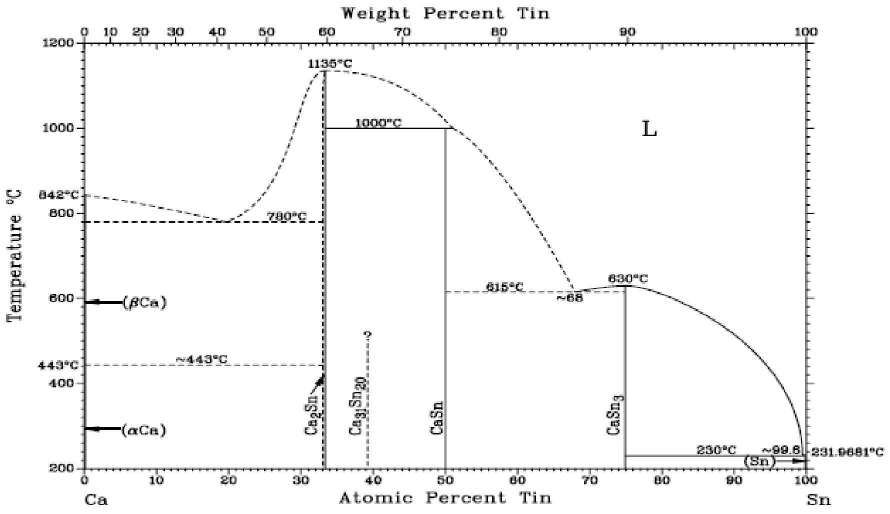

Figure (5): Ca-Sn phase diagram [68].

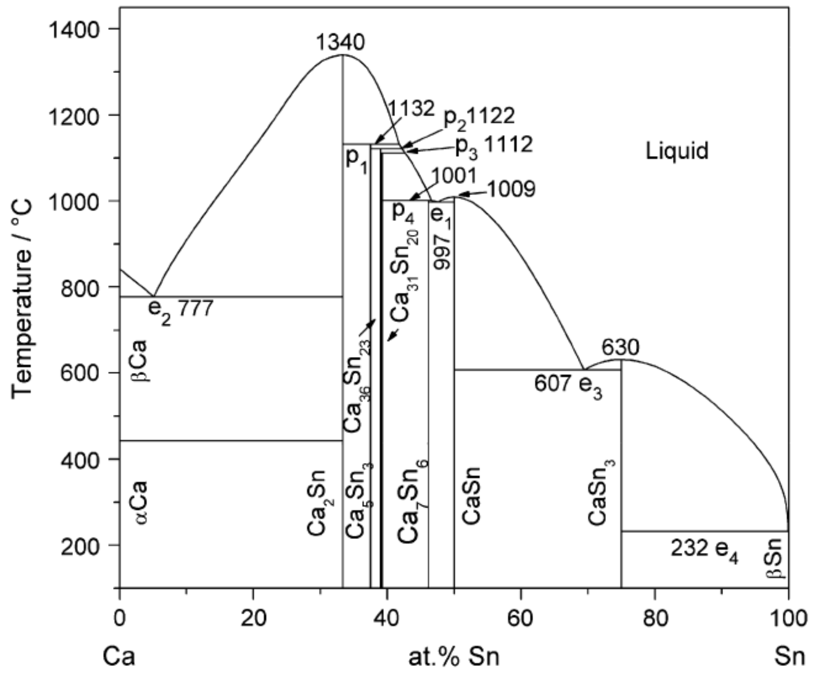

Figure (6): Ca-Sn phase diagram [88].

2.3.4 Mg-Sn-Ca Phase diagram

The ternary Mg-Sn-Ca phase diagram has recently obtained great attention and was preliminarily developed by Gröbner et al. [89] and given quantitatively in detail by Kozlov et al. [79,90]. The newly developed ternary Mg-Sn-Ca phase diagram confirmed the presence of the ternary $Ca_{2-x}Mg_xSn$ in equilibrium with (Mg). The notation $Ca_{2-x}Mg_xSn$ is shorthand for the terminal solid solution point of the $Ca_{2-x}Mg_xSn$. The formation of Mg_2Sn or Mg_2Ca phase was expected according to the mentioned binary Mg-Sn and Mg-Ca phase diagrams. The first investigation of phase equilibrium for ranges of composition and temperature of the Mg-Sn-Ca system was performed in [90], see Figures (7a-b). In the mentioned study a combination of experiments, first-principle calculations of finite temperature properties of the compounds and Calphad computational thermochemistry was employed [79,90]. Phase diagram investigations of Mg-Sn-Ca alloys have been performed also involving thermal analysis. In general, this technique is also used to indicate the liquidus and solidus temperatures of magnesium alloys.

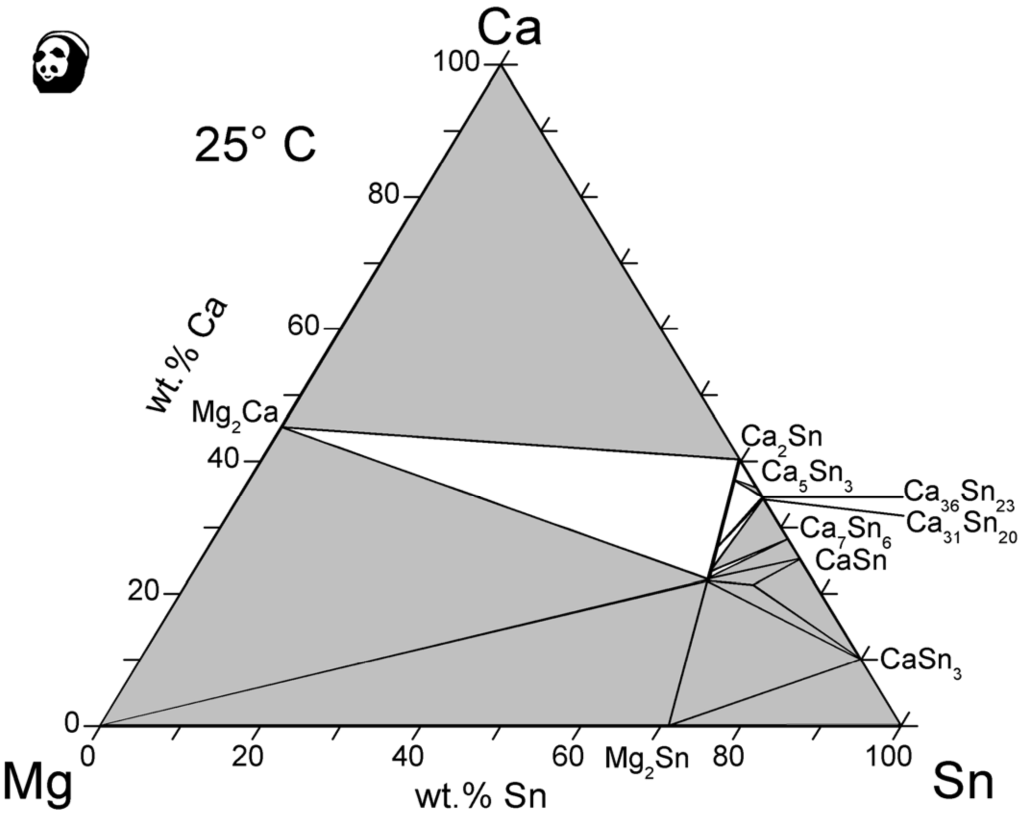

(a)

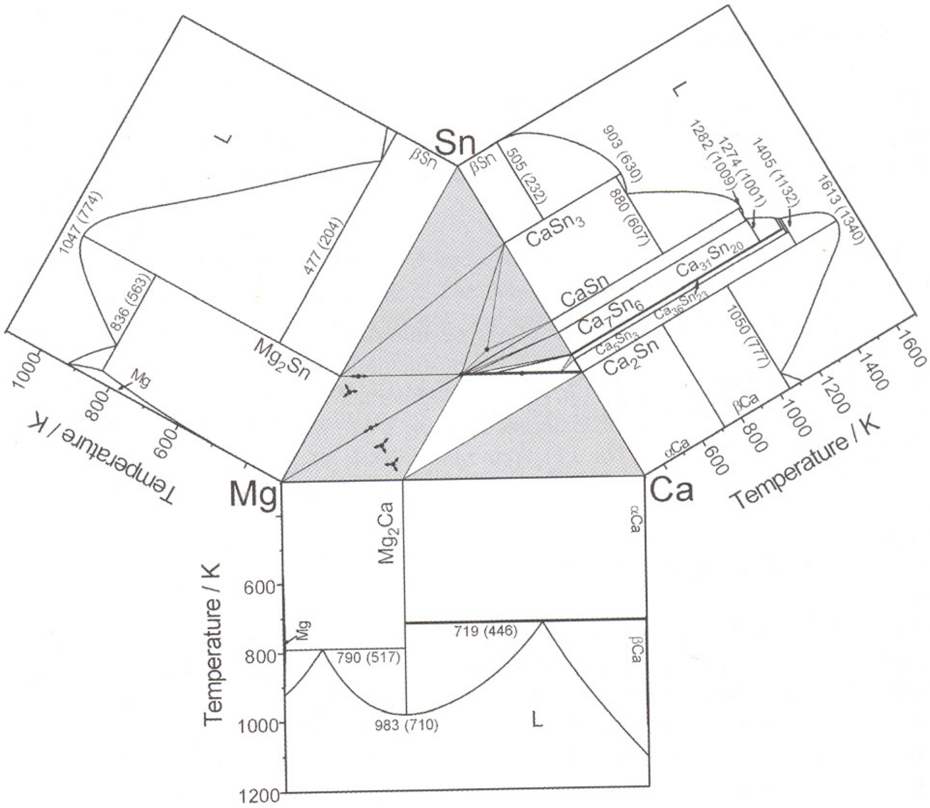

(b)

Figure (7): Calculated isothermal section of the Mg-Sn-Ca phase diagram at 25 °C [89].

Figure (7) illustrates a room-temperature isothermal section of the Mg-Sn-Ca system. The calculated results confirm the ternary $Ca_{2-x}Mg_xSn$ phase, which forms during solidification. The calculated phase diagrams and phase identification have significant implications to creep resistance of Mg-alloys and provide important guidance in further alloy development and optimization.

2.4 Development of Mg-alloys containing Sn (past-present)

2.4.1 Past

Sn as a major alloying element

Some patents of Mg-alloys containing Sn were reported in the 1930s [104-108]. Wood [104-105] examined the Mg-Sn-Zn alloys system and developed an alloy that has good physical and tensile properties in combination with good corrosion resistance. Murphy [106] investigated the corrosion resistance of the Mg-Sn-Zn by addition of Cd to this alloys system. The Mg-Sn-Zn-Cd retains its mechanical properties after this examination.

Sn as a ternary alloying element

Gann et al. [107] examined the Mg-Cd-Sn alloys system and developed a high tensile strength with a good corrosion resistance. The investigation of the Mg-Al-Sn-Ca system was reported by Bradbury [108]. The developed alloy has an excellent high temperature creep resistant at approx. 130-300°C in combination with good casting qualities, corrosion resistance and free micro porosity.

2.4.2 Present

Sn as a major alloying element

The interest in tin additions in Mg-alloys has been renewed in recent years and Japanese patents included Sn among the alloying element that is beneficial for creep properties [109-112]. The effect of Sn addition was also investigated in Mg-Sn-Si in various aspects, especially in creep resistance [110]. In other publications, the influence of Sn on mechanical properties of Mg-Al alloys has been investigated. Bakke et al. [113] reported the presence of the Mg_2Sn precipitation in the Mg-Sn alloys system. It was pointed out that the precipitates are expected to facilitate a stabilized matrix structure at elevated temperature, which is required for creep resistance. It was also reported by Bakke et al. [91,113] that the castability of Mg-alloys containing Sn can be improved by the addition of Al. The microstructure of Mg-Al-Sn alloys consists of α-Mg matrix with Al and Sn in solid solution and containing eutectic Mg-Mg_2Sn at grain boundaries. The Mg_2Sn phase is pushed into pockets at grain nodes with increasing amount of Al. While the creep resistance of the investigated alloys increases with addition of further amount of Sn, it decreases with rising Al-content. Furthermore, alloys with high Sn and Al contents demonstrate tensile yield strength above that of AZ91D in addition to unaffected UTS values [113].

Bowles et al. [114] studied the microstructure and corrosion properties of Mg-Sn based alloys with addition of various composition of Al. The Mg-Sn system shows promise corrosion and creep resistance due to the formation of Mg_2Sn phase (Figure (1)). Additionally, Bowles et al. [115] also examined the creep properties of Mg-Sn based alloys with addition of various ternary allying elements, such as Al, Zn, RE [115]. Mg-Sn-Al was selected with various compositions in order to be investigated on its microstructure and creep. Due to the presence of the $Mg_{17}Al_{12}$ phase, the Mg-Sn-Al alloys exhibit poor creep resistance. Later, Anopuo et al. [116] investigated the Mg-Sn-Si system. The examination was undertaken to determine the phases that can be formed in the Mg-5Sn-1Si and their effect on the corrosion properties. Both Mg_2Sn and Mg_2Si were detected in this study. It was reported, that the investigated Mg-5Sn-1Si alloys exhibit bad corrosion resistance.

Kang et al. [117] examined the Mg-Sn-Al-Si in term of its microstructure and creep properties. It was reported that the mentioned die cast TAS831 forms both of the Mg_2Sn and Mg_2Si phases. The presence of the mentioned phases significantly improves the creep resistance of the designated TAS831 alloy. Later, Kang et al. [118] studied the effect of the formation mechanism of the nano-particles during solidification and their effect on the creep properties of the alloy TAS831. The addition of Zn to the Mg-Sn alloys was investigated by Sasaki et al. [119]. It was reported that the addition of Zn leads to finer precipitations of Mg_2Sn and the precipitations are uniformed dispersed. In addition, the results of the hardness investigations on the Mg-2.2at.-%Sn increase from 60 HV to 80 HV after the addition of 0.5 at.-% of Zn. The addition of Zn and Na to the based alloys Mg-Sn and the effect of age hardening were examined by Mendis et al. [120]. They reported that the addition of Zn to the Mg-1.3at.-%Sn alloy results to significant effect on age behavior. Furthermore, the addition of Na and Zn leads in further improvement in the age hardening response and substantial accelerations in the time to peak hardness at 200°C.

The microstructure, tensile properties, and creep behavior of the binary Mg-Sn alloys system with Sn in the ranges of 1 to 10 wt.-% has been studied by Liu et al. [121]. The investigation confirmed the presence of the Mg_2Sn phase. It was also mentioned that the microhardness of the studied alloys rises when the amount of Sn increases. In addition, the Mg-5Sn exhibit higher values of tensile and elongation, while the Mg-10Sn exhibit at parameter (150°C at 30MPa) good creep resistance, which is also better than the AE42-alloy. Liu et al. [122] examined the microstructure and mechanical properties of Mg-5Sn based alloy with addition of 0-2.6 wt.-% of Dy (Dy present neodymium “Nd” and praseodymium “Pr”). The $Sn_x(Nd,Pr)_y$ phase was defected in various shapes dependent on the amount of Dy. Furthermore, it was reported that Mg-5Sn and Mg-5Sn-2Dy alloys offer good compressive properties. In other publication mentioned by Liu et al. [123], the tensile and indentation creep behavior of Mg-5Sn with addition of 2wt.-% of Dy as ternary alloying element was further investigated. The results showed that the investigated alloys exhibit comparative tensile properties and even significantly better indentation creep better than AE42-alloy. Wei et al. [124] investigated the effect of the La additions on the Mg-Sn binary alloys system. It was reported that the addition of 2wt.-% of La to the Mg-5Sn, Mg-6.5Sn, and Mg-8.5Sn alloys leads for improvement of the creep resistance.

Sn as a ternary alloying element

The effect of tin additions on the microstructure and mechanical properties of rolled Mg-MM alloy (MM: misch-metal) sheets was investigated by [125]. The shape and the size of the phases changed and decreased and thus the ductility of the Mg-MM-Sn-alloy improves. The Mg-Zn-Sn based alloys were also reinvestigated by A. Katsman et al. [126] and Cohen et al. [127]. The Mg_2Sn and MgZn phases were detected in the mentioned system. However, the studied system showed insufficient structural stability at elevated temperatures. Therefore, additional research has been done by Harosh et al. [128] investigated the microstructure of the Mg-Zn-Sn-Al system. The mentioned system was selected to investigate the effect of Al additions to the mentioned system Mg-Zn-Sn [126,127]. The Mg-Zn-Sn-Al showed a stable microstructure after the addition of Al due to the formation of the precipitates, which exhibit higher temperatures in comparison to the same precipitates in the Mg-Zn-Sn alloys system. Furthermore, Jehua et al. [129-130] studied the effect of Sn addition on microstructure and mechanical properties of Mg-Zn-Al.

2.4.3 Mg-Sn-Ca alloys system

Very few studied were published about the Mg-Sn-Ca based alloys system. The mechanical properties including the creep resistance were investigated besides the corrosion resistance. Bowles et al. [115] examined Mg-Sn based alloys with addition of various ternary allying elements, in particular Ca. The creep resistance of the selected alloys concluded that the Mg-Sn-Ca alloy system exhibit a promising creep resistance compared to other investigated alloys. Anopuo et al. [116] determine the (Ca,Mg,Sn) phase that can be formed in the alloys Mg-5Sn-1Ca and Mg-5Sn-2Ca. It was reported, that they exhibit a good corrosion resistance. In earlier studies on the Mg-Sn alloys with addition of Ca, it was reported that most of the Mg-Sn-Ca alloys are promising corrosion [136] and creep resistance [137]. They have even better corrosion resistance after extrusion [61,131-137]. Based on the given publications, the Mg-Sn-Ca becomes further attention by other researcher. Kim et al. [138] has examined the microstructure evolution and creep resistance in Mg-Sn-Ca alloys system. It was reported that the alloys containing Ca more than 2 wt.-% increases the creep resistance, due to the presence of the Mg_2Ca phase.

The alloy was investigated after the addition of Ce [139] and Y [140]. It was reported that the presence of a few amounts of Ce or Y (0.5wt.-%) leads for decreasing of the volume fraction and the size of $Ca_{2-x}Mg_xSn$ phase. Further addition of Ce (1-2wt.-%) forms a new phase $Mg_{12}Ca$ and the $Ca_{2-x}Mg_xSn$ can be refined however; the Mg_2Ca phase has not been changed. It was mentioned that due to the refinement of the mentioned phase, the mechanical properties of the investigated alloys Mg-3Sn-2Ca-Ce could be improved. Addition of 1-1.5 wt.-% of Y to the as-cast Mg-3Sn-2Ca leads for the formation of new phase CaMgY. The addition of Y shows an increase of the tensile and creep resistance of the alloy [140].

2.5 Corrosion

Magnesium is the most corrosive metal used in engineering applications due to its high chemical reactivity [141]. The low standard reduction potential (highly negative electrochemical potential) of magnesium achieves -2.37 V, whereas aluminum and iron have a standard electrode potential of -1.71 V and -0.44 V, respectively [11]. A noble metal such as silver (Ag) has a positive potential of 0.80 V. The standard electrode potential of Ag is the highest one among the given elements in Table (6).

Table (6): Standard reduction potentials [11].

Electrode	Reaction	Potential [V]
Mg, Mg^{2+}	$Mg^{2+} + e^{-1} \rightarrow Mg$	-2.37
Al, Al^{3+}	$Al^{3+} + e^{-1} \rightarrow Al$	-1.71
Zn, Zn^{2+}	$Zn^{2+} + e^{-1} \rightarrow Zn$	-0.76
Fe, Fe^{2+}	$Fe^{2+} + e^{-1} \rightarrow Fe$	-0.44
Cd, Cd^{2+}	$Cd^{2+} + e^{-1} \rightarrow Cd$	-0.40
Ni, Ni^{2+}	$Ni^{2+} + e^{-1} \rightarrow Ni$	-0.24
Sn, Sn^{2+}	$Sn^{2+} + e^{-1} \rightarrow Sn$	-0.14
Cu, Cu^{2+}	$Cu^{2+} + e^{-1} \rightarrow Cu$	0.34
Ag, Ag^{2+}	$Ag^{+} + e^{-1} \rightarrow Ag$	0.80

Magnesium shows good resistance to atmospheric exposure, which is attributed to the formation of a highly protective magnesium hydroxide $Mg(OH)_2$ film [142]. The mentioned layer is very stable in pure alkaline aqueous solutions with pH value more than 11, since the cracks are sealed with $Mg(OH)_2$. In that case, the alkalinity suppresses the solubility of the $Mg(OH)_2$ film, and thus improves its protective nature. The unprotected magnesium can be more resistant to the atmospheric environment than mild steel [5] but they are not as good as Al-alloys [11, 143-144]. The $Mg(OH)_2$ film is unstable in aqueous solutions with a pH value less than 11. The low corrosion resistance of Mg-alloys results from the high inherent dissolution tendency of magnesium [145]. There are also high compressive stresses within the layer, which cause cracks. In addition, chloride ions greatly promote attack of magnesium in aqueous solution. The hydrogen released during the corrosion process causes additional disconnection of the layer. The $Mg(OH)_2$ film tends to break down in salt spray, even if exposed to small amounts; therefore, chloride solutions are obviously corrosive. Magnesium also has a poor resistance to acids with exceptions of both hydrofluoric acid (HF) and chromic acid (H_2CrO_4). Hydrofluoric acid does not attack magnesium to an appreciable extent, due to the formation of an insoluble, protective magnesium fluoride film on the magnesium [141]. Pure H_2CrO_4 attacks magnesium and its alloys at a very low rate. However, traces of chloride ions in the acid will markedly increase this rate. H_2CrO_4 is commonly used to remove corrosion products from magnesium alloys without attacking the base metal. Figure (8) shows the Pourbaix diagram of magnesium at 25°C in water and presents the three theoretical regions corrosion, immunity, and passivation.

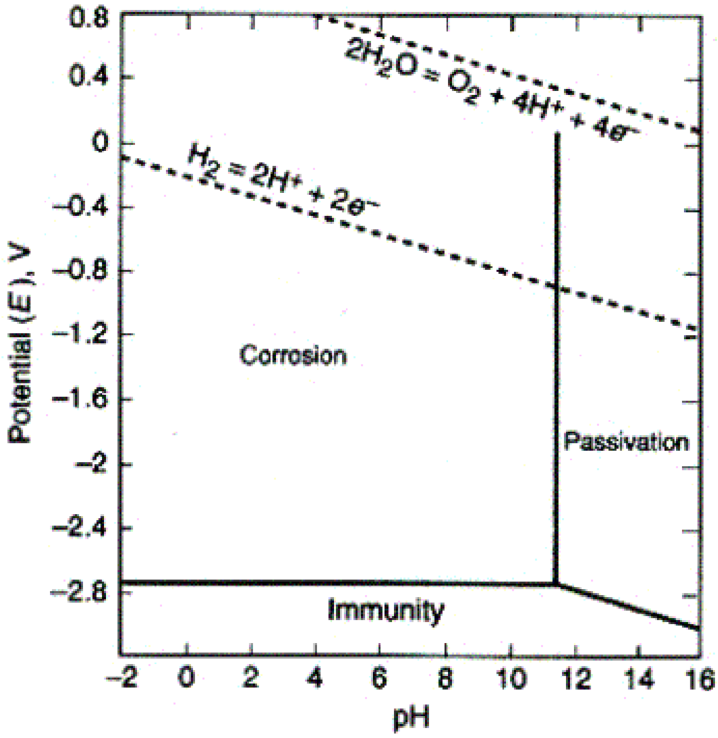

Figure (8): Potential pH diagram for magnesium at 25°C in water showing the theoretical domains of corrosion, immunity and passivation [11].

It can be seen that Mg dissolves as Mg^{+2} attended by hydrogen evaluation. The dissolution of Mg in an aqueous environment produces magnesium hydroxide and hydrogen gas [146]. This reaction is represented in the usual form in accordance with the following equations (1-3). However, reaction (1) is based on the other reactions (2-3):

$$Mg + 2H_2O \rightarrow Mg(OH)_2 + H_2 \quad (1)$$

$$2H_2O + 2e^- \rightarrow H_2 + 2(OH)^- \text{ (cathodic reaction)} \quad (2)$$

$$Mg \rightarrow Mg^{+2} + 2e^- \text{ (anodic reaction)} \quad (3)$$

$$Mg^{+2} + 2(OH)^- \rightarrow Mg(OH)_2 \quad (4)$$

The reaction ordinarily begins at the surface with the transfer of electrons from one metal to another. When two dissimilar materials are coupled in a corrosive electrolyte (galvanic effect) depending on the electrolyte, all metals dissolve to some degree when they are wetted with a conductive liquid.

The contact of magnesium itself with most other metals and the impurities in it are in practical applications unavoidable. Therefore, magnesium alloys are highly susceptible to galvanic corrosion because Mg is the most anodic structural metal [142]. The corrosion mechanism is usually attributed to micro galvanic corrosion between the matrix and the more noble or cathodic intermetallic particles [28]. Corrosion resistance of the alloy can be influenced by impurities that are very harmful impurities. The well-known impurities are iron, nickel, and copper. They should be controlled in the parts-per-million range in Mg-alloys in order to avoid their trivial effects. For good corrosion resistance, the upper limit amounts to 0.005 wt.-% for Fe and Ni, while copper in an amount larger than 0.05 wt.-% affects the corrosion properties [4,11]. The impurities can be easily picked up during the casting. They increase the corrosion rate of magnesium alloys in salt water and thus reduce corrosion resistance [147]. The presence of a cathodic metal, such as Fe in addition to electrolyte will lead to the occurrence of galvanic corrosion. On the other side, elements, such as Al, Mn, and Zn can lead to an improvement of the corrosion resistance [144,146]. Mn, for example, removes impurities from the matrix and forms stable precipitates, such as Fe-Mn-Al-phases [147-149]. It was reported by Beck [1] that even small additions of Mn (0.2 wt.-%) can increase corrosion resistance. Therefore, the development of a new Mg-alloy is a significant topic where corrosion resistant alloys are required. The new alloy should subsequently promise an excellent corrosion resistance and thus a long lifetime [150].

The steady-state potential of pure magnesium in a one mole sodium chloride (NaCl) solution is -1.72 V while for Al and Fe reached -0.86 V and -0.72 V, respectively. This comparison is given in Table (7).

Table (7): The steady-state potential of Mg, Al and Fe in a 1 mole NaCl solution [151].

Metal	Potential in NaCl solution [V]
Mg	-1.72
Al	-0.86
Fe	-0.72

There is a lot of information concerning corrosion of Mg-alloys, which can be found in the ASM handbook [141]. A detailed discussion of the significant improvement concerning the corrosion resistance of Mg-alloy can be also found in more recent studies [152-155].

2.6 Creep

To understand the creep resistance of metals, it is first necessary to obtain a description of the phenomenon of creep. In material science, creep is defined as time-dependent slow and permanent deformation of a material, under a steady stress at a certain temperature [50]. Creep becomes progressively more significant at elevated temperatures. Furthermore, materials show rate dependent plasticity or creep even at low temperatures. Nevertheless, as temperatures are increased plastic deformation becomes much more strain rate (creep rate) dependent. While in elastic-plastic creep, the strain is a function of stress and temperature T, strain rate is a function of stress, temperature, and time. This is explained in the equations (5) and (6) respectively:

$$\varepsilon = f(\sigma, T) \tag{5}$$

$$\dot{\varepsilon} = f(\sigma, T, t) \tag{6}$$

where ε is the creep strain, $\dot{\varepsilon}$ is the strain rate, σ is the stress, T stands for temperature, and t stands for the time [50].

Creep tests are normally classified into two different tests depends on how specimen is loaded. They are either tensile or compressive test. Figure (9) illustrates typically a creep strain versus time. Basis on the creep curve taken from Figure (9), the strain rate after time t is illustrated in Figure (10) showing the three-stages: primary, secondary, and tertiary. The first stage is the primary or sliding one. It can be produced when the load is first applied. The strain continues to increase during the decreasing of the creep rate $\ddot{\varepsilon}<0$ [156]. The most important part of the curve, the secondary „steady-state” stage, usually represents a steady-state creep region with a constant creep rate ($\ddot{\varepsilon}=0$, $\ddot{\varepsilon}=\ddot{\varepsilon}_s$). The secondary period is of enormous significance, owing to the lifetime of a machine component. In this stage, the minimum creep rate can be determined from the slop. The tertiary stage occurs at relatively temperature and stress, which is also characterized by an accelerated creep rate of the specimen that finally leads to rupture ($\ddot{\varepsilon}>0$) [156]. The primary and the tertiary stages often are short time periods as compared to the secondary one.

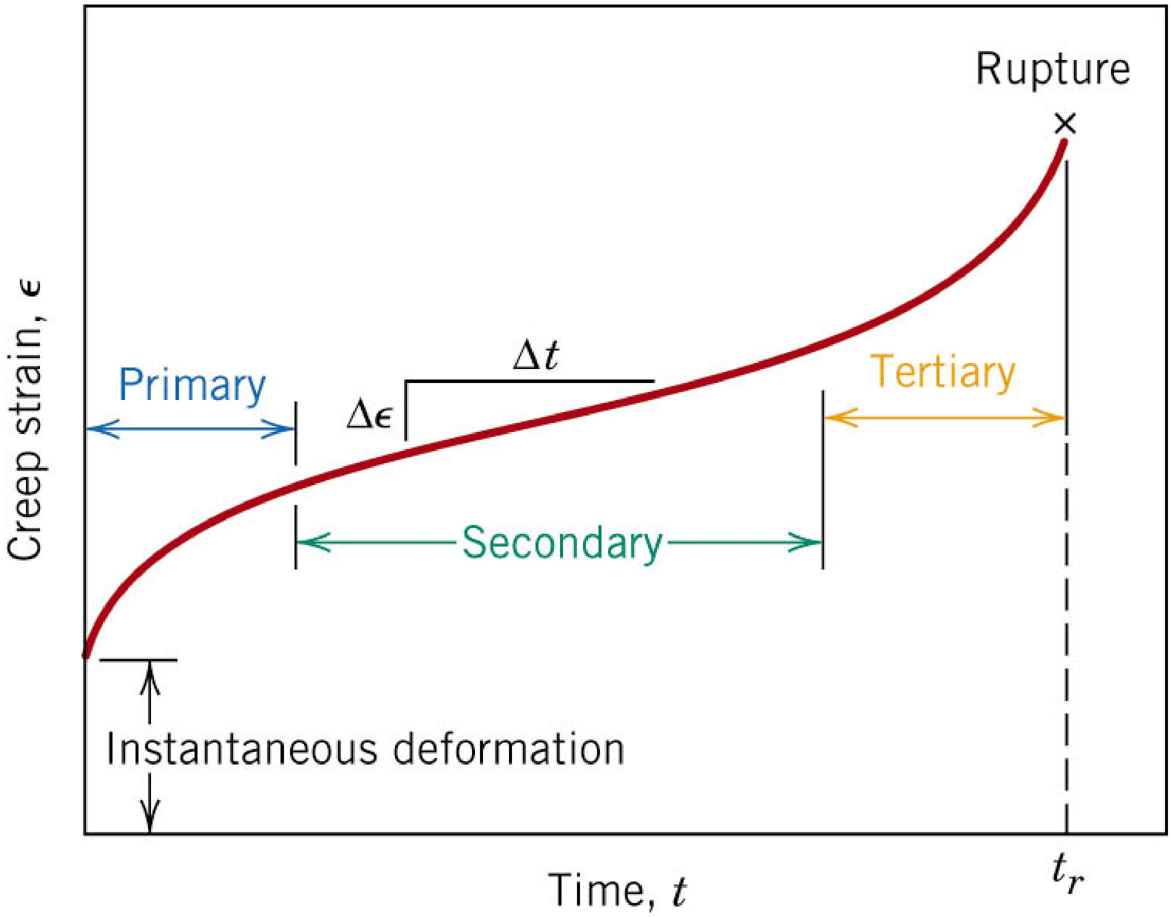

Figure (9): A schematic diagram of a typical creep strain after time showing three stages: primary, secondary, and tertiary creep [7].

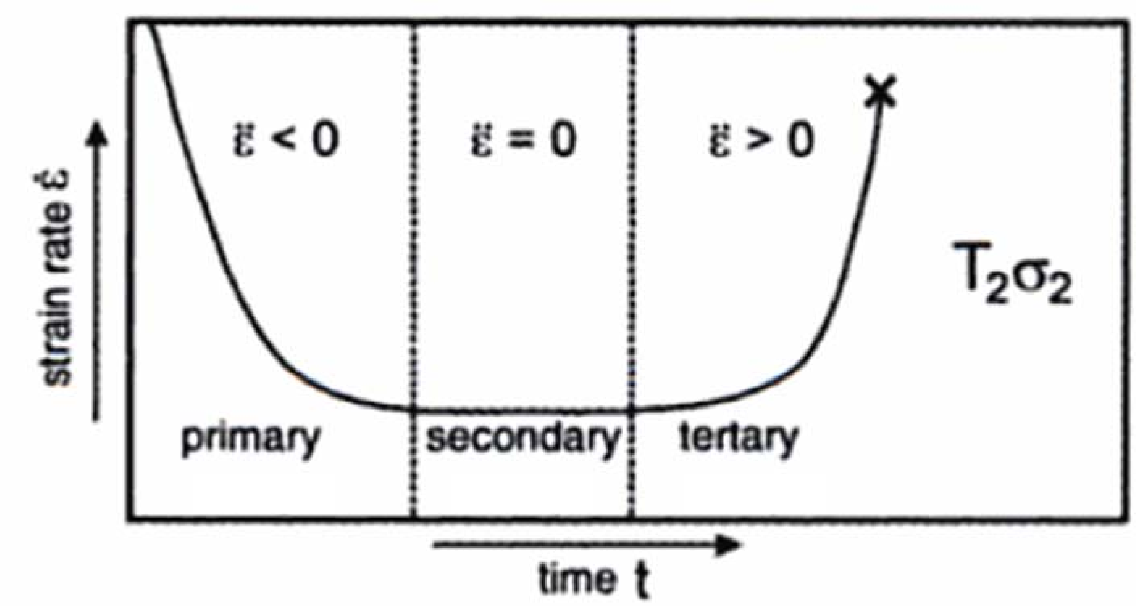

Figure (10): A schematic diagram of a typical strain rate after time t showing three stages: primary, secondary, and tertiary creep [7].

2.6.1 Temperature and stress of the secondary creep

The secondary creep that occurs as a linear function of time is strongly dependent on temperature and stress. Creep usually becomes essential only at temperatures higher than 0.4 of the obsolute melting point of the metal ($0.4T_m$). In general, if the material can be used at temperatures lower than $0.4T_m$ creep will not cause difficulties. Table (8) represents the melting point of Mg compared to other metals showing that creep becomes relevant in the same temperature like aluminum.

Table (8): Melting temperature T_m and $0.4T_m$ of pure magnesium compared to other pure metals.

Pure metal	T_m	$0.4T_m$
Mg	650	96
Al	660	100
Ti	1668	504
Fe	1536	451

The time duration of the creep stages reduces significantly by increasing the temperature and the applied stress, which leads to an increase of the minimum creep rate, as shown schematically in Figure (11).

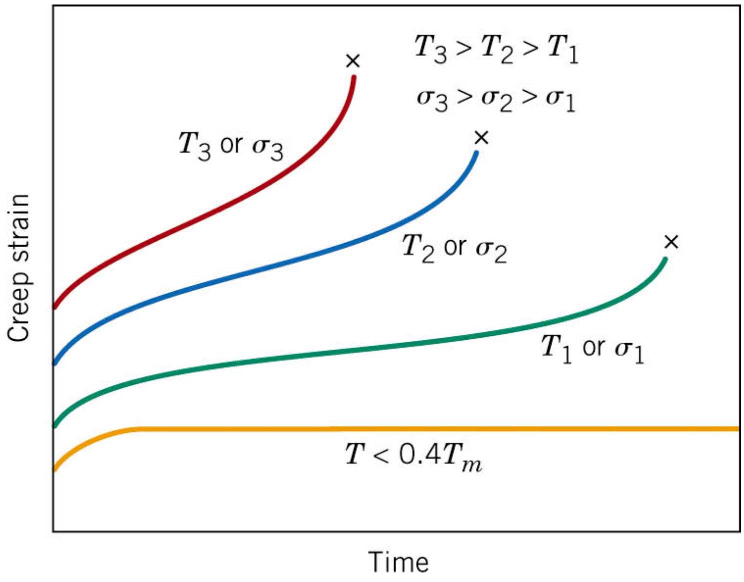

Figure (11): A schematic diagram of a typical creep strain vs. time showing a creep diagram of a specimen at different T and σ [7].

In general, secondary creep can be described using an Arrhenius approach for the creep strain rate:

$$\dot{\varepsilon}_s \sim \exp\left(-\frac{Q_c}{RT}\right) \text{ by } (\sigma = \text{constant}) \tag{7}$$

where $\dot{\varepsilon}$ is the secondary creep rate, Q_c stands for the activation energy for creep, R is the general gas constant (8.314 J/mol.K), and T is the temperature.

This approach towards the analysis of creep of pure metals at higher temperatures has shown that the activation energy for creep Q_c for a given material depends on the creep mechanism. The activation energy Q_c can be viewed as a measure of the temperature dependence of the underlying diffusion processes. Furthermore, the temperature dependence is determined by the Young's modulus and the stacking fault energy.

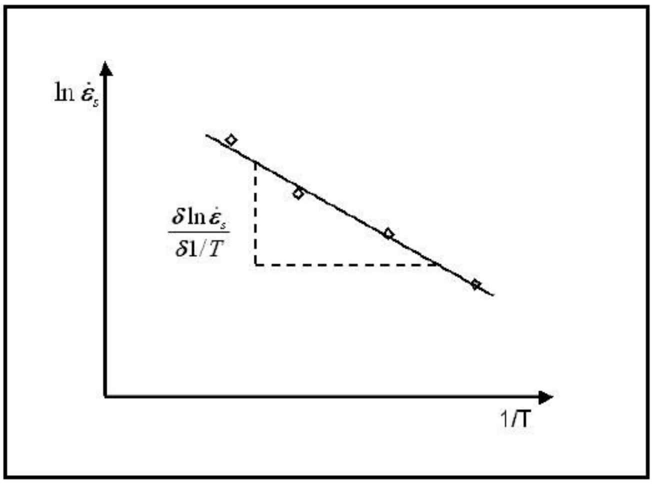

Figure (12): A schematic diagram for calculation of activation energy [7].

The creep response of the material to stress in the secondary creep regime is called Norton's Law. According to this law, creep is a thermally activated process, as shown in Figure (12). It is used to describe the relationship between the stress and the secondary creep rate of many metals and alloys:

$$\dot{\varepsilon}_s \sim \sigma^n \text{ by } (T = \text{constant}) \tag{8}$$

In which n stands for stress exponent and the index s stands for secondary creep.

In crystalline materials, it is found that the activation energy Q_c is roughly equal to the activation energy self-diffusion of the material.

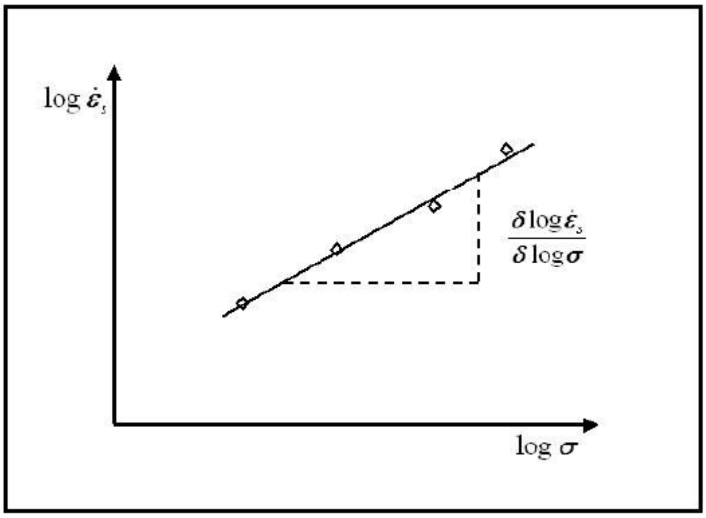

Figure (13): A schematic diagram for calculation of exponent n [7].

This expression is the basis of the power law creep that is often used to describe high-temperature creep. It has proved its utility through many experimental results. Varying creep mechanisms and other factors leads to variations in the values of the stress exponent n. The value of n can be seen as a sign of atomic-scale creep. A schematic diagram for calculation of exponent n is illustrated in Figure (13). The combination of both equations leads to the following approach that is accomplished to describe real creep processes:

$$\dot{\varepsilon} = A_0 \cdot \sigma^n \exp\left(-\frac{Q_c}{RT}\right) \tag{9}$$

where A_0 is a constant, R is the universal gas constant, Q_c is the apparent activation energy for creep, and n is the stress exponent.

The activation energy and the stress exponent can be used to understand the dominant creep mechanism for an alloy in specific ranges of stress and temperature.

2.6.2 Creep mechanisms

Three basic mechanisms can contribute to creep in metals, namely diffusion creep, dislocation creep, grain boundary gliding.

Diffusion creep

Diffusion creep is a process where the grain boundaries are sources and sinks of vacancies. It was argued by Frost and Ashby that diffusion creep is to be rate controlling at high temperatures less than 0.8 T_m and low stresses. In this regime, Nabarro and Herring reported in their so-called Nabarro-Herring creep model that creep occurs by stress directed vacancy flow. These vacancies move to grain boundaries with compressive stress or lower values of the tensile stress. The formation of vacancies occurs at grain boundaries with a normal vector oriented in the direction of the tensile stress. The material itself moves in the opposite direction from region with compressive to those with tensile current density is calculated and related to the strain rate [157].

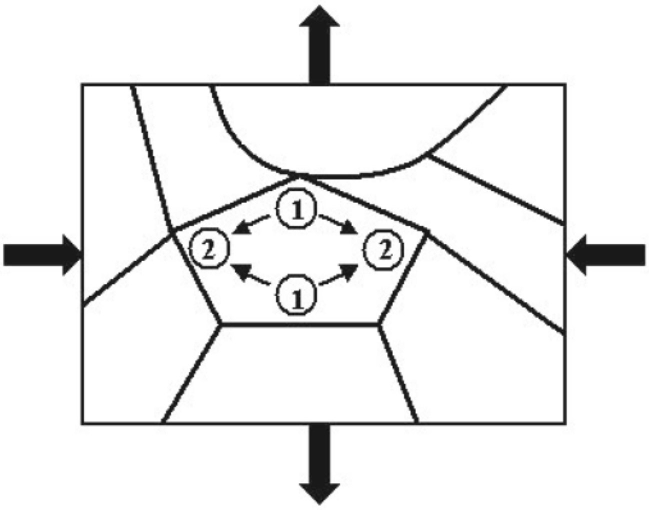

Figure (14): Schematic sketch of the stress flow after Nabarro-Herring creep model.

The mentioned theory predicts values for the stress exponent n of 1 and an increase in creep rate with decreasing grain sizes. It is expected that the apparent activation energy is similar to that of self-diffusion. The Nabarro-Herrring creep is illustrated in Figure (14) and described by the following equation:

$$\dot{\varepsilon}_s = \left(\frac{14\sigma b^3 D_v}{kTd^2} \right) \tag{10}$$

In which b is the burgers vector, D_v is the lattice diffusion coefficient, k stands for Boltzmann’s constant, and d is the grain diameter.

At low temperatures, the diffusion along the grain boundaries is dominant and thus the mentioned model can be modified. As a result, the creep rate becomes even more dependent on the grain size ($1/d^3$) and the activation energy for creep Q decreases and reaches a value close to that of the grain boundary diffusion. The Colbe creep model is considered important at temperatures approx. 0.4 T_m and at low stress.

The mentioned diffusion flow models explain the important increase in creep rate with reduction of grain size and increase in number of boundaries.

Dislocation creep

Dislocations play a significant role in the time-dependent plastic deformation of the material. Dislocation creep is based on an effect that leads to hardening at low temperatures because of dislocations are locked in front of material barriers (precipitations, grain boundaries, other dislocations, etc.). At higher temperatures, the dislocations can bypass these barriers. Besides the so-called cross-slip, the main mechanism for bypassing is the heat-activated “climbing” of dislocations that is close related to diffusion processes. Therefore, the creep rate depends not only on temperature and stress, but also on material-specific properties, particularly the Young’s modulus.

In some materials, the particles in precipitation hardened alloys usually coarse with time; i.e. the microstructure can be changed at elevated temperatures. In this case, there will be no stationary region with constant creep resistance of the material. Instead, the creep rate continuously increases after a minimum has reached.

Grain boundary glide

Grain boundary gliding is the process where the grains glide over each other without undergoing any marked deformation i.e. the shape of the previous does not change. It can result either from complex and local solution / precipitations processes and dislocation responses, or from a low heat resistance of the boundary phase.

The grain boundary gliding is significant due to the following two reasons:

First, diffusion creep, grain boundary sliding ensures the compability of the grains during the deformation, which is illustrated in Figure (15).

Second, at points where grain boundaries meet (triple points), movement of the grain boundaries by sliding can cause a large concentration in local stresses and thus induce damage by rupture of the grain boundaries.

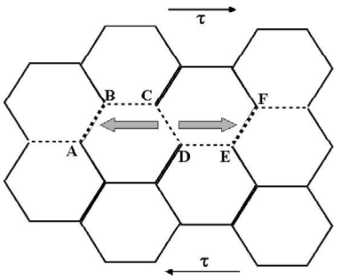

Figure (15): Schematic sketch of the grain boundary glide.

2.6.3 Creep of pure magnesium

In order to explain the creep of magnesium, there is a need to describe the crystal structure of this element. The magnesium lattice parameters at room temperature are a = 0.32092 nm and c = 0.52105 nm with a c/a ratio of 1.6236. These parameters corresponded nearly perfectly to those of the close-packed hexagonal structure with an ideal c/a ratio of 1.633 [2, 4, 11, 77]. The hexagonal structure of the magnesium unit cell is demonstrated in Figure (16) showing the major planes and directions [11].

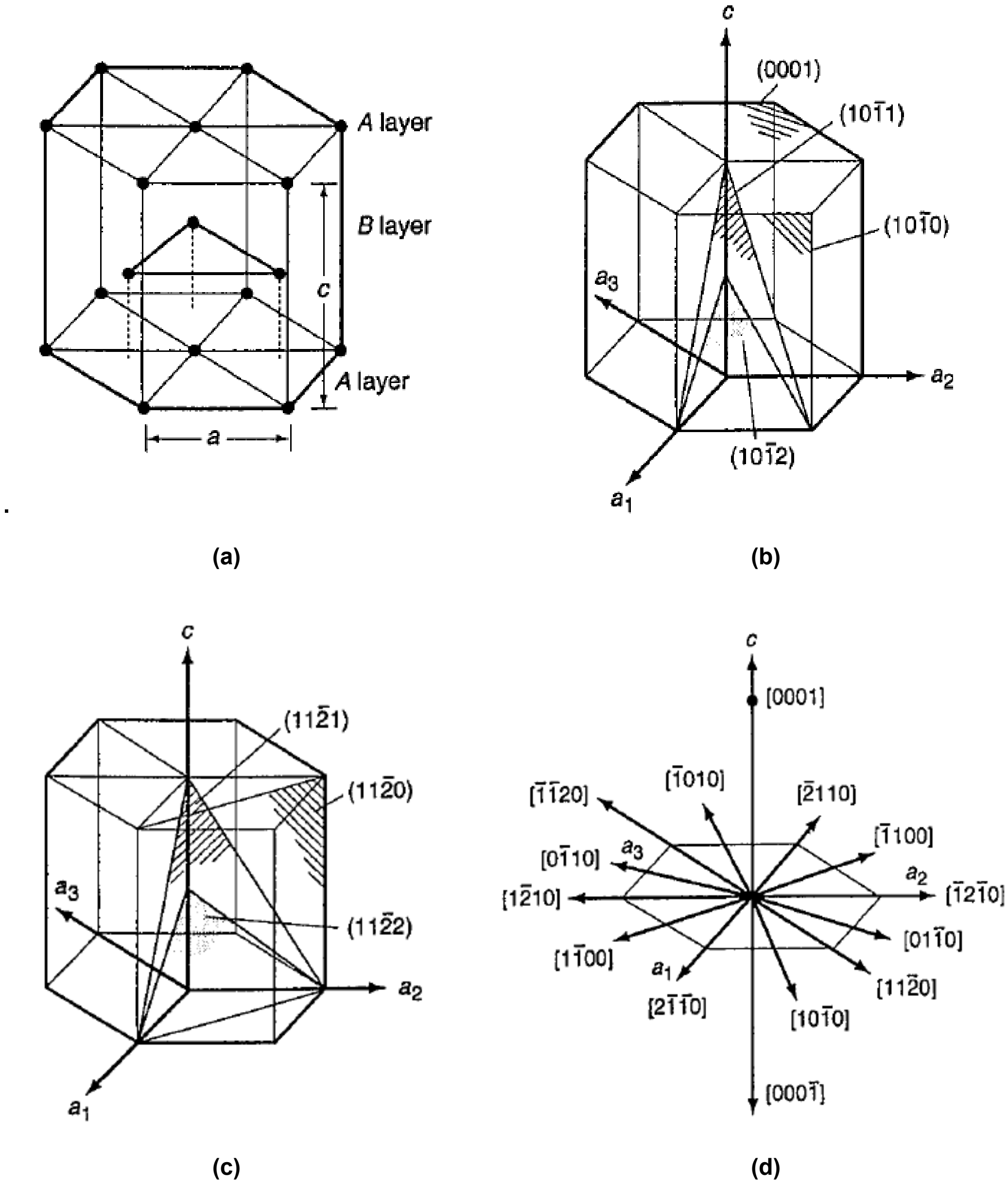

(a) (b)

(c) (d)

Figure (16): The hcp crystal structure showing unit cell, major planes and directions [11].

In general, primary and secondary slip and twinning occur at room and elevated temperatures. Primary slip takes place on the (0001) basal plane and in the $<11\bar{2}0>$ most closely packed direction of the plane at room temperature, while secondary slip occurs in the $<11\bar{2}0>$ direction on the $\{10\bar{1}0\}$ prism face planes. On the other hand, primary twinning happens across the $\{10\bar{1}2\}$ planes and secondary twinning occurs on the $\{30\bar{3}4\}$. Slip can also occur in the $<11\bar{2}0>$ direction on the $\{10\bar{1}1\}$ pyramidal planes and the twinning occurs across the $\{10\bar{1}3\}$ planes.

In 1960, Roberts has studied the mechanism of creep in pure magnesium within a temperature range of 90-300°C and at stresses level of 8-70MPa. It has been observed that pure magnesium exhibits basal slip on the {0001} planes within the grains, and sub-grain formation at low temperatures At higher temperatures, diffusion-dependent mechanism of grain boundary deformation and sliding steady-state creep, become predominant. In addition, the same type of change was observed to occur as the stress level at high temperature reduces. Non-basal slip on the pyramidal and prismatic slip planes and grain boundary deformation and sliding were observed (steady-state-creep). Figure (17) illustrates the deformation map for pure magnesium with a grain size of 0.1 mm.

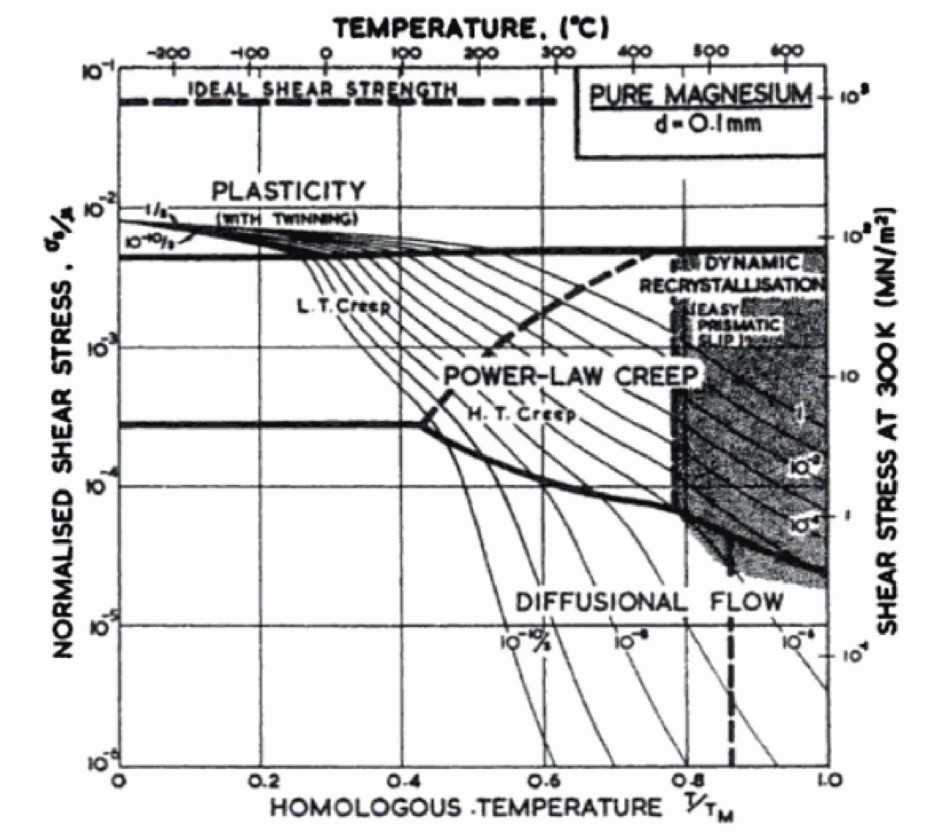

Figure (17): Deformation map for pure magnesium with a grain size of 0.1 mm [158].

2.6.4 Creep of magnesium alloys

Most of the commonly used Mg-Al alloys containing 2-9 wt.-% Al suffer from poor creep resistance at higher temperatures. The microstructure of the AZ91, AM50/60 is characterized by the β-$Mg_{17}Al_{12}$ eutectic at the grain boundaries. The mentioned phase is incoherent with alpha magnesium matrix. In addition, it was reported that discontinuous type of precipitation during aging effecting multiplies the grain-boundary are available for easy deformation at elevated temperature creep and attributed the relatively poor elevated temperature resistance.

The creep mechanism of AM50 has been studied by Pekguleryuz [50]. AZ91, AS21, and AE42-alloys have been studied by Dargusch [13]. For magnesium and its alloys, a stress exponent n of approx. 2 and 5 has been determinated at low and high stress, respectively [36]. For an AZ91D activation energy of 30-45 kJ/mol was found in the stress range where an exponent of stress n=2 occurred. This is particularly smaller than the activation energy of Mg self-diffusion (135 kJ/mol). In the mentioned alloy grain boundary, sliding has been observed for low stresses. This is related to the discontinuous β-$Mg_{17}Al_{12}$ phase and has activation energy of 30 kJ/mol. However, the activation energy for high stresses (n=5) attains 95 kJ/mol. The activation energy of diffusion of Al in Mg and of grain boundary diffusion is 143 kJ/mol, and 80 kJ/mol, respectively [14]. On the other hand, creep by dislocation climb is proposed as the dominant mechanism for creep at high stress (n=5). The stress level, where the transition between these two creep mechanisms occurs, depends on the particular alloy and temperature. The poor creep resistance in the AZ91 alloy occurs due to the essential amount of β-$Mg_{17}Al_{12}$ phase in this alloy that leads to grain boundary sliding and migration [13, 14].

AS21 and AE42-alloys contain less supersaturated α-Mg. As a result, less discontinuous β-$Mg_{17}Al_{12}$ phase is formed during elevated temperature exposure. Furthermore, the presence of Mg_2Si and Al_4RE in AS21 and AE42, respectively, is likely to pin grain boundaries and hinder both grain boundary migration and sliding. Therefore, it is expected that there will be no problems preventing creep in stressed components.

3 Experimental procedures

3.1 Materials selection

The investigation in this work is focused on the binary Mg-Sn and the ternary Mg-Sn-Ca-alloys (TX-alloys) in various compositions. The TX-alloys contain nominal additions of Sn and Ca with various levels in the ranges of 2–6 wt.-% and 0-3 wt.-%, respectively. The alloys AZ91D and AE42 have also been investigated. They were selected to be reference alloys due to the good room-temperature properties of the AZ91D-alloy and the well-known high temperature creep resistant AE42-alloy. The alloying elements used in this study contain high purity magnesium 99.99% (Hydro Magnesium, Norway), Sn 99.90 % (MCP HEK, Germany), and Ca 98.50% (Merck, Germany). The AZ91D- and AE42-alloys were supplied by Norsk Hydro. Table (9) represents the chemical composition of AZ91D- and AE42-alloys and Table (10) summarizes the total matrix of the nominal compositions of all selected TX-alloys with various compositions. As mentioned earlier in (section 2.2.1), the Mg-Sn-Ca alloys were tentatively designated as TC-alloys and subsequently named as TX-alloys.

Table (9): Chemical compositions of AZ91D- and AE42-alloys in wt.-%.

AZ91D									
Element	**Al**	**Zn**	**Mn**	**Si**	**Fe**	**Ni**	**Cu**	**Si**	**Sn**
at.- %	8.79	0.59	0.18	0.0438	0.0019	0.0008	0.0058	0.04	0.0031
Element	**Ag**	**Be**	**Ca**	**Zr**	**Ce**	**La**	**Mg**		
at.- %	< 0.0001	0.00062	0.0008	<0.0006	0.0009	<0.0002	90.38		
AE42									
Element	**Al**	**Ce**	**Nd**	**La**	**Pr**	**Y**	**Mn**	**Sn**	**Zn**
at.- %	3.94	0.0032	0.417	~ 0.8	0.126	0.00987	0.208	0.0052	0.00319
Element	**Ag**	**Ca**	**Ni**	**Pb**	**Si**	**Cu**			
at.- %	0.00121	0.00306	<0.0002	<0.00053	0.00606	0.00194			

Table (10): The nominal composition of the TX-alloys in wt.-%.

Alloys	Abbreviation	Ratio Sn:Ca	Sn	Ca	Mg
[wt.-%]					
Mg-3Sn			3	0	rem.
Mg-5Sn			5	0	rem.
Mg-3Sn-0.5Ca	TX30x	6:1	3	0.5	rem.
Mg-3Sn-1Ca	TX31	3:1	3	1	rem.
Mg-3Sn-1.5Ca	TX32x	2:1	3	1.5	rem
Mg-3Sn-2Ca	TX32	1.5:1	3	2	rem.
Mg-3Sn-3Ca	TX33	1:1	3	3	rem.
Mg-2Sn-2Ca	TX22	1:1	2	2	rem.
Mg-4Sn-2Ca	TX42	2:1	4	2	rem.
Mg-4.5Sn-1.5Ca	TX42x	3:1	4.5	1.5	rem.
Mg-5Sn-0.5Ca	TX50x	10:1	5	0.5	rem.
Mg-5Sn-1Ca	TX51	5:1	5	1	rem.
Mg-5Sn-1.5Ca	TX52x	3.33:1	5	1.5	rem.
Mg-5Sn-2Ca	TX52	2.5:1	5	2	rem.
Mg-6Sn-2Ca	TX62	3:1	6	2	rem.
Mg-6Sn-3Ca	TX63	2:1	6	3	rem.

3.2 Casting

The selected alloys were molten at 720°C in a large steel crucible placed in an electrical furnace (Nabertherm). A view of the electrical casting furnace is illustrated in Figure (18). A sulphur hexafluoride and argon mixture (0.3%SF_6+Ar) gas was used during the casting in order to guarantee the quality of the casting. This gas forms a thin protective layer on the molten bath surface and prevents a surface reaction and an exhausting. To accelerate the dissolution of the elements in magnesium the melt was stirred for 20 min using an electrical drill with a rotation of 200 rpm. Afterwards the melt was cast in a permanent mould, which was pre-heated at 200°C. The selected alloy was then cast to achieve cylindrical billets of 100 mm in diameter and 400 mm long. The weight of each obtained alloy reached 8 kg. The cylindrical cast ingot was then cooled down to room temperature by air-cooling. The steel mould and the obtained cast billet are shown in Figure (19).

Figure (18): View of the electrical casting furnace.

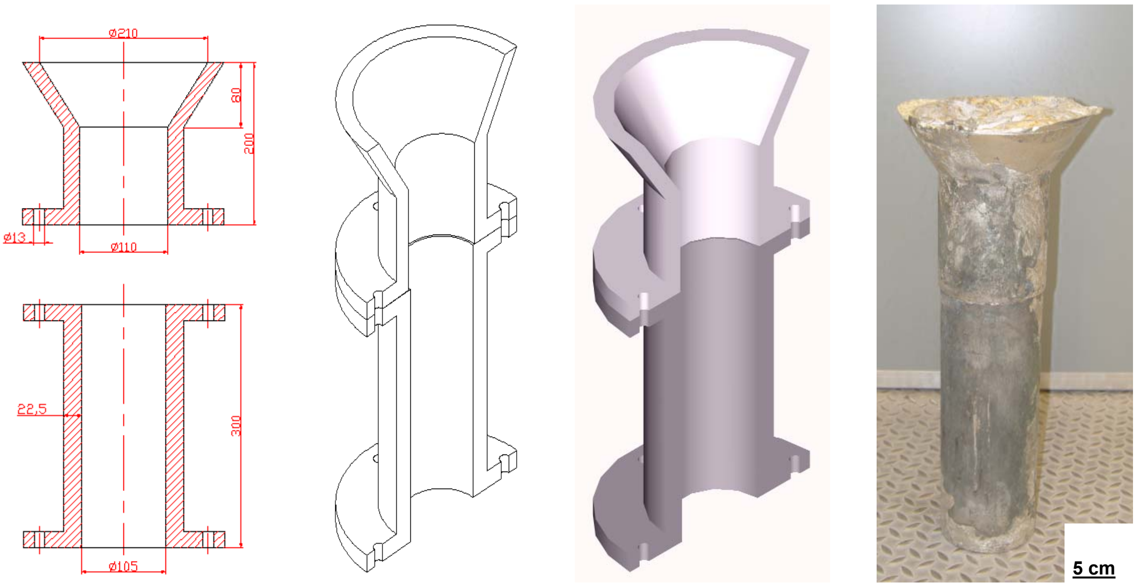

(a) (b) (c) (d)

Figure (19): Sketch of cylindrical mould “dimensions in mm” (a-c) and the cast billet (d).

3.3 Sample preparation and investigations

3.3.1 Microstructure and phase identification

The slices were cut from the upper part of each billet (300 mm higher than the bottom). Each slice has a thickness of approx. 12 mm and 100 mm diameter. In order to ensure that all of the investigated alloys represent a similar condition the samples were taken from the same location. Figure (20) shows the slice after cutting from the billet and the location of the prepared specimens.

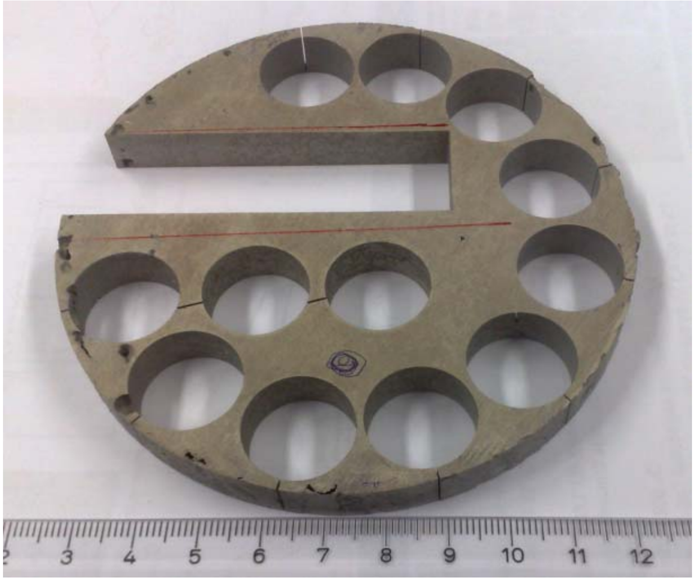

Figure (20): Slices of billet with location of prepared samples.

Round discs with about 4 mm thickness and 18 mm in diameter were prepared in order to examine the microstructure and the phases of the TX-alloys. The samples were mounted with cold setting plastic, which consisted of a powder and liquid Demotec 70 that was mixed at room temperature in the ratio of 1:1. After 30 minutes, the Demotec paste cured and solidified. Afterwards, the used mould was removed. The microstructure sample is shown in Figure (21). The samples were ground with silicon carbide "SiC" paper to 2400 grit for light optical microscopy (LM) and scanning electron microscopy (SEM) investigations. Then they were polished sequentially with diamond paste of 6 µm and 1 µm size. In addition, OPS^{TM} suspension was used followed by etching with picric acid. Afterwards the specimens were cleaned with ethanol to avoid the reaction with water and finally blow-dried. These samples were further etched in a solution of 8 g picric acid, 5 ml acetic acid, 10 ml distilled water and 100 ml ethanol for 10 seconds. Finally, they were again washed using ethanol and then blow-dried [162]. The X-ray diffraction (XRD) samples were mainly ground with 1200 grit SiC paper. Afterwards they were cleaned with ethanol and then blow-dried. Transmission electron microscopy (TEM) samples were ground mechanically to about 70 µm. Then they were thinned used electro polishing in a twin jet system using a solution of 5% $HClO_4$ and 95 % ethanol at about -30°C and a voltage of 40 V.

Figure (21): Microstructure sample.

LM was performed on a Reichert-Jung MeF3 microscope to which a digital camera and a computer were connected to get digital images of the samples. The obtained micrographs were taken at magnification of x10, x50, X100, x200, x500, and x1000. The grain size measurements were carried out using a4i analysis imaging software [162].

In order to get more information about the phases of the investigated alloys, a ZEISS DSM-962 SEM was used and operated at 15kV with a working distance of 25 mm. The micrographs were taken using back scattered electrons (BSE) and secondary electron (SE). The SEM with energy dispersive x-ray spectrometry (EDX) was used for chemical analysis in selected areas by carrying out line and spot analyses. The EDX point analyses were obtained with a minimum live time of 200 seconds while the line scans were observed with a holding time of 30 minutes. WINEDS software has been used for this purpose. The phases were identified using X-Ray diffraction by means of Siemens D5000 diffractometer operating at a voltage 40 kV and 40 mA with Cu K_α radiation. The measurements were conducted by step scanning 2θ in the range 20 to 120° with a step size of 0.02° and holding time of 3 seconds.

The TEM observations were performed on JEOL 2000 transmission electron microscope operating at 200kV, which has been equipped with an energy dispersive x-ray analysis (EDX) system.

3.3.2 Differential thermal analysis (DTA), differential scanning calorimetry (DSC) measurements and thermodynamic calculations

Specimens with a weight up to 100 mg were prepared for differential scanning calorimetry (DTA). Each specimen was sealed in steel X5 CrNi 18 9 (1.4301) crucibles in order to avoid evaporation and oxidation.

The DTA measurements were performed using DTA equipment type Mettler Toledo GmbH. In addition, a heat-flow DSC of type Netzsch DSC 404C with a high-accuracy temperature sensor Pegasus was used for the DSC measurements. The DTA/DSC analysis of the selected alloys was performed under flowing Ar of high purity (99.9999%). The gas flow was controlled by a flow meter and set to approx. 50 ml. The temperature was measured with thermocouple placed inside the DSC. Then the specimen was heated with a heating and cooling rate of 2 or 10 K/min from room temperature up to 700°C. The melting range was calculated from the DTA/DSC curve; the estimated error of measurements is in the range of +/-5K. The DSC equipment was evacuated to and refilled with Ar before the experiment was started. This cycle was repeated 10 times in order to ensure that the entire air inside the DSC equipment is replaced with argon gas. The conditions of DTA and DSC are represented in Table (11).

Furthermore, the microstructure evolution during solidification was simulated using Scheil modeling with the Pandat software [163]. The comparison between the simulation and experimental results are given in this study.

Table (11): The conditions of the used DTA/DSC tests.

Equipment	DTA	DSC
Company	Mettler Toledo GmbH	Netzsch
Temperature range	25-700K/700-25K (one time)	25-700K/700-25 K (two times)
Heating and cooling rate	2K/min	2K/min
Weight of sample	up to approx. 100 mg	
Protection gas	Argon	
Crucible	Stainless steel X5 CrNi 18 9 (1.4301)	
		Al_2O_3 crucible was only used for the pure Mg specimen

3.3.3 Corrosion

Samples were prepared in order to conduct two kinds of corrosion tests, namely, potentio-dynamic measurements and salt spray tests. The specimens for both test procedures with 18 mm diameter and 4 mm in thickness were ground with 1200 grit SiC paper. The potentio-dynamic test samples were ground only on one side. However, the salt spray test samples for preliminary tests were ground on both sides and have a hole on the edge to hang the sample in the salt spray chamber. The samples are shown in Figure (22).

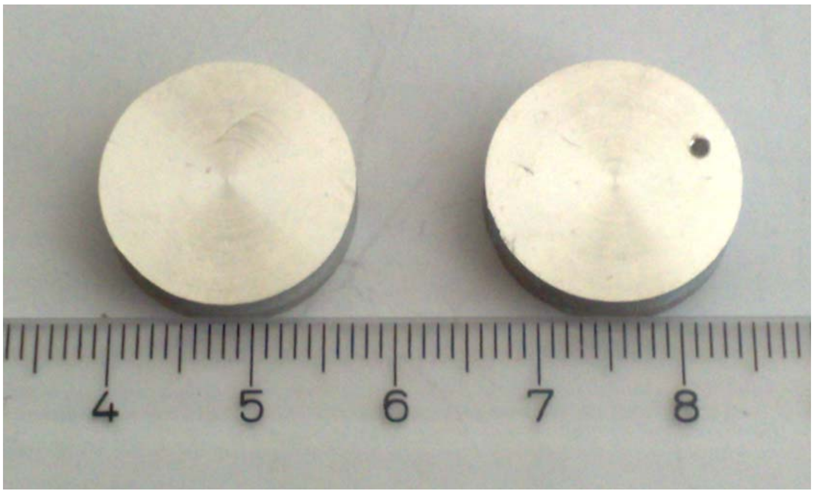

Figure (22): Samples for corrosion tests: (left) polarization and (right) salt spray.

Potentio-dynamic test

The potentio-dynamic polarization measurements in accordance with ASTM G5-82 [164] were conducted for the selected alloys in a 5% NaCl solution at room temperature. The pH value was adjusted to 11 using a NaOH solution. The measurements were performed in a three-electrode setup, namely the reference, auxiliary, and working electrode. Each specimen was exposed to the corrosive medium with an area of 1.54 cm^2. It was also in contact with the electrolyte in conjunction with an Ag/AgCl reference electrode and a platinum counter electrode. The experimental setup is illustrated in Figure (23a,b) showing the galvanic cell. After recording the free corrosion potential for 30 minutes, the polarization scan was started at -250 mV relative to the free corrosion potential (E_{corr}) with a scan rate of 0.2 mV/s. The corrosion rate was calculated using the current determined from the intersection of the cathodic Tafel slope with the vertical through the free corrosion potential from the cathodic branch of the polarization curve as shown in Figure (24) [143].

The following equation that has been used to obtain the corrosion rate is

$$\text{Corrosion rate: } r = \frac{87.6 * u * 3600 * I_{corr}}{1000 * z * F * \rho * A} \text{ given in [mm/year]} \qquad (11)$$

where u stands for atomic weight of Mg in mg/mole, I_{corr} is the corrosion current in mA, z for the number of electrons (Mg = 2), F for Faraday's constant 96486.7 coulomb/mole, ρ is the density in g/cm^3, and A stands for the specimen area that was exposed to the corrosive medium in mm^2.

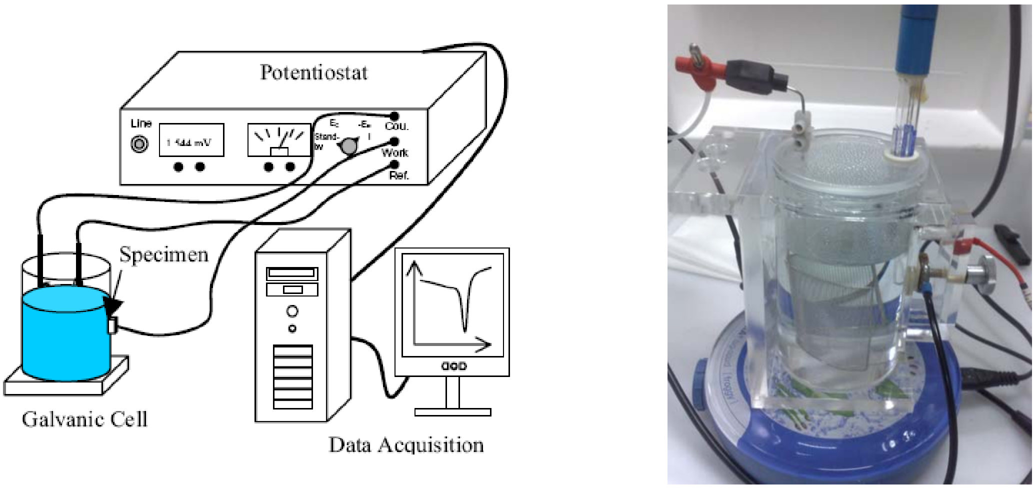

(a) **(b)**

Figure (23): Sketch of polarization setup (a) [165] and view of galvanic cell (b).

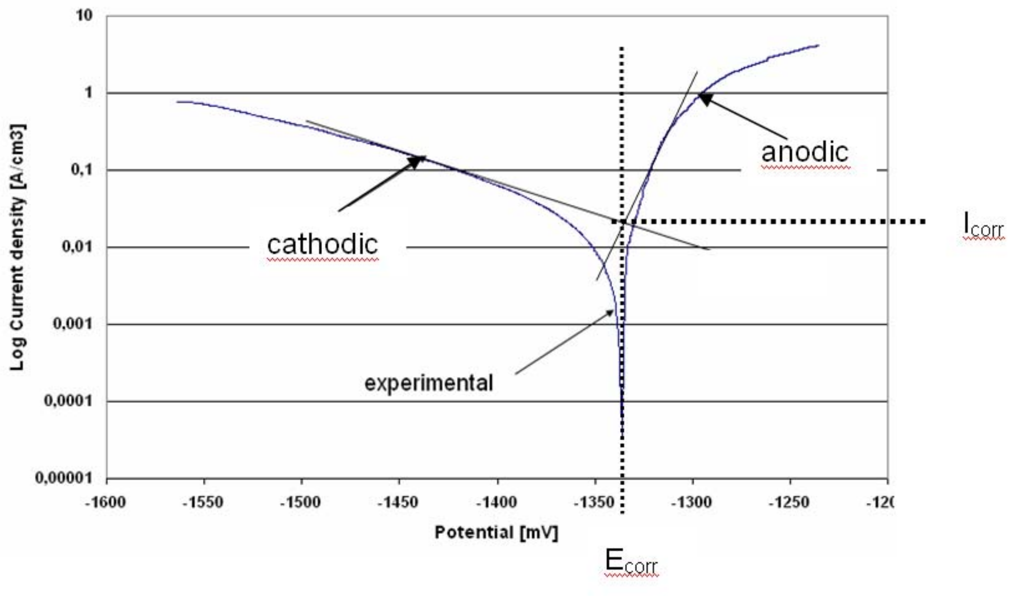

Figure (24): Polarization curve showing the anodic and cathodic reaction.

Salt spray test

According to ASTM-B117 [166], the specimens were exposed in a salt spray chamber (Figure (25)) to a 5% NaCl solution of pH value 7 for 48 hours. The temperature inside the salt spray chamber of type SC40 (WEISS) was controlled at 35°C. Before the test, the samples were weighed to milligram and the thickness as well as the diameter was measured to the nearest millimeter. After the test, the corroded specimens were rinsed with water, cleaned in chromic acid to remove the oxides, and dried subsequently. Afterwards, the samples were reweighed and the weight loss of the specimens was used to calculate the average corrosion rate in millimeters per year. The equation that has been used is given below [143]:

$$r = \frac{87.6 * W}{\rho * A * t} \tag{12}$$

where W stands for weight loss in mg, ρ stands for density of the specimen in g/cm^3, A is the area of specimen in square centimeter, and t represent the exposure time in hours.

Figure (25): Salt spray test chamber.

3.3.4 Mechanical properties

Compression and tension

The investigated compressive and tensile specimens were selected according to DIN 50106 and DIN 50125, respectively [167-168]. The cylindrical compression test samples have a length of 16.5 mm and a diameter of 11 mm prepared from the location shown in Figure (20). The tensile samples have a gauge length of 35 mm, 6 mm diameter and fine threaded screw heads. Figure (26) shows both mentioned test samples and the universal Zwick Z050 machine, which has been used for tension/compression tests, can be seen in Figure (27).

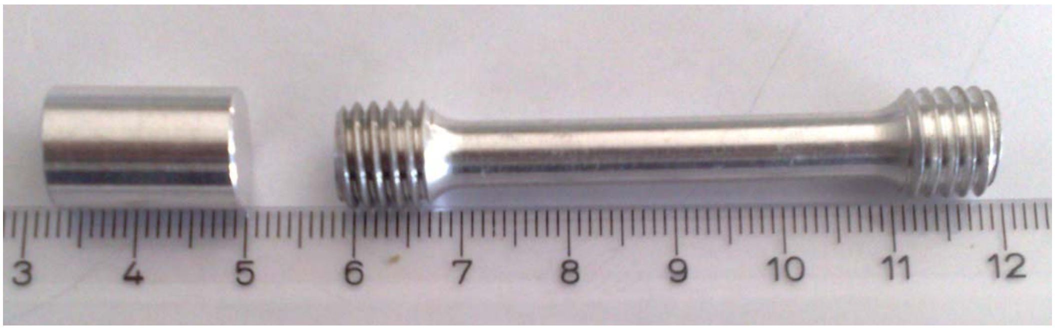

Figure (26): compression (left) and tension (right) test samples.

Figure (27): View of the compression and tensile machine (left) with tensile test (right) side.

Hardness

Samples with approx. 4 mm thickness were used to examine the Vickers hardness of the TX-alloys. They were mounted in the same way like for LM. However, they were ground with silicon carbide paper to 1200 grit. Then, they were cleaned with ethanol and finally blow-dried.

Optical vicker hardness testing equipment, type Frankoskop Nr. 532 Company Karl Frank GmbH, was used. The measurements were performed with 10 kg weight and holding time of 15 seconds according to ASTM E92-82 [169]. Afterwards, the Vickers hardness behavior of the samples was evaluated from a HV/time spot representation. The average of 10 various readings of each test sample was used as a result.

Compressive creep

Cylindrical specimens of 15 mm length and 6 mm diameter were used for the compressive creep tests. The dimensions of the specimens were defined by ASTM specification. The compressive creep test sample is shown in Figure (28).

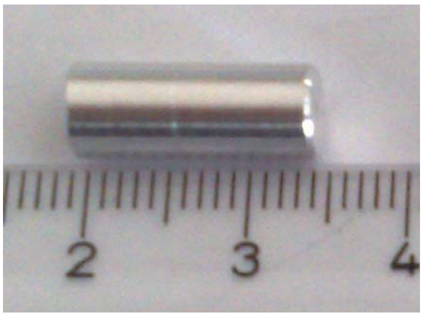

Figure (28): Compressive creep sample.

Creep tests were performed in uniaxial compression on an American Testing System (ATS) machine, which can be seen in Figure (29). After heating and subsequent soaking time of 30 minutes, the tests were started automatically. The temperature was measured with a Ni-CrNi thermocouple and maintained within the range ± 1 °C. The strain was measured by a vertical extensometer [170].

The compressive creep was examined at different temperatures and stresses. The parameters were selected based on the creep behavior requirements for gearbox housing (80-85MPa@135°C) and engine block (80MPa@150,175°C) [4]. In addition, one of the best alloys was also investigated at parameter of (60,70MPa@150°C). All of the investigated tests were stopped after 150 hours. The TX-alloys are given in Table (12).

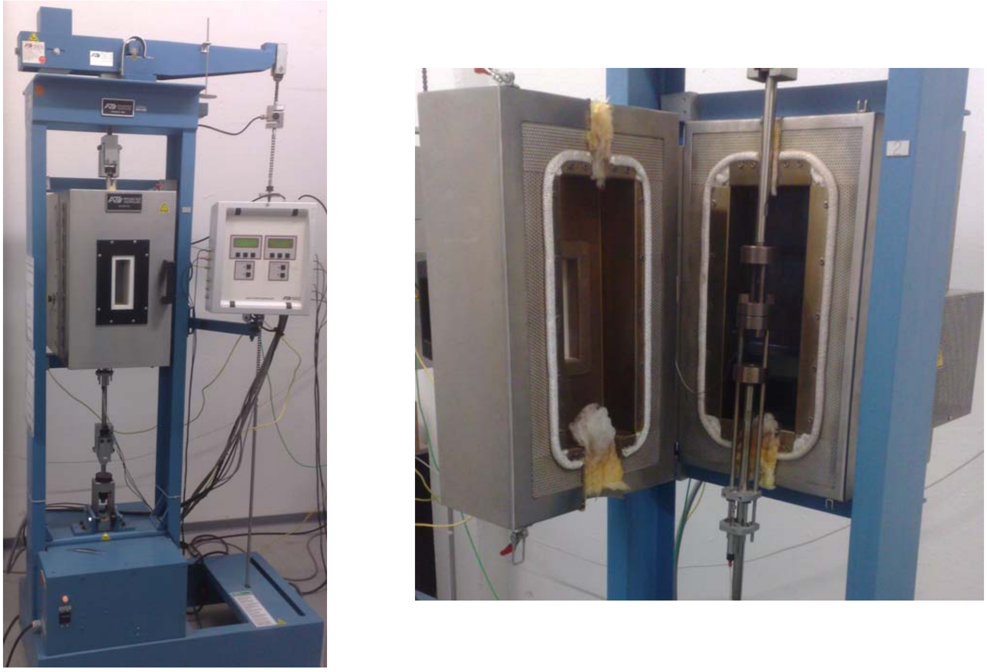

Figure (29): View of the creep machine.

Table (12): All of investigated TX-alloys in wt.-% (yes: investigated; no: not investigated).

Alloys	135°C		150°C			175°C
	80MPa	85MPa	60MPa	70MPa	80MPa	
Mg-3Sn	no	yes	no	no	yes	no
TX31	no	yes	no	no	yes	no
TX32	yes	yes	yes	yes	yes	yes
TX33	no	no	no	no	yes	yes
TX22	no	no	no	no	yes	yes
TX42	no	no	no	no	yes	yes
TX42x	no	yes	no	no	yes	no
TX51	no	yes	no	no	yes	no
TX52	no	yes	no	no	yes	no
TX62	no	yes	no	no	yes	no
TX63	no	no	no	no	yes	yes

4 Results

4.1 Microstructure and phase characterization

4.1.1 LM

Binary Mg-Sn-alloys

The light optical micrograph of the binary Mg-3Sn-alloy in the as-fabricated condition shows the coarse grains of this alloy with a very few Mg_2Sn precipitates is illustrated in Figure (30).

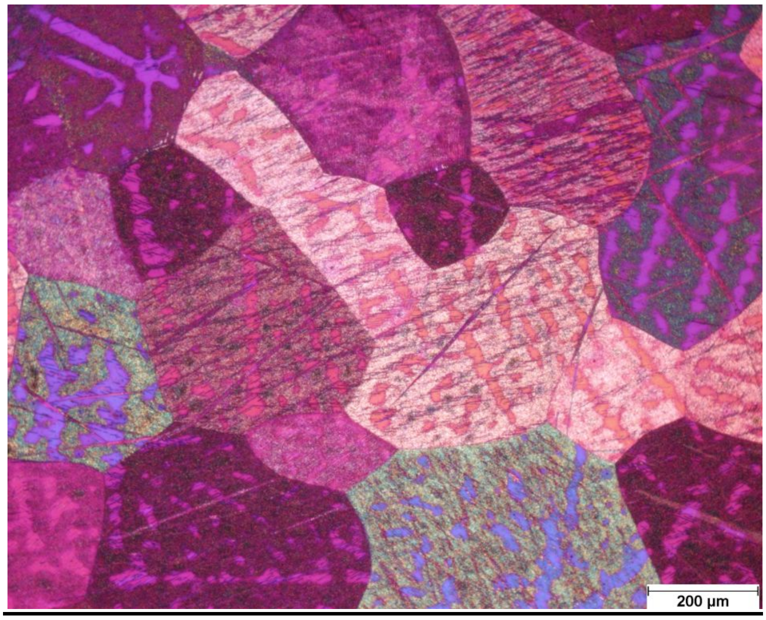

Figure (30): LM micrograph of Mg-3Sn alloy.

Ternary Mg-Sn-Ca-alloys

All of the TX-alloys revealed the formation of ternary $Ca_{2-x}Mg_xSn$ particles. This phase shows various bright round or long shapes. They are randomly distributed throughout the matrix and at grain boundaries with different morphologies. The LM micrographs of the ternary TX-alloys were found to be dependent on the ratio of Sn:Ca. The Mg-3Sn-1Ca (TX31), Mg-4.5Sn-1.5Ca (TX42x), and Mg-6Sn-2Ca (TX62) are given in Figure (31). Only the $Ca_{2-x}Mg_xSn$ phase was found in the mentioned alloys and the quantity of this phase increases with further addition of the amount of both Sn and Ca by keeping the same Sn:Ca ratio of 3:1.

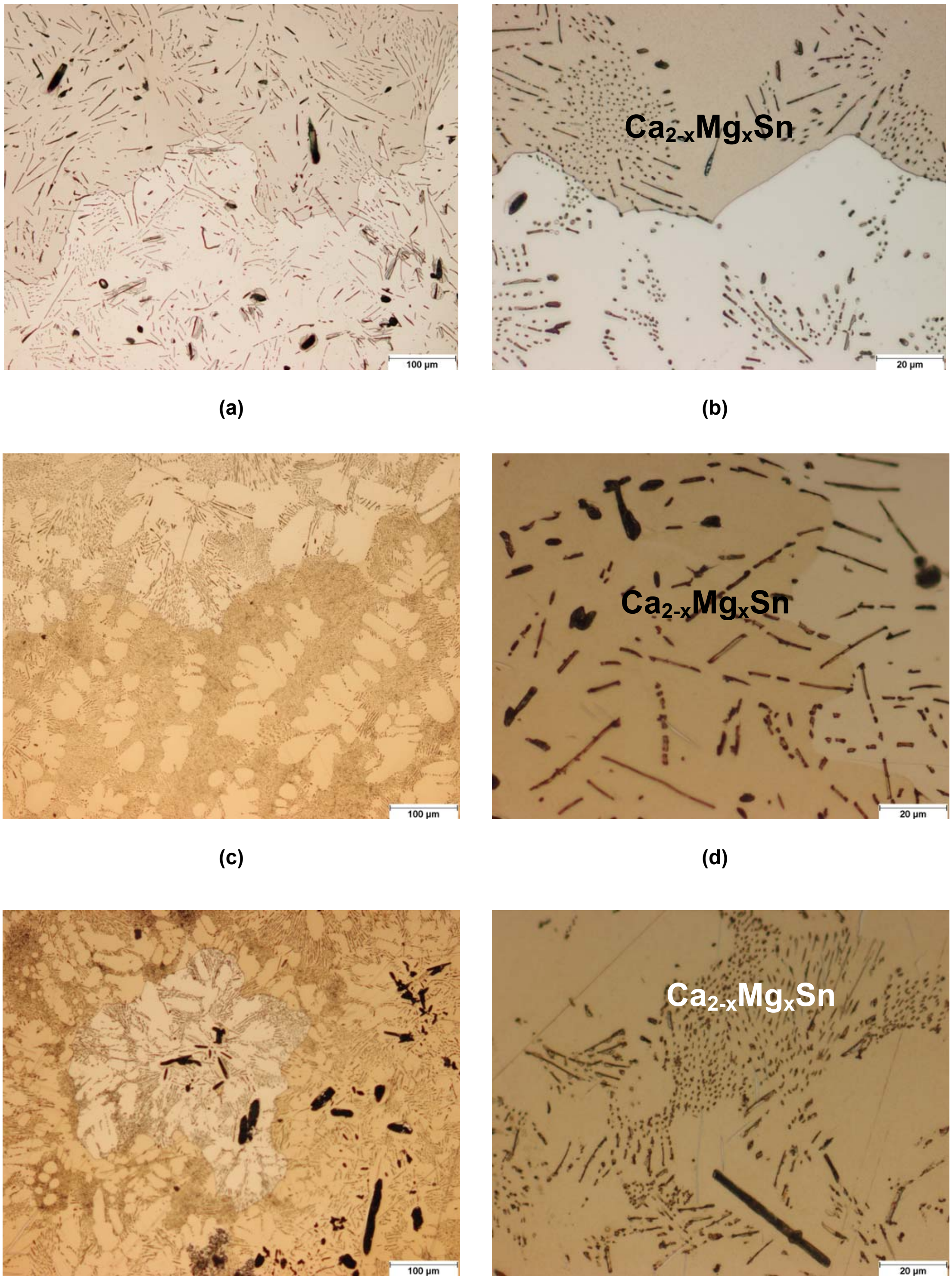

(a) (b)

(c) (d)

(e) (f)

Figure (31): LM micrographs of (a-b) TX31-, (c-d) TX42x-, and (e-f) TX62-alloys with a Sn:Ca ratio 3:1 at (a) lower and (b) higher magnifications image form showing $Ca_{2-x}Mg_xSn$ phase.

Figure (32) presents the light optical microscope investigations of TX32-alloy with a Sn:Ca ratio of less than 3:1. The ternary phase can be clearly seen in these micrographs. Besides the mentioned ternary phase, a binary Mg_2Ca phase was found in the TX32-alloy. These phases exhibit various shapes and randomly distributed at the matrix and at grain boundary.

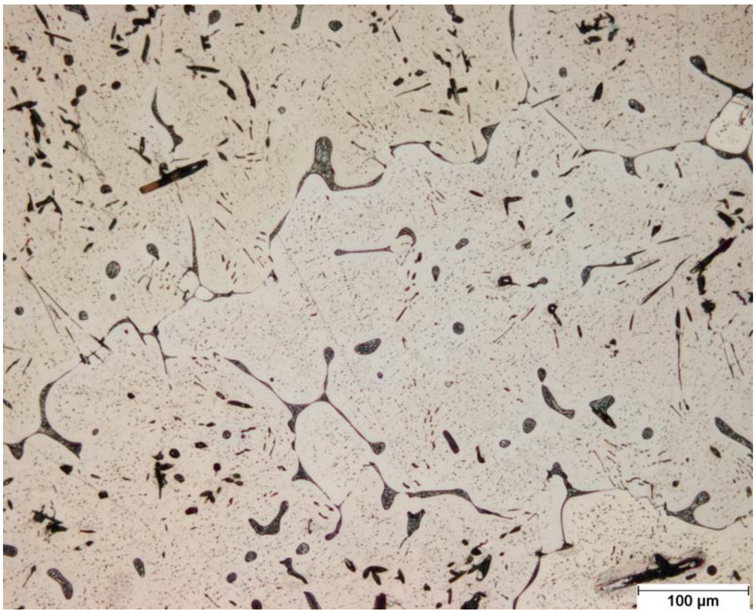

(a)

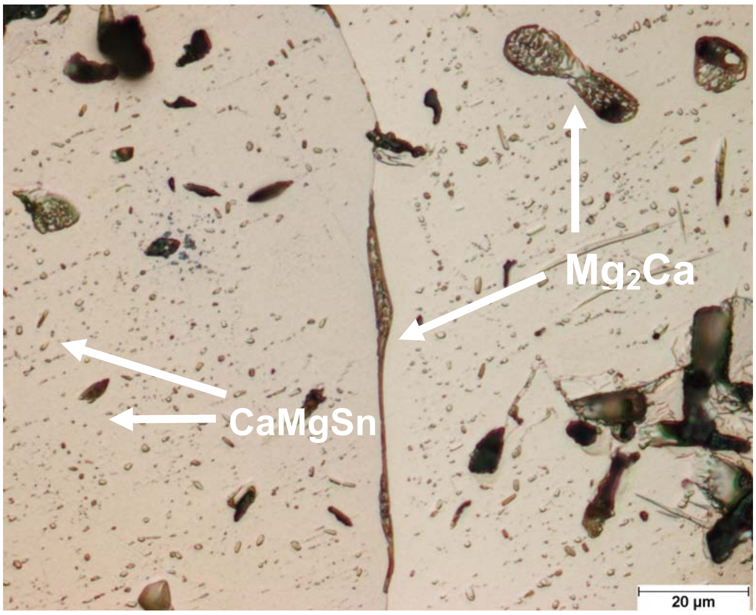

(b)

Figure (32): LM micrographs of (a-b) TX32-alloy with a Sn:Ca ratio less than 3:1 at (a) lower and (b) higher magnifications image form showing $Ca_{2-x}Mg_xSn$ and Mg_2Ca phases.

The LM of the TX-alloys, which have Sn:Ca ratio of more than 3:1 have also been investigated. In this case, another kind of binary phase has been detected. The particles of the binary particles Mg_2Sn with have various shapes, such as round or long were found besides the $Ca_{2-x}Mg_xSn$ phase. They are randomly distributed throughout the matrix and at grain boundaries. Figure (33) present the TX51-alloy that has a Sn:Ca ratio of more than 3:1.

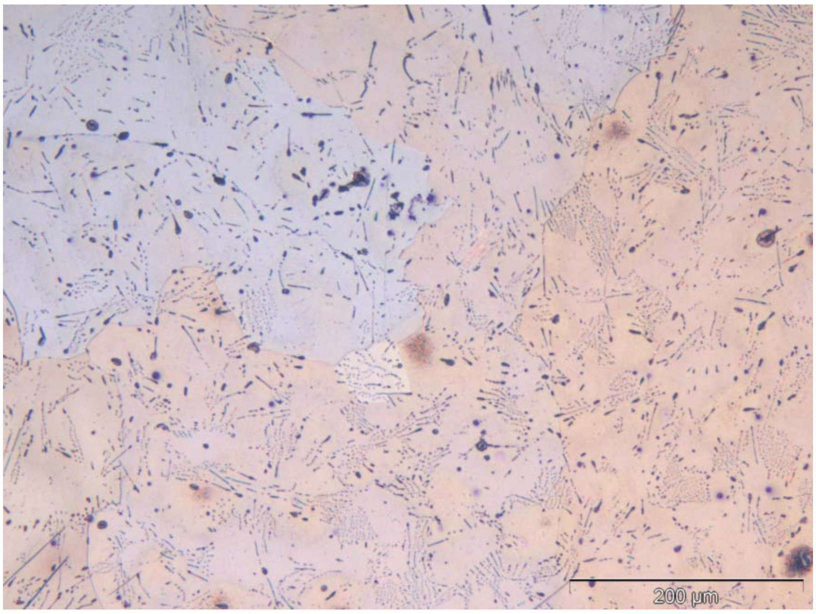

(a)

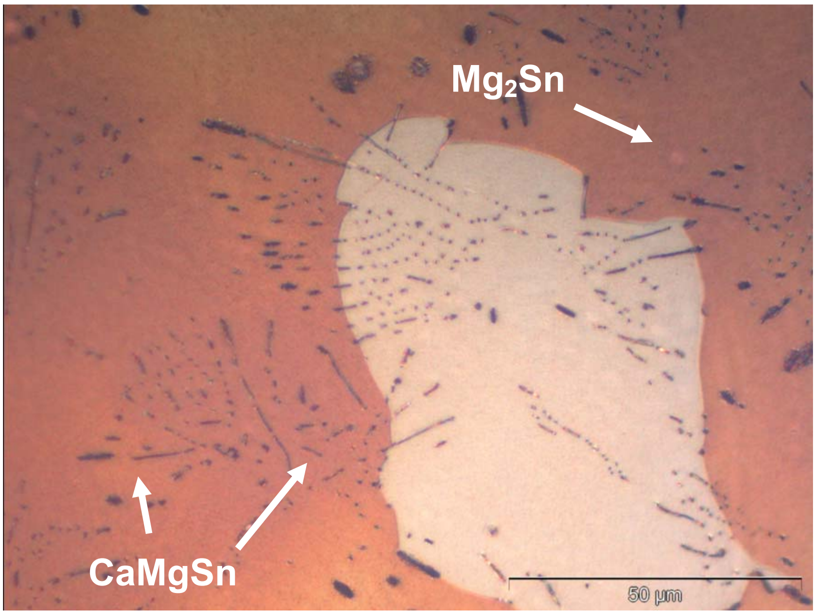

(b)

Figure (33): LM micrographs of (a-b) TX51-alloy with a Sn:Ca ratio more than 3:1 at (a) lower and (b) higher magnifications image form showing $Ca_{2-x}Mg_xSn$ and Mg_2Sn phases.

The grain sizes and the size of $Ca_{2-x}Mg_xSn$ particles of some TX-alloys were measured, as shown in Figure (34). Light optical microscopy measurement indicated that the grain size of the TX-alloys varies from 300-800 µm for the ratio Sn:Ca below 3:1 to 600-800 µm when the ratio is more than 3:1. The grain sizes of TX-alloys with a ratio of 3:1 achieved around 500 µm.

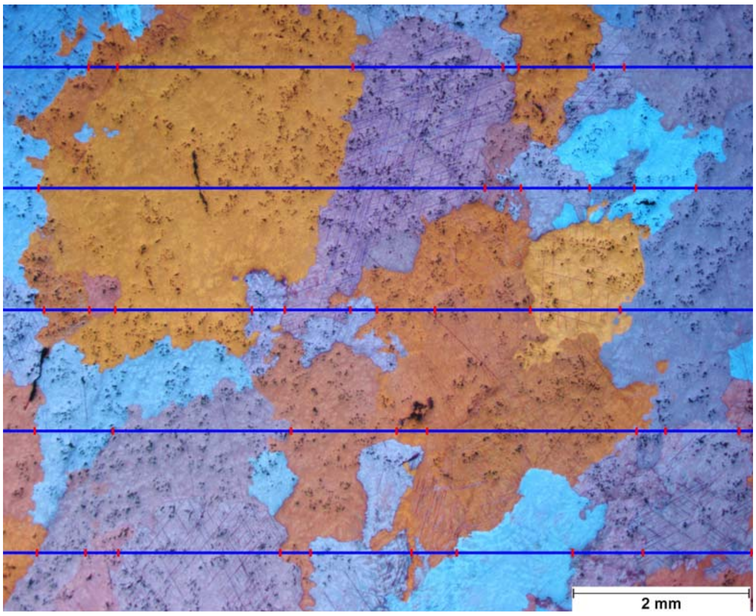

(a)

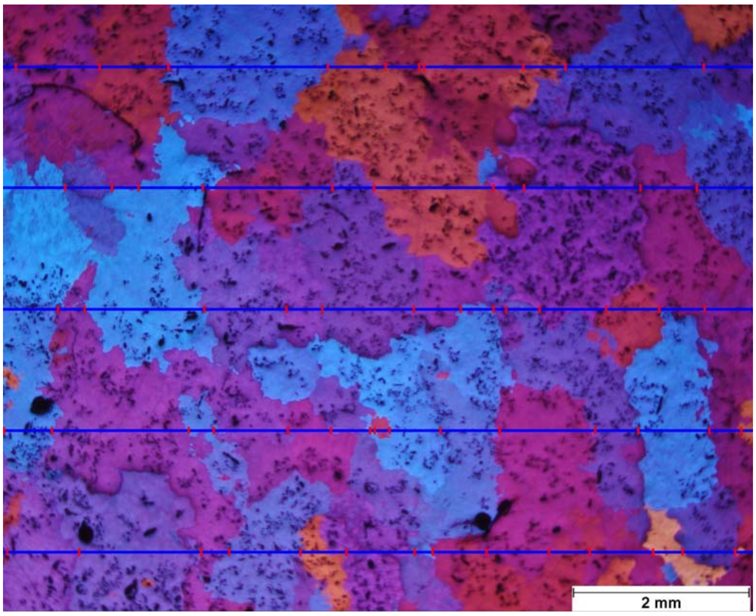

(b)

Figure (34): LM micrographs of (a) TX31-, and (b) TX62-alloys, with Sn:Ca ratio 3:1 showing the coarse grains of TX-alloys.

4.1.2 SEM / EDX

Binary Mg-Sn-alloys

Figure (35a-b) shows the SEM micrographs of the binary alloys Mg-3Sn and Mg-5Sn. They exhibit a small volume fraction of precipitates, which decorate the continuous linear network of Sn-enriched regions. Very few amounts of particles with lamellar shape were detected and their composition is close to that of Mg_2Sn phase. The increase of Sn content from 3 wt.-% to 5 wt.-% leads to higher amounts of particles.

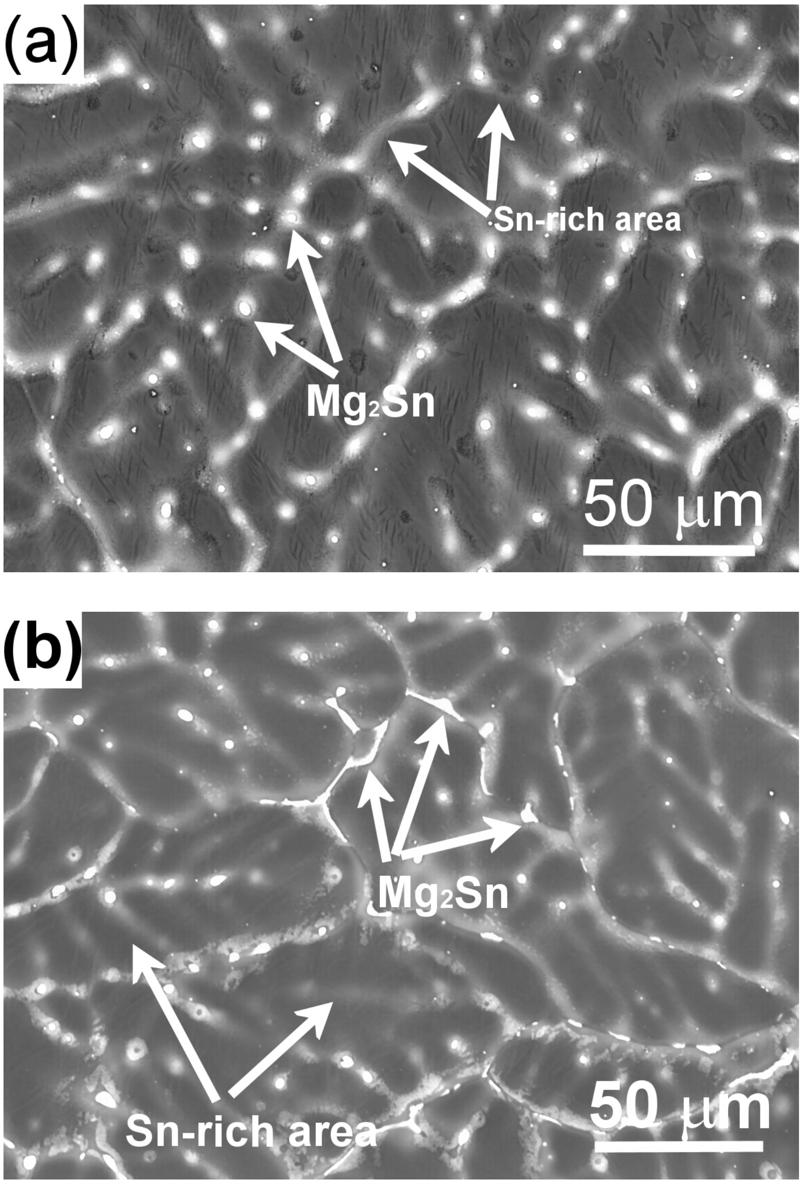

Figure (35): SEM micrographs of: (a) Mg-3Sn- and (b) Mg-5Sn-alloys.

Table (13): Results of SEM/EDX analysis of Mg-3Sn and Mg-5Sn alloys showing their related phase.

Alloys [wt.-%]	**phase**
Mg-3Sn	α-Mg, **Mg_2Sn**
Mg-5Sn	

The identification of Mg_2Sn precipitates was supported by EDX analysis. The results indicate that the diffusive bright bands are attributed to the enrichment of Sn at the dendritic boundaries. Figures (36 a-b) represent the spectrum of Mg-3Sn-alloy corresponding to the matrix (M) and the bright spots (P). They indicate some presence of Sn and strong peaks of Sn, respectively. The spectra are related to the SEM micrograph shown in Figure (36c). The results of the microstructure investigations of the binary Mg-Sn-alloys containing Mg_2Sn phase are given in Table (13).

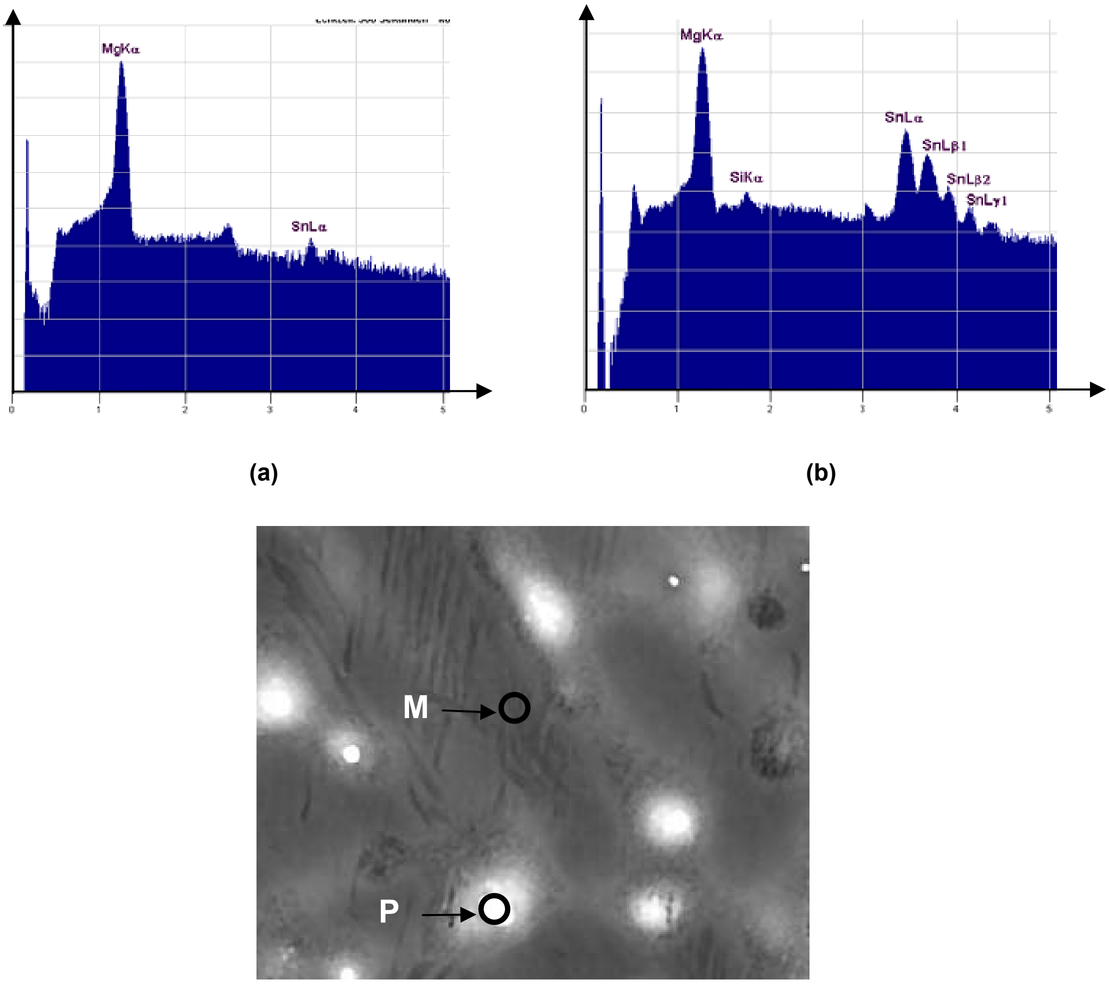

(a)

(b)

(c)

Figure (36): Results of EDX analysis of binary Mg-3Sn-alloy showing spectra of (a) matrix (M) and (c) bright particle (P) related to (c) SEM micrograph.

Ternary Mg-Sn-Ca-alloys

Figure (37 a-f) illustrates the three alloys (TX31, T42x, and TX62), which have the same ratio Sn:Ca of 3:1 contains the $Ca_{2-x}Mg_xSn$ phase. The increase of the content of Sn and Ca by keeping the same ratio leads to an increase of the volume fraction of this phase.

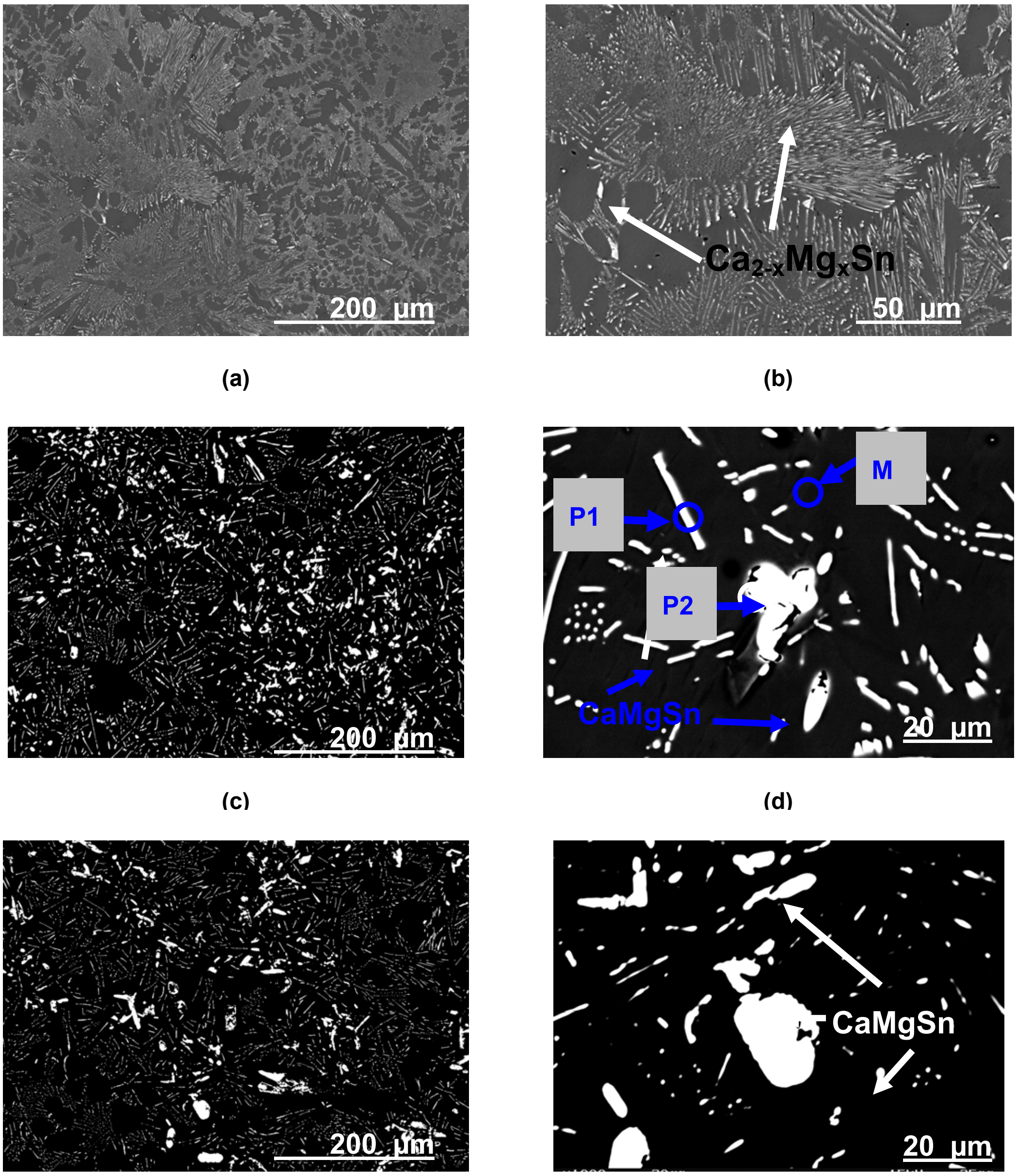

(a) (b)

(c) (d)

(e) (f)

Figure (37): SEM micrographs of (a-b) TX31-, (c-d) TX42x-, and (e-f) TX62-alloys with Sn:Ca ratio 3:1 at (left) lower and (right) higher magnifications showing $Ca_{2-x}Mg_xSn$ phase; M, P1, P2 in (d) are given in Table (15).

Table (14) lists the result of the investigation, which is corresponded to analysed Matrix (M) and Particle (P1) in Figure (37 d).

Table (14): Results of SEM/EDX analysis of TX-alloys in wt.-% with same Sn:Ca ratio 3:1 showing their related phases.

Alloys [wt.-%]	Abbreviation	Phases
Mg-3Sn-1Ca	TX31	α-Mg, $Ca_{2-x}Mg_xSn$
Mg-4.5Sn-1.5Ca	TX42x	α-Mg, $Ca_{2-x}Mg_xSn$
Mg-6Sn-2Ca	TX62	α-Mg, $Ca_{2-x}Mg_xSn$

EDX analysis estimated the volume fraction of phases. Table (15) presents the calculated compositions from spectra obtained at significant locations such as particles (P1 and P2) and matrix (M) of TX42x-alloy. Bright long (P1) and round (P2) particles can be seen in Figure (37b). According to the spectra of the bright particles, they clearly indicate the presence of both Sn and Ca and thus it can be identified as a $Ca_{2-x}Mg_xSn$ phase. In contrast, a very low content of Sn but no Ca can be found in the matrix.

Table (15): Results of EDX analysis of TX42x-alloy with ratio Sn:Ca 3:1 in wt.-% and at.-% showing phases from matrix (M) "α-Mg", bright long (P1), and round particle (P2) "$Ca_{2-x}Mg_xSn$".

Mg-3Sn-1Ca [wt.-%] or Mg-0.64Sn-0.63Ca [at.-%]							
		Matrix (M)		Particle (P1)		Particle (P2)	
		wt.-%	at.-%	wt.-%	at.-%	wt.-%	at.-%
Elements	Mg	99.58	99.91	60.96	83.42	26.86	59.81
	Sn	0.42	0.09	28.79	8.07	65.49	29.86
	Ca	-	-	10.25	8.51	7.65	10.33
Phases		α-Mg		$Ca_{2-x}Mg_xSn$			

In the case that the ratio Sn:Ca is less than 3:1 further Mg_2Ca phase can be formed besides the $Ca_{2-x}Mg_xSn$ one. The series of investigated alloys, which have such ratio, are Mg-2Sn-2Ca (TX22), Mg-3Sn-2Ca (TX32), Mg-3Sn-3Ca (TX33), Mg-3Sn-2Ca (TX32), Mg-4Sn-2Ca (TX42), Mg-5Sn-2Ca (TX52), Mg-6Sn-3Ca (TX63). They belong to the group with a Sn:Ca in the range of 1:1 up to 2.5:1. The EDX-results of the mentioned alloys are summarized in Table (16).

Table (16): Results of SEM/EDX analysis of TX-alloys with ratio Sn:Ca less than 3:1 shows their related phases.

Alloys [wt.-%]	Abbreviation	Phases
Mg-2Sn-2Ca	TX22	α-Mg, $Ca_{2-x}Mg_xSn$, Mg_2Ca
Mg-3Sn-3Ca	TX33	α-Mg, $Ca_{2-x}Mg_xSn$, Mg_2Ca
Mg-3Sn-2Ca	TX32	α-Mg, $Ca_{2-x}Mg_xSn$, Mg_2Ca
Mg-3Sn-1.5Ca	TX32x	α-Mg, $Ca_{2-x}Mg_xSn$, Mg_2Ca
Mg-4Sn-2Ca	TX42	α-Mg, $Ca_{2-x}Mg_xSn$, Mg_2Ca
Mg-6Sn-3Ca	TX63	α-Mg, $Ca_{2-x}Mg_xSn$, Mg_2Ca
Mg-5Sn-2Ca	TX52	α-Mg, $Ca_{2-x}Mg_xSn$, Mg_2Ca

The related microstructures illustrated in Figure (38a-l) show the mentioned detected phases. The micrographs of these TX-alloys revealed the bright $Ca_{2-x}Mg_xSn$ in addition to the round grey Mg_2Ca particles.

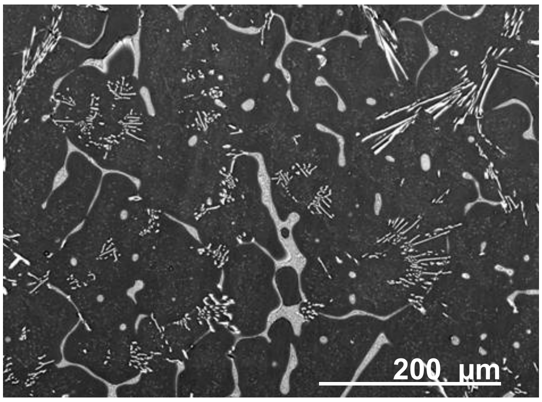

(a)

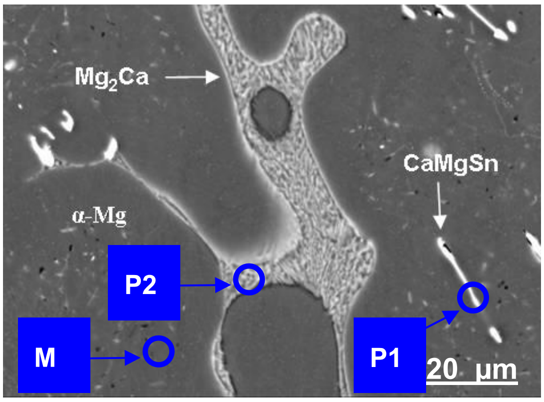

(b)

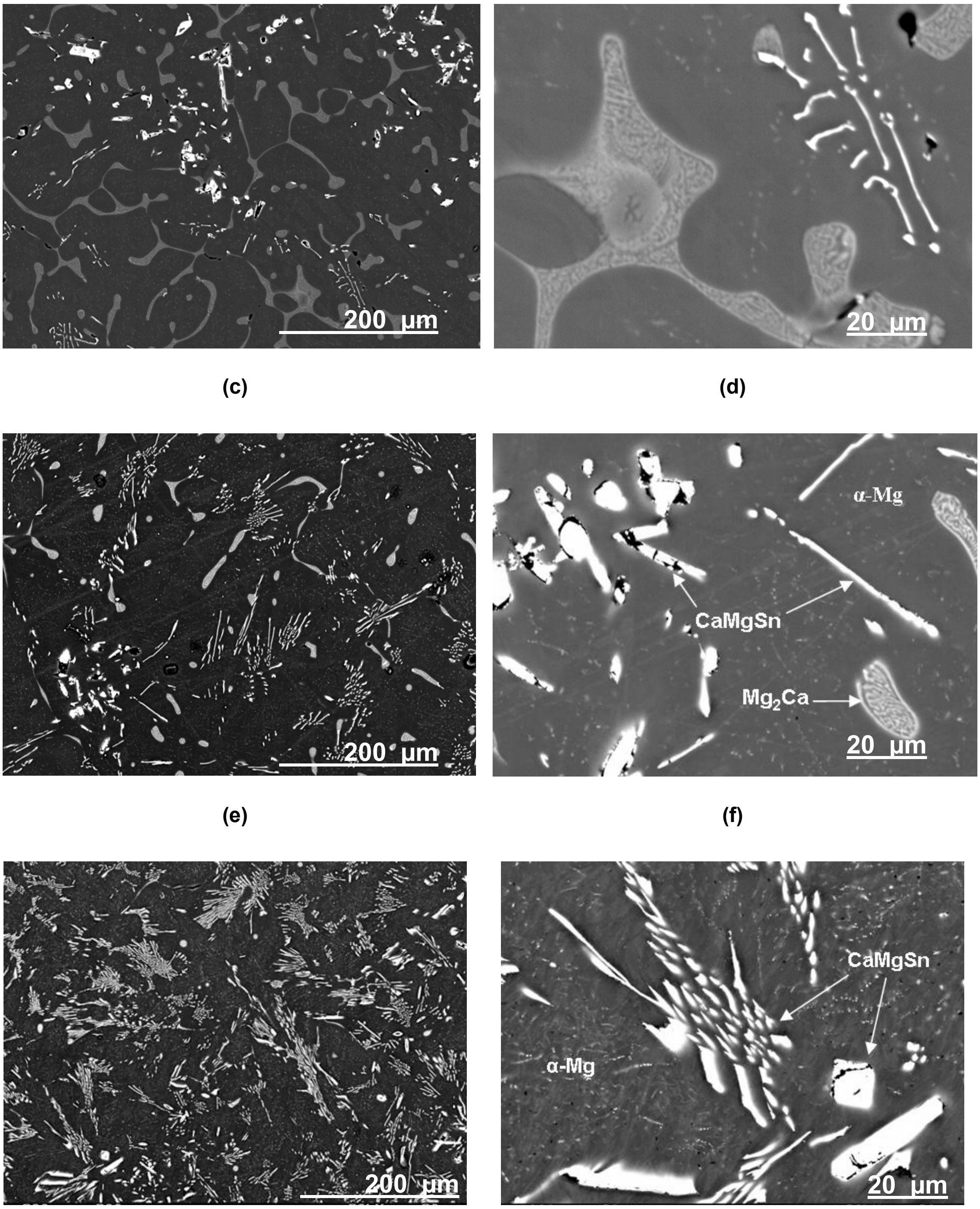
200 µm
20 µm
200 µm
α-Mg
CaMgSn
Mg_2Ca
20 µm
200 µm
CaMgSn
α-Mg
20 µm

(c) (d)

(e) (f)

(g) (h)

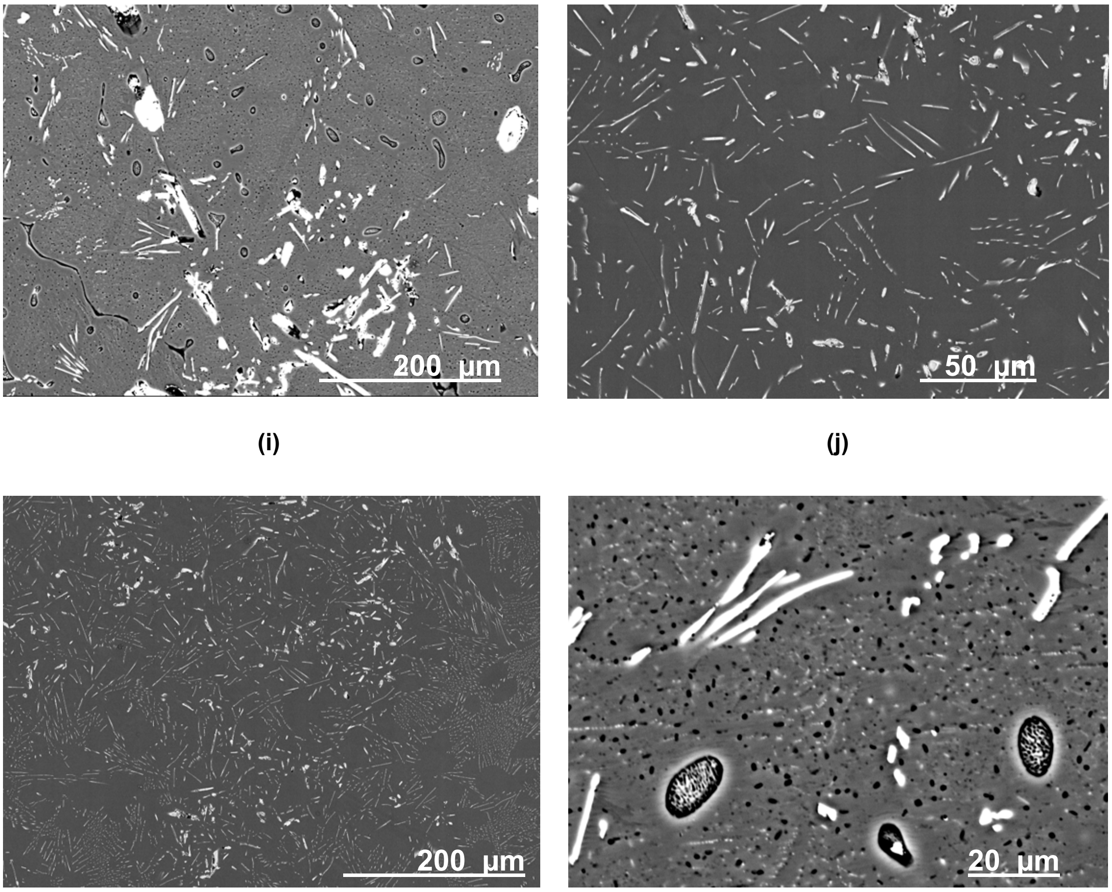

(i) (j)

(k) (l)

Figure (38): SEM micrographs of (a-b) TX22-, (c-d) TX33-, (e-f) TX32-, (g-h) TX42-, (i-j) TX63-, and (k-l) TX52-alloys with Sn:Ca ratio below (3:1) at lower (left) and higher (right) magnifications showing $Ca_{2-x}Mg_xSn$ and Mg_2Ca phases; M, P1, P2 in (b) are given in Table (17).

The results of EDX investigations corresponding to the matrix of the TX32-alloys, which exhibit a ratio less than 3:1, show the existence of Mg in the matrix (M) with very few amounts of Ca. The spectra corresponding to the two different particles indicate the occurrence of the $Ca_{2-x}Mg_xSn$ (P1) and Mg_2Ca (P2) phases. Figure (38b) shows some selected points in the matrix (M) as well as at two different particles “P1”, “P2”. Table (17) summarizes the results of EDX investigations.

Table (17): Results of EDX analysis of TX32-alloy with ratio Sn:Ca below 3:1 in wt.-% and at.-% showing phases from matrix (M) "α-Mg", bright long (P1) "$Ca_{2-x}Mg_xSn$" and grey particle (P2) "Mg_2Ca".

Mg-3Sn-2Ca [wt.-%] or Mg-0.63Sn-1.25Ca [at.-%]							
Detected		Matrix (M)		Particle (P1)		Particle (P2)	
		wt.-%	at.-%	wt.-%	at.-%	wt.-%	at.-%
Elements	Mg	99.92	99.95	85.89	95.02	80.35	87.08
	Sn	-	-	4.00	2.69	-	-
	Ca	0.02	0.01	10.11	2.29	19.65	12.92
Phases		α-Mg		$Ca_{2-x}Mg_xSn$		Mg_2Ca	

Table (18) and Figures (39a-d) summarize the results of the SEM/EDX investigations where the ratio Sn:Ca is more than 3:1. In this case, the binary phase Mg_2Sn was detected besides the ternary phase $Ca_{2-x}Mg_xSn$. The following alloys belong to this group, namely: Mg-3Sn-0.5Ca (TX30x), Mg-5Sn-0.5Ca (TX50x), and Mg-5Sn-1.5Ca-alloy (TX52x).

Table (18): Results of SEM/EDX analysis of TX-alloys in wt.-% with Sn:Ca ratio more than 3:1 showing their related phases.

Alloys [wt.-%]	Abbreviation	Phases
Mg-3Sn-0.5Ca	TX30x	α-Mg, $Ca_{2-x}Mg_xSn$, Mg_2Sn
Mg-5Sn-0.5Ca	TX50x	α-Mg, $Ca_{2-x}Mg_xSn$, Mg_2Sn
Mg-5Sn-1Ca	TX50	α-Mg, $Ca_{2-x}Mg_xSn$, Mg_2Sn
Mg-5Sn-1.5Ca	TX52x	α-Mg, $Ca_{2-x}Mg_xSn$, Mg_2Sn

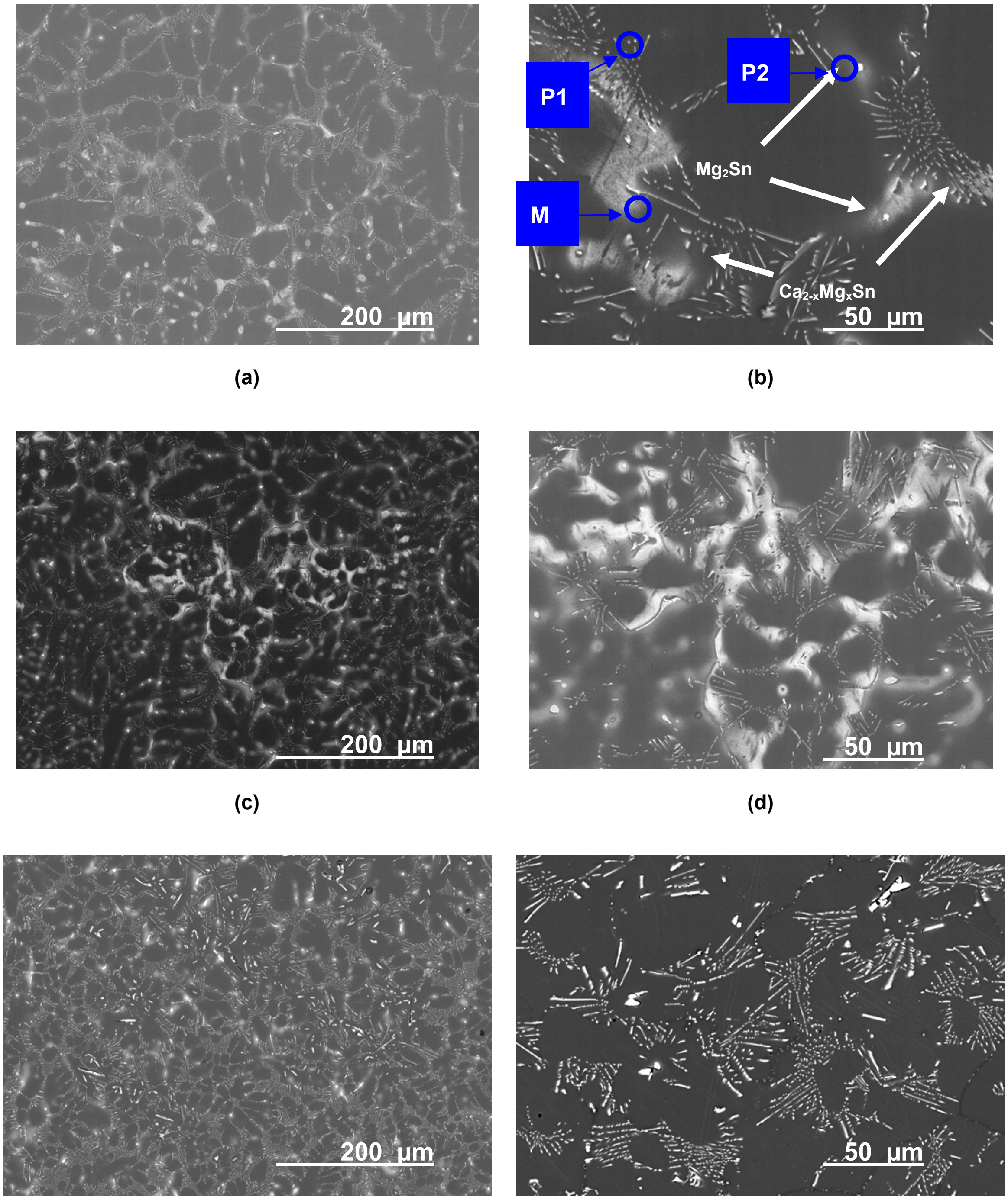

(a) (b)

(c) (d)

(e) (f)

Figure (39): SEM micrographs of (a-b) TX30x-, (c-d) TX50x- and (e-f) TX51- alloys with a Sn:Ca ratio of more than 3:1 at (left) lower and (right) higher magnifications showing $Ca_{2-x}Mg_xSn$ and Mg_2Sn phases; M, P1, P2 in (b) are given in Table (19).

The EDX spectra corresponding to the matrix and particles in alloys, which exhibit a ratio higher than 3:1, are found in Table (19). The TX51-alloy indicates the presence of Sn in the matrix with no trace of Ca. The spectrum corresponding to the $Ca_{2-x}Mg_xSn$ particles indicates that most of the Sn and Ca are partitioned to the particle phase. Finally, the other analyzed particles were Mg_2Sn, where the rest of Sn is collected in the particle phase.

Table (19): Results of EDX analysis of TX51-alloys with ratio Sn:Ca more than 3:1 in wt.-% and at.-% showing phases from matrix (M) "α-Mg", bright long (P1) "$Ca_{2-x}Mg_xSn$" and grey particle (P2) "Mg_2Sn".

Mg-5Sn-1Ca [wt.-%] or Mg-1.07Sn-0.63Ca [at.-%]							
Detected		Matrix (M)		Particle (P1)		Particle (P2)	
		wt.-%	at.-%	wt.-%	at.-%	wt.-%	at.-%
Elements	Mg	97.37	99.45	22.19	49.33	76.03	93.93
	Sn	2.63	0.55	60.74	27.65	23.97	6.07
	Ca	-	-	17.07	23.01	-	-
Phases		α-Mg		$Ca_{2-x}Mg_xSn$		Mg_2Sn	

4.1.3 XRD

Binary Mg-Sn-alloys

Figure (40) shows x-ray diffraction patterns of the Mg_2Sn phase in both of the Mg-3Sn and Mg-5Sn alloys. XRD confirms the results of SEM/EDX examinations showing the observation of only Mg_2Sn in the binary Mg-Sn-alloys. The intensities of the peaks of Mg_2Sn in the Mg-5Sn are higher than the alloy Mg-3Sn as it can be seen in the same figure.

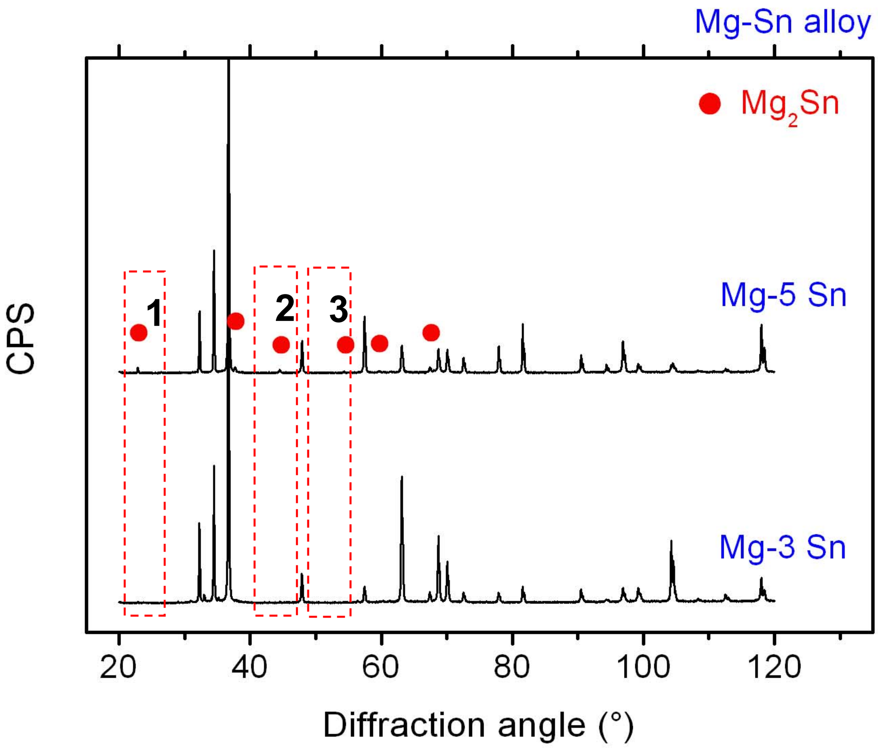

Figure (40): XRD patterns of Mg-3Sn- and Mg-5Sn-alloys showing the detected Mg_2Sn.

Ternary Mg-Sn-Ca-alloys

The XRD pattern in Figure (41) confirms the presence of $Ca_{2-x}Mg_xSn$ as a second phase in the TX-alloys with a ratio 3:1. Neither Mg_2Ca nor Mg_2Sn was observed in such alloys.

Figure (42) shows the pattern of the Mg-3Sn based alloys with addition of Ca. In all investigated Mg-Sn-Ca alloys, the $Ca_{2-x}Mg_xSn$ phase was confirmed. Furthermore, the obtained diffractograms demonstrate that the peak intensities of the $Ca_{2-x}Mg_xSn$ increase with the increase of the amount of Sn and Ca.

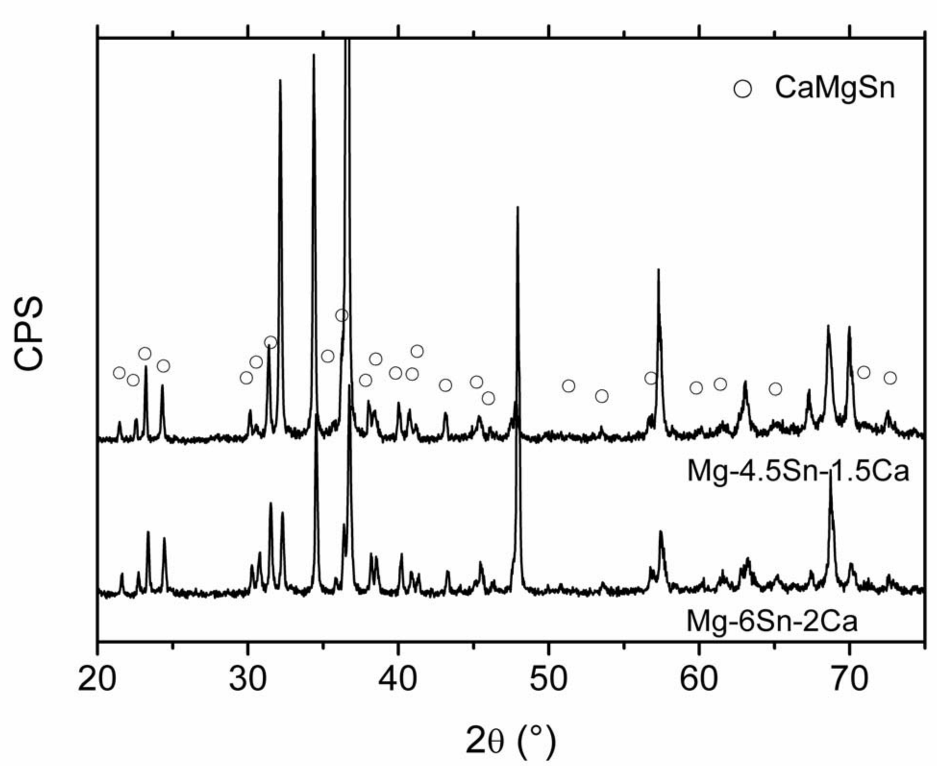

Figure (41): XRD patterns of the TX-alloys with a ratio of 3:1 showing $Ca_{2-x}Mg_xSn$ phase.

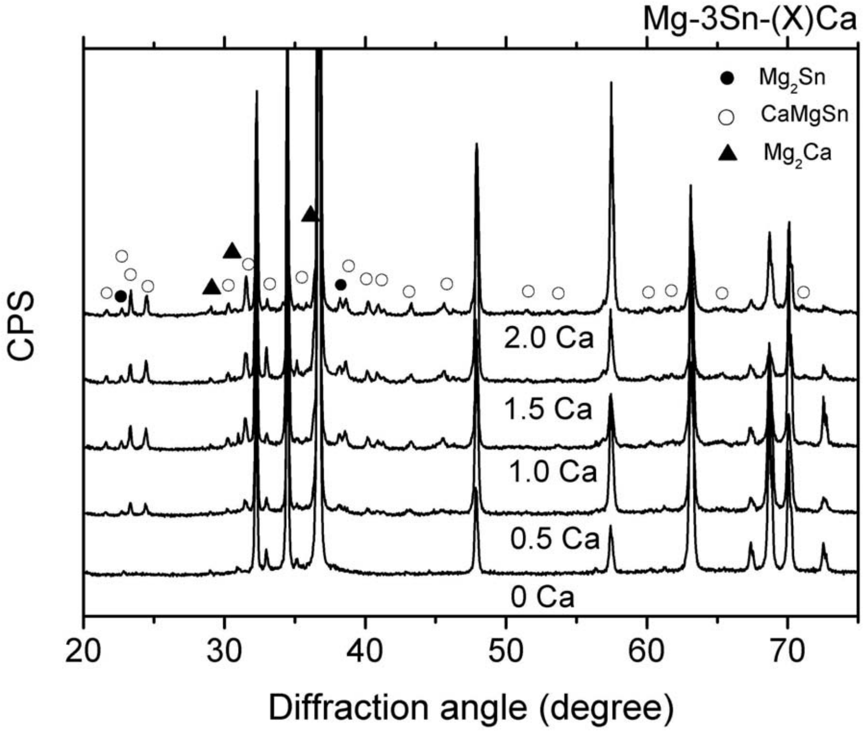

Figure (42): XRD patterns of Mg-3Sn based alloys system showing $Ca_{2-x}Mg_xSn$, Mg_2Sn, and Mg_2Ca phases.

The $Ca_{2-x}Mg_xSn$ phase was also confirmed by XRD in all investigated Mg-Sn-Ca alloys based on the Mg-5Sn alloys system. Furthermore, the obtained diffractograms demonstrate that the peak intensities of the $Ca_{2-x}Mg_xSn$ phase are dependent on the amount of Sn and Ca, which can be shown in Figure (43). With increasing the amount of Sn and thus the changes in the ratio of Sn:Ca the peak intensities of the $Ca_{2-x}Mg_xSn$ phase raises. The binary Mg_2Sn phase can also be confirmed in most of the cases.

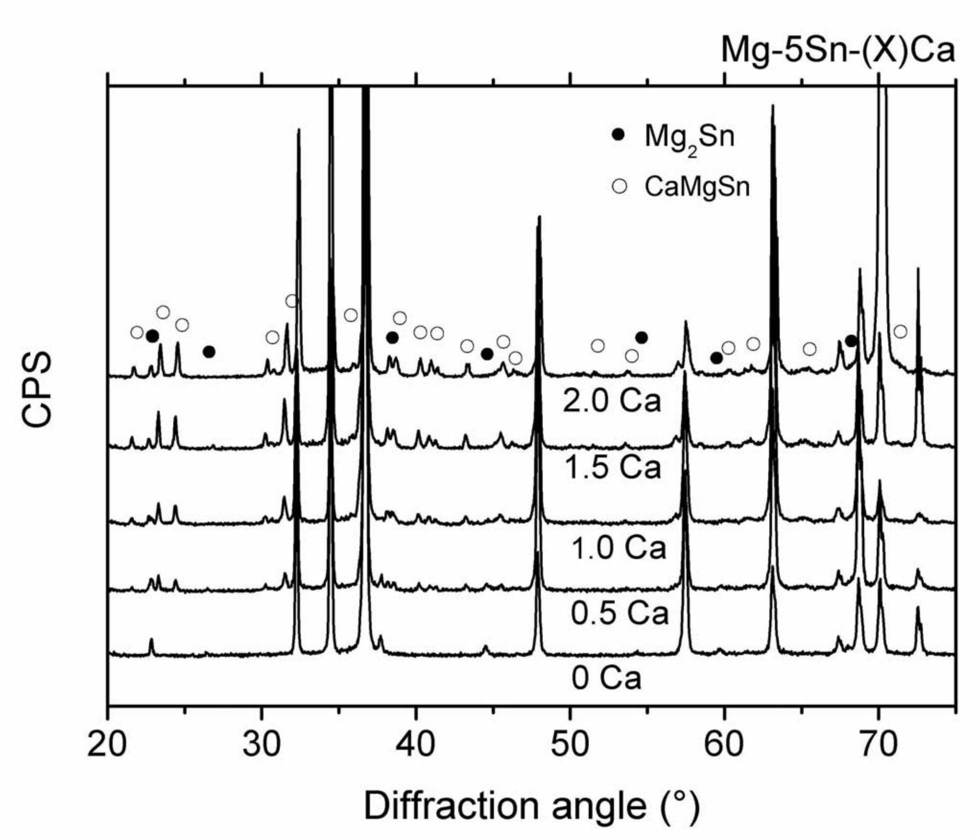

Figure (43): XRD patterns of Mg-5Sn based alloys system showing $Ca_{2-x}Mg_xSn$, Mg_2Sn, and Mg_2Ca phases.

4.1.4 TEM

The microstructure and the composition of Mg-5Sn-alloy were studied by TEM. Figure (44) reveal a high magnification image of fine Mg_2Sn particles in the mentioned alloy inside a grain. Figure (45) shows a TEM image of TX32-alloy at low magnification. In the same Figure, lamellar particles can be seen inside the grains in the TX32-alloy.

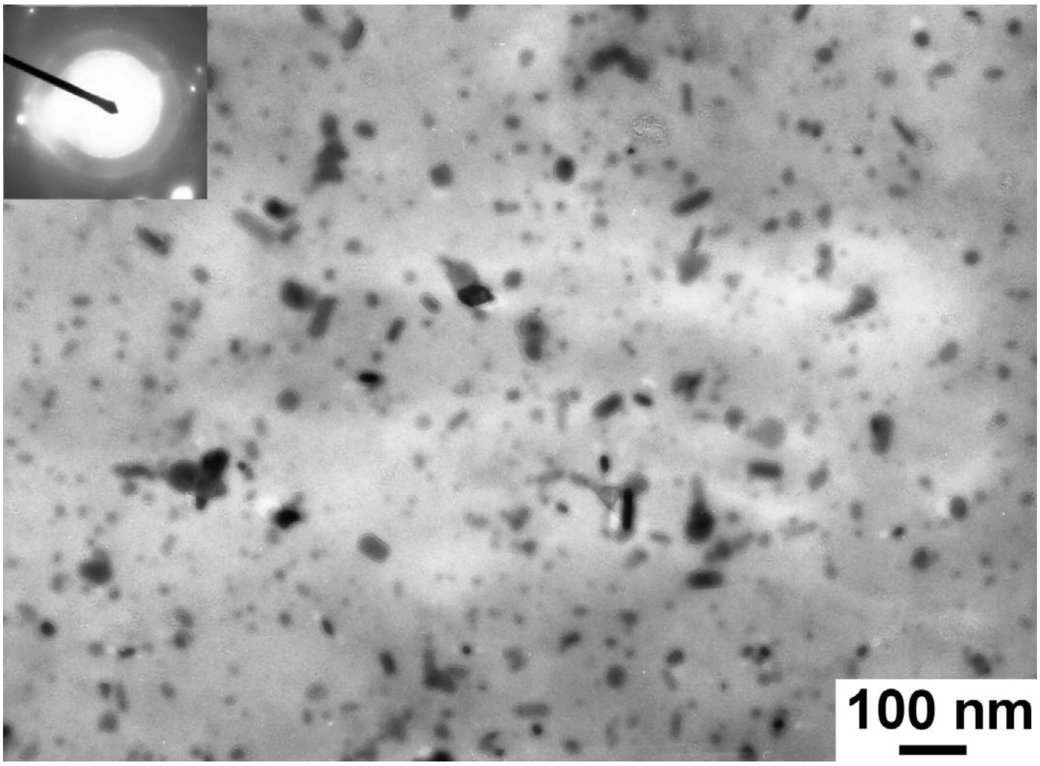

Figure (44): TEM investigation showing fine particles Mg_2Sn inside the grain in Mg-5Sn alloy.

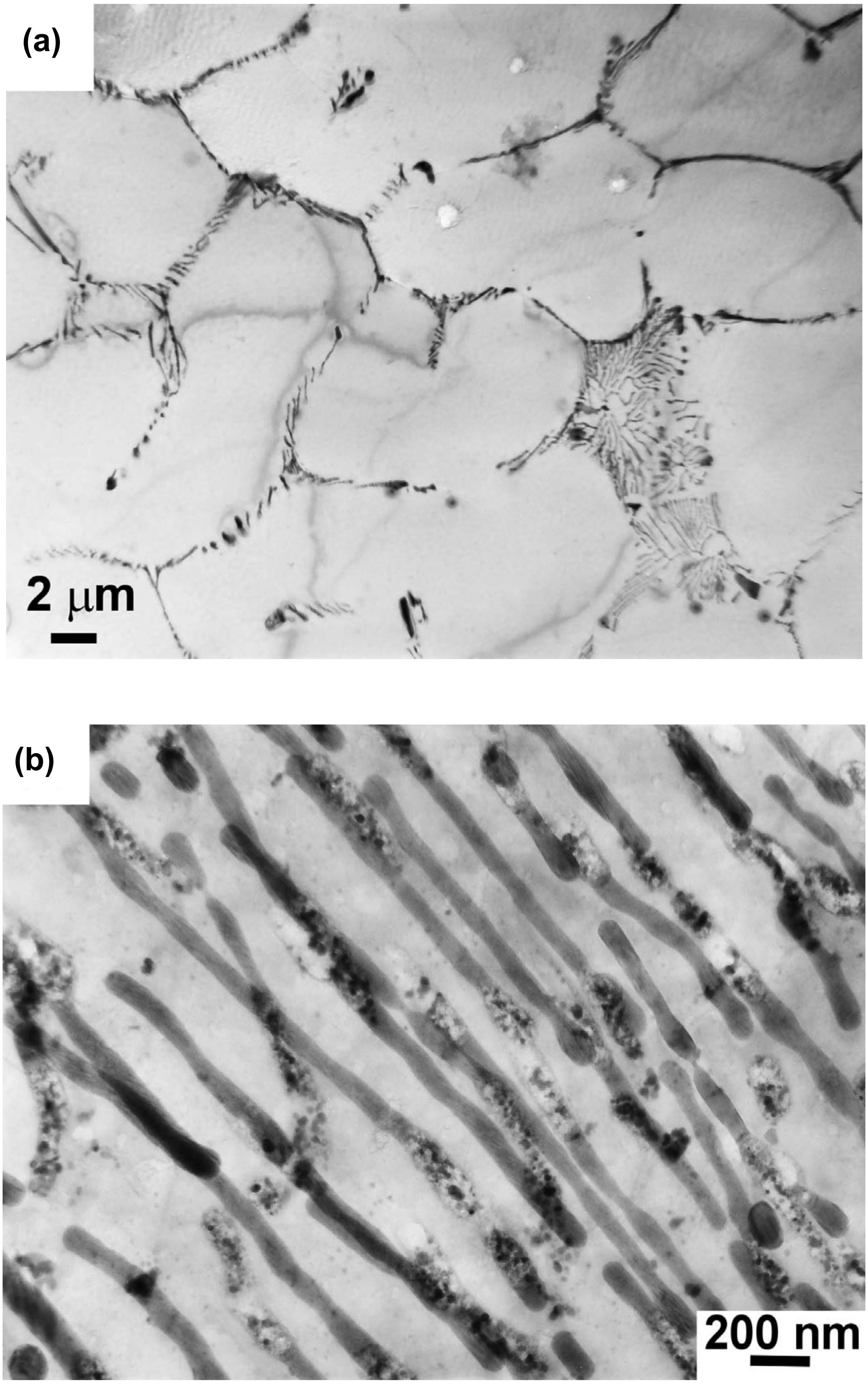

Figure (45): TEM investigation of TX32-alloy showing lamellar particles at (a) low magnification and (b) high magnification.

Figure (46) shows a low magnification image of particles in the TX51-alloy. The $Ca_{2-x}Mg_xSn$ particles with different shapes are observed at dendrite boundaries or at grain boundaries.

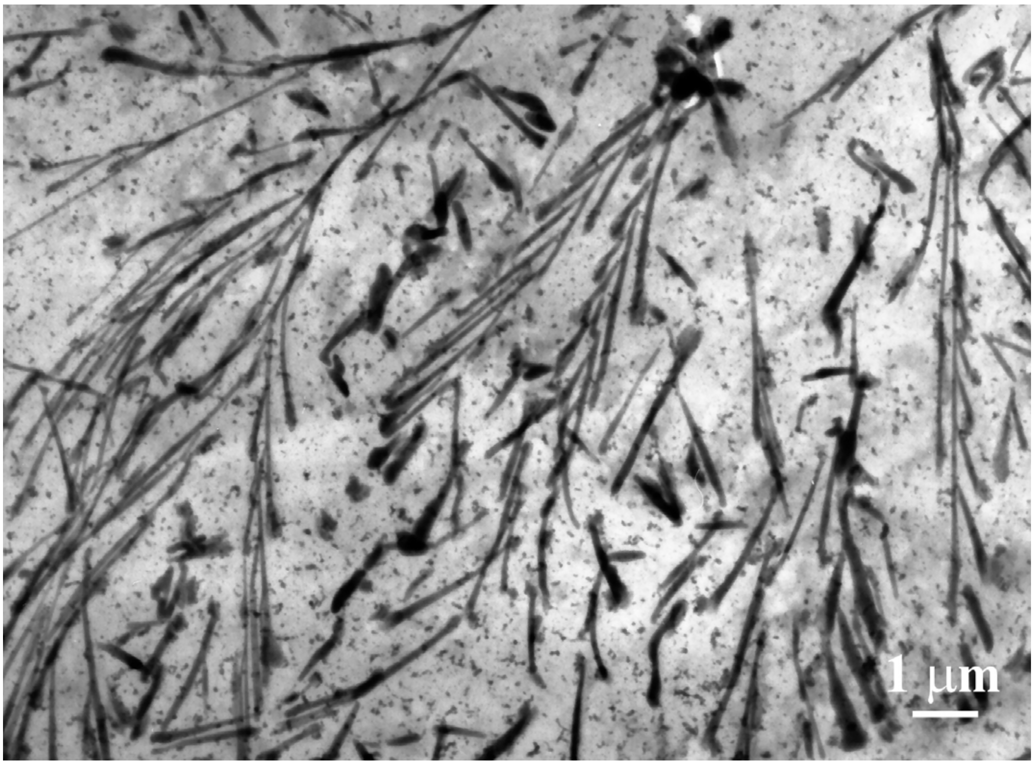

Figure (46): TEM investigation showing observations of particles in the TX51-alloy.

$Ca_{2-x}Mg_xSn$ particles can also be observed within the grains itself, as can be seen in Figure (47). The morphology is shown in Figure (47a), while Figure (47b) shows a diffraction pattern obtained of a particle by which the precipitates can be identified as the $Ca_{2-x}Mg_xSn$ phase.

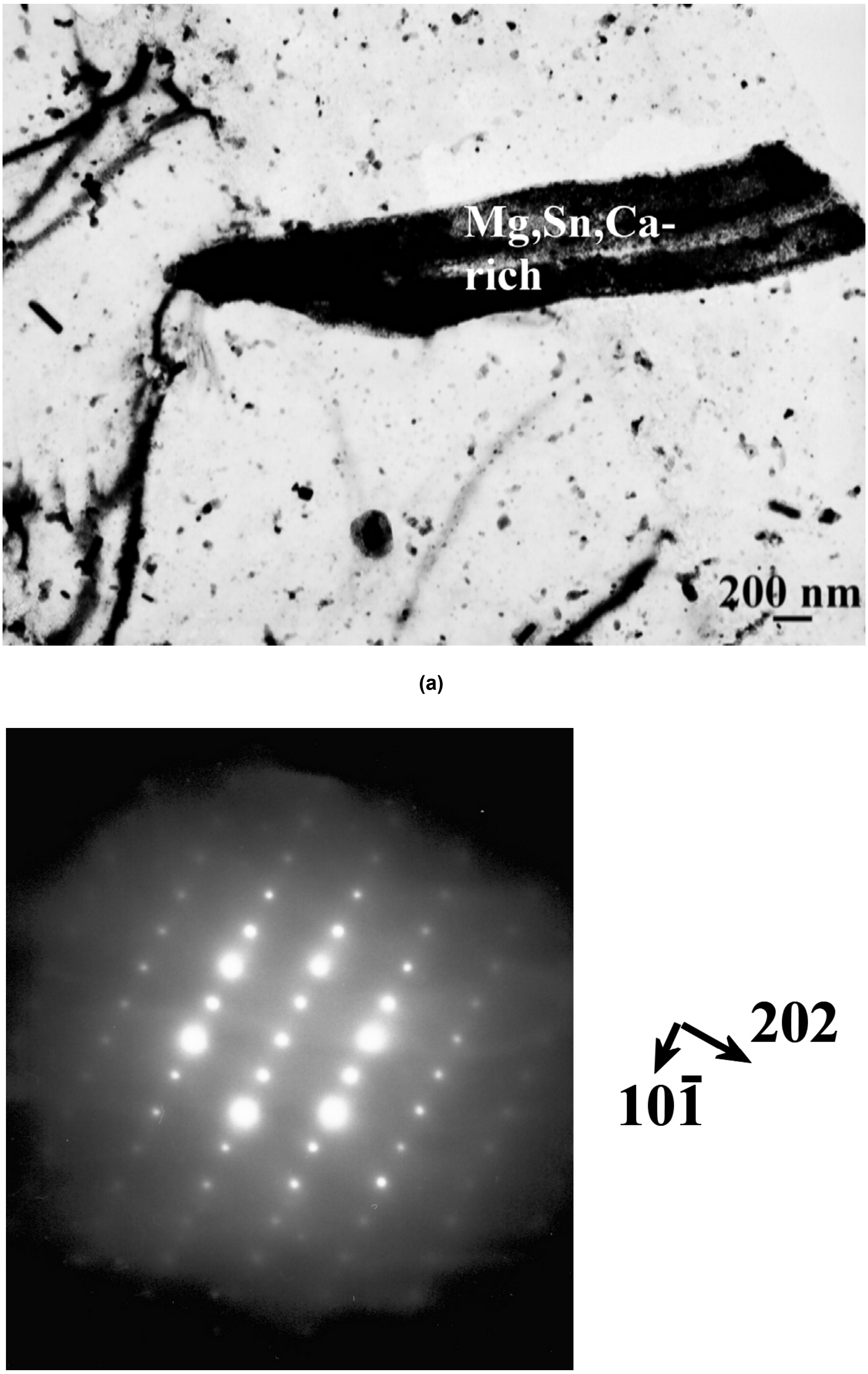

(a)

(b)

Figure (47): TEM investigation showing observation of (a) morphology of the $Ca_{2-x}Mg_xSn$ particle and (b) diffraction pattern, the zone axis is [040] in TX51-alloy

In the TX51-alloy, fine Mg_2Sn particles are found besides the ternary $Ca_{2-x}Mg_xSn$ phase. The particles have a size of several nanometer, Figure (48a). They only occur inside the grains. Figure (48b) shows a diffraction pattern obtained from the area image in Figure (48a).

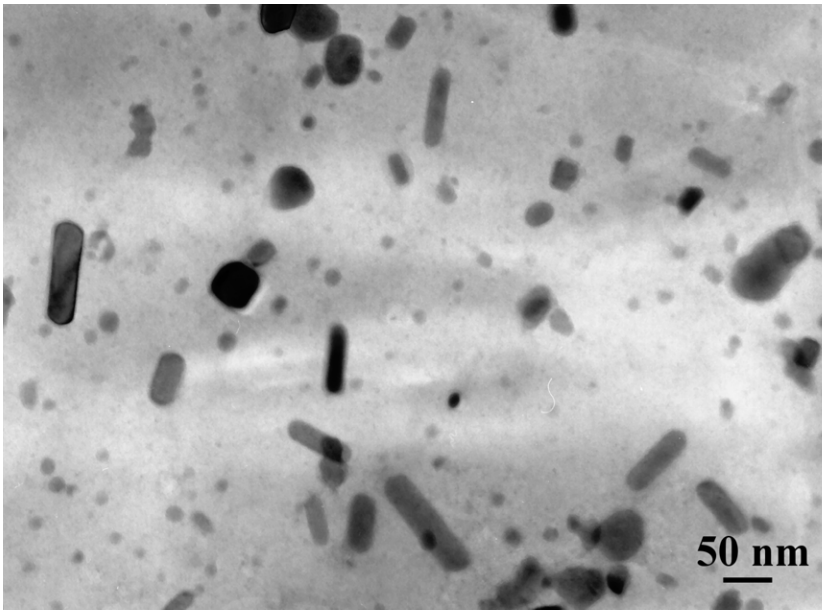

(a)

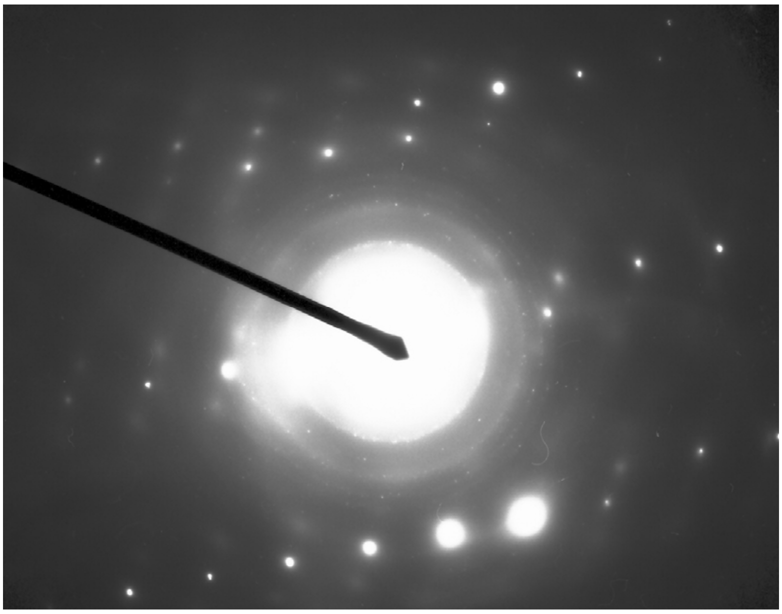

(b)

Figure (48): TEM investigation showing (a) the morphology of the Mg_2Sn particles and (b) diffraction rings from this area in TX51-alloy.

4.1.1 Differential thermal analysis (DTA), differential scanning calorimetry (DSC) measurements and thermodynamic calculations

The results of DTA analysis for TX-alloys show various values of melting and solidification temperatures. They are lower than that of pure magnesium and the Mg-3Sn. The start of their melting temperature ranges between 620-640 °C with heating and cooling rate of 2 K/min and 10 K/min. The results indicate that the TX-alloys with a Sn:Ca ratio equal or more than 3:1 reveal only one peak of melting and solidification temperature, while the TX-alloys with Sn:Ca ratio below 3:1 shows the presence of further signal. The additional peak exhibits temperature at approx. 516 °C. The results of DTA investigations are summarized in Tables (20-21) showing their melting and solidification temperatures. The alloys showing the curves and their related temperature signals are given in Figures (49-52) and in Figures (81-90) in appendix.

Table (20): The DTA measurement showing melting and solidification temperature of investigated TX-alloys.

Alloys	Abbr.	Ratio	Onset heating	Onset cooling	Onset heating	Onset cooling
			temperature [°C]			
[wt.-%]			DTA (2K/min)		DTA (10K/min)	
Mg-3Sn			632.49	644.49	633.85	644.15
Mg-3Sn-0.5Ca	TX30x	6:1	625.36	624.84	624.84	639.67
Mg-3Sn-1Ca	TX31	3:1	640.70	641.29	638.37	640.25
Mg-3Sn-1.5Ca	TX32x	2:1	631.96	640.13	625.70	640.08
Mg-3Sn-2Ca	TX32	1.5:1	623.54	639.05	625.80	639.28
Mg-5Sn			620.53	640.93	622.44	641.66
Mg-5Sn-0.5Ca	TX50x	10:1	633.98	641.68	625.75	639.71
Mg-5Sn-1Ca	TX51	5:1	634.83	640.40	633.90	640.31
Mg-5Sn-1.5Ca	TX52x	3.33:1	648.50	640.20	638.68	640.44
Mg-5Sn-2Ca	TX52	2.5:1	640.37	641.42	633.73	640.46
Mg-2Sn-2Ca	TX22	1:1	622.95	637.33	-	-
Mg-3Sn-3Ca	TX33	1:1	634.94	638.50	-	-
Mg-4Sn-2Ca	TX42	2:1	627.25	640.05	-	-
Mg-4.5Sn-1.5Ca	TX42x	3:1	639.50	641.19	-	-
Mg-6Sn-2Ca	TX62	3:1	640.08	640.98	-	-
Mg-6Sn-3Ca	TX63	2:1	636.27	638.51	-	-

Table (21): The DTA measurement showing melting and solidification temperature of additional peak.

Alloys [wt.-%]	Onset heating	Onset cooling
	temperature [°C]	
	DTA (2K/min)^1 DTA (10K/min)^2	
TX22	519.42^1	508.13^1
TX32	520.11^1	504..65^1
	516.57^2	514.33^2
TX33	519.31^1	515.68^1

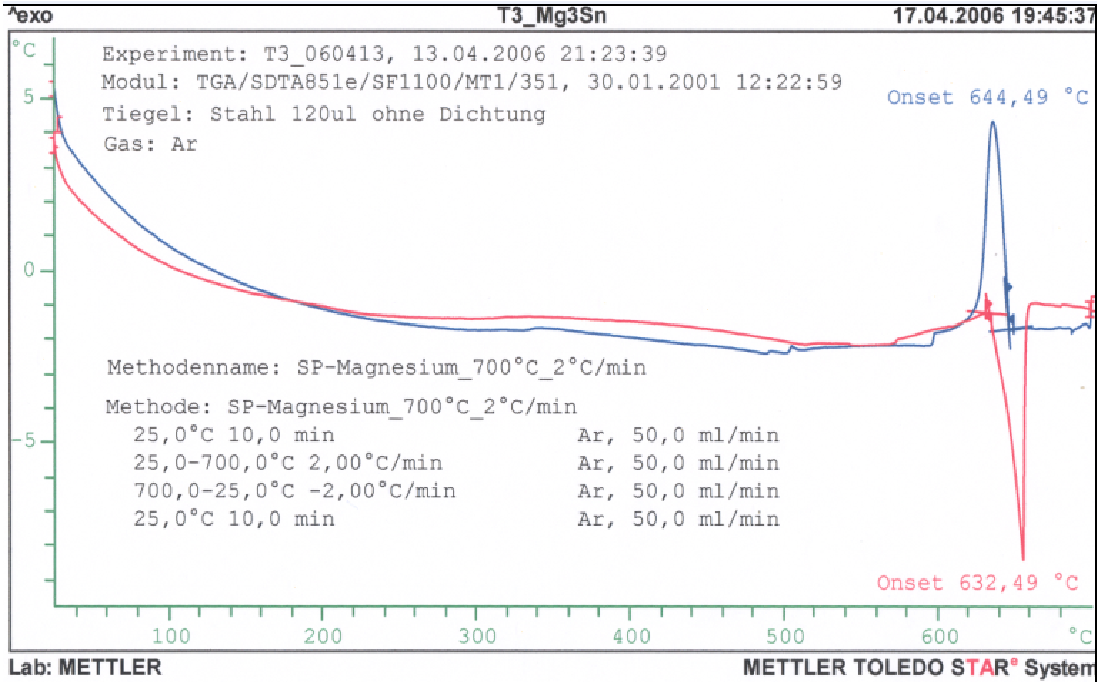

^exo T3_Mg3Sn 17.04.2006 19:45:37

Experiment: T3_060413, 13.04.2006 21:23:39
Modul: TGA/SDTA851e/SF1100/MT1/351, 30.01.2001 12:22:59
Tiegel: Stahl 120ul ohne Dichtung
Gas: Ar

Onset 644,49 °C

Methodenname: SP-Magnesium_700°C_2°C/min

Methode: SP-Magnesium_700°C_2°C/min

```
  25,0°C 10,0 min                 Ar, 50,0 ml/min
  25,0-700,0°C 2,00°C/min         Ar, 50,0 ml/min
  700,0-25,0°C -2,00°C/min        Ar, 50,0 ml/min
  25,0°C 10,0 min                 Ar, 50,0 ml/min
```

Onset 632,49 °C

Lab: METTLER METTLER TOLEDO STAR^e System

Figure (49): DTA analysis of Mg-3Sn alloy using stainless crucible, first heating (red curve) and first cooling (blue curve)

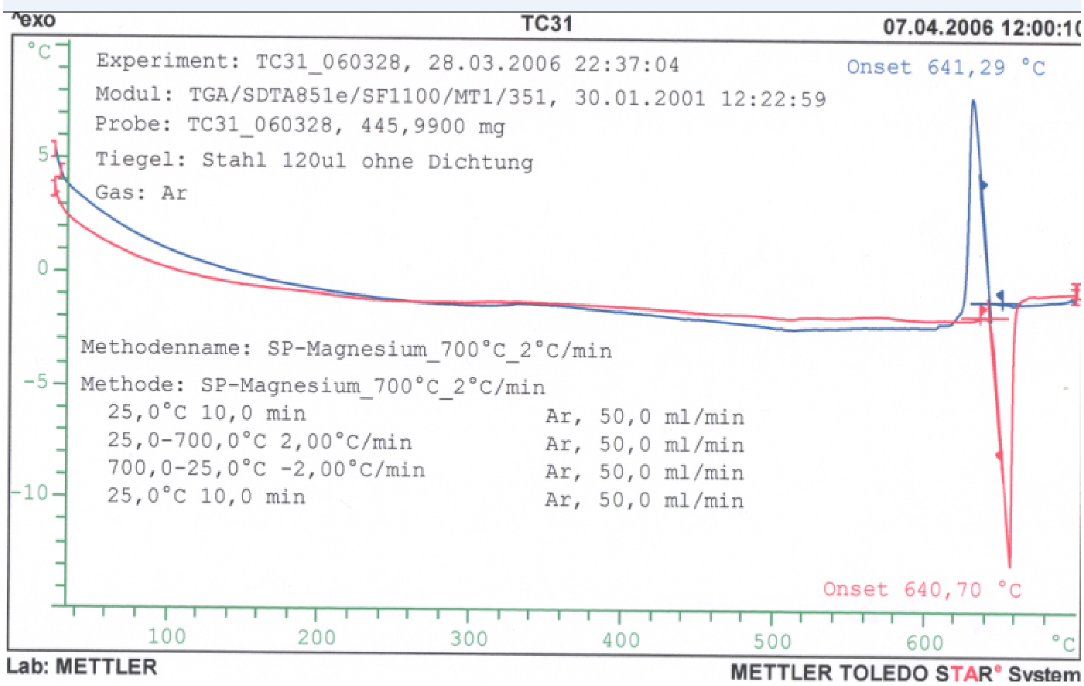

TC31

07.04.2006 12:00:1

Experiment: TC31_060328, 28.03.2006 22:37:04
Modul: TGA/SDTA851e/SF1100/MT1/351, 30.01.2001 12:22:59
Probe: TC31_060328, 445,9900 mg
Tiegel: Stahl 120ul ohne Dichtung
Gas: Ar

Methodenname: SP-Magnesium_700°C_2°C/min
Methode: SP-Magnesium_700°C_2°C/min
25,0°C 10,0 min Ar, 50,0 ml/min
25,0-700,0°C 2,00°C/min Ar, 50,0 ml/min
700,0-25,0°C -2,00°C/min Ar, 50,0 ml/min
25,0°C 10,0 min Ar, 50,0 ml/min

Onset 641,29 °C

Onset 640,70 °C

Lab: METTLER

METTLER TOLEDO STAR® System

Figure (50): DTA analysis of Mg-3Sn-1Ca alloy using stainless crucible, first heating (red curve) and first cooling (blue curve).

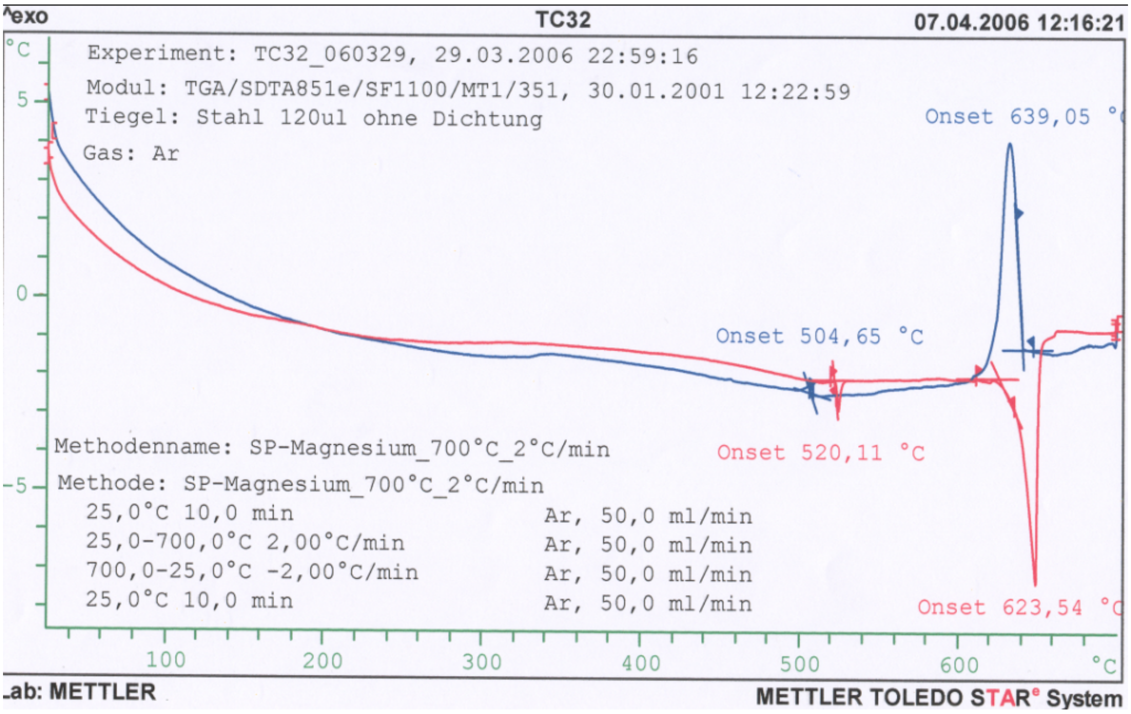

TC32

07.04.2006 12:16:21

Experiment: TC32_060329, 29.03.2006 22:59:16
Modul: TGA/SDTA851e/SF1100/MT1/351, 30.01.2001 12:22:59
Tiegel: Stahl 120ul ohne Dichtung
Gas: Ar

Methodenname: SP-Magnesium_700°C_2°C/min
Methode: SP-Magnesium_700°C_2°C/min
25,0°C 10,0 min Ar, 50,0 ml/min
25,0-700,0°C 2,00°C/min Ar, 50,0 ml/min
700,0-25,0°C -2,00°C/min Ar, 50,0 ml/min
25,0°C 10,0 min Ar, 50,0 ml/min

Onset 639,05 °C

Onset 504,65 °C

Onset 520,11 °C

Onset 623,54 °C

Lab: METTLER

METTLER TOLEDO STAR® System

Figure (51): DTA analysis of Mg-3Sn-2Ca alloy using stainless crucible, , first heating (red curve) and first cooling (blue curve).

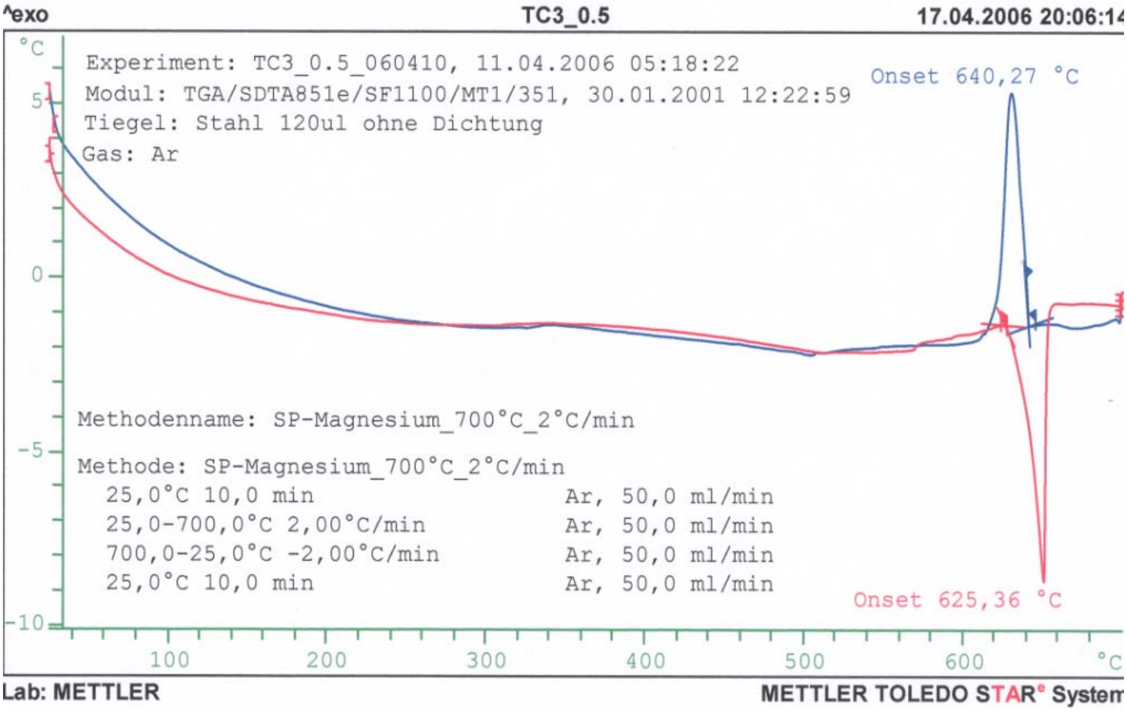

Figure (52): DTA analysis of Mg-3Sn-0.5Ca alloy using stainless crucible, first heating (red curve) and first cooling (blue curve).

Binary Mg3Sn, Mg-Mg-5Sn, and ternary TX-alloys with a ratio of Sn:Ca equal to 3:1 or more show a detected peak at approx. 505°C. This seems to be a reaction of Mg with Ni (Stainless steel X5 CrNi 18 9 (1.4301) crucible. This peak was even observed by using a stainless crucible for the investigation of pure Mg. However, the DSC analysis of pure Mg using an aluminum oxide (Al_2O_3) crucible didn't show the same peak at the temperature of 505 °C. Figure (53) illustrates the result of pure Mg using Stainless steel crucible showing the observed reaction Ni with Mg at approx. 505 °C, while Figure (54) shows the results of DSC using Al_2O_3 crucible without any signal at the same temperature.

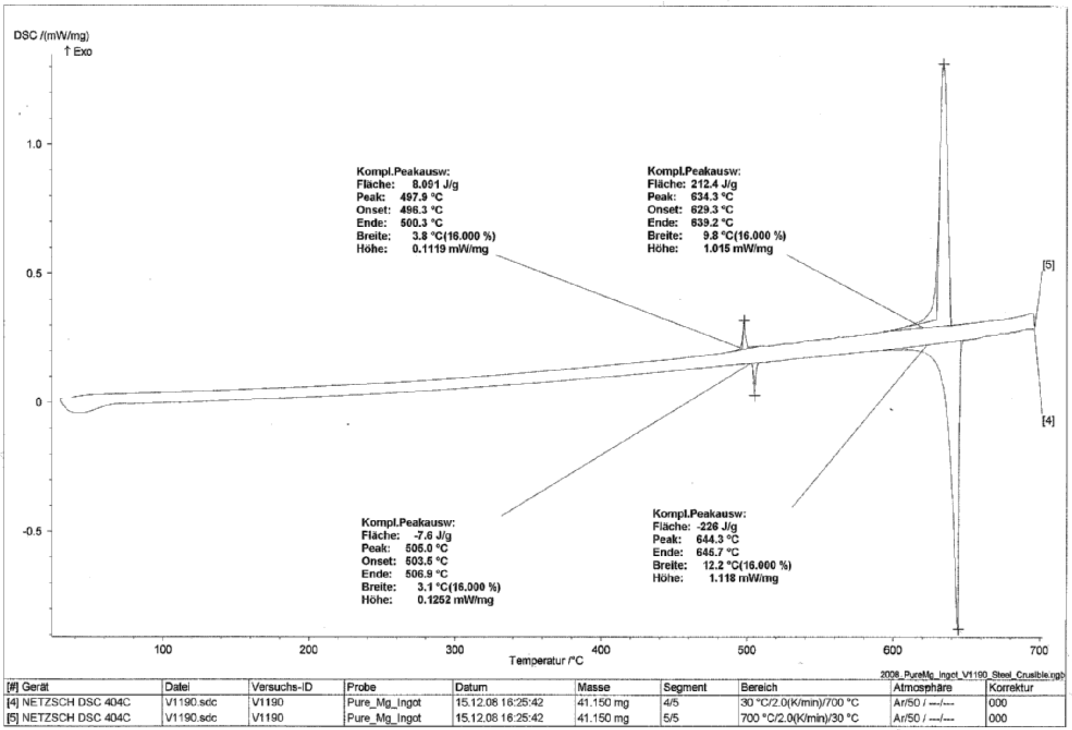

Kompl.Peakausw:
Fläche: 8.091 J/g
Peak: 497.9 °C
Onset: 496.3 °C
Ende: 500.3 °C
Breite: 3.8 °C(16.000 %)
Höhe: 0.1119 mW/mg

Kompl.Peakausw:
Fläche: 212.4 J/g
Peak: 634.3 °C
Onset: 629.3 °C
Ende: 639.2 °C
Breite: 9.8 °C(16.000 %)
Höhe: 1.015 mW/mg

Kompl.Peakausw:
Fläche: -7.6 J/g
Peak: 505.0 °C
Onset: 503.5 °C
Ende: 506.9 °C
Breite: 3.1 °C(16.000 %)
Höhe: 0.1252 mW/mg

Kompl.Peakausw:
Fläche: -226 J/g
Peak: 644.3 °C
Ende: 645.7 °C
Breite: 12.2 °C(16.000 %)
Höhe: 1.118 mW/mg

[#] Gerät	Datei	Versuchs-ID	Probe	Datum	Masse	Segment	Bereich	Atmosphäre	Korrektur
[4] NETZSCH DSC 404C	V1190.sdc	V1190	Pure_Mg_Ingot	15.12.08 16:25:42	41.150 mg	4/5	30 °C/2.0(K/min)/700 °C	Ar/50 / ---/---	000
[5] NETZSCH DSC 404C	V1190.sdc	V1190	Pure_Mg_Ingot	15.12.08 16:25:42	41.150 mg	5/5	700 °C/2.0(K/min)/30 °C	Ar/50 / ---/---	000

Figure (53): DSC analysis of pure magnesium showing the peak at 505 °C using stainless crucible X5 CrNi 18 9 (1.4301).

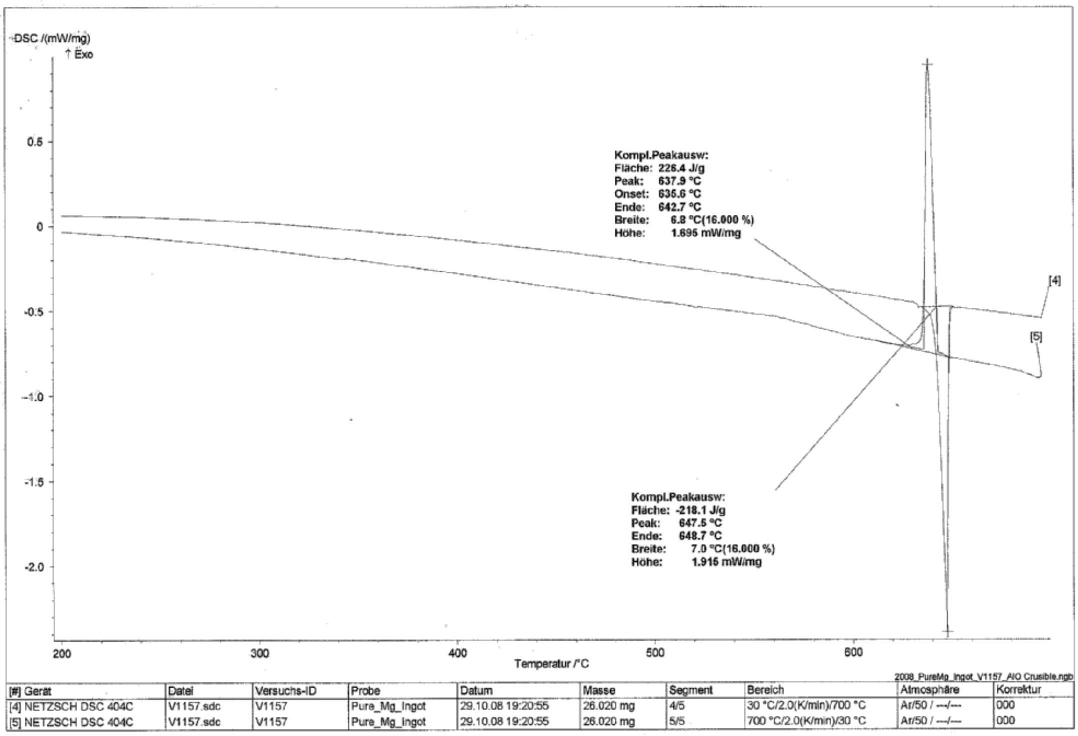

Kompl.Peakausw:
Fläche: 226.4 J/g
Peak: 637.9 °C
Onset: 635.6 °C
Ende: 642.7 °C
Breite: 6.8 °C(16.000 %)
Höhe: 1.695 mW/mg

Kompl.Peakausw:
Fläche: -218.1 J/g
Peak: 647.5 °C
Ende: 648.7 °C
Breite: 7.0 °C(16.000 %)
Höhe: 1.915 mW/mg

[#] Gerät	Datei	Versuchs-ID	Probe	Datum	Masse	Segment	Bereich	Atmosphäre	Korrektur
[4] NETZSCH DSC 404C	V1157.sdc	V1157	Pure_Mg_Ingot	29.10.08 19:20:55	26.020 mg	4/5	30 °C/2.0(K/min)/700 °C	Ar/50 / ---/---	000
[5] NETZSCH DSC 404C	V1157.sdc	V1157	Pure_Mg_Ingot	29.10.08 19:20:55	26.020 mg	5/5	700 °C/2.0(K/min)/30 °C	Ar/50 / ---/---	000

Figure (54): DSC analysis of pure magnesium using Al_2O_3 crucible.

4.2 Corrosion

The density of all alloys was weighed in a scale and was automatically measured according to the Archimedes law. They were determined and the obtained values from three samples of each alloy with their deviations are given in Table (22). The density of the binary Mg-3Sn reaches 1.78 gcm^{-3} and the addition of 1 wt.-% Ca to the mentioned binary alloy remains the value constant. With addition of 2-3 wt.-% Ca, the binary alloy, like in the TX32- and TX33-alloys, their obtained values slightly decrease to 1.77 gcm^{-3} and 1.76 gcm^{-3}, respectively. On the other hand, TX52- and TX62-alloys show higher values of 1.80 gcm^{-3} and 1.82 gcm^{-3}, respectively. The density of the investigated alloys ranges between 1.76 gcm^{-3} and 1.82 gcm^{-3}, whereas TX62-alloy exhibits the highest density and the TX33-alloy the lowest one. The density of TX-alloys is with maximum of +0.06 gcm^{-3} compared to pure magnesium. They exhibit almost the same density like AZ91D- and AE42-alloys. All of the data are given in Table (23).

Table (22): Density of the investigated alloys compared to AZ91D- and AE42-alloys.

Alloys [wt.-%]	Ratio Sn:Ca [wt.-%]	Density [g cm^{-3}]
Mg-3Sn	-	1.78 ± 0.21
TX31	3:1	1.78 ± 0.12
TX32	1.5:1	1.77 ± 0.04
TX33	1:1	1.76 ± 0.06
TX22	1:1	1.76 ± 0.08
TX42	2:1	1.78 ± 0.11
TX52	2.5 : 1	1.80 ± 0.09
TX62	3:1	1.82 ± 0.11
TX63	2:1	1.81 ± 0.14
TX42x	3:1	1.78 ± 0.12
TX51	5:1	1.79 ± 0.08
AZ91D	-	1.79 ± 0.13
AE42	-	1.79 ± 0.09

There are differences in the results obtained using the two different test methods. In general, salt spray test indicated higher corrosion rates for all TX-alloys. In addition, all of the TX-alloys including the binary Mg-3Sn alloy exhibit higher corrosion rate than that of AZ91D- and AE42-alloys. They are also less noble than the AZ91- and AE42-alloys. The results of the corrosion properties are summarized in Table (23-24) and the weight loss of the salt spray investigations are illustrated in the appendix in Figures (103-107).

The effect of individual alloying elements on corrosion rates was studied by the change of one alloying element at a time by keeping the other element constant. Furthermore, the addition of amounts of Sn and Ca at the same time by increasing the ratio of Sn:Ca was also investigated. It is obvious that the addition of Ca in the ternary TX-alloys increases the corrosion rate and thus reducing the corrosion resistance in both polarization and salt spray tests. TX31-alloy shows an average corrosion rate of 2.07 mm/yr and 2.34 mm/yr for polarization and for salt spray tests, respectively. After 1 wt.-% Ca addition to the mentioned alloy, the corrosion rate increases to an average of 5.92 mm/yr in polarization and to 5.99 mm/yr in salt spray test. The same trend can occur when 1 wt.-% of Ca is added to the TX62-alloy. The result of the polarization and salt spray tests investigations of TX62-alloy shows corrosion rate values of 3.01 mm/yr and 3.77 mm/yr, respectively. The obtained corrosion rates of TX63-alloy reached values of 4.02 mm/yr and 5.13 mm/yr for both polarization and salt spray test, respectively. Furthermore, all of the TX-alloys are less noble than Mg-3Sn. The TX31 and TX62 is less noble than TX32 and TX63.

Table (23): Corrosion rates measured through potentio-dynamic polarization test on some TX-alloys and their related phases compared to AZ91D- and AE42-alloys.

Alloys [wt.-%]	Ratio Sn:Ca [wt.-%]	Corrosion rate [mm/yr]	Corrosion potential [mV]	I_{corr} [mA]
Mg-3Sn	-	1.41 ± 0.62	-1364.80 ± 14.80	0.02 ± 0.01
TX31	3:1	2.07 ± 0.31	-1366.60 ± 11.70	0.11 ± 0.04
TX42x	3:1	2.46 ± 0.82	-1379.49 ± 13.95	0.15 ± 0.05
TX62	3:1	3.01 ± 0.70	-1382.65 ± 6.87	0.14 ± 0.03
TX22	1:1	2.98 ± 0.67	-1406.36 ± 2.21	0.20 ± 0.05
TX33	1:1	4.60 ± 0.21	-1407.38 ± 6.55	0.31 ± 0.01
TX32	1.5:1	5.92 ± 0.23	-1403.62 ± 6.52	0.40 ± 0.02
TX42	2:1	3.28 ± 0.02	-1394.68 ± 2.76	0.23 ± 0.02
TX63	2:1	4.02 ± 0.45	-1379.10 ± 6.47	0.23 ± 0.00
TX52	2.5 : 1	5.36 ± 0.62	-1361.76 ± 10.01	0.24 ± 0.03
TX51	5:1	3.49 ± 0.57	-1372.04 ± 4.18	0.16 ± 0.02
AZ91D	-	0.21 ± 0.08	-1276.56 ± 12.04	0.01 ± 0.01
AE42	-	0.10 ± 0.02	-1337.98 ± 3.53	0.01 ± 0.00

Table (24): Corrosion rates measured through salt spray test on some TX-alloys and their related phases compared to AZ91D- and AE42-alloys.

Alloys [wt.-%]	Ratio Sn:Ca [wt.-%]	Corrosion rate [mm/yr]	Weight loss [mg]
Mg-3Sn	-	1.65 ± 0.05	10.80 ± 1.93
TX31	3:1	2.34 ± 0.07	17.27 ± 0.85
TX42x	3:1	3.36 ± 0.73	23.43 ± 4.95
TX62	3:1	3.77 ± 0.40	27.10 ± 2.95
TX22	1:1	1.97 ± 0.28	13.80 ± 1.97
TX33	1:1	7.66 ± 0.43	53.77 ± 2.86
TX32	1.5:1	5.99 ± 0.44	39.90 ± 4.36
TX42	2:1	3.06 ± 0.28	21.80 ± 1.87
TX63	2:1	5.13 ± 0.74	36.83 ± 5.29
TX52	2.5 : 1	9.84 ± 0.81	31.44 ± 9.78
TX51	5:1	5.06 ± 1.44	64.27 ± 6.27
AZ91D	-	0.78 ± 0.12	5.67 ± 0.85
AE42	-	0.23 ± 0.01	1.63 ± 0.06

On the other side, it is shown that increasing amount of tin improves the corrosion resistance in these alloys. The comparisons of TX32 with TX62 or TX33 with TX63 are examples of this phenomenon. The corrosion rate of TX32 decreases after addition of 3wt.-% Sn by approx. 2.9 mm/yr from 5.92 mm/yr to 3.01 mm/yr (polarization) and by approx. 2.2 mm/yr to 3.77 mm/yr for salt spray test. The result of the salt spray investigations of TX33- and TX63-alloy show values of corrosion rate of 7.66 mm/yr and 5.13 mm/yr, respectively. The obtained corrosion rate values after polarization of the mentioned alloys show values of 4.60 mm/yr and 4.02 mm/yr, respectively. In addition, the corrosion resistance of the alloys TX62 and the TX63 alloys are nobler than the TX32 and TX33, respectively. The results obtained on the TX-alloys investigations, which have the same ratio of Sn and Ca but with varying amounts of Sn and Ca indicates that the corrosion rate increases. The TX33- compared to TX22-alloys (ratio 1:1) or TX63-, TX42-alloys (ratio 2:1) are examples of the mentioned trend. The alloys TX31, TX42x, and TX62 that have a ratio of 3:1 also indicated same corrosion resistance. It shows that increasing the amount of alloying elements with keeping the same ratio Sn:Ca the corrosion resistance decreases. The increase of the amount of alloying elements with keeping the same ratio Sn:Ca leads to decrease of the corrosion potential. TX22- and TX42- are less noble than the TX33-, and TX63-alloys, respectively. The TX31-alloy is nobler than the TX42x-, and TX62-alloys.

4.3 Mechanical properties

4.3.1 Compression and tension

Average test result of compression and tension tests at room temperature of TX-alloy compared to Mg-3Sn-alloy, AZ91D- and AE42-alloys are summarized in Figures (55) and (56). As it can been seen, the results of the mechanical properties on the TX-alloys after compression and tension tests are not similar. Their ultimate strength values are consistently greater in compression than in tension and they are considerably more deformable as well.

Figure (55) presents the results of the compression investigations. The CYS values of TX-alloys are comparable to AZ91-alloy and some of them demonstrate even higher values than that of AE42-alloy. However, their UCS values are weaker than that of AZ91D- and AE42-alloys. The results show that increasing of further amounts of Ca to the TX-alloys leads for an increasing of the CYS and UCS values. The effect can be seen on the alloys TX31, TX32, and TX33. The mentioned alloys have CYS values of 52.16 MPa, 58.20 MPa, and 63.43 MPa as well as UCS values of 207.26 MPa, 219.50 MPa, and 221.15 MPa, respectively. It can be added that the addition of further amounts of Ca also leads for making the alloys more deformable. Their CYS values are higher than Mg-3Sn but their UCS values are lower. The opposite effect can be reached with increasing the amount of Sn to TX-alloys. Its additions lead for decreasing of their values. The CYS value of TX31-alloy slightly decreases from 52.16 MPa to 48.32 MPa for TX51-alloy. The values of TX31-alloy of both UCS and the elongation increases by the addition of 2 wt.-% from 207.26 MPa and 13.76 to 217.13 MPa and 15.00, respectively. The highest obtained values of CYS and UCS Among the investigated TX-alloys have been indicated for the TX42-alloys. While the lowest achieved value of CYS and UCS was for the TX51 and TX52, respectively. With increasing the Sn:Ca ratio more than 3:1 the yield strength decreases while it increases with a reduction of the Sn:Ca ratio less than the mentioned ratio.

Figure (56) shows the results of the mechanical properties of the TX-alloys under tensile load at room temperature. It can be seen that the addition of Ca leads for an increasing of the TYS values but for decreasing the UTS values. The TYS value of Mg-3Sn alloy increase by Ca additions from 35.01 MPa to 53.08MPa, 53.92 MPa, and 58.44 MPa in comparison to the alloys TX31, TX32, and TX33, respectively. The UTS values of the binary alloy decreases from 108.54 MPa to 98.43 MPa, 80.80MPa, and 71.19 MPa for the same mentioned TX-alloys, respectively. With increasing further amounts of Ca, the TX-alloys are also less deformable. The opposite effect plays the alloying element Sn. With an increase of Sn content, the UTS can be improved, while the UTS values decreases and its deformable is lower.

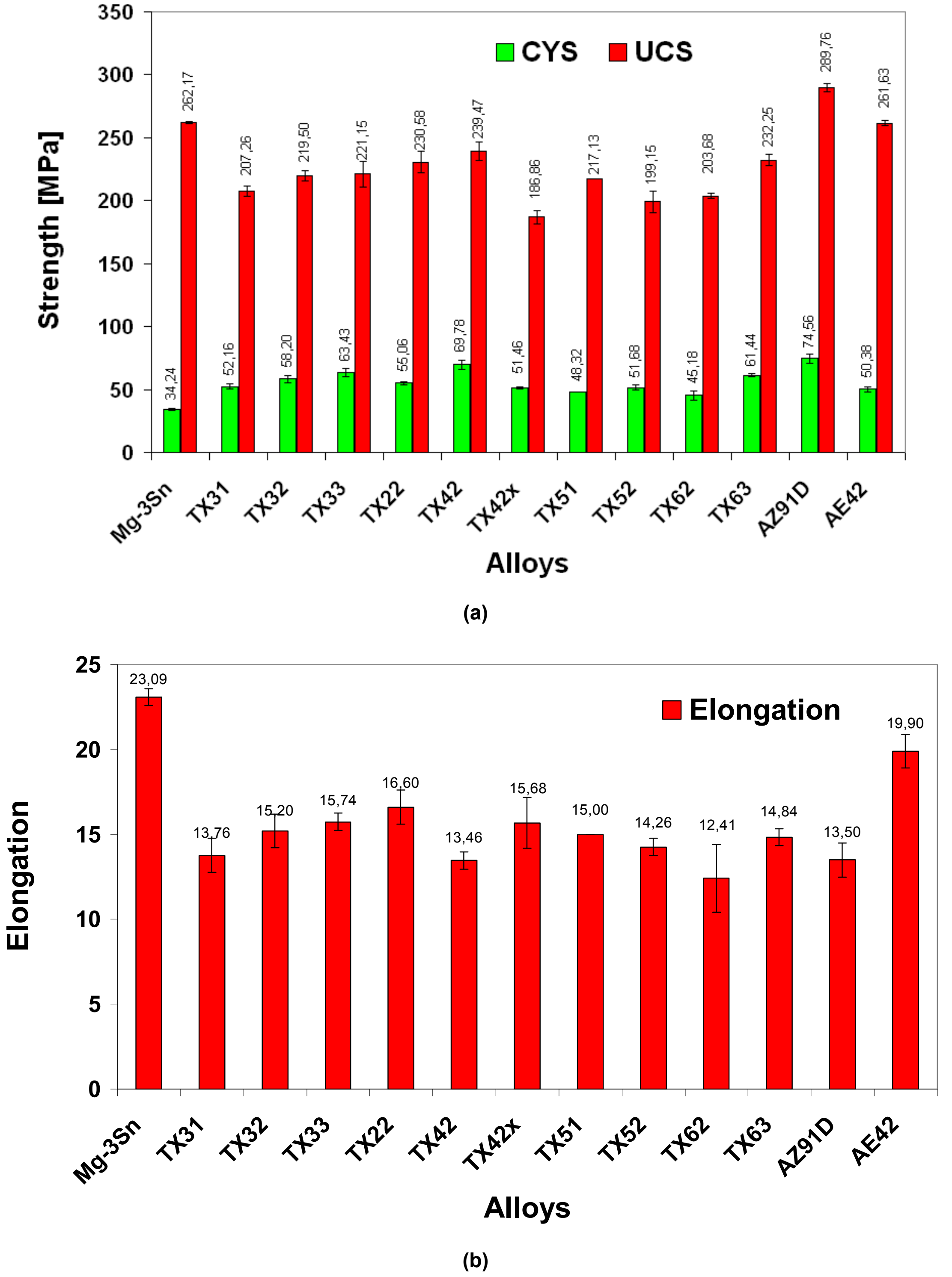

Figure (55): The mechanical properties under compression load at room temperature for TX-alloys compared to AZ91D- and AE42-alloys.

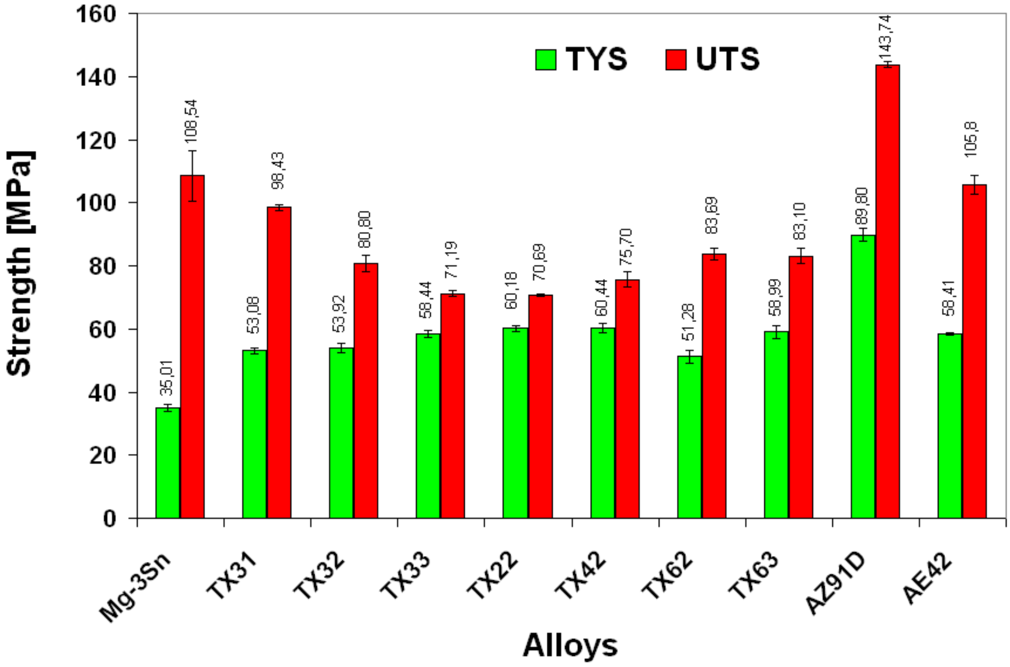

(a)

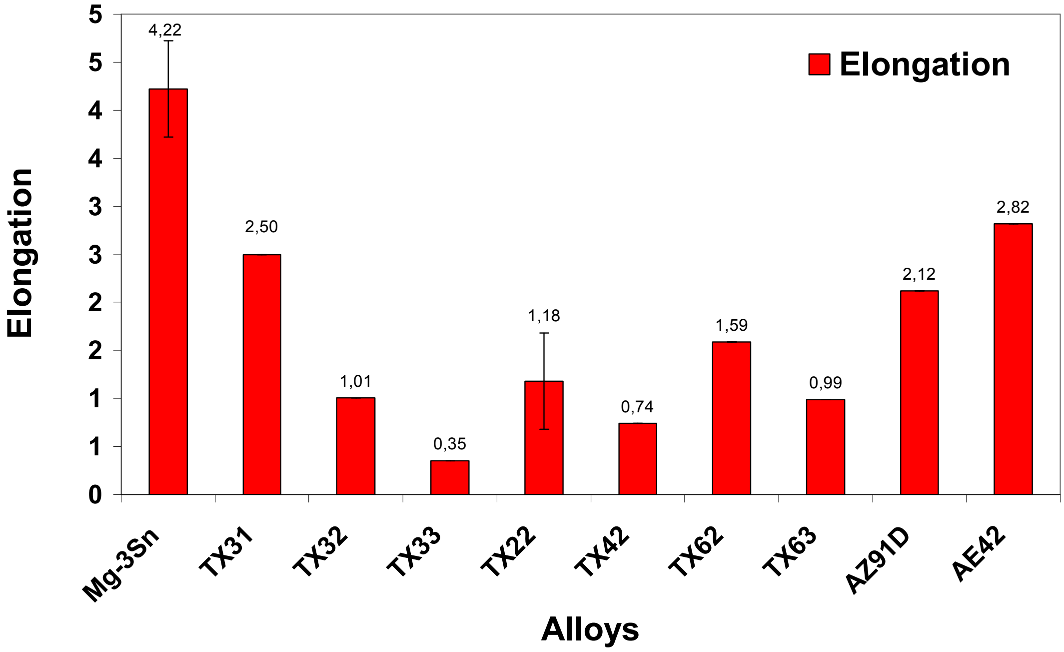

(b)

Figure (56): The mechanical properties under tensile load at room temperature for TX-alloys compared to AZ91D- and AE42-alloys.

4.3.2 Hardness

The results of hardness Vickers investigations of the selected alloys are summarized in Table (25). The binary Mg-3Sn alloy shows the lowest hardness value of 27.8 HV but it consequently increases with addition of Ca. The addition of further Ca can be seen in the alloys TX31, TX32, and TX33. The mentioned alloys have hardness values of 34.6 HV, 39.7 HV, and 47.1 HV. In most investigated alloys, increasing the amount of Sn also leads for rising of the HV values. The alloys TX32, TX42, TX52, and TX62 show hardness values of 39.7 HV, 42.3 HV, 42.8 HV, and 43.8 HV. However, the TX51-alloy shows lower hardness value of about 37 HV compared to 34.6 HV for TX31-alloys. In general, the values are comparable with AE42-alloy however, but they exhibit lower values compared to AZ91D-alloy.

All of the results are given in Figures (108-118) in the Appendix.

Table (25): Vickers hardness values of TX-alloys compared to AZ91D- and AE42-alloys.

Alloys [wt.-%]	HV 10
Mg-3Sn	27.8±1.9
TX31	34.6±2.6
TX32	39.7±3.3
TX33	47.1±2.0
TX22	45.2±2.5
TX42	42.3±3.7
TX42x	42.0±3.6
TX51	36.7±1.8
TX52	42.8±1.7
TX62	43.8±2.1
TX63	43.6±3.5
AZ91D	57.8±2.5
AE42	39.1±3.2

4.3.3 Compressive creep

Compressive creep behavior of selected TX-alloys was first studied at parameter of gearbox housing. The results of the compressive investigations at 85 MPa and at 135° C are presented in Table (26) and in Figure (57). TX31-, TX42x-, and TX62-aloys exhibit almost same creep behavior. Their creep rates are very high and thus their resistance is poor. While the TX51-alloy shows the poor, creep behavior compared to other investigated ternary alloys. However, the TX32-alloy exhibit better creep resistance than AZ91D-alloy and is comparable with AE42-alloy.

The creep rates of TX31-, TX42x-, and TX62-alloys are 51.4E-09, 66.3E-09, and 56.3E-09, respectively. As it can be seen, they exhibit approx. the same value. The TX51-alloy reveals the very poor creep resistance within the TX-alloys with a creep rate of 172.0E-09. With increasing 1 wt.-% to the TX51-alloy leads for improvement in creep properties of the TX52-alloy. With 3 wt.-% of Sn and 2 wt.-% Ca, the creep properties of TX32-alloy shows excellent improvement with a creep rate of 2.24E-09 s^{-1}. The TX32-alloy exhibit one power to ten values compared to the conventional alloys, AZ91D and AE42. The result of these investigations is also presented in Table (26).

Table (26): Creep rate and compressive creep deformation obtained at 85MPa@135°C on TX-alloys compared to Mg-3Sn-, AZ91D- and AE42-alloys.

Alloys [wt.-%]	Ratio Sn : Ca	Creep rate [E-09 s^{-1}]	Deformation [%]
Mg-3Sn	-	220.00	-
TX31	3:1	51.40	8.14
TX42x	3:1	66.30	15.72
TX62	3:1	56.30	13.85
TX32	1.5:1	2.24	1.38
TX52	2.5 : 1	36.20	10.56
TX51	5:1	172.00	22.32
AZ91D	-	36.70	4.03
AE42	-	24.76	2.98

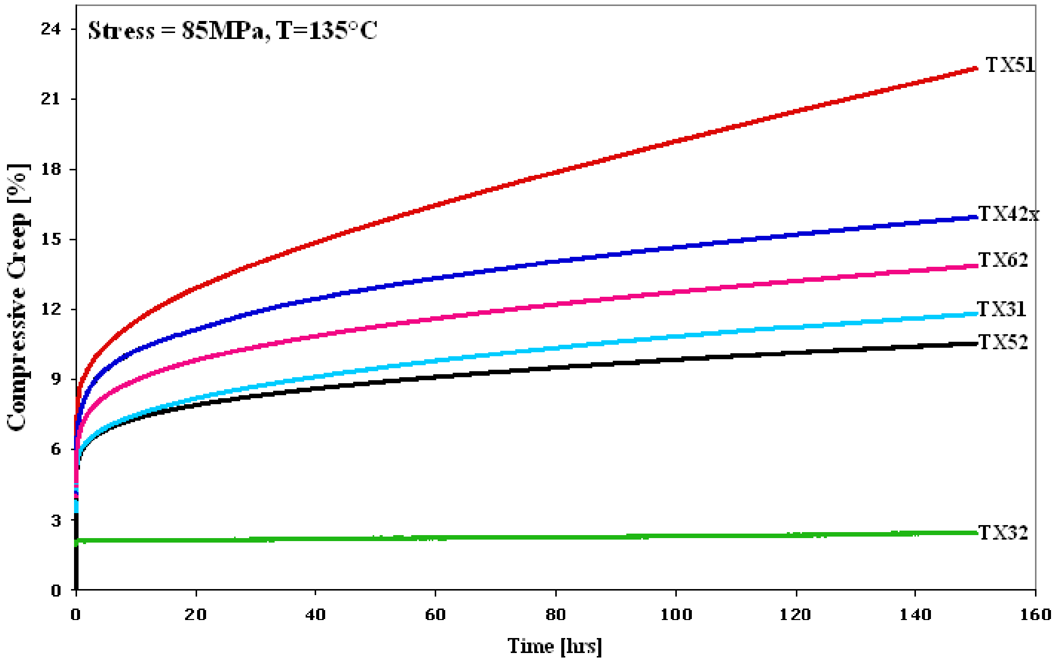

Figure 57: Compressive creep curves on some TX-alloys compared to AZ91D- and AE42-alloys obtained at 85MPa@135°C.

Table (27) and Figure (58) summarize the results of compressive creep investigations of TX-alloys under the conditions: 80MPa@150°C. They show that the entire ternary TX-alloys exhibit better creep resistance than that of the binary Mg-3Sn alloy. The specimens of the binary Mg-Sn ruptured immediately. Their creep life is close to zero and no elongation was measured. The ternary TX-alloys, which have a Sn:Ca ratio of 3:1 like TX31, TX42x, and TX62 or more than this ratio such as TX51-alloy, rupture within 3 hours. The creep resistance improved only after the addition of more amounts of Ca and thus after decreasing the ratio of Sn:Ca (< 3:1). Alloys, such as TX22, TX32, TX33, or TX63 exhibit a very good creep resistance and are comparable with AE42-alloy. The creep rate of the mentioned TX-alloys reached 2.53E-08 s^{-1}, 2.24E-08 s^{-1}, 3.18E-08 s^{-1}, and 2.25E-08 s^{-1} compared to 3.67E-08 s^{-1} and 1.37E-08 s^{-1} for both AZ91D, and AE42, respectively. On the other side, the creep deformation of TX-alloys is with 1.78 %, 1.38 %, 2.71 %, and 1.51 % lower than the creep deformation for AZ91D with 4.03% and for AE42 with 3.09 %.

Table (27): Creep rate and compressive creep deformation obtained at 80MPa@150°C on TX-alloys compared to cast Mg-3Sn-, AZ91D- and AE42-alloys.

Alloys [wt.-%]	Creep rate [E-08 s^{-1}]	Deformation [%]
Mg-3Sn	-	-
TX31	208.00	22.00
TX42x	173.00	34.08
TX62	97.00	16.43
TX22	2.53	1.78
TX33	2.24	1.38
TX32	3.18	2.71
TX42	21.20	2.90
TX63	2.25	1.51
TX52	90.40	26.01
TX51	505.05	19.41
AZ91D	3.67	4.03
AE42	1.37	3.09

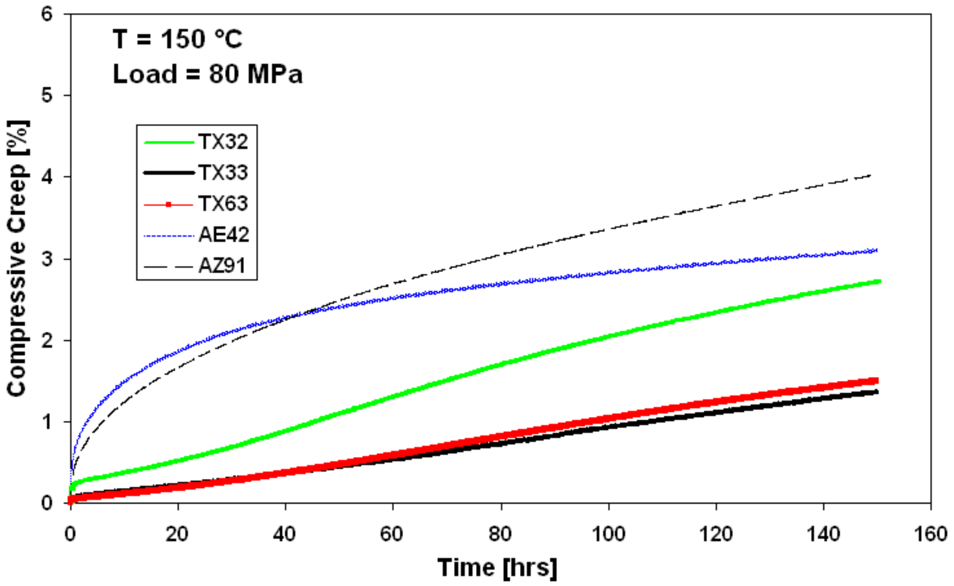

Figure (58): Compressive creep curves on some of TX-alloys compared to AZ91D- and AE42-alloys obtained at 80MPa@150°C.

In general, the increment of Sn content has a negative effect on the creep properties. The creep resistance of the investigated alloys can be increased by adding more amount of Ca and thus decreasing the ratio 3:1. From previous obtained results, further creep studies were undertaken only on TX-alloys with a Sn:Ca ratio of below 3:1 that exhibit a very good creep resistance. This included TX22-, TX32-, TX33-, and TX63-alloys. The results of creep investigations of TX-alloys at stress of 80 MPa and temperature of 175 °C were carried out. Table (28) and Figure (59) summarize the data of creep rate and deformation of TX-alloys in comparison to AZ91D- and AE42. It can be seen that even at higher temperature the TX-alloys (ratio below 3:1) kept their good behavior. As it can be illustrated in Figure (59), the TX-alloys exhibit very good creep resistance compared to AZ91D- and even to AE42-alloys. The creep rate of TX-alloys range between 3-7E-08 s^{-1} compared to approx. 14E-08 s^{-1} for AE42-alloy. On the other hand, AZ91D-alloy ruptured after almost 130 hours.

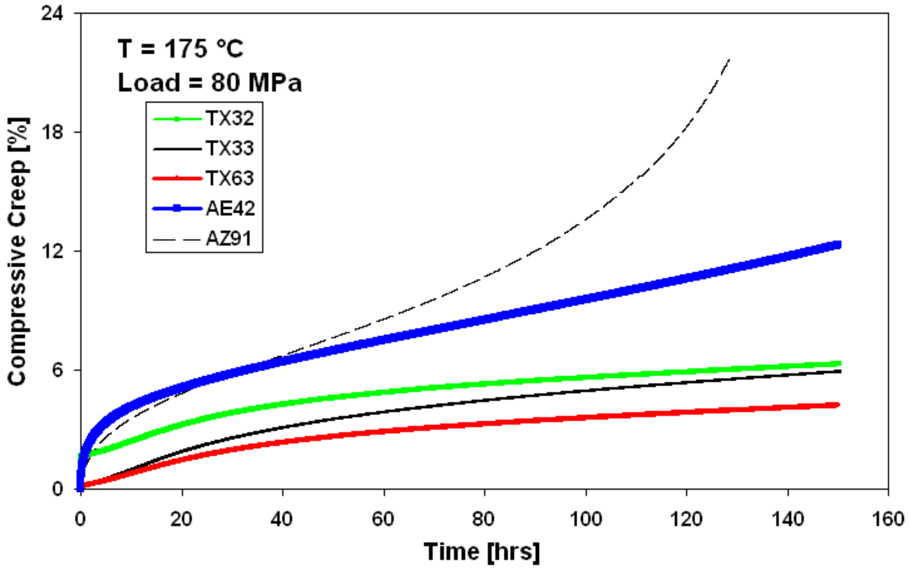

Figure (59): Compressive creep curves on TX32-, TX33-, and TX63-alloys compared to AZ91D- and AE42-alloys obtained at 80MPa@175°C.

Table (28): Creep rate and compressive creep deformation obtained at 80MPa@175°C on TX-alloys compared to AZ91D- and AE42-alloys.

Alloys [wt.-%]	Creep rate [E-08 s^{-1}]	Deformation [%]
TX22	5.74	5.05
TX33	4.96	5.93
TX32	4.10	6.30
TX42	6.51	7.12
TX63	3.25	4.22
AZ91D	25.40	21.93
AE42	16.50	12.30

Table (29) shows the creep rate of the investigated TX32-, AZ91D-, and AE42-alloys. TX32-alloy shows higher creep resistance than AZ91 and AE42. The creep rate of TX32 is 5.70E-09 $^{-1}$ compared to the AZ91D and AE42-alloys with 18.70E-09 s^{-1} and 14.41E-09 s^{-1}, respectively. A creep deformation of 0.48 %, 3.25 %, and 1.36 % was indicated for TX32-, AZ91D-, and AE42-alloys, respectively.

Table (29): Creep rate and compressive creep deformation obtained at 80MPa@135°C on only TX32-alloy compared to cast AZ91D- and AE42-alloys

Alloy [wt.-%]	Ratio Sn : Ca	Creep rate [E-09 s^{-1}]	Deformation [%]
TX32	1.5:1	5.70	0.48
AZ91D	-	18.70	3.25
AE42	-	14.41	1.36

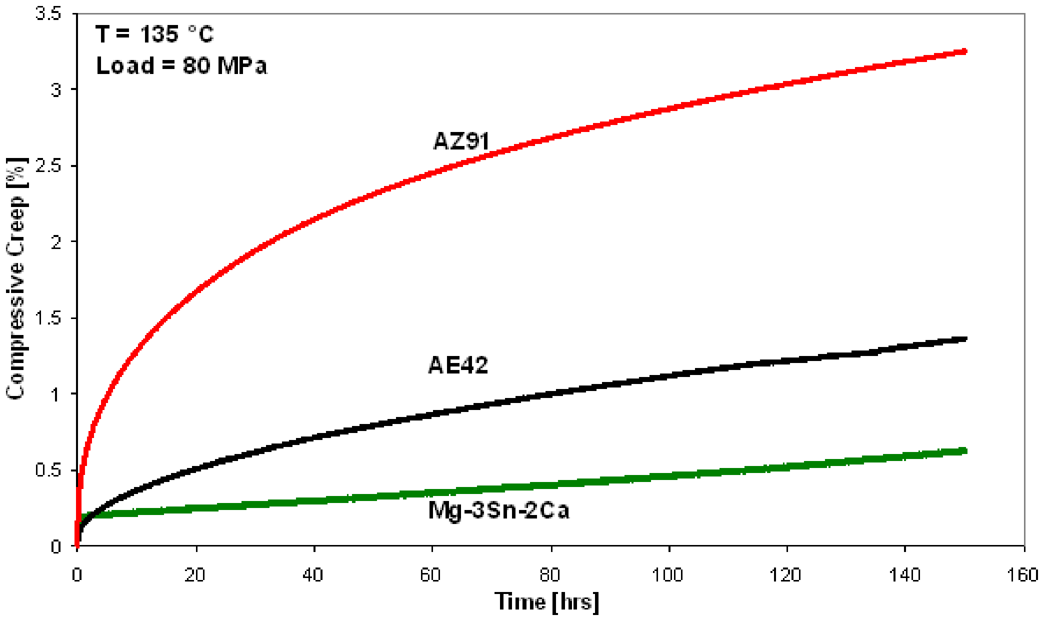

Figure (60): Compressive creep curves on TX32-alloys compared to AZ91D- and AE42-alloys obtained at 80MPa@135°C.

Table (30) shows the creep rate and the deformation of the investigated TX32-alloy at various loads and at temperature of 150 °C. TX32-alloy shows lower creep properties at higher load 70-80 MPa, while its creep resistance is improved at lower loads. The creep rate of TX32 at temperature of 150°C and load of 40 MPa is 0.08E-09 $^{-1}$ compared to 31.80E-09 $^{-1}$ for the same investigated alloy at the same temperature. A very low creep deformation of 0.08 % was measured for the investigated alloy at lower load of 40 MPa compared to 2.71 % for the same alloy after investigation at the same temperature of 150 °C and higher load of 80 MPa. The same difference can be indicated if the same alloy will be compared at loads of 60 MPa and 70 MPa at the same temperature as mentioned above. The curve of the alloy, which was investigated at various loads and at temperature of 150 °C is given in Figure (61).

Table (30): Creep rate and compressive creep deformation obtained at 40-80MPa@150°C on only TX32-alloy

Parameter		Creep rate [E-09 s^{-1}]	Deformation [%]
(150°C)	40 MPa	0.08	0.21
	60 MPa	0.78	0.43
	70 MPa	35.00	2.30
	80 MPa	31.80	2.71

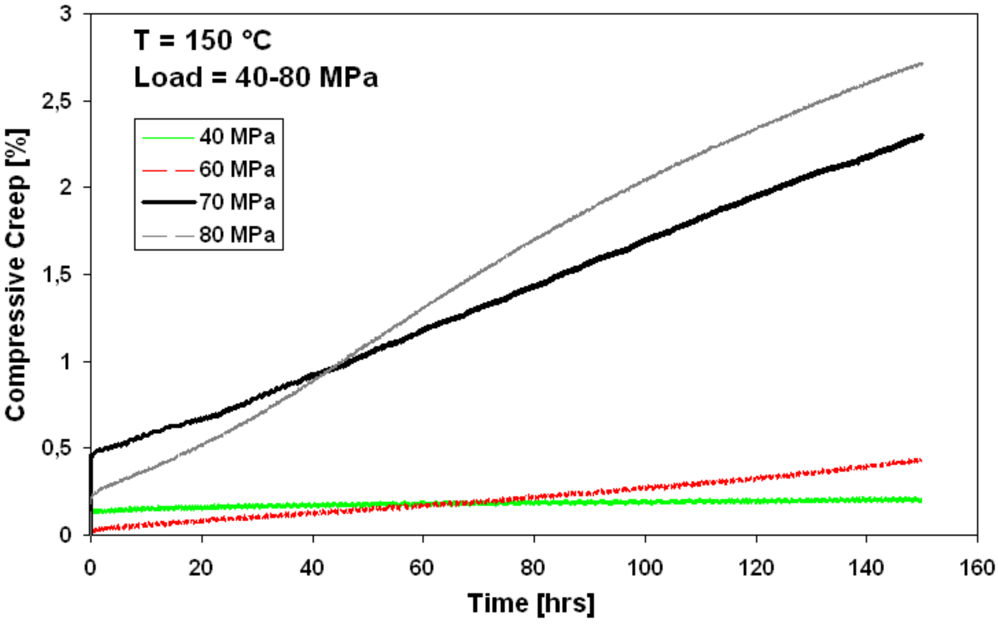

Figure (61): Compressive creep curves on TX32-alloys obtained at 40-80MPa@150°C.

5 Discussion

5.1 Microstructure and phase characterization

5.1.1 Binary Mg-Sn alloys

The microstructure of binary alloys Mg-3Sn and Mg-5Sn was examined in this study. It was found that the phase composition changed gradually towards the matrix. While very few precipitations of Mg_2Sn were detected in the Mg-3Sn-alloy by SEM/EDX, more precipitations of Mg_2Sn were observed in the Mg-5Sn-alloy. This difference is expected due to the higher content of Sn in the Mg-5Sn alloy. The very low and higher amounts of Mg_2Sn in the Mg-3Sn and Mg-5Sn alloys, respectively, were also confirmed by XRD. A very few and small peaks of Mg_2Sn were detected in the Mg-3Sn-alloy, more and higher peaks of Mg_2Sn were observed in the Mg-5Sn-alloy. This difference is due to the higher amount of volume fraction of the precipitated Mg_2Sn phase in the Mg-5Sn-alloy. The observation of this phase was expected according to the reported binary Mg-Sn phase diagram [77]. The result is also with a good agreement with the published reports [115,121].

5.1.2 Ternary Mg-Sn-Ca- (TX-alloys)

The addition of Ca to the binary Mg-Sn alloys causes the precipitation of ternary $Ca_{2-x}Mg_xSn$ particle. In this alloy range the composition of $Ca_{2-x}Mg_xSn$ is essentially CaMgSn (x=1). In other words the atomic ration is Sn:Ca = 1:1 (at), corresponding to a weight ratio of 3:1. The term “ratio” in the following is always the wt. ratio. Further phases, such as Mg_2Sn or Mg_2Ca were also observed depend on the ratio Sn:Ca. The type of the particles and thus their properties are found to be dependent on the Sn:Ca ratio and thus can be divided into three groups: The first one if the Sn:Ca ratio is nearly to 3:1, the second one when it is below 3:1, and finally if it is more than the mentioned ratio. Therefore, it is easier to discuss the investigated alloys regarding to their ratios. Table (31) summarizes the calculated nominal compositions of the investigated TX-alloys in at.-%.

Table (31): The nominal composition of the selected binary Mg-Sn and TX-alloys in wt.-% and at.-%.

Ratio wt.-%	Alloys	Sn	Ca	Mg
	[wt.-%]	[at.-%]		
	Mg-3Sn	0.63	-	rem.
	Mg-5Sn	1.07	-	rem.
1:1	Mg-2Sn-2Ca	0.42	1.24	rem.
	Mg-3Sn-3Ca	0.64	1.88	rem.
1.5:1	Mg-3Sn-2Ca	0.63	1.25	rem.
2:1	Mg-3Sn-1.5Ca	0.63	0.93	rem
	Mg-4Sn-2Ca	0.85	1.26	rem.
	Mg-6Sn-3Ca	1.31	1.93	rem.
2.5:1	Mg-5Sn-2Ca	1.08	1.28	rem.
3:1	Mg-3Sn-1Ca	0.63	0.63	rem.
	Mg-4.5Sn-1.5Ca	0.96	0.95	rem.
	Mg-6Sn-2Ca	1.30	1.28	rem.
3.33:1	Mg-5Sn-1.5Ca	1.07	0.95	rem.
5:1	Mg-5Sn-1Ca	1.07	0.63	rem.
6:1	Mg-3Sn-0.5Ca	0.63	0.31	rem.
10:1	Mg-5Sn-0.5Ca	1.07	0.32	rem.

TX-alloys with ratio Sn:Ca 3:1

The phase $Ca_{2-x}Mg_xSn$ was observed as a secondary phase in the alloys with a ratio of Sn:Ca 3:1. The mostly type appearing was bright needle and large particle. Neither Mg_2Sn nor Mg_2Ca were detected in this group. The addition of Sn and Ca in the TX-alloys by keeping the same ratio increases the amount of phases. This can be clearly seen in the selected alloys, TX31, TX42x, and TX62. As shown in Table (31) from the mentioned alloys, the same amount of atomic percent of Sn and calcium can form with magnesium the mentioned ternary $Ca_{2-x}Mg_xSn$. In the case of TX31-alloy, the same quantity of 3 wt.-% (0.67 at.-%) of Sn and 1 wt.-% (0.67 at.-%) Ca could form with Mg the mentioned phase.

TX-alloys with ratio Sn:Ca below 3:1

In the TX-alloys with ratio less than 3:1, the amount of Sn and Ca ranges between 0.42-1.31 at.-% and 0.93-1.93 at.-%, respectively. This indicates that the amount of Ca is more than Sn. Therefore, it was to expect that after the formation of $Ca_{2-x}Mg_xSn$ phase the remaining amount of Ca either will go in solid solution or will form new phase, namely Mg_2Ca. Due to the low solubility of Ca in Mg, the formation of the binary phase was found. This result is with a good agreement with the calculated results mentioned by Kozlov [90], which will be also discussed in the next section.

TX-alloys with ratio Sn:Ca more than 3:1

In the alloys system group with Sn:Ca ratio of more than 3:1, the amount of Sn and Ca ranges between 0.63-1.07 at.-% and 0.31-0.95 at.-%, respectively. In this case, the $Ca_{2-x}Mg_xSn$ phase was found besides the Mg_2Sn phase. Due to the high solubility of Sn in Mg, few amounts of Sn can go to solid solution.

The obtained results of the XRD investigations also illustrate that the peak intensities of the $Ca_{2-x}Mg_xSn$ phase are dependent on the amount of Sn and Ca. With increasing Sn content, the peak intensities of the $Ca_{2-x}Mg_xSn$ phase increases due to the changes in the ratio of Sn:Ca and the binary phases can also be confirmed in most of the cases. However, there is technical limitation in the XRD equipment and thus few phases dependent on the type and weight cannot be detected. As example, the binary Mg_2Ca phase in the TX52 or in the TX42 was not confirmed by using XRD as shown in Figure (42). However, the few phases of Mg_2Sn in the Mg-3Sn-0.5Sn were detected because this phase is heavier than the Mg_2Ca one. In addition, the peak intensities of the $Ca_{2-x}Mg_xSn$ phase increases by adding more amount of Sn to the TX-alloys, which is illustrated in Figure (62). The grain sizes of the TX-alloys are very high since these alloys were cast in large billet and their cooling rate is slow due to the large diameter of 100 mm and the 400 mm in length. The maximum cooling rate of the TX32-alloy of approx. 3 K/s in the ranges of 638-570 °C was measured after the primary solidification.

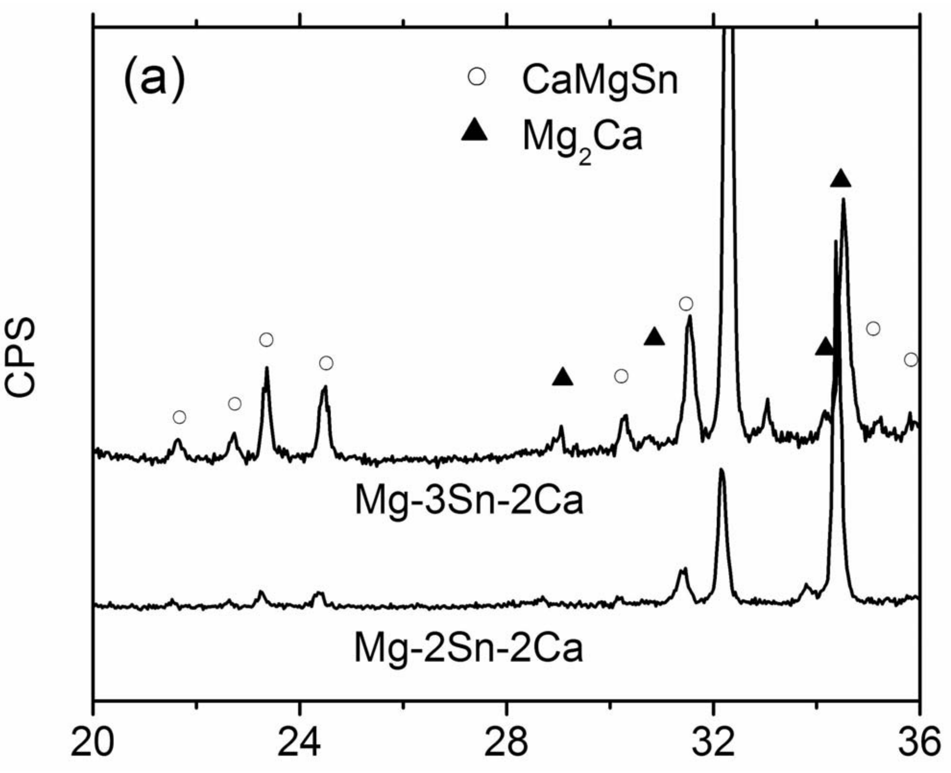

(a)

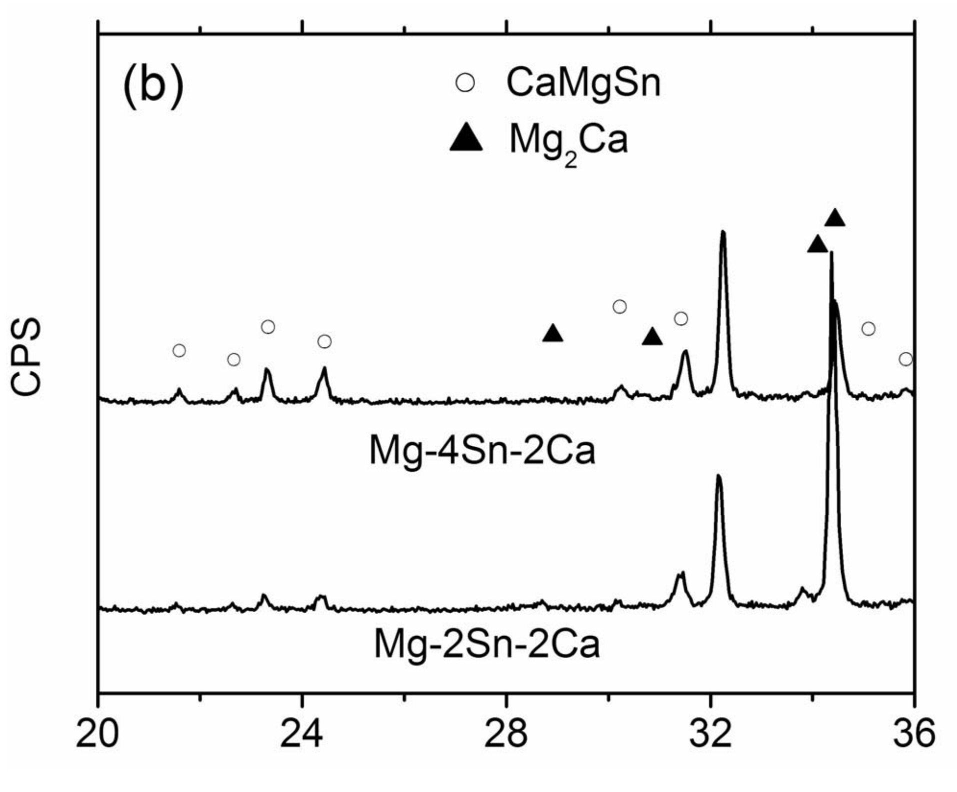

(b)

Figure (62): XRD patterns reveal the effect of Sn content on the second phase $Ca_{2-x}Mg_xSn$ and Mg_2Ca in TX-alloys, a) TX32 compared to TX22, b) TX42 compared to TX22.

5.2 DTA/DSC measurements and thermodynamic calculations

The results of the thermal analysis data of DTA of some TX-alloys were studied and their results will be compared to the calculated thermodynamic data from Kozlov et al. [90].

In this study DTA and DSC measurement were carried out using stainless steel X5 CrNi 18 9 (1.4301). The Mg-Ni phase diagram, which is illustrated in the Figure (102) in appendix, shows a reaction of Mg with Ni. This reaction is the reason of the detected peak at the temperature 506 °C, as mentioned in the results in Figure (53-54). However, this peak was not detected at this temperature by using the Al_2O_3 crucible.

Figure (63) illustrates the calculated liquidus surface in the Mg-rich corner showing the investigated alloys (a) TX30x, (b) TX32, (c) TX51, (d) TX52, and (f) TX22. The primary field of α-Mg crystallization is relatively flat with just 10 K temperature difference between the melting temperature of Mg and the maximum m_4. According to this phase diagram, only TX30x-, TX31-, and TX51-alloys belong to the primary crystallization field of α-Mg with the $Ca_{2-x}Mg_xSn$ as a secondary phase. The microstructure of all investigated alloys below the eutectic indicates that the secondary phase forms in a lamellar morphology jointly with α-Mg at the grain boundaries and not in needle shape, Figures (39a). The formation of the primary and secondary phases for the mentioned three alloys has a temperature difference less than 5 K. The remaining of the investigated alloys TX22, TX32, TX52 is placed in field of primary $Ca_{2-x}Mg_xSn$ and the α-Mg secondary phase, Figure (63). The maximum mentioned m_4 plays a significant role in the phase diagram. It is divided into two significant fields. In the two fields, the alloys hit the eutectic trough, which is either to the left or to the right of m_4. In the first case, the following secondary reaction can be occurring: $L \rightarrow \alpha\text{-Mg} + Ca_{2-x}Mg_xSn$ down towards the ternary eutectic E_3: $L \leftrightarrow \alpha\text{-Mg} + Ca_{2-x}Mg_xSn + Mg_2Ca$ at 515°C. In the case when the alloys hit the eutectic to the right of m_4, the reaction will follow down to the ternary eutectic: E_2: $L \leftrightarrow \alpha\text{-Mg} + Ca_{2-x}Mg_xSn + Mg_2Sn$ at 562.8°C. This is confirmed in the microstructures by the formation of various third phases, Mg_2Ca in the earlier and Mg_2Sn in the final case.

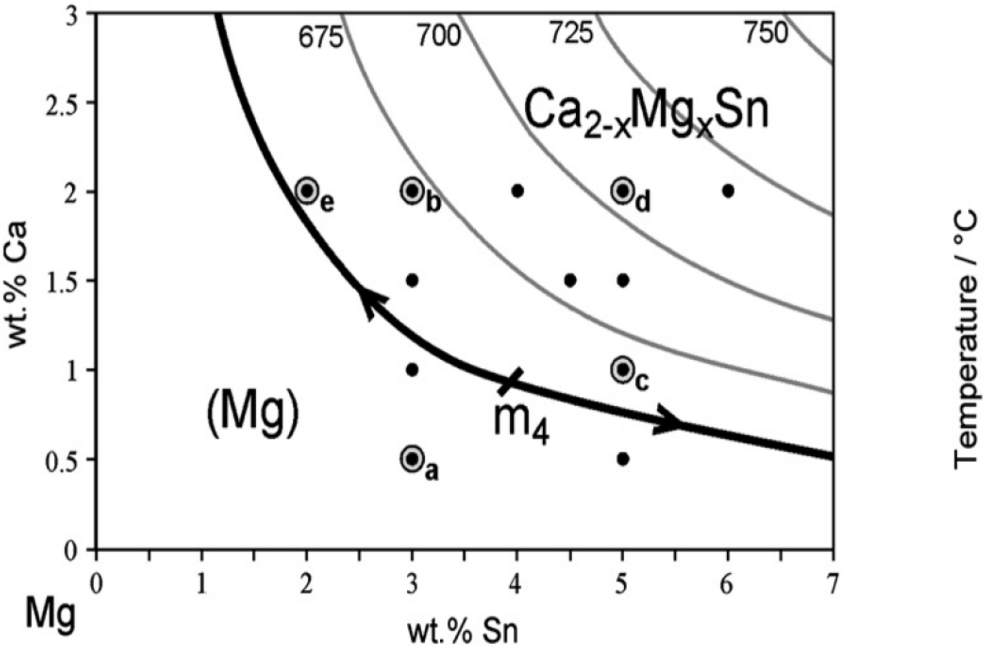

Figure (63): Calculated liquids surface of the Mg-rich corner. The dots represent investigated alloys (a) TX30x-, (b) TX32-, (c) TX51-, (d) TX52-, (e) TX22-alloys [90].

Further detailed solidification sequences are given by the calculated phase diagram section at 3 wt.-%, 5 wt.-% Sn, and 2 wt.-% Ca as shown in Figures (64,66,67), respectively. The mentioned Figures are corresponding to the composition range of Figure (63). The equilibrium solidification terminates in wide composition ranges at the solidus boundary of the α-Mg + $Ca_{2-x}Mg_xSn$ two-phase field without the achievement of any ternary eutectic. This is due to the extended solid solution range in the $Ca_{2-x}Mg_xSn$ phase and the solubility of Sn in α-Mg that decreases with temperature and forming V-shaped boundaries. This result in a second reasonably remarkable partition for the solid-state precipitation in all three diagrams: the Mg_2Ca or Mg_2Sn phase can appear on the Ca-rich or Sn rich side, respectively. Various solidification paths for extremely slow (~Equilibrium) versus more rapid (~Scheil mode) solidification can be expected due to the solid solubility dominant role.

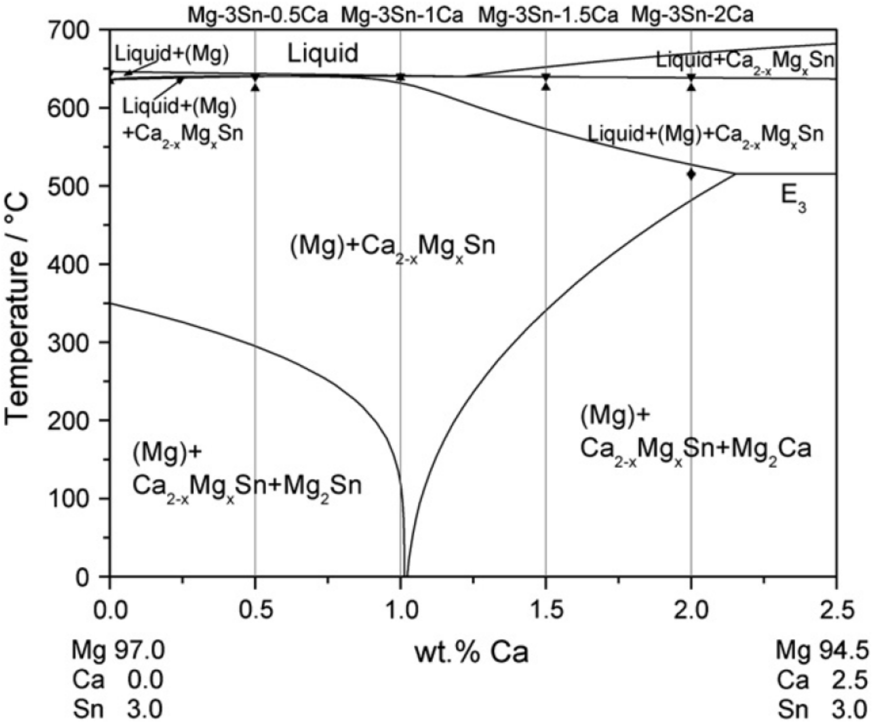

Figure (64): Calculated vertical phase section with constant 3 wt.-% Sn for investigated TX30x-, TX31-, TX32x-, and TX32-alloys with their related DTA signals [90].

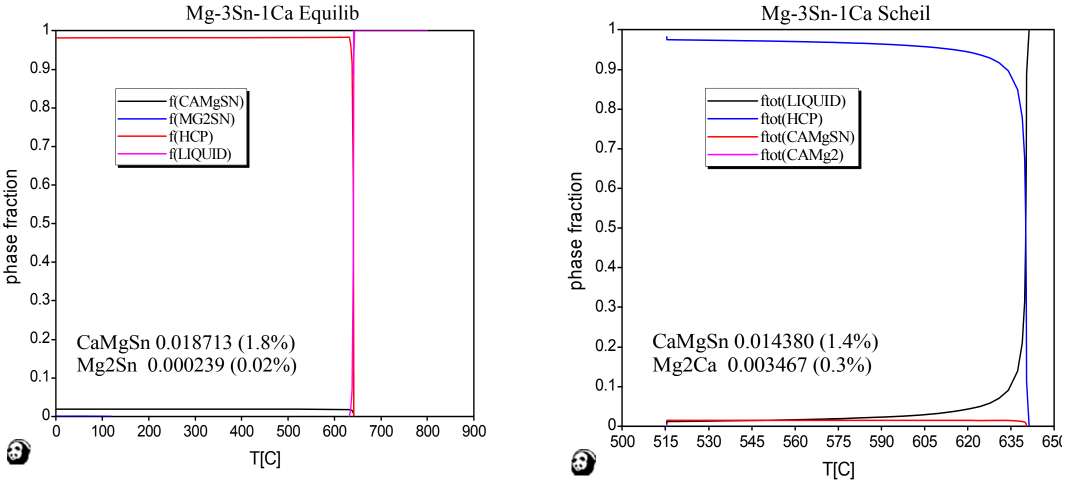

(a) **(b)**

Figure (65): Volume fraction of TX31-alloy under (a) equilibrium and (b) Scheil condition.

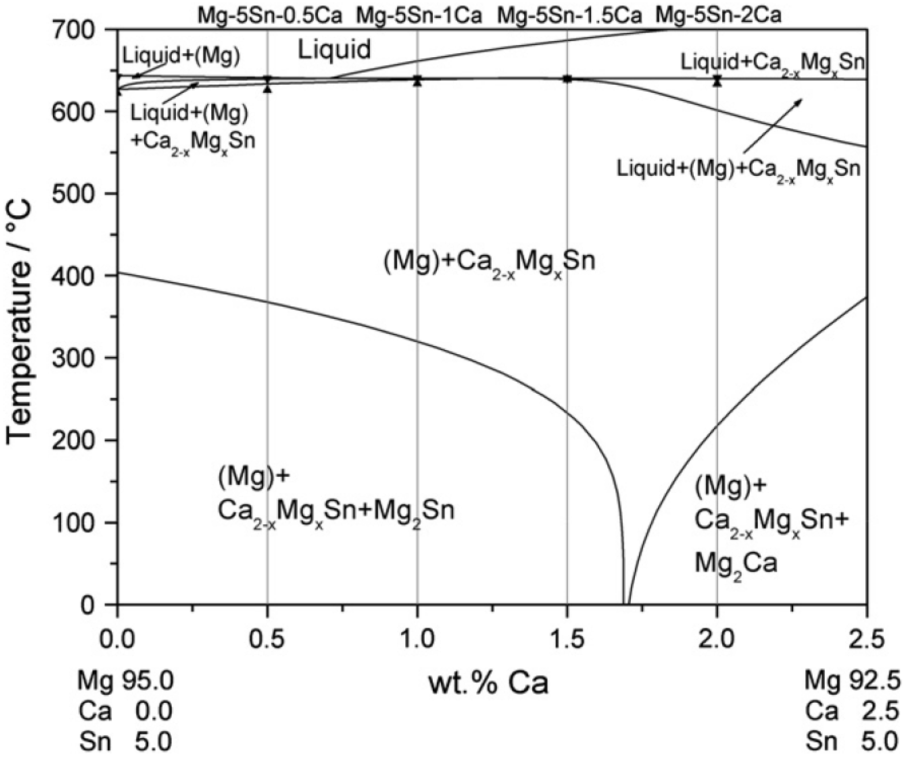

Figure (66): Calculated vertical phase section with constant 5 wt.-% Sn for investigated TX50x-, TX51-, TX52x-, and TX52-alloys with their related DTA signals [90].

The DTA results of the investigated Mg-3Sn-(0.5-2) Ca are illustrated in the Figure (64) showing the critical high maximum for primary α-Mg at 1.22 wt.-%. Alloys, which contain less amount of Ca, show only 5 and 2 K temperature differences between primary α-Mg and secondary $Ca_{2-x}Mg_xSn$ phases. At higher content of Ca, the primary crystallization of $Ca_{2-x}Mg_xSn$ is predicted and can clearly be seen in particular in TX32 by a larger isolated needle. The SEM micrograph was illustrated in Figure (38e,f). In spite of this observation, the phase $Ca_{2-x}Mg_xSn$ is too small to create an identifiable thermal signal in the DTA trace line. As a result, the initial thermal signal on cooling must be related to the beginning of the L→α-Mg + $Ca_{2-x}Mg_xSn$ reaction. All alloys located in the $Ca_{2-x}Mg_xSn$ field in Figure (63) are involved in this occurrence.

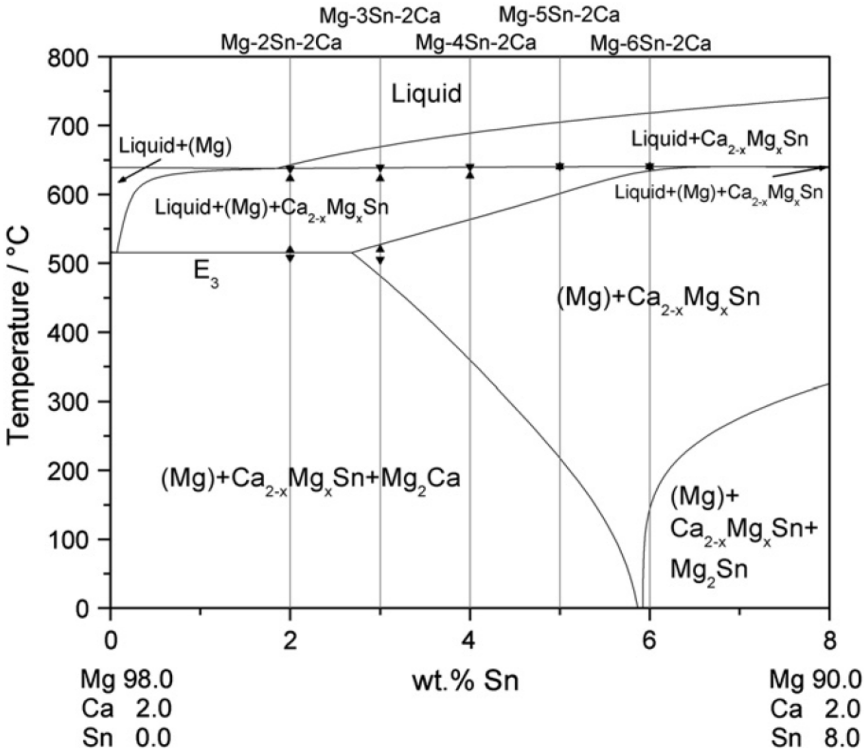

Figure (67): Calculated vertical phase section with constant 2% Ca for investigated TX22-, TX32-, TX42x-, TX52-, TX62-alloys and their related DTA signals [90].

The equilibrium solidification calculation of TX31x-alloy specified the solid-state precipitate of Mg_2Sn from the two-phase assembly α-Mg + $Ca_{2-x}Mg_xSn$ at 295°C. On the other side, Scheil calculation demonstrates that Mg_2Sn phase should form in the earlier mentioned reaction E_2: L ↔ α-Mg + $Ca_{2-x}Mg_xSn$ + Mg_2Sn at 562.8°C. As mentioned earlier, due to the technical limitations of the XRD equipment small particles of the Mg_2Sn phase (in both cases below 1%) were not detected. They were observed only by using SEM and EDX equipments which was shown in Figure (39a). The microstructure of the mentioned Figure is in agreement of the entire calculated solidification path with primary L → α-Mg, secondary L → α-Mg + $Ca_{2-x}Mg_xSn$ and finally L→ α-Mg + $Ca_{2-x}Mg_xSn$ + Mg_2Sn. In the microstructure of the TX31-alloy, only two phases were detected, namely, α-Mg and $Ca_{2-x}Mg_xSn$. The calculated vertical section with constant 3 wt.-%Sn for various alloys including TX31-alloy is illustrated in Figure (64). The calculated Scheil solidification also predicts a very low amount of approx. 0.3 % of the third Mg_2Ca phase. Furthermore, even a smaller amount of approx. 0.04% of Mg_2Sn was detected at 118°C under equilibrium; see Figure (65).

The amount of Mg_2Ca phase raises by increasing the amount of Ca up to 1.5 or 2 wt.-%Sn by keeping the same amount of 3 wt.-% constant, such as in TX32x-, and TX32-alloys. This was confirmed by SEM/EDX analysis. In addition, this phase also forms from the solid state below 341 and 489°C as it can also be seen in Figure (64). The equilibrium calculation of TX32x- and TX32-alloys as well as calculations for Scheil condition reveals the amount of its phase that reached 1 and 2% in both cases, respectively. However, the formation of the volume fraction under Scheil condition was during solidification from residual liquid through the eutectic reaction of the earlier mentioned E_3. The round shape of Mg_2Ca besides the isolated needles of some $Ca_{2-x}Mg_xSn$ phases as well as the main body from the joint precipitation of $L \rightarrow \alpha\text{-Mg} + Ca_{2-x}Mg_xSn$ were shown in the microstructure of TX32-alloy. The Mg_2Ca particles were formed in the ternary eutectic E_3 rather than in a solid-state precipitation due to the weak and diffuse DTA signal near the reaction E_3 at 515°C, Figure (64). In this case, the Scheil condition reflected the real solidification behavior of this alloy.

The Mg-rich section of Mg-5Sn based alloys with addition of 0.5-2%Ca is illustrated in Figure (66). The result of the mentioned alloys confirmed the major solidification reactions. For the Mg-5Sn based alloys with addition of Ca the primary $Ca_{2-x}Mg_xSn$ phase followed by the eutectic trough, Figure (63). Only for the TX50x-alloy, the primary phase α-Mg is expected at 1K lower by the secondary phase $Ca_{2-x}Mg_xSn$. The type of the third phase, either Mg_2Sn or Mg_2Ca, marks an important variation in the 5 wt.-% Sn alloy series. One of the mentioned binary phases should precipitate in the solid state below the V-shaped phase boundary in Figure (66). While the amount of Mg_2Sn reached, 2.5 and 1.5 wt.-% for both samples TX50x- and TX51-alloys with a ratio above 3:1, respectively. The Scheil calculations indicate the formation of Mg_2Sn phase in the eutectic reaction E_2, however in smaller amounts of 0.4 and 0.1, respectively. With a ratio less than 3:1 like in TX52-alloy, the Mg_2Ca phase can be detected under both equilibrium and Scheil condition with an amount of 0.6 and 0.8, respectively. The TX52x-alloy marks the transition between the alloy 1 wt.-% and 2 wt.-%Ca and the corresponding Mg_2Ca phase appearing as a third phase. Very few amounts of a third phase are expected for the TX52x. Only 0.4% of Mg_2Sn and 0.1% of Mg_2Ca are expected for Equilibrium and Scheil, respectively. Because of the very small volume fraction of the phase, it can be concluded that only the majorities of α-Mg and $Ca_{2-x}Mg_xSn$ were only found.

As it can be seen in Figure (67), the Mg_2Ca should precipitate under equilibrium condition below the V-shaped phase boundaries up to the divide at 5.9 wt.-% Sn. On the other hand, Mg_2Ca precipitates under Scheil condition always in the eutectic reached E_3 at 515°C up to a higher limit of 7 wt.-% Sn in these alloys. Only two phases namely $\alpha\text{-Mg} + Ca_{2-x}Mg_xSn$ are expected at the mentioned limits. The third phase Mg_2Sn or Mg_2Ca starts to form by increasing or decreasing the amount of Sn, respectively. Alloys, such as TX31, TX42x-, and TX62-alloys, with a ratio of 3:1 belong to this group. In both alloys the Mg_2Ca phase was not, detected using SEM/EDX and no signal can be seen in DTA analysis, Figures (91), (92), and (93). This is in agreement with the low amounts, which were calculated under Scheil (0.3%), and under equilibrium (0.04%) conditions as can be seen in Figures (68, 69).

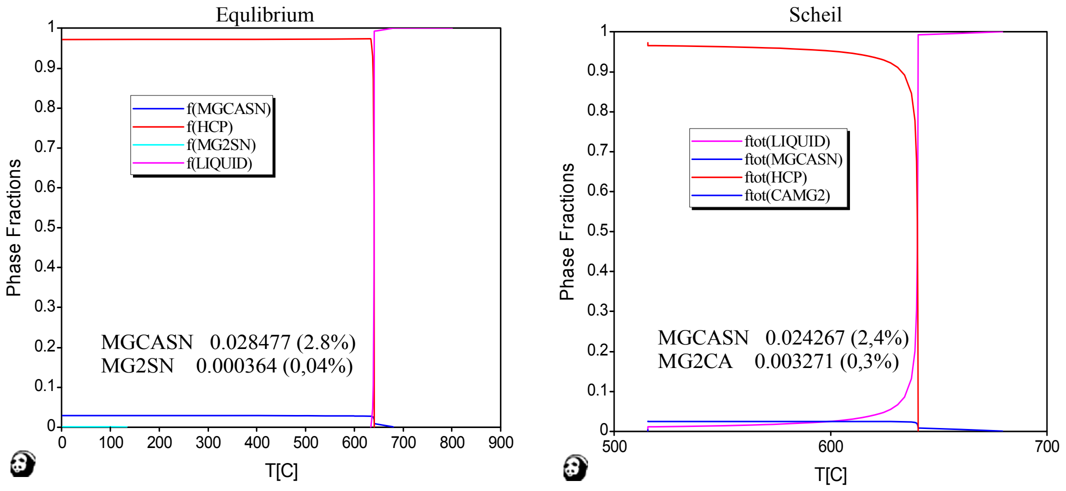

(a) (b)

Figure (68): Volume fraction of TX42x-alloy under (a) equilibrium and (b) Scheil condition.

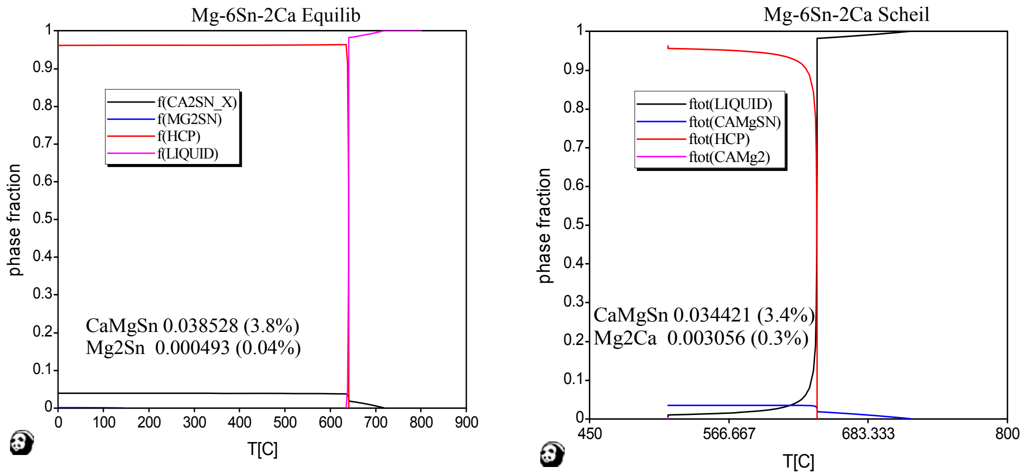

(a) **(b)**

Figure (69): Volume fraction of TX62-alloy under (a) equilibrium and (b) Scheil condition.

All of the mentioned experimental results are in agreement with the calculated data by Kozlov et al. [79,90]. According to thermodynamic calculation, which confirm the experimental work, it can be stated that ternary phase $Ca_{2-x}Mg_xSn$ can be detected in all of Mg-rich TX-alloys. The appearances of the mentioned ternary phase and the possibility of the formation of additional phases such as Mg_2Sn or Mg_2Ca are dependent on the Sn:Ca ratio. This ratio is responsible for the formation of the third phase changes in the following order: [$Ca_{2-x}Mg_xSn$, Mg_2Ca] to [$Ca_{2-x}Mg_xSn$] to [$Ca_{2-x}Mg_xSn$, Mg_2Sn]. The limiting ratio for negligible amount of the third phase is above the ratio 3:1 to 3.5:1. This transition ratio is even valid for constant addition of only small amounts of Ca (0.1 wt.-%). The calculated phase diagram section revealed in this case 0.3 wt.-% Sn as the divide between third phase precipitation Mg_2Ca and Mg_2Sn.

All of the TX-alloys showing their detected phases by using SEM/EDX and XRD (experimental) with the amount of their related calculated mol atoms obtained by Kozlov et al. [79,90] are summarized in Table (32).

Table (32): TX-alloys showing their detected phases by using SEM/EDX and XRD (experimental) and their related calculated data obtained by Kozlov et al. [79,90]).

Alloy [wt.-%]	Phases (experimental detected)			Phases (calculated)		
	Mg_2Sn	Mg_2Ca	$Ca_{2-x}Mg_xSn$	Mg_2Sn	Mg_2Ca	$Ca_{2-x}Mg_xSn$
[2]Mg-3Sn	yes	no	no	1.89	no	no
TX30x	yes	no	yes	0.96	no	0.93
TX31	yes	no		0.02	no	1.87
TX32x	no	yes		no	0.89	1.90
TX32	no	yes		no	1.84	1.90
TX33	no	yes		no	3.73	1.91
TX22	no	yes		no	2.45	1.26
[3]TX42	no	yes		no	1.20	2.56
TX42x	yes	no		0.04	no	2.85
TX50x	yes	no		2.26	no	0.95
TX51	yes	no		1.31	no	1.90
TX62	yes	no		0.05	no	3.85
[2]TX52x	yes	no		0.36	no	2.85
[2]TX52	no	yes		no	0.56	3.22
TX63	no	yes		no	1.85	3.92

---

[2] very few Mg_2Sn were detected by XRD.

[3] Mg_2Ca were not detected by XRD.

5.3 Corrosion

In order to calculate the corrosion resistance, there was a need to identify the density of the investigated alloys. The density rises by the addition of 3 wt.-% of Sn to the pure Mg. With increasing Sn by keeping the same amount of Ca constant in the ternary TX-alloys, like in TX22-, TX42-, TX52-, and TX62-alloys their density increases. This is caused due to the high density of the element Sn (7.31 gcm^{-3}), which is approx. four times higher than the density of Mg. In spite of this, by adding Ca to the binary alloy Mg-3Sn, the density of the ternary alloys, TX31, TX32, or TX33 will slightly decrease.

The results of corrosion investigations for TX-alloys in comparison to Mg-3Sn, AZ91D and AE42 using the salt spray and polarization techniques are shown in Figures (70) and (71). There are variations in the results obtained using the two different test methods. In general, the polarization test show lower corrosion rates values compared to the salt spray tests due to the environmental conditions for both tests. The pH value for polarization test was adjusted to 11 using a NaOH solution, while the pH value for the salt spray test was seven. Therefore, during the polarization a stable film of $Mg(OH)_2$ can be formed demonstrating more passivity compared to the salt spray test, which show films that are more corrosive on the surface of the samples. The corrosion resistance of the TX-alloys ranges between 2 to 6 and between 2 and 10 mm/yr for polarization and salt spray test, respectively. All TX-alloys are also less noble than the AZ91- and AE42-alloys, which can be seen in Figure (71).

The entire results of TX-alloys investigations show that they exhibit less corrosion resistance compared to AZ91D- and AE42-alloys. Their corrosion rates are 10-40 times higher than AZ91D- and AE42-alloys. In addition, TX-alloys are less noble than the mentioned alloys.

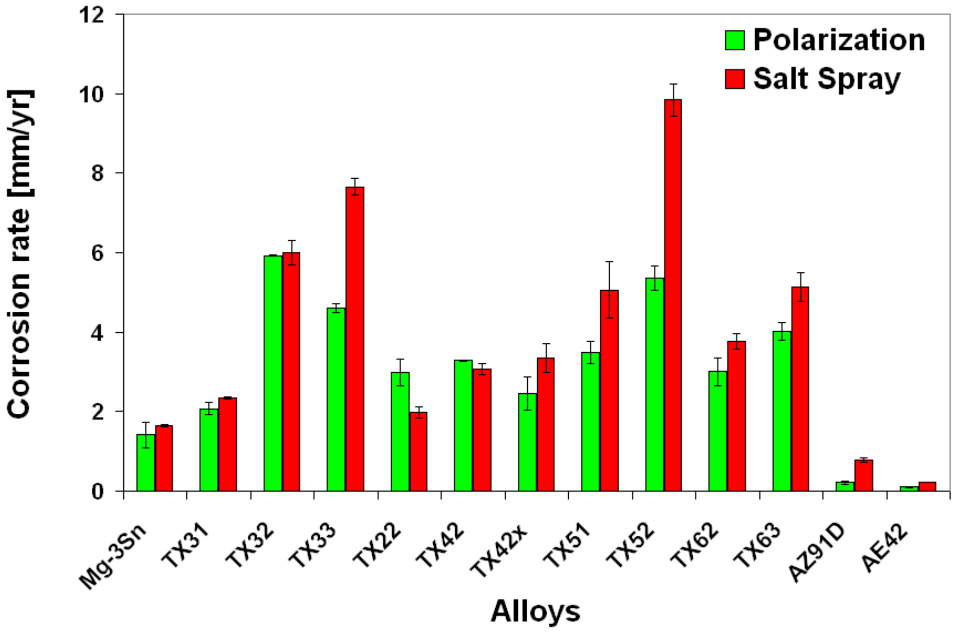

Figure (70): The measured corrosion rates compared to AZ91D- and AE42-alloys.

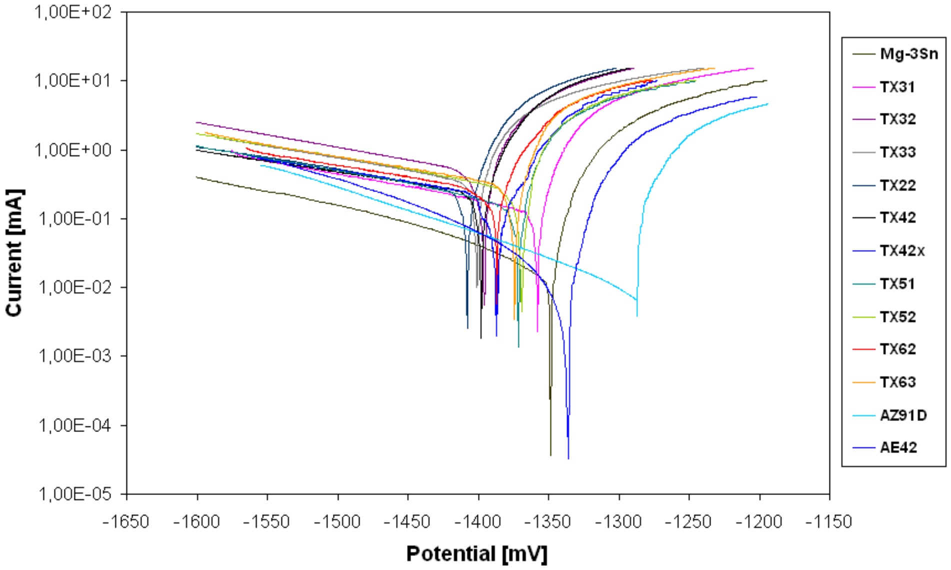

Figure (71): The polarization curves of the TX- compared to AZ91D- and AE42-alloys.

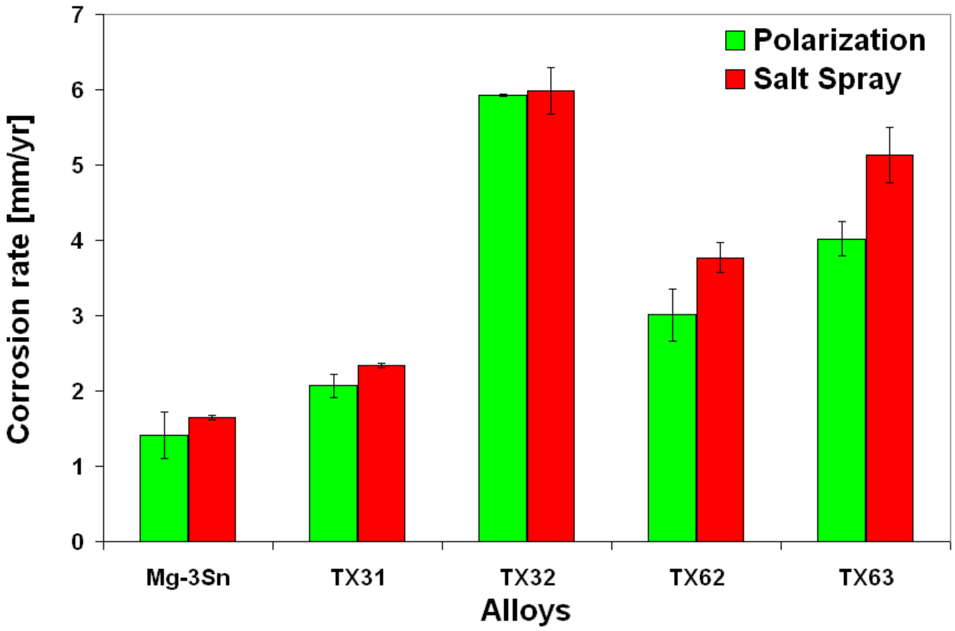

Figure (72): Influence of the amount of Ca on the measured corrosion rates.

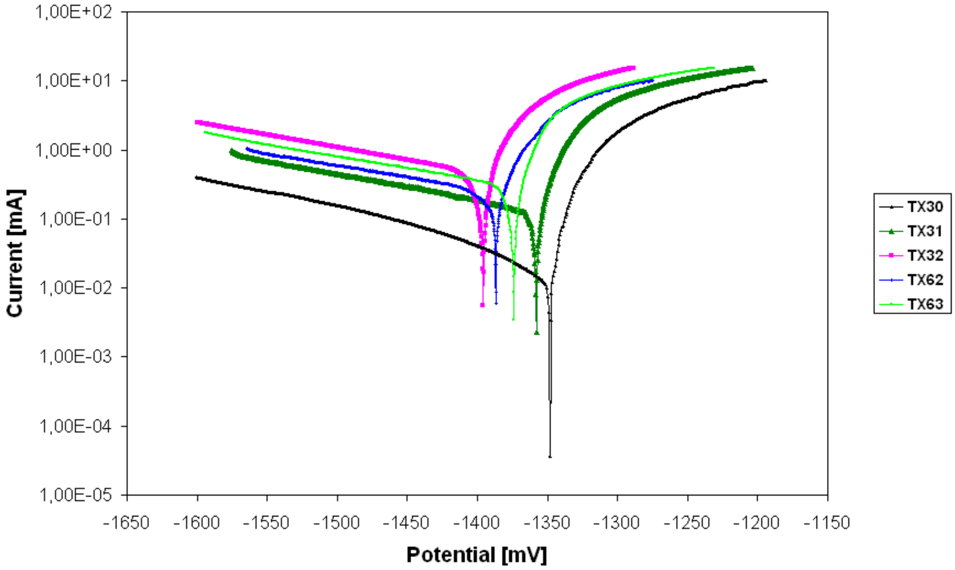

Figure (73): Influence of the amount of Ca on the polarization curves.

The corrosion result of the binary Mg-3Sn-alloy was used as a base in order to identify the influence of the Ca additions. From the mentioned results, it is now clear that tin and calcium have opposite effects as far as corrosion is concerned. It indicates that the corrosion resistance can be affected by the addition of amounts of Ca. This is shown in Figure (72) and (73). Several selected ternary alloys have shown lower corrosion resistance, i.e. higher corrosion rates comparable to those measured for the binary Mg-3Sn-alloy. This caused due to the formation of the binary Mg_2Ca phase.

On the other side, increasing amount of tin improves the corrosion resistance in the TX-alloys. Figure (74) and (75) demonstrate the effect of the addition of Sn to TX-alloys. This trend clearly indicates the beneficial role of tin in the ternary TX-alloys in reducing the corrosion rate of Mg-alloys. This is in a good agreement with the reported data by [2] that Sn increases the corrosion resistance of Mg.

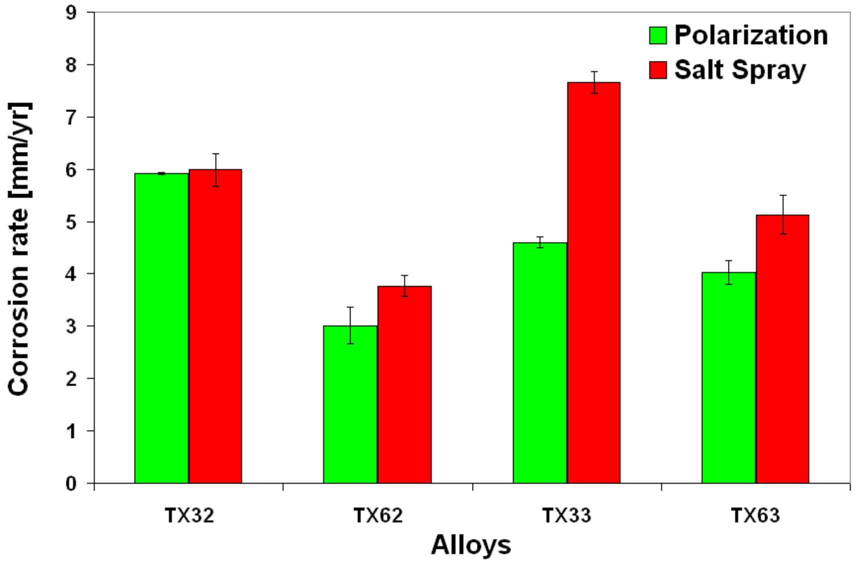

Figure (74): Influence of the amount of Sn on the measured corrosion rates.

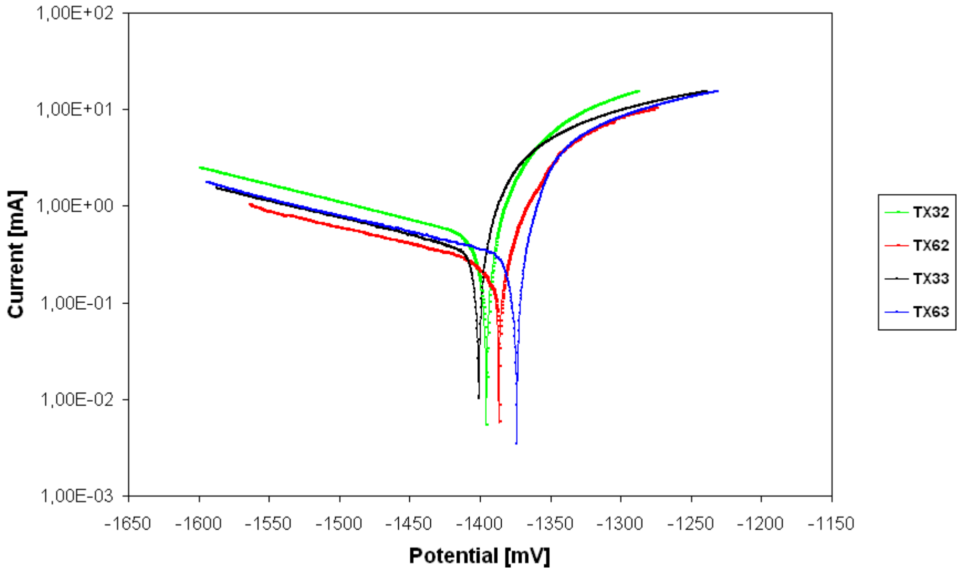

Figure (75): Influence of the amount of Sn on the polarization curves.

However, from Figure (70) and (71) it is shown that even with high calcium content (2wt.-%) the ternary TX62-ally exhibits good corrosion resistance whereas same amount of Ca in alloy TX32 gave poor corrosion resistance. As mentioned in the result, the formation of the phases in TX-alloys is dependent on the ratio Sn:Ca. The detected phases, their size and their volume fraction as well as their distribution play a significant role in the corrosion behavior. Therefore, systematic studies on corrosion rates can be conducted on the investigated TX-alloys in consideration of the ratio Sn:Ca. Therefore, it was more meaningful if the relative amounts of Sn and Ca are considered rather than amounts of individual elements. The results obtained on three alloys having same ratio of Sn to Ca but with varying amounts of Sn and Ca. like TX31-, TX42x, and TX62 indicate that the corrosion rates are almost similar. The ratio of Sn to Ca obviously plays a significant role in corrosion resistance of such ternary systems as well as the amount of alloying elements. The corrosion potential of the TX-alloys with Sn:Ca ratio 3:1 is nobler and its current corrosion I_{corr} is about 2 times lower than that of the TX-alloys with Sn:Ca ratio below 3:1. TX63- and TX52-alloys are excluded and the reason can be related to their higher volume fraction which contain more amount of $Ca_{2-x}Mg_xSn$ compared with the other alloys in the same group (ratio < 3:1). According to the calculated data given in Table (32), obtained by Kozlov et al. [79,90], the volume fraction of $Ca_{2-x}Mg_xSn$ of TX31-, TX51- and TX32-alloy are similar. Due to the presence of Mg_2Ca phase in only TX32-alloy its corrosion resistance is poor compared to TX31- and TX51-alloys. The increasing of Sn and Ca on the same time by keeping the ratio (3:1) similar, the corrosion resistance decreases due to the increasing of the amount of the volume fraction of the $Ca_{2-x}Mg_xSn$ in these alloys. This also can be occurs when the amount of volume fraction of both Mg_2Ca and $Ca_{2-x}Mg_xSn$ increases, like in the TX-alloys which have a ratio of 1:1 like TX22 and TX33 or ratio Sn:Ca of 2:1 for TX42 and TX63-alloys. In general, it was shown that the Mg_2Sn phase can enhances the corrosion resistance while the $Ca_{2-x}Mg_xSn$ affect a little the corrosion resistance nevertheless Mg_2Ca phase affect their corrosion resistance more.

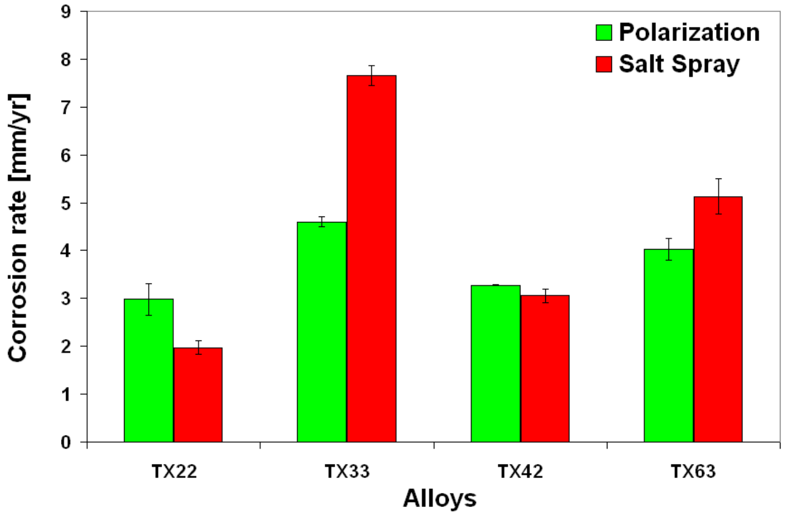

Figure (76): Influence of TX-alloys with proportions of Sn and Ca with a ratio of Sn:Ca 1:1 and 2:1 on the measured corrosion rates.

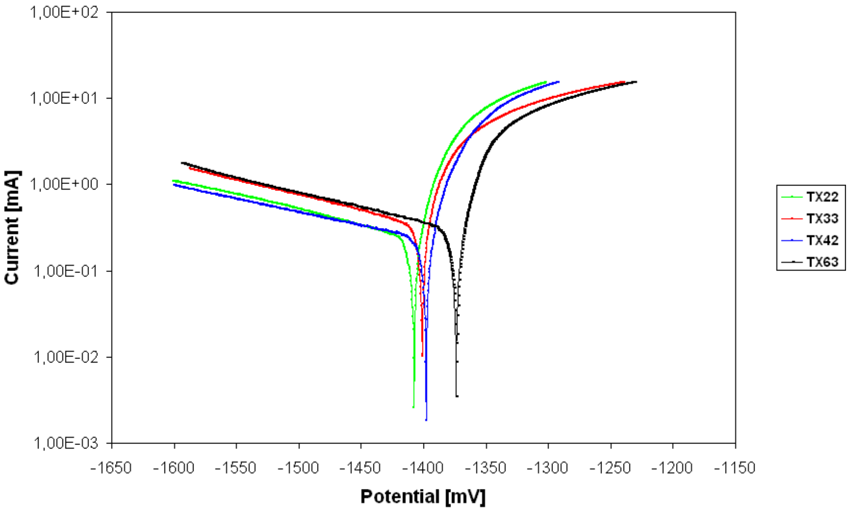

Figure (77): Influence of TX-alloys with proportions of Sn and Ca with a ratio of Sn:Ca 1:1 and 2:1 on on the polarization curves.

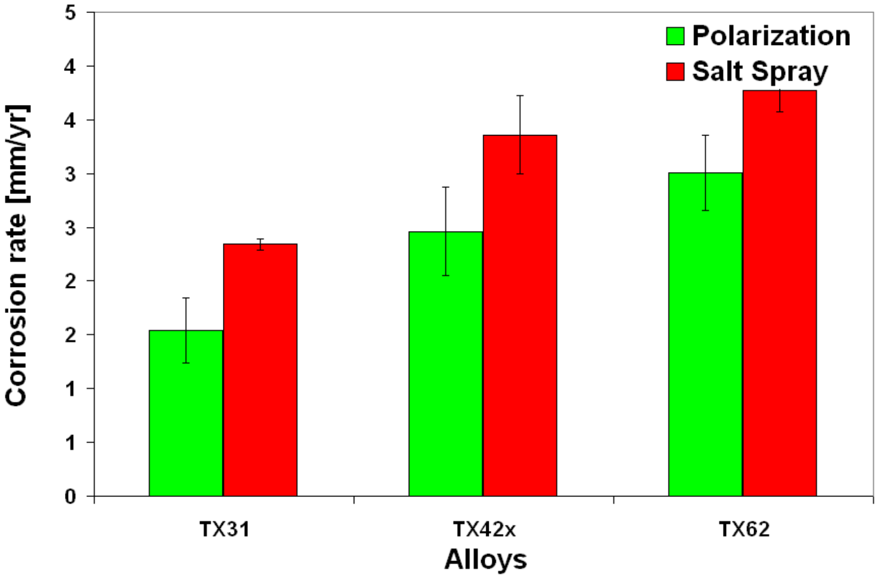

Figure (78): Influence of TX-alloys with same proportions of Sn and Ca with a ratio of Sn:Ca 3:1 on the measured corrosion rates.

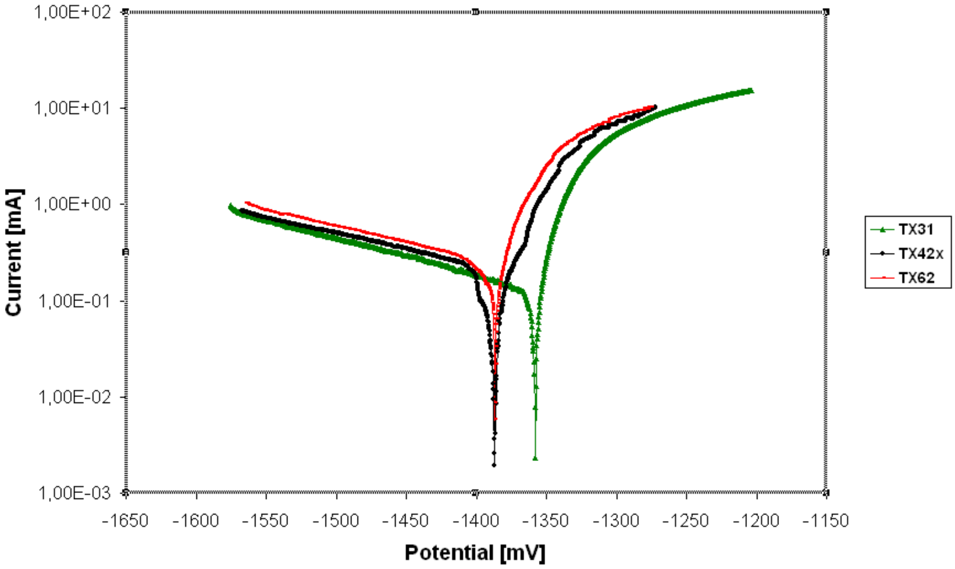

Figure (79): Influence of TX-alloys with same proportions of Sn and Ca with a ratio of Sn:Ca 3:1 on the polarization curves.

5.4 Mechanical properties

The mechanical properties of the TX-alloys are dependent on the ratio Sn:Ca. The detected $Ca_{2-x}Mg_xSn$, Mg_2Sn, and Mg_2Ca phases, their size and their volume fraction as well as their distribution play a significant role in the mechanical properties. It is also obvious, that an increase in strength is coupled with a decrease in elongation to fracture.

5.4.1 Compression and tension

The relatively low values regarding yield strength in the current study can be related to the presence of defects generated in the matrix due to non-optimized casting conditions. With regard to the permanent mould casting, the materials have a relatively coarse microstructure, which results in the low values. This observation is not in agreement with the good creep behavior. One explanation is that Sn enriched towards the grain boundary. This leads to a lowered melting temperature of the material at the grain boundary. Therefore, the grain boundary is softened leading to early failure at the grain boundary when the material is loaded, especially when the load is applied relatively fast as it is in compression testing.

The large differences in the ultimate strength appear to be associated with a combination of enhanced strength of the TX-alloys and the greater deformability of these alloys in compression. The tensile yield strength (TYS) of the TX-alloys increases with addition of Ca and their ultimate tensile strength (UTS) decreases. The elongation values are consistently lower in tension than in compression. The TYS values of TX-alloys decreases with Sn addition but their UTS increases. By increasing the Sn:Ca ratio more than 3:1 the yield strength decreases while it increases with a reduction of the Sn:Ca ratio less than the mentioned ratio.

Aluminum as alloying element stays in solid solution and forms β-$Mg_{17}Al_{12}$-phases in AZ91D. The two strengthening mechanisms (solid solution strengthening and precipitation strengthening) based on Al are obviously more effective as solid solution strengthening in Mg-Sn and the phases $Ca_{2-x}Mg_xSn$ and Mg_2Ca in the TX32-alloy.

5.4.2 Hardness

The increase of hardness values are related to the addition of calcium and thus to the formation of the ternary $Ca_{2-x}Mg_xSn$ and the binary Mg_2Ca phases. The addition of Sn also increases the HV values of most investigated alloys. However, the addition of 2 wt.-% of Sn to TX31-alloy decreases the value of the obtained TX51-alloy. The same results can be seen by adding 1wt.-% of Sn to TX22-alloy. This indicates the role of the formations of the phases. It is clearly that the formation of more amounts of $Ca_{2-x}Mg_xSn$ and Mg_2Ca increases the HV values, while Mg_2Sn decreases the HV values. The hardness values of the investigated TX-alloys are comparable and even higher than AE42-alloy but less than the one of AZ91D-alloy.

5.4.3 Compressive creep

It was found that the creep resistance of the investigated alloys is related to the kind and amount of the phases in the alloys, which depends on the ratio of Sn:Ca. Therefore, the results of creep investigations are divided into three groups. The first one when this ratio is 3:1, the second group if the ratio is less than 3:1 and finally when the Sn:Ca ratio is more than 3:1.

The TX-alloys with Sn:Ca ratio 3:1, such as TX31, TX42x, TX62 and the TX-alloys with Sn:Ca ratio above 3:1 like TX51-alloy showed high creep deformation and thus poor creep properties. The mentioned alloys exhibit poor creep resistance due to the formation of only $Ca_{2-x}Mg_xSn$ or both $Ca_{2-x}Mg_xSn$ and Mg_2Sn phases, respectively. They were only investigated at 80 MPa at 135 °C or 150 °C. Due to their poor creep resistance at the mentioned parameter, the investigated TX-alloys were dropped from further examinations at temperature of 175 °C at load of 80 MPa.

The third group, which has a Sn:Ca ratio below 3:1 like TX22-, TX32-, Tx33-, and TX63-alloys showed very good creep resistance. This caused due to the presence of the phases $Ca_{2-x}Mg_xSn$ and Mg_2Ca. They offer very good creep properties compared to cast AZ91D- and even AE42-alloys. However, based on the results of XRD studies and the reported results by kozlov et al. [79,90] the TX42 and TX52 show very low volume fraction of binary Mg_2Ca phase. Therefore, their creep resistance is poor compared to the other TX-alloys, which have a Sn:Ca ratio of less than 3:1. The obtained result at high temperatures of 150 °C and 175 °C is in a good agreement with the published data [43,96,103], which indicate the significant role of the binary Mg_2Ca phase in Mg-alloys.

From the mentioned data, creep rates for all these alloys are presented in Figure (80) as a function of Sn to Ca ratio. It is evident from the Figure that the relative ratio of Sn and Ca plays a very critical role in determining the creep resistance of TX-alloys rather than just their individual amounts. From the results obtained from the creep tests, it is now evident that alloys with a ratio less than 3:1 exhibit very good creep resistance compared to the alloys with ratio 3:1 or more.

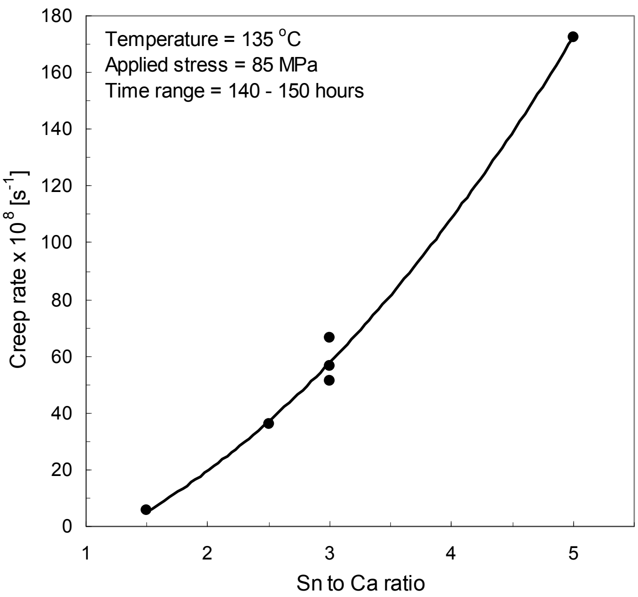

Figure (80): Influence of the proportion of Sn to Ca on the measured creep rates of TX-alloys.

As mentioned earlier, TX-alloys with a ratio Sn:Ca of 3:1 or higher show generally higher creep rates and thus poor creep resistance. The creep rates of TX31-, TX42x-, and TX62-alloys reveal higher creep rate than that of TX51-alloy. In contrast to this, the TX32-alloy shows a higher creep resistance. The mentioned alloy exhibit one power to ten values compared to the conventional alloys, AZ91D and AE42. As mentioned earlier, both of $Ca_{2-x}Mg_xSn$ and Mg_2Ca phases were observed in TX32-alloy. This shows that $Ca_{2-x}Mg_xSn$ and Mg_2Ca phase play a significant role in term of creep resistance.

The volume fraction of Mg_2Ca in TX52-alloy is according to the calculation by Kozlov et al. [79,90] is four times less than TX32-alloy. However, it has more volume fraction of $Ca_{2-x}Mg_xSn$ phase, due to the presence of more amount of Sn, (Table (32)).

The characteristics of a large volume fraction of thermally stable Mg_2Ca particles can be formed. Therefore, the creep resistance of TX-alloys increases if the ratio less than 3:1. The Mg_2Ca phase has a high melting point and thus results in metallurgical stability of the grain boundaries at elevated temperatures. This is likely to be the cause of the good creep resistance of the TX-alloys (where the phase forms) at high temperatures.

This caused due the formation of the ternary $Ca_{2-x}Mg_xSn$ and binary Mg_2Sn or Mg_2Ca phases. The existence of the ternary $Ca_{2-x}Mg_xSn$ and the binary Mg_2Ca phases plays a significant role for pinning the grain boundaries. They enable to improve the creep resistance at high temperature. Therefore, there creep resistance is higher than the others. The TX-alloys also exhibit very good creep resistance compared to the as-cast AZ91D- and AE42-alloys.

The increase of the Sn content and thus the ratio of Sn:Ca has a negative effect on the creep properties.

In order to compare the TX-alloys (with ratio Sn:Ca below 3:1) the creep deformation and the minimum creep rates for TX32- and AZ91D- as well as AE42-alloys at 150 hours are given in Table (33). However, due to the early failure of the creep deformation of AZ91D-alloy for the test at 80MPa@175°C, the data are given at 130 hours. The TX32-alloy shows very good creep behavior compared to AZ91D for all testing conditions. Even compared to the AE42-alloy at 80MPa@135°C and 80MPa@175°C the TX32-alloy is having improved creep resistance. The good creep behavior of the TX32-alloy is based on the precipitates Mg_2Ca and $Ca_{2-x}Mg_xSn$ as well. While Mg_2Ca is mainly found on the grain boundaries, needle type $Ca_{2-x}Mg_xSn$ precipitates are seen within the grain and at the grain boundary Figure (38e-f). This type of precipitates as well as their distribution within the grains and at the grain boundaries is obviously more effective than only the α-phase in the AZ91D-alloy in combination with the aluminum atoms in solid solution. A similar conclusion can be drawn when comparing AE42-alloy with TX32-alloy. Under the chosen testing regime, the TX32-alloy performs better.

Table (33): Creep rates and creep deformation of TX32-alloy compared to AZ91D- and AE42-alloys.

Alloys	Test condition 150 hours	Creep rate [E-08 1/ s^{-1}]	Creep deformation [%]
TX32	80 MPa@135 C 150h	0.99	0.63
AZ91D		1.90	3.25
AE42		1.40	1.36
TX32	80 MPa@150 °C 150 h	3.18	2.71
AZ91D		3.67	4.03
AE42		1.37	3.09
TX32	80 MPa@175 C 150 h	4.1	6.30
AZ91D*		25.40	21.93
AE42		14.20	11.14

The investigated TX32-alloy at various low loads, in particular at 40, 60 MPa and at temperature of 150 °C shows superior creep as shown in the results in Table (30) and Figure (61). The result was expected due to the low mechanical properties of the investigated TX-alloys.

The grain boundary phase $Mg_{17}Al_{12}$ that has a melting point of 437 °C acts as a strengthening phase at lower temperatures. However it is known that this phase is thermal not stable at temperatures above 120 °C and the phase can soften at 150 °C. Therefore, this phase cannot serve to pin the grain boundaries and thus it exhibit a poor creep resistance at temperature such as 150 °C or 175 °C.

6 Conclusions

The conclusions of the experimental results can be summarized as follows:

[1] **Microstructure and phase characterization:** The results of the microstructure examinations indicate that Ca additions to the binary Mg-Sn alloys causes the formation of the ternary $Ca_{2-x}Mg_xSn$ phase in the form of thin plates or needles in all of investigated alloys. This phase has been observed in the matrix and at grain boundaries. In addition, large particles of the mentioned phase have a lamellar shape. Additional phases, such as binary Mg_2Sn or Mg_2Ca phase were also observed. They have been detected within the grain and in the matrix as well. It was also found that the formation of the phases is dependent on the ratio Sn:Ca. As a general role, if this wt.-% ratio is nearly 3:1 they show clearly that only $Ca_{2-x}Mg_xSn$ can be formed without a third phase. On the other hand, if the Sn:Ca ratio is below than 3:1 additional phase can be formed besides $Ca_{2-x}Mg_xSn$, namely Mg_2Ca. The third possibility where the ratio of Sn:Ca is more than 3:1. In this case, both $Ca_{2-x}Mg_xSn$ and Mg_2Sn phases were observed. A good agreement between the observations of the phases and the calculated data obtained by Kozlov et al. [79,90] were found. The three groups-results of the microstructure investigations match with results from corrosion, tensile, compression, hardness, and compressive creep investigations.

[2] **Corrosion:** The corrosion behavior of the TX-alloys was investigated using polarization and salt spray test methods. The results of both methods indicated that the corrosion rates of the selected TX-alloys are approx. 3 to 30 times and 8 to 60 times higher than that of AZ91D- or AE42-alloys, respectively. Within the TX-alloys, the addition of Sn increases the corrosion resistance, while it decreases with addition of Ca. However, it was indicated, that the ratio Sn:Ca plays a significant role. Increasing both Sn and Ca by keeping the same Sn:Ca ratio at the same time the corrosion resistance will decrease. The results of the corrosion investigations showed that corrosion resistance is influenced by the phases present in the alloys, with Mg_2Sn being the most compatible within the detected phases followed by $Ca_{2-x}Mg_xSn$ and finally by Mg_2Ca.

[3] **Mechanical properties**

Compression and tensile:

The results of the tensile yield strength and ultimate tensile strength of the investigated TX-alloys show that the ultimate strength values are consistently greater in compression than in tension. In addition, they are also considerably more deformable in compression than in tension. The large differences in the ultimate strengths appear to be associated with a combination of enhanced strength of the TX-alloys and the greater deformability of these alloys in compression. By increasing the Sn:Ca ratio more than 3:1 the yield strength decreases while it increases with a reduction of the Sn:Ca ratio less than the mentioned ratio. In general the results at room temperature are below the AZ91-alloys but still comparable with AE42-alloy.

Hardness:

The obtained results of the hardness Vickers studies of the TX-alloys at ambient temperature showed that the addition of Ca to Mg-Sn alloy increases the HV values. When further amounts of Sn were added to the TX-alloys, there was an only minor change in the result. In general, the HV values of the investigated TX-alloys are below the AZ91D-alloys values but still comparable with AE42-alloy. The hardness Vickers values are ranging from 40 to 50 HV for TX-alloys.

Compressive creep:

Calcium additions to Mg-Sn alloys decrease the creep rate and thus enhance the creep resistances by only taking into consideration of the ratio Sn:Ca. The formed phases impede the sliding of grain boundaries also partly contributes to the improvement of creep resistance. It was clearly seen that the TX-alloys with Sn:Ca ratio higher than 3:1 exhibit poor creep resistance, while alloys with a ratio Sn:Ca of 3:1 showed improved creep resistance. However, most of the TX-alloys (TX22, TX32, TX33, and TX63), with a ratio of less than 3:1, demonstrate a great creep resistance and are very good in this respect to AZ91D- and even to AE42-alloys.

The casting conditions should be optimized to avoid the presence of defects generated in the matrix, which leads for low values regarding yield strength in the current study. Finally, this work demonstrated that the amount of Sn and Ca additions to the TX-alloys system should be added in a certain range so that the obtained Sn:Ca ratio of less than 3:1 (in particular less than 2:1) can be achieved. As a result, some of the TX-alloys can be used as creep resistant alloys at high temperature applications.

7 References

1 A. Beck, Magnesium und seine Legierungen, Julius Springer Verlag, Berlin, Germany, 1939, in German.

2 E. F. Emley, Principles of Magnesium Technology, Oxford, Pergamon Press, 1966.

3 C. Kammer, Magnesium-Taschenbuch, Aluminum-Verlag, Düsseldorf, Germany, 2000, in German.

4 H. Friedrich, B. Mordike, Magnesium Technology, Springer Verlag, 2006.

5 http://www.magnesium.com

6 Magnesium, Alloys preparation, properties, applications, ed. F. Habashi, Wiley-VCH, Weinheim, Germany, 1998.

7 W. D. Callister, Materials science and engineering: An introduction, 7th Edition, John Wiley & Sons, New Jersy, USA, 2007.

8 F. Von Buch, B. L. Mordike, Hochtemperatureeigenschaften von Magnesiumlegierungen, Magnesium, Eigenschaften, Anwendungen, Potentiale, ed. K.-U. Kainer, Wiley-VCH, Weinheim, 2000, p. 111-136, in German.

9 B. Mordike, T. Ebert, Magnesium properties – applications - potential, Materials science and engineering, A 302, 2001, p. 37-45.

10 S. Schumann, F. Friedrich, The use of magnesium in cars–Today and in the future, Proceeding of the 4th international conference on magnesium alloys and their applications, eds. B. L Mordike, K. U. Kainer, Wiley-VCH Weinheim, Wolfsburg, Germany, 1998, p. 3-13.

11 Magnesium and magnesium alloys, ASM speciality Handbook, ed. M. M. Avedesian and H. Baker, ASM speciality Handbook, ASM International, Metals Park Ohio, USA, 1999.

12 M. S. Dargusch, The role of microstructure in the creep of die cast magnesium alloys, PhD Thesis, The University of Queensland, Brisbane, Australia, 1999.

13 M. S. Dargusch, G. L. Dunlop, Elevated temperature creep and microstructure of die cast Mg-Al alloys, Proceeding of the 4th international conference on magnesium alloys and their applications, eds. B.L. Mordike, K.U. Kainer, Wiley-VCH Verlag GmbH, Wolfsburg, Germany, 1998, p. 277-282.

14 M.S. Dargusch, G. L. Dunlop, and Pettersen, Trans. 19th international die casting congress, North America Die Casting Association, Rosemont, Illinois, 1997, pp. 131-137.

15 A. A. Luo, Recent magnesium alloy development for elevated temperature applications, International Materials Review, Volum 49, 2004, p. 13-30.

16 http://minerals.usgs.gov/minerals

17 D. L. Albright and T. Ruden, Magnesium utilization in the North American automotive industry, 1994, p. 26-28.

18 A. Luo, M. O. Pekguleryuz, Review cast magnesium alloys for elevated temperature applications, Journal of Materials Science, 29, 1994, p. 5259-5271.

19 I. J. Polmear, Overview - Magnesium alloys and applications, Materials Science and Technology, Vol. 10, 1994, p. 1-15.

20 R. E. Brown, Magnesium industry growth in the 1990 period, Magnesium Technology 2000, The Minerals, Metals & Materials (TMS), eds. H. Kaplan, J. Hryn, B. Clow, Nashville, Tennesse, USA, 2000, p.3-12.

21 Communication from the commission to the council and the european parliament, COM (95) 689 final, Brussels, 20.12.1995.

22 Communication recommendation of 5 February 1999 on the reduction of CO_2 emissions from passenger cars (1999/125/EC).

23 Assembly Bill Nr. 1493, approved by Governor, 2002.

24 http://www.nhtsa.dot.gov.

25 http://www.unfccc.int

26 H. Westengen, P. Bakke, D. Albright, Advanced in magnesium alloy development, Proceeding 61st Annual World Magnesium Conference 2004 New Orleans, USA, 2004, p. 81-86.

27 S. Koike, K. Washizu, S. Tanaka, T. Baba, K. Kikawa, Development of lightweight oil pans made of a heat-resistant magnesium alloy for hybrid angines, SAE Technical paper 2000-01-117, Detroit, MI, 2000.

28 R. Beals, L. Kopka, J. Allison, J. A. Hines, B. McCune, Fundamental research needs for the magnesium powertrain cast components (MPCC) project, Magnesium Technology 2004, The Minerals, Metals & Materials (TMS), ed. A. A. Luo, Charlotte, NC, USA, 2004, p. 11-17.

29 T. K. Aune, and T. J. Ruden, SAE 920070, Detroit, Michigen, 1992.

30 A. Barth, Mg application in the 7G Tronic gear; Proc. 61st Annual World Magnesium Conference, New Orleans, USA, 2004, p. 81-86.

31 L. L. Rokhlin, Magnesium alloys containing rare earth metals, eds. J.N. Fridlyander and D.G. Eskin, Taylor & Francis Inc., 2003.

32 J. F. King, P. Lyon, K. Savage, Influence of rare earth elements and minor additions on properties and performance of magnesium-yttrium alloys in critical aerospace applications, proceedings of the 59th annual world magnesium conference, Montreal, Canada, 2002, p. 15.

33 P. Bakke, K. Pettersen, H. Westengen, Improving the strength and ductility of magnesium die-casting alloys via rare-earth addition, Journal of the Minerals, Metals and Materials Society, Volume 55, Number 11, 2003, p. 46-51.

34 N. Li, R. Osborne, B. Cox, D. Penrod, Magnesium engine cradle-The US car structural cast magnesium development project, SAE technical paper 2005-01-0337, 2005.

35 H. Westengen, P. Bakke, J. I. Skar, H. Gjestland, New magnesium die casting alloys: driving development of critical automotive applications, 63rd annual World Magnesium Conference, IMA, Beijing, China, 2006.

36 A. A. Luo, M. P. Balogh, and B. P. Powell, Creep and microstructure of magnesium-aluminum-calcium based alloys, Metallurgical and Materials Transactions, Vol. 33 A, 2002, p. 567-574.

37 M.O. Pekguleryuz, E. Baril, Creep resistant magnesium diecasting alloys based on alkaline earth elements, Materials Transactions, Volume 42 Nr. 7, 2001, pp. 1258-1267.

38 M.O. Pekguleryuz and A. Luo, A., The creep resistant magnesium alloys for die casting, Technologie Magnesium, World patent WO96/25529, 1996.

39 B.R. Powell, V. Rehets, A. A. Luo, B. L. Tiwari, Creep resistant magnesium alloy die castings, USA patent US 6264763, 2001.

40 B. Bronfin, E. Aghion, F. von Buch, S. Schumann, M. Ktsir, Die casting magnesium alloys for elevated temperature applications, Magnesium Technology 2001, The Minerals, Metals & Materials (TMS), ed. J. N. Hryn, New Orleans, Louisiana, USA, 2001, p. 127-130.

41 B. Bronfin, E. Aghion, F. v. Buch, S. Schumann, Creep resistant magnesium alloys with impoved castability, patent no. US 2003/0086811 A1, 2003.

42 B. L. Mordike, Creep-resistant magnesium alloys, Materials Science Engineering, A 324, 2002, p. 103-112.

43 B. Bronfin, E. Aghion, F. v. Buch, S. Schumann, H. Friedrich, Development of new magnesium alloys for advanced applications, Proceeding of the 6th international conference on magnesium alloys and their applications, ed. K. U. Kainer, Wiley-VCH, Weinheim, Germany, 2004, p. 55-61.

44 E. Aghion, B. Bronfin, F. v. Buch, S. Schumann, and H. Friedrich, Dead Sea magnesium alloys developed for high temperature applications, Magnesium Technology 2003, The Minerals, Metals & Materials (TMS), ed. H. I. Kaplan, San Diego, California, USA, 2003, p. 177-183.

45 E. Baril, P. Labelle, M.O. Pekguleryuz, Elevated temperature Mg-Al-Sr: creep resistance, mechanical properties, and microstructure, Journal of The Minerals, metals and materials society (JOM), 2003, p. 34-49.

46 A.P. Druschitz, E.R. Showalter, J.B. McNeill, D. L. White, Evaluation of structural and high-temperature magnesium alloys, SAE Technical paper series, 2002-01-0080, 2002.

47 Y. Fasoyinu, R. Bouchard, T. Castles, M. Sahoo, P., Labelle, Mechanical properties of high pressure die cast magnesium alloys AE42 and Noranda new alloy (AJ52X) for high temperature applications.

48 A. Fischersworring-Bunk, C. Landerl, A. Fent, J. Wolf, The new BMW inline six-cylinder composite Mg/Al crankcase, 62rd annual World Magnesium Conference*,* IMA*,* Berlin, Germany, 2005.

49 M. Pekguleruz, P. Labelle, D. Argo, E. Baril, Magnesium diecasing alloy AJ62X with superior creep resistance, ductility and diecastability, SAE 2003-01-0190, 2003.

50 M. O. Pekguleryuz, A. A. Kaya, Creep resistant magnesium alloys for power-train applications, Proceeding of the 6th international conference on magnesium alloys and their applications, ed. K. U. Kainer, Wiley-VCH, Weinheim, Germany, 2004, p. 74-93.

51 E. Baril, P. Labelle, A. Fischersworring-Bunk, AJ (Mg-Al-Sr) alloys system used for new engine block, SAE 2004-01-0659, 2004.

52 M. O. Pekguleryuz, A. A. Kaya; Magnesium die casting alloys for high temperature applications; Magnesium Technology 2004, The Minerals, Metals & Materials (TMS), ed. A. A. Luo, Charlotte, North Carolina, U.S.A, 2004, p. 281-287.

53 David L. Heiseman, Exploring chemical elements and their compounds;1992.

54 CRC Handbook of chemistry and physics, 77th edition.

55 S. Ramakrishnan, P. Koltun; A comparison of the greenhouse impacts of magnesium produced by electrolytic and pidgeon processes; Magnesium Technology 2004, The Minerals, Metals & Materials (TMS), ed. A. A. Luo, Charlotte, North Carolina, USA, 2004, p. 173-180.

56 O. Wallevik, K. Amundsen, A. Faucher, T. Mellerud, Magnesium electrolysis – a monopolar viewpoint, *Magnesium Technology 2000*, The Minerals, Metals & Materials (TMS), eds. H. Kaplan, J. Hryn, B. Clow, Nashville, Tennesse, USA, 2000, p.13-16.

57 P. Koltun, A. Tharumarajah, S. Ramakrishnan, Life cycle environmental impact of magnesium automotive compnents, Magnesium Technology 2005, The Minerals, Metals & Materials (TMS), eds. N. R. Neelameggham, H. I. Kaplan, B. R. Powell, San Francisco, California, USA, 2005, p. 43-48.

58 Standard Practice for condification of certain nonferrous metals and alloys, cast and wrought, designation: B275-05.

59 T. Abu Leil, K. P. Rao N. Hort, Y. Huang, C. Blawert, H. Dieringa and K.U. Kainer, Microstructure, Corrosion and Creep of Cast Magnesium Alloys Mg2Sn2Ca and Mg4Sn2Ca, Magnesium Technology 2007, The Minerals, Metals & Materials (TMS), eds. R.S. Beals, M.O. Pekguleryuz, R. Neelameggham, and A.A. Luo, TMS 2007, Orlando, Florida, USA, p. 281-286.

60 E. D. Morales, C. Blawert, W. Dietzel, K.U. Kainer, C. Scharf and A. Ditze, Corrosion behaviour of a new AZ based secondary alloy with improved tolerance limits against impurities.

61 T. Abu Leil, N. Hort, W. Dietzel, C. Blawert, Y. Huang, K.U. Kainer, K.P. Rao, Microstructure and Corrosion behavior of Mg-Sn-Ca alloys after extrusion, Transactions of Nonferrous Metals Society of China, Volume 19, Issue 1, 2009, p. 40-44.

62 http://www.key-to-metals.com

63 http://www.magnesium-elektron.com

64 F. Kaiser, J. Bohlen, D. Letzig, K. U. Kainer, A. Styczynski, C. Hartig, Correlation of microstructure and mechanical properties of rolled magnesium sheet AZ31, Proceeding of the 6th international conference on magnesium alloys and their applications, ed. K. U. Kainer, Wiley-VCH, Weinheim, Germany, 2004, p. 456-462.

65 P. Bakke, K. Pettersen, and H. westengen, Enhanced ductility and strength through RE addition to magnesium die casting alloys, Magnesium Technology 2003, The Minerals, Metals & Materials (TMS), ed. H. I. Kaplan, 2003, p. 171-176.

66 A. L. Bowles, Moderate temperature ageing of high pressure die cast Mg-Al alloys, PhD-Thesis, University of Queensland Australia, 2002.

67 A. Kielbus, M. Sozanska, L. Cizek, Microstructural charcterisation of AZ91 magnesium alloy, Proceeding of the 6th international conference on magnesium alloys and their applications, ed. K. U. Kainer, Wiley-VCH, Weinheim, Germany, 2004, p. 190-195.

68 N. S. Kurnakow, N. J. Stepanow, Über die Legierungen des Magnesiums mit Zinn und Blei, Zeitschrrift anorganische Chemie Band, 46, p. 177-192, 1905, in German.

69 G. Grube, Über die Legierungen des Magnesiums mit Zinn und Thallium Zeitschrift anorganischen allgemein Chemie, 46, 1905, p. 76-84, in German.

70 W. Hume-Rothery, Research on the nature, properties and conditions of formations of intermetallic compounds, with special reference to certain compounds of Tin I.-V., Annual general meeting, London, UK, 1926, p. 295-361.

71 G. V. Raynor, The constitution of the magnesium-rich alloys in the systems magnesium-lead, magnesium-tin, magnesium-germanium, and magnesium-silicon, Journal of Institute of Metals, 6, 1940, p. 403-426.

72 M. Hansen and K. Anderko, Constitution of binary alloys, Mg-Sn Magnesium-Tin, McGraw-Hill book, New York, USA, 1958, p. 918-919.

73 A. Steiner, E. Miller, and K. L. Komarek, Magnesium-tin phase diagram and thermodynamic properties of liquid magnesium-tin alloys, Transactions of the Metallurgical Society of American Institute of Mining and Materials Engineers (TMS-AIME), Vol. 230, 1964, p. 1361.

74 A. K. Nayak, W. Oelsen, Thermal analysis of magnesium-tin alloys by calorimetric measurement for the determination of the solidus and liqudus curves (part 1), Transactions of the Indian Institute of Metals, 21, 1968, p. 15-20.

75 A. K. Nayak, W. Oelsen, Quantitative thermal analysis of magnesium-tin alloys by calorimetric measurement for the determination of the solidus and liqudus curves, Transactions of the Indian Institute of Metals, 21, 1969, 53-58.

76 J. Ellmer, K. E. Hall, R. W. Kamphefner, J. T. Pfeifer, V. Stamboni, and C. D. Grahm, On the liquidus in Tin-rich Sn-Mg alloys, Metallurgical Transactions, Vol. 4, 1973, p. 889-891.

77 Phase diagrams of binary magnesium alloys, eds. A. A. Nayeb-Hashemi, J. B. Clark, ASM International, Metals Park, USA, Ohio, 1998.

78 Fries SG, Lukas HL. J Chem Phys 1993;90:181-187.

79 A. Kozlov, M. Ohno, R. Arroyave, Z. K. Liu and R. Schmid-Fetzer, Phase equilibria and Thermodynamics of the Mg-Sn-Ca system, Part 1: Thermodynamic modeling of ternary Mg-Sn-Ca equilibria, Intermetallics Volume 16, 2008, p. 299-315.

80 W. Bulian, E. Fahrenhorst, Über die Löslichkeit von Kalzium in Magnesium Metall, Laboratorium der Wintershall A.G, Werk Heringen 11, Herringen, Germany, 1945, in German.

81 H. Voßkühler, Reine und angewandte Metallkunde, 29, 1937, p. 236-237, in German.

82 W. Klemm, F. Dinkelacker, Über das Verhalten des Magnesiums zu Calcium, Strontium and Barium, Zeitschrift Anorganische Allgemeine Chemie, 255, 1947, p. 2-12, in German.

83 W. Klemm, D. Kunze, The alkali metals, 1967, p. 3-23, in German.

84 M. Hansen and K. Anderko, constitution of binary alloys, Ca-Mg Calcium-Magnesium, McGraw-Hill book, New York, USA, 1958, p. 401-402.

85 Agarwal R, Lee JJ, Lukas H-L, Sommer F. Z Metallkd 1995;86:103e8.

86 Zhong Y, Ozturk K, Sofo JO, Liu ZK. J Alloys Compd 2006;420: 98e106.

87 Y.C. Lee, A.K. Dahle, D. H. StJohn, Grain refinement of magnesium, Magnesium Technology 2000, The Minerals, Metals & Materials (TMS) eds. H. Kaplan, J. Hryn, B. Clow, Nashville, Tennesse, USA, 2000, p. 211-218.

88 Ohno M, Kozlov A, Arroyave R, Liu ZK, Schmid-Fetzer R. Acta Mater,

89 J. Gröbner, A. Kozlov, M. Hampl, R. Schmid-Fetzer, Phase formation in Mg-Sn alloys modified by Ca and Ce, Magnesium 2006, Proceeding of the 7th international conference on magnesium alloys and their applications, ed. K.U. Kainer, Wiley-VCH, Weinheim, Germany, 2006, p. 32-36.

90 A. Kozlov, M. Ohno, T. Abu Leil, N. Hort, K. U. Kainer and R. Schmid-Fetzer, Phase equilibria and Thermodynamics of the Mg-Sn-Ca system, Part 2: Experimental Investigation of ternary Mg-Sn-Ca phase equilibria and solidification microstructure, Intermetallics, volume 16, 2008, p. 316-321.

91 K. Pettersen, P. Bakke, and D. Albright, Magnesium die casting alloy design, Magnesium Technology 2002, The Minerals, Metals & Materials (TMS), ed. H.I. Kaplan, Seattle, Washington, USA, 2002, p. 171-176.

92 M. O. Pekguleryuz, P. Labelle, D. Argo, M. Dierks, T. Sparks, T. Waltematte, Creep resistant magnesium alloys for power-train applications, Annual world magnesium conference, IMA 2001, 2001, p. 27-33.

93 G. Pettersen, H. Westengen, R. Hoier and O. Lohne, Microstructure of a pressure die cast magnesium-4wt.-% aluminum alloy modified with rare earth additions, Materials Science and Engineering, A207, 1996, p. 115-120.

94 V. V. Agalakov, Development of the new creep resistant alloy AS31, Proceeding of the 6th international conference on magnesium alloys and their applications, ed. K. U. Kainer, Wiley-VCH, Weinheim, Germany, 2004, p. 18-24.

95 G. Frommeyer, S. Beer, K. Von Oldenburg, Microstructure and mechanical properties of Mg_2Si-Al, Zeitschrift Metallkunde, 85, Carl Hanser Verlag, München, Germany,1994, p. 372-377.

96 G. Foerster, Improved magnesium die casting alloys, Proceeding of the 8th SDCE international die casting exposition and congress, 1975, Paper no. G-T75-112.

97 G.S. Foerster. Proc. 7th SDCE International Die Casting Congress (1972), paper no. 9372.

98 J. F. King, Development of practical high temperature magnesium casting alloys, Proceeding of the 5th international conference on magnesium alloys and their applications, ed. K. U. Kainer, Wiley-VCH, Weinheim, Germany, 2000, pp.14-22.

99 B. P. Powell, V. Rezhets, M. P. Balogh, and R. A. Waldo, The relationship between microstructure and creep behavior in AE42 magnesium die casting alloy, Magnesium Technology 2001, The Minerals, Metals & Materials (TMS), New Orleans, Louisiana, USA, 2001, p. 175-181.

100 B. R. Powell, V. Rezhets, M. P. Balogh, R. A. Waldo, Microstructure and creep behaviour in AE42 magnesium die-casting alloy, Journal of the Minerals, metals and materials society (JOM), 2002, p. 34-38.

101 K. E. Nelson, Magnesium die casting alloys, presented on the 6th SDCE International die casting congress, Cleveland, Ohio, 1970, paper no. 13.

102 J. Aragones, K. Goundan, S. Kolp, R. Osborne, L. Ouimet and W. Pinch, Development of the 2006 corvette Z06 structural cast magnesium cross-member, SAE technical paper 2005-01-0340, 2005.

103 http://www.azom.com

104 R.T. Wood, Magnesium-tin-zinc alloys, American Magnesium Corporation, USA patent no. 1,831,987, 1931.

105 R.T. Wood and H.R. Block, Great Britain patent no. 380669, 1932.

106 A. J. Murphy, Imrovements in magnesium base alloys and the production thereof, Great Britain patent GB 451,229, 1936.

107 J. A. Gann and F. L. Reynolds, Improved magnesium based alloys, American Magnesium Corp., Great Britain patent no. 394551, 1933.

108 R.M. Bradbury, A new magnesium base alloy, Great Britain patent GB 596,102, 1947.

109 T. Horie, H. Iwabori, Y. Awano, T. Takeuchi, H. Iba, A. Matsui, Japanese patent 07,003,374 A, 1993.

110 T. Horie, Toyoda Central research and development laboratory, Japan, patent JP7, 018,363, 1995.

111 A. Aikawa, K. Taketani, US patent 1994.

112 K. Nakamura, T. Hirane, T. Ushida, T. Abe, High strength Mg based alloy and its uses, European patent application, EP 1,108,799 A2, 2001.

113 P. Bakke, K. Pettersen, H. Westengen, The influence of Sb, Si, and Sn on the mechanical properties of Mg-Al alloys, Magnesium Technology 2004, The Minerals, Metals & Materials (TMS), ed. A. Luo, 2004, Charlotte, North Carolina, USA, 2004, p. 289-296.

114 A. L. Bowles, C. Blawert, N. Hort, K. U. Kainer, Microstructural investigations of the Mg-Sn and Mg-Sn-Al alloy systems, Magnesium Technology 2004, ed. A. Luo, Charlotte, North Carolina, U.S.A, 2004, p. 307-310.

115 A. L. Bowles, H. Dieringa, C. Blawert, N. Hort, K. U. Kainer, Investigations in the Magnesium-Tin system, Materials Science Forum 488-489, 2004, p. 135-138.

116 O. Anopuo, Y. D Huang, C. Blawert, N. Hort, K.U. Kainer, Microstructure and thermal response of Mg-Sn alloys, Magnesium Technology 2006, The Minerals, Metals & Materials (TMS), eds. A. Luo, N. R. Neelameggham, R. S. Beals, San Antonio, Texas, USA, 2006, p. 529-534.

117 D. H. Kang, S S. S. Park, N. J. Kim, Development of creep resistant die cast Mg-Sn-Al-Si alloy, Materials Science and Engineering A 413-414, 2005, p. 555-560.

118 D. H. Kang, S.S. Park, Y. S. Oh, N. J. Kim, Effect of nano-particles on the creep resistance of Mg-Sn based alloys, Materials Science and Engineering A 449-451, 2007, p. 318-321.

119 T.T. Sasaki, K. Oh-ishi, T. Ohkubo and K. Hono, Enhanced age hardening response by the addition of Zn in Mg-Sn alloys, Scripta Materialia, Vol. 55, 2006, p. 251-254.

120 C. L. mendis, C. J. Bettles, M. A. Gibson, C. R. Hutchinson, An enhanced age hardening response in Mg-Sn based alloys containing Zn, Materials Science and Engineering A 435-436, 2006, p. 163-171.

121 H. Liu, Y. Chen, Y. Tang, S. Wei, G. Niu, The microstructure, tensile properties, and creep behavior of as-cast Mg-(1-10)%Sn alloys, Journal of Alloys and Compounds 440, 2007, p. 122-126.

122 H. Liu, Y. Chen, Y. Tang, D. Huang, G. Niu, The microstructure and mechanical properties of permanent-mould cast Mg-5%Sn-(0-2.6)%Di alloys, Materials Science and Engineering A 437, 2006, p. 348-355.

123 H. Liu, Y. Chen, Y. Tang, S. Wei, G. Niu, Tensile and indentation creep behavior of Mg-5%Sn and Mg-5%Sn-2%Di alloys, Materials Science and Engineering A 464, 2007, p. 124-128.

124 S. Wei, Y. Chen, Y. Tang, X. Zhang, M. Liu, S. Xiao, Y. Zhou, Compressive creep behaviour of Mg-Sn-La alloys, Materials Science and Engineering A 508, 2009, p. 59-63.

125 H. K. Lim, S. W. Sohn, D. H. Kim, J. Y. Lee, W. T. Kim, D. H. Kim, Effect of addition of Sn on the microstructure and mechanical properties of Mg-MM (misch-metal) alloys, Journal of alloys and compounds, 2007.

126 A. Katsman, S. Cohen, G. Goren-Muginstein and M. Bamberger, Phase formation, precipitation and strengthening mechanisms in Mg-Zn-Sn based alloys, Magnesium Technology 2004, The Minerals, Metals & Materials (TMS), ed. A. A. Luo, Charlotte, NC, USA, 2004, p. 297-300.

127 S. Cohen, G. Goren-Muginstein, S. Avraham, G. Dehm, and M. Bamberger, Phase formation, precipitation and stresnthning mechanisim Mg-Zn-Sn and Mg-Zn-Sn-Ca alloys, Magnesium Technology 2004, The Minerals, Metals & Materials (TMS), ed. A. A. Luo, Charlotte, NC, USA, 2004, p. 301-305.

128 S. Harosh, L. Miller, G. Levi, M. Bamberger, Microstructure and properties of Mg-5.6Sn-4.4%Zn-2.1%Al alloy, Journal of Materials Science, 2007, pp. 9983-9989.

129 C. Jihua, C. Zhenhua, Y. Hongge, Z. Fuquan, L. Kun, Effect of Sn addition on microstructure and mechanical properties of Mg-Zn-Al alloys, Journal of alloys and compounds, 2007.

130 C. Jihua, C. Zhenhua, Y. Hongge, Z. Fuquan, Microstructure characterization and mechanical properties of Mg-6Zn-3Sn-2Al alloy, Journal of alloys and compounds, 2008.

131 N. Hort, K. P. Rao, T. Abu Leil, H. Dieringa, V. Y. R. K. Prasad, K. U. Kainer, Creep and hot working behaviour of a new magnesium alloy Mg-3Sn-2Ca, in Magnesium Technology 2008, Editors: M. Pekguleryuz, N. Neelameggham, R. Beals, E. Nyberg, TMS 2008, New Orleans, Louisiana, USA, p. 401-406.

132 Y. Huang, T. Abu Leil, N. Hort, K. U. Kainer and Yilin Liu, Effect of microstructural inhomogeneity on creep response of Mg-Sn alloys, Key Engineering Materials Vols. 345-346, pp. 561-564.

133 T. Abu Leil, K.P. Rao, N. Hort, H. Dieringa, C. Blawert, Y. Huang, K.U. Kainer, Development and characterization of a series of Mg-Sn-Ca alloys, in Magnesium Technology in global age, Editors, M.O. Pekgueryuz and L.W. Mackenzie, CIM 2006, Montreal, Canada, p. 739-749.

134 J. Buršík, V. Buršíková, Y. Jirásková, T. Abu Leil, C. Blawert, W. Dietzel, N. Hort, K. U. Kainer, Microstructure and Micromechanical Properties of as-cast Mg-Sn-Ca and Mg-Sn-Mn Alloys, Magnesium, Dresden, Germany, p. 37-42.

135 J. Buršík, K. Zábranský, Y. Jirásková, V. Buršíková, T. Abu Leil, C. Blawert, Y. Huang, W. Dietzel, N. Hort, K. U. Kainer and K. P. Rao, Effect of Heat Treatment on the Microstructure, Microhardness and Corrosion Behavior of Cast Mg-3Sn-2Ca Alloy, Magnesium 2006, Dresden, Germany, p. 49-54.

136 T. Abu Leil, K. P. Rao, N. Hort, C. Blawert and K.U. Kainer, Corrosion behaviour and microstructure of a broad range of Mg-Sn-X alloys, Magnesium Technology 2006, The Minerals, Metals & Materials (TMS), eds. A. Luo, N. R. Neelameggham, R. S. Beals, San Antonio, Texas, USA, 2006, p. 281-286.

137 T. Abu Leil, Y. Huang, H. Dieringa, N. Hort, K.U. Kainer, J. Buršík, Y. Jirásková and K.P. Rao, Effect of heat treatment on the microstructure and creep behavior of Mg-Sn-Ca alloys, Materials Science Forum Vols. 546-549, pp. 69-72.

138 Do Hyung Kim, Hyun Kyu Lim, Ju Youn Lee, Won Tae Kim, Microstructural evolution and creep resistance in Mg-Sn-Ca alloy, in Magnesium Technology 2008, Editors: M. Pekguleryuz, N. Neelameggham, R. Beals, E. Nyberg, TMS 2008, New Orleans, Louisiana, USA, p. 401-406.

139 M. Yang, F. Pan, L. Cheng, J. Shen, Effects of cerium on as-cast microstructure and mechanical properties of Mg–3Sn–2Ca magnesium alloy, Volume 512, Issues 1-2, 25, 2009, p. 132-138.

140 M. Yang, F. Pan, Effects of Y addition on As-cast microstructure and mechanical properties of Mg-3Sn-2Ca (wt.%) magnesium alloy, Volume 512, Issues 1-2, 25, 2009, p. 132-138.

141 A. Froats, T. Kr. Aune, D. Hawke, W. Unsworth, and J. Hillis, Corrosion of magnesium and magnesium alloys, ASM Handbook, ed. J. R. Davis, J. D. Destefani, Vol. 13, 4th edition, ASM International, Materials Park, OH, USA, 1992.

142 L. Whitby, Magnesium and its alloys, Corrosion of metals and alloys, 2nd edition, New York, USA, 1965.

143 M. G: Fontana, N. D. Greene, Corrosion engineering.

144 L.L. Shreier, R.A. Jarman, G.T. Burstein; Corrosion 1, Metal/Environment Reactions 3rd edition.

145 G. Song, A. Atrens: Understanding magnesium corrosion, Advanced Engineering Materials, Vol. 5, No. 1, 2003, p. 837-858.

146 H. H. Uhlig, R.W. Revie, Corrosion and corrosion control. An introduction to corrosion science and engineering 3rd edition, Wiley, NY, USA, 1985.

147 J. D. Hanawalt, C. E. Nelson, J. A. Peloubet, Corrosion studies of magnesium and its alloys, Transactions American Institute of Mining and Materials Engineers “Trans. AIME”, 1942, p. 273-299.

148 K. Pettersen, P. Bakke, D. Albright, Magnesium die casting alloy design, Transactions of the metallurgical society of American Institute of Mining and Materials Engineers (TMS-AIME), eds. H. I. Kaplan, 2002, p. 171-176.

149 O. Lunder, J.E. Lein, T.Kr. Aune, and K. Nisancioglu, The role of $Mg_{17}Al_{12}$ phase in the corrosion of Mg alloy AZ91, Corrosion, Volum 45, No. 9, 1989, p. 741-748.

150 P. Kurze, Corrosion and corrosion protection of magnesium, Proceeding of the 6th international conference on magnesium alloys and their applications, eds. B. L. Mordike, K.U. Kainer, Wiley-VHC, Weinheim, Germany, 2003.

151 Corrosion, Volume 2, Metal/Environment Reactions, eds. L.L. Sheir, R. A. Jarman, G. T. Burstein,

152 E. Ghali, in Uhlig’s Corrosion Handbook, ed. R. W. Revie, Wiley, Chichester, UK, 2000, p. 793.

153 G. Song, A. L. Bowles, D. H. StJohn, Corrosion resistance of aged die cast magnesium alloy AZ91D, Materials Science Engineering A366, 2004, p. 74-86.

154 S. G. Song, J. S. Vetrano, S. M. Bruemmer, Pinning effect of solute atoms on grain boundary dislocation dissociation, Materials Science and Engineering A232, 1997, p. 23-30.

155 G. Song, A. Atrens, Corrosion mechanisms of magnesium alloys, Advanced Engineering Materials, Materials, 1, 1999, p. 11-33.

156 W. K. Miller, Creep of die cast AZ91 magnesium at room temperature and low stress, Advanced in magnesium alloys and composites, eds. H. G. Paris, W. H. Hunt, 1988, p. 41-55.

157 J. Roesler, H. Harders, M. Baeker, Mechanical behaviour of engineering materials, metals, ceramics, Springer, NY, 2007.

158 H.J. Frost und M. F. Ashaby, Deformation-Mechanism Maps, Pergamon Press Oxford, 1982, p. 43.

159 K.U. Kainer, F. Von Buch, The current state of technology and potential for development of magnesium applications, Proceeding of the 6th international conference on magnesium alloys and their applications, eds. B. L. Mordike, K.U. Kainer, Wiley-VHC, Weinheim, Germany, 2003, p.1.

160 F. Höllrigl-Rosta, E. Just, J. Köhler, H.J. Melzer, Light metals age, 37t Annual World Magnesium Conference, 38, Dayton, OH, USA, 1980, p. 22-29.

161 http://www. Hydromagnesium.com

162 V. Kree, J, Bohlen, D. Letzig, K.U. Kainer, practical metallography, 2004, 41 (5), p. 233.

163 R. Schmid-Fetzer, J. Groebner, Focussed development of magnesium alloys using the calphad approach, Advanced Engineering Materials, volume 3, 2001, p. 947.

164 ASTM G5-82 standard reference test methods for making potentiostatic and potentiodynamic anodic polarization measurements, West Conshohocken, PA, ASTM international, 2003.

165 D. M. Seeger, C. Blawert, W. Dietzel, Y. Bohne, S. Mändl, B. Rauschenbach, Comparision of as-cast and plasma deposited commercial magnesium alloys, Magnesium Technology 2005, The Minerals, Metals & Materials (TMS), eds. N. R. Neelameggham, H. I. Kaplan, B. R. Powell, San Francisco, California, USA, 2005, p. 323-328.

166 ASTM B117-07a G85 standard practice for operating salt spray (fog) apparatus, West Conshohocken, PA, ASTM international, 2003.

167 DIN 50106, 1991.

168 DIN 50125, 1991.

169 ASTM E92-82(2003) e2, Standard test methods for Vickers hardness of metallic materials, ASTM international, West Conshohocken, PA, ASTM international, 2003.

170 H. Dieringa, Vergleichende Untersuchungen zum Zug- und Druckkriechverhalten der verstärkten und unverstärkten Magnesiumlegierung AE42, PhD-Thesis, Hamburg University of Technology, Hamburg, Germany, 2006, in German.

8 Appendix

8.1 DTA/DSC measurements and thermodynamic calculations

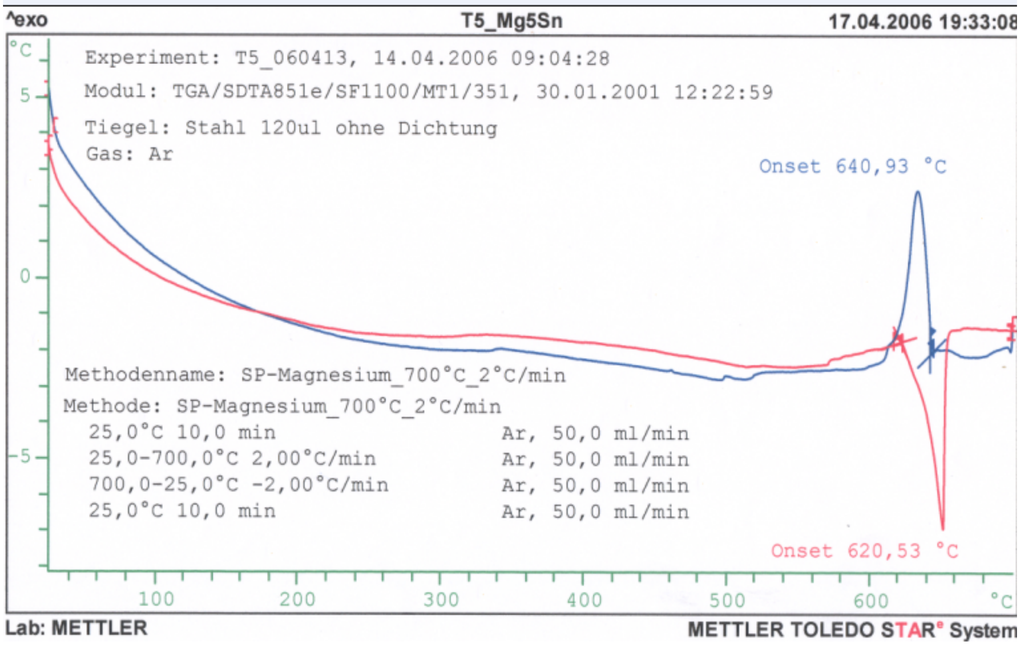

```
^exo                                T5_Mg5Sn                    17.04.2006 19:33:08
Experiment: T5_060413, 14.04.2006 09:04:28
Modul: TGA/SDTA851e/SF1100/MT1/351, 30.01.2001 12:22:59
Tiegel: Stahl 120ul ohne Dichtung
Gas: Ar
Methodenname: SP-Magnesium_700°C_2°C/min
Methode: SP-Magnesium_700°C_2°C/min
  25,0°C 10,0 min                   Ar, 50,0 ml/min
  25,0-700,0°C 2,00°C/min           Ar, 50,0 ml/min
  700,0-25,0°C -2,00°C/min          Ar, 50,0 ml/min
  25,0°C 10,0 min                   Ar, 50,0 ml/min
Lab: METTLER                                   METTLER TOLEDO STAR® System
```

Figure (81): DTA analysis of Mg-5Sn alloy using stainless crucible.

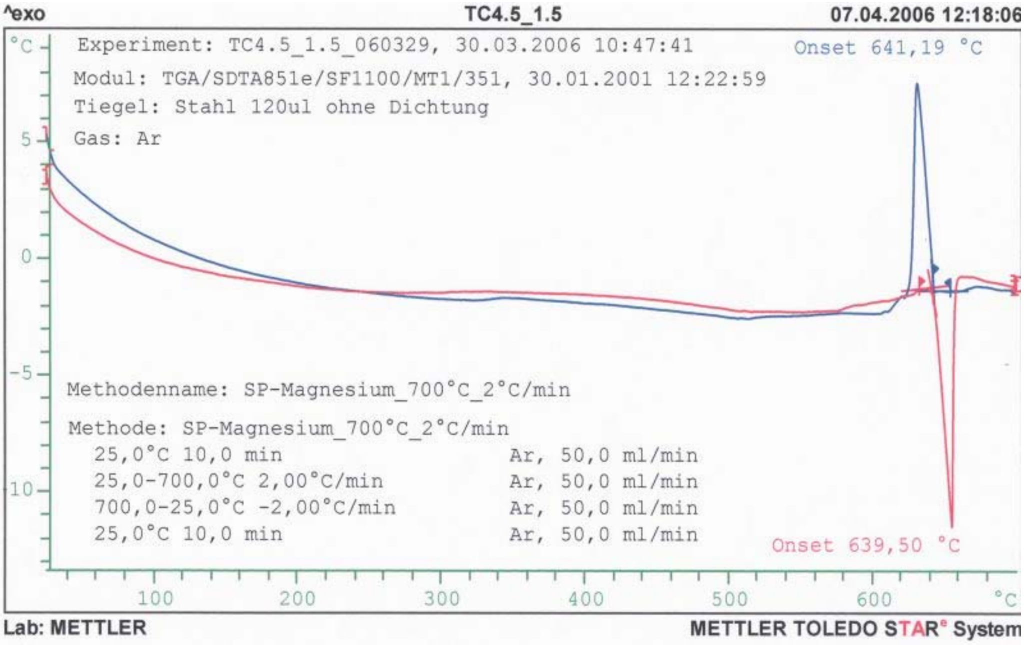

```
^exo                                TC4.5_1.5                   07.04.2006 12:18:06
Experiment: TC4.5_1.5_060329, 30.03.2006 10:47:41
Modul: TGA/SDTA851e/SF1100/MT1/351, 30.01.2001 12:22:59
Tiegel: Stahl 120ul ohne Dichtung
Gas: Ar
Methodenname: SP-Magnesium_700°C_2°C/min
Methode: SP-Magnesium_700°C_2°C/min
  25,0°C 10,0 min                   Ar, 50,0 ml/min
  25,0-700,0°C 2,00°C/min           Ar, 50,0 ml/min
  700,0-25,0°C -2,00°C/min          Ar, 50,0 ml/min
  25,0°C 10,0 min                   Ar, 50,0 ml/min
Lab: METTLER                                   METTLER TOLEDO STAR® System
```

Figure (82): DTA analysis of Mg-4.5Sn-1.5Ca alloy using stainless crucible.

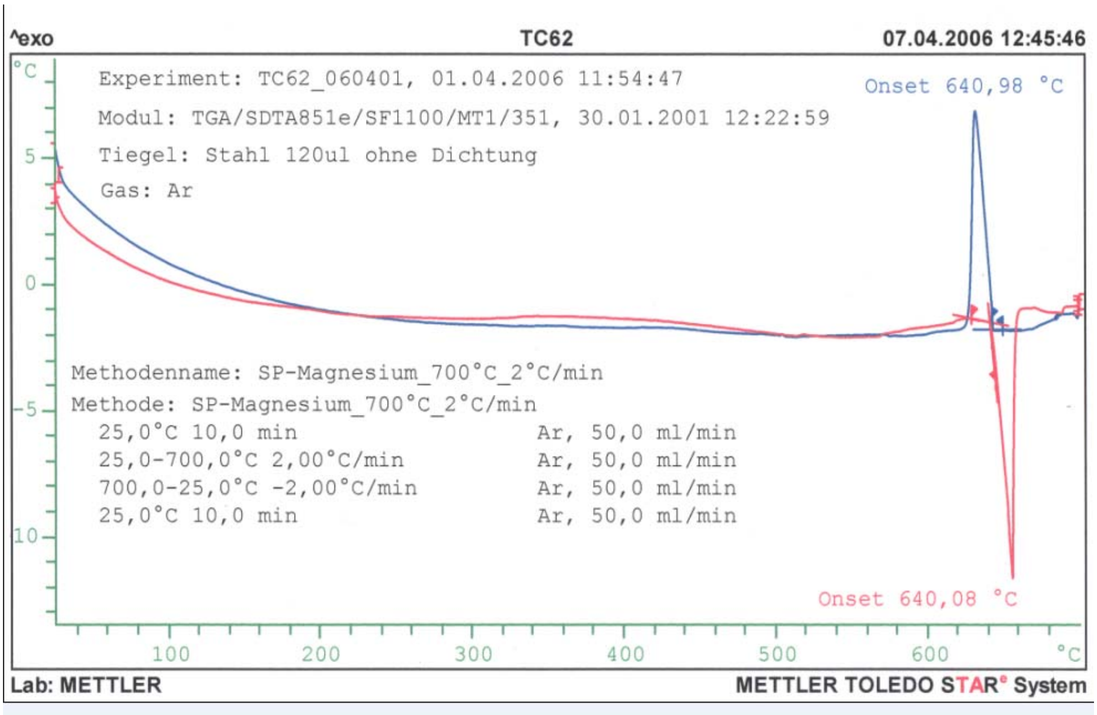

Figure (83): DTA analysis of Mg-6Sn-2Ca alloy using stainless crucible.

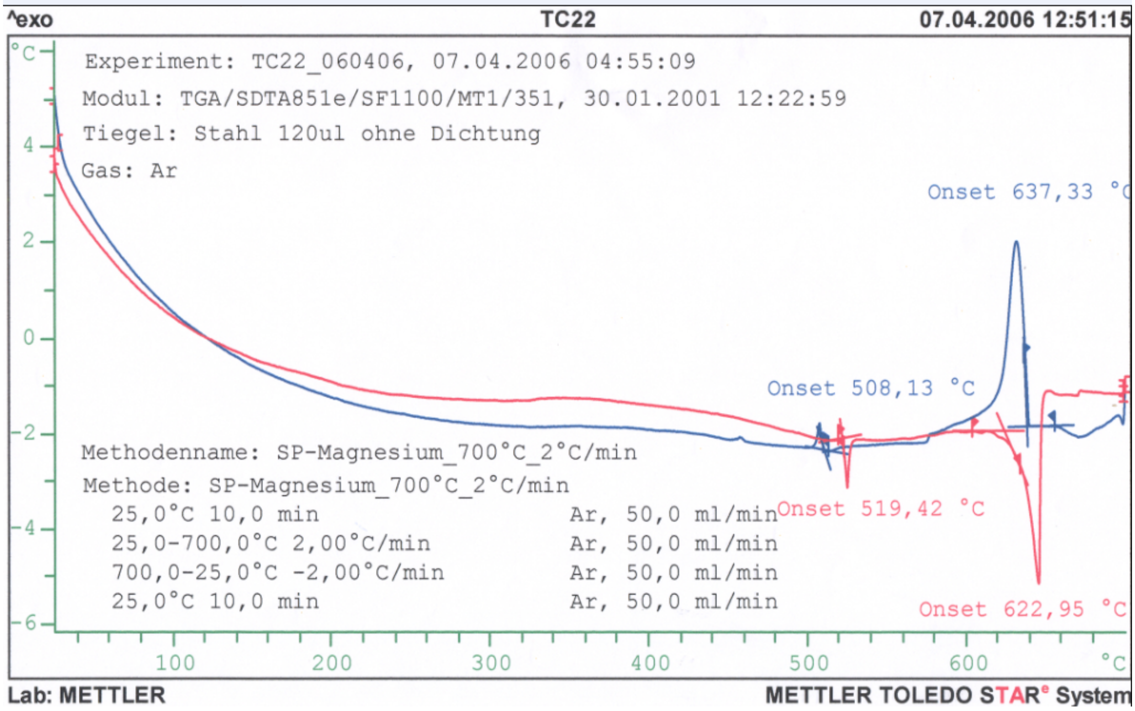

Figure (84): DTA analysis of Mg-2Sn-2Ca alloy using stainless crucible.

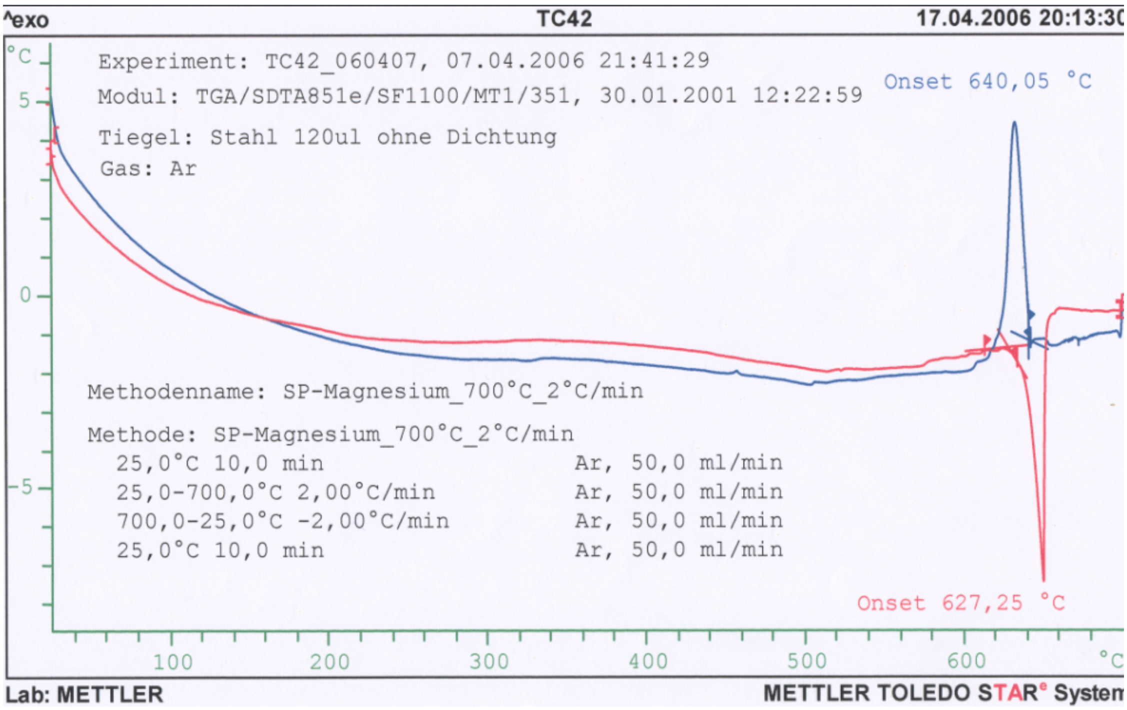

Experiment: TC42_060407, 07.04.2006 21:41:29
Modul: TGA/SDTA851e/SF1100/MT1/351, 30.01.2001 12:22:59
Tiegel: Stahl 120ul ohne Dichtung
Gas: Ar

Methodenname: SP-Magnesium_700°C_2°C/min

Methode: SP-Magnesium_700°C_2°C/min
25,0°C 10,0 min Ar, 50,0 ml/min
25,0-700,0°C 2,00°C/min Ar, 50,0 ml/min
700,0-25,0°C -2,00°C/min Ar, 50,0 ml/min
25,0°C 10,0 min Ar, 50,0 ml/min

Figure (85): DTA analysis of Mg-4Sn-2Ca alloy using stainless crucible.

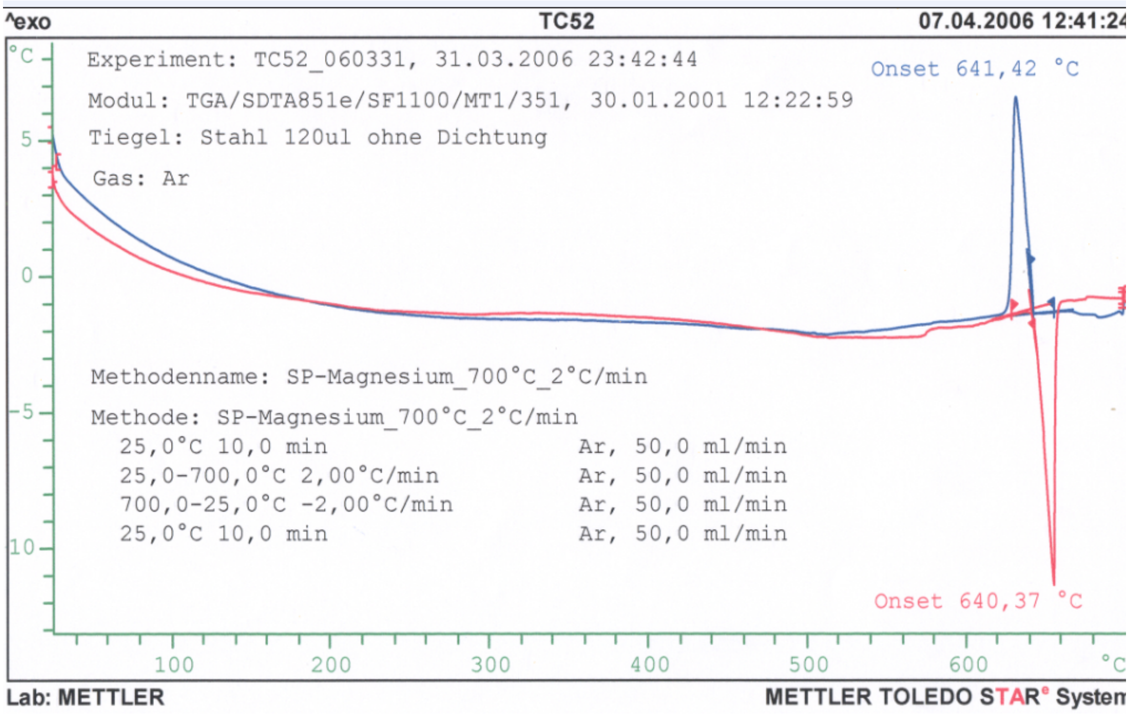

Experiment: TC52_060331, 31.03.2006 23:42:44
Modul: TGA/SDTA851e/SF1100/MT1/351, 30.01.2001 12:22:59
Tiegel: Stahl 120ul ohne Dichtung
Gas: Ar

Methodenname: SP-Magnesium_700°C_2°C/min

Methode: SP-Magnesium_700°C_2°C/min
25,0°C 10,0 min Ar, 50,0 ml/min
25,0-700,0°C 2,00°C/min Ar, 50,0 ml/min
700,0-25,0°C -2,00°C/min Ar, 50,0 ml/min
25,0°C 10,0 min Ar, 50,0 ml/min

Figure (86): DTA analysis of Mg-5Sn-2Ca alloy using stainless crucible.

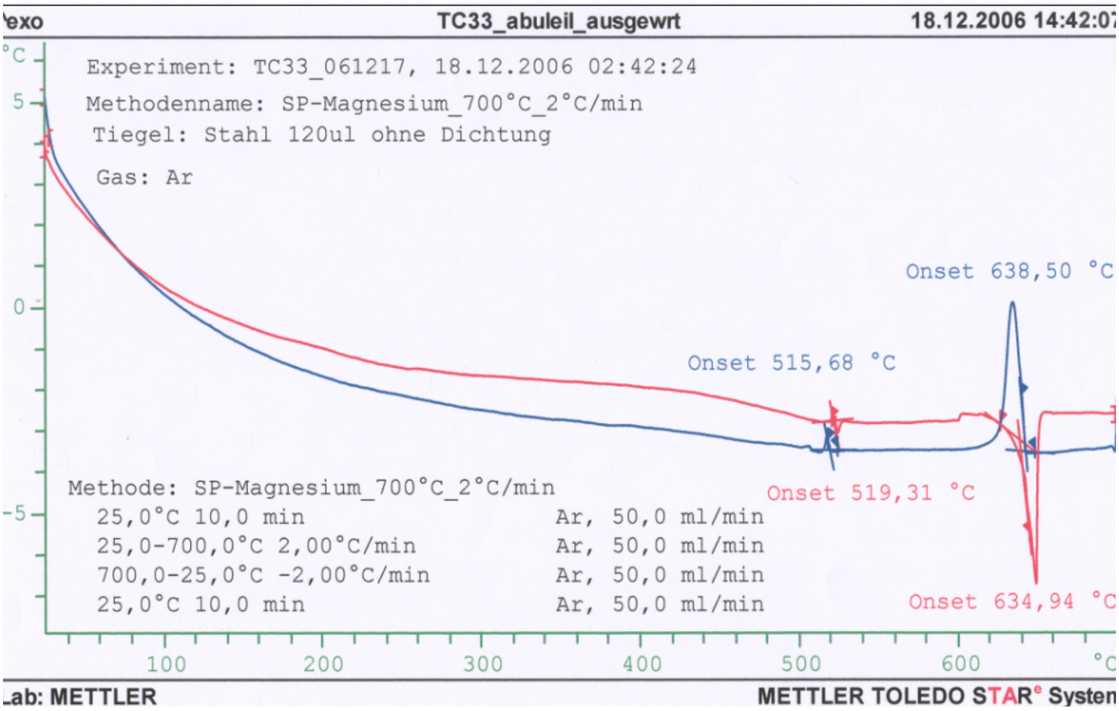

Figure (87): DTA analysis of Mg-3Sn-3Ca alloy using stainless crucible.

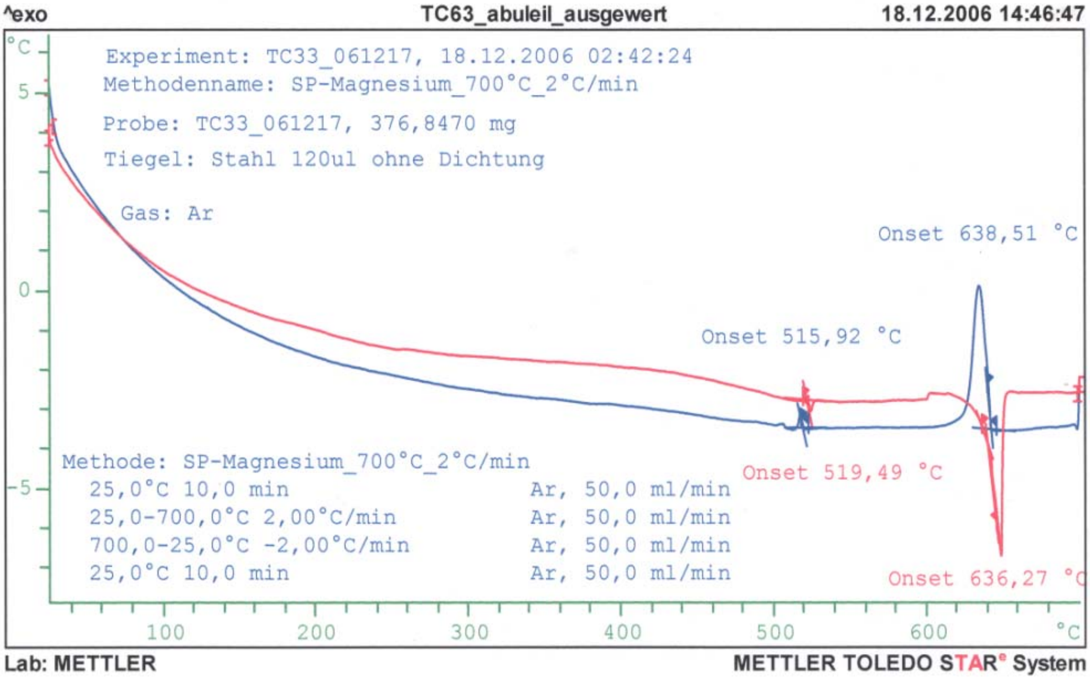

Figure (88): DTA analysis of Mg-6Sn-3Ca alloy using stainless crucible.

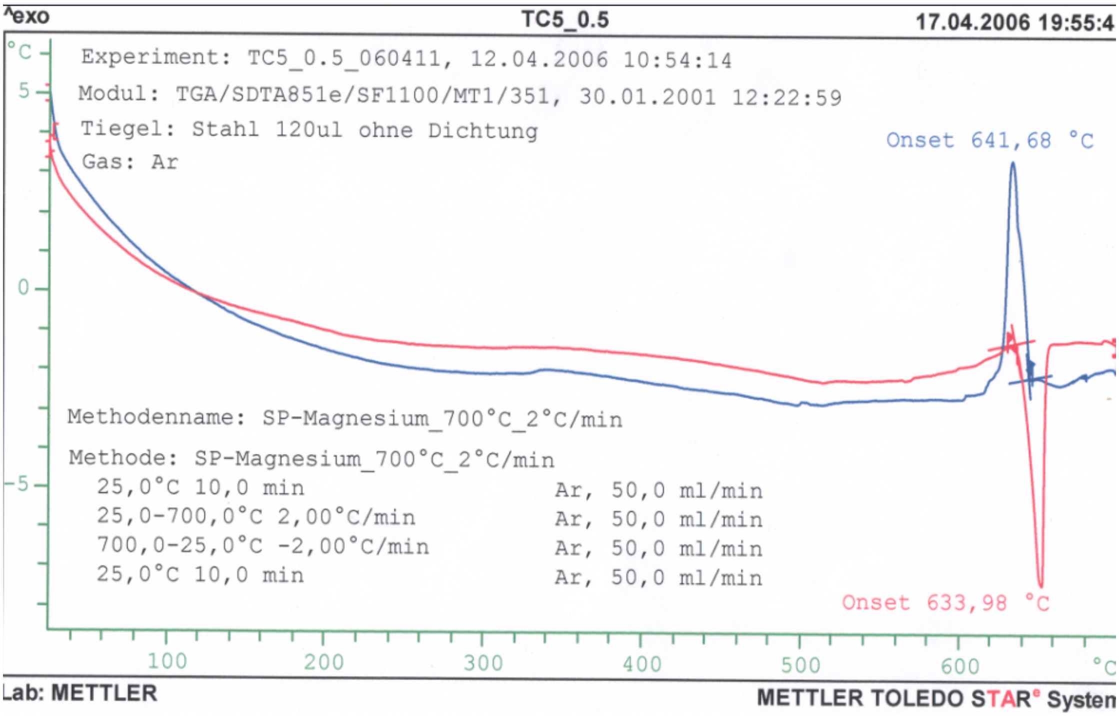

Experiment: TC5_0.5_060411, 12.04.2006 10:54:14
Modul: TGA/SDTA851e/SF1100/MT1/351, 30.01.2001 12:22:59
Tiegel: Stahl 120ul ohne Dichtung
Gas: Ar

Methodenname: SP-Magnesium_700°C_2°C/min

Methode: SP-Magnesium_700°C_2°C/min

25,0°C 10,0 min	Ar, 50,0 ml/min
25,0-700,0°C 2,00°C/min	Ar, 50,0 ml/min
700,0-25,0°C -2,00°C/min	Ar, 50,0 ml/min
25,0°C 10,0 min	Ar, 50,0 ml/min

Figure (89): DTA analysis of Mg-5Sn-0.5Ca alloy using stainless crucible.

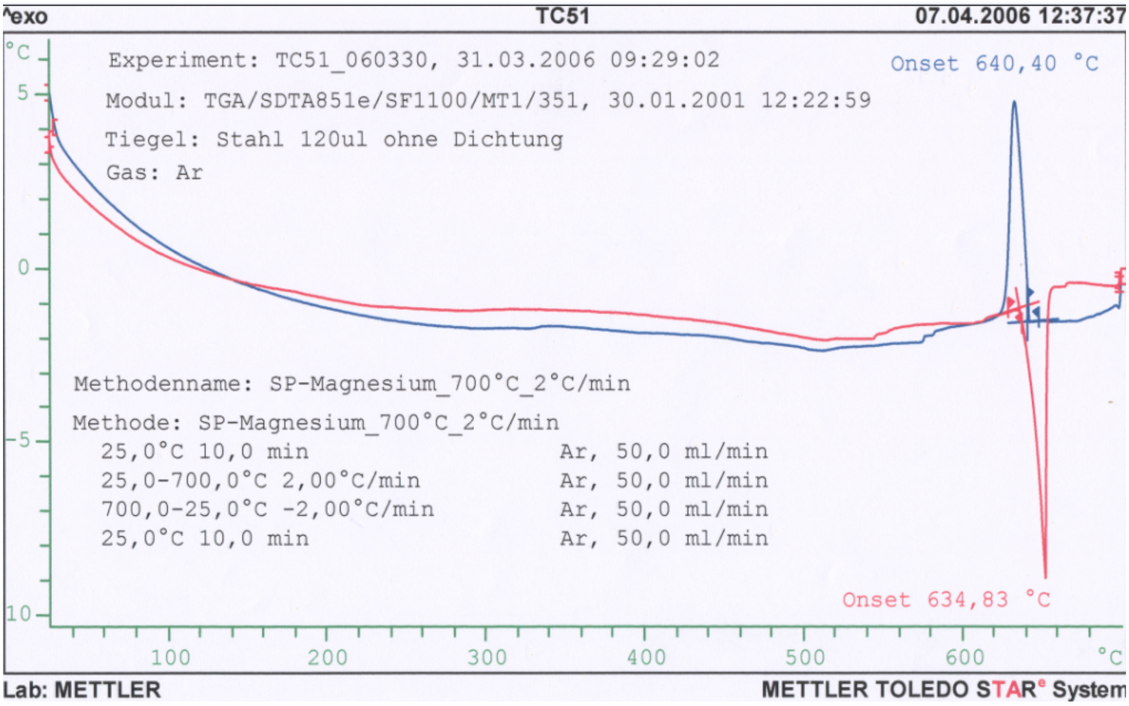

Experiment: TC51_060330, 31.03.2006 09:29:02
Modul: TGA/SDTA851e/SF1100/MT1/351, 30.01.2001 12:22:59
Tiegel: Stahl 120ul ohne Dichtung
Gas: Ar

Methodenname: SP-Magnesium_700°C_2°C/min

Methode: SP-Magnesium_700°C_2°C/min

25,0°C 10,0 min	Ar, 50,0 ml/min
25,0-700,0°C 2,00°C/min	Ar, 50,0 ml/min
700,0-25,0°C -2,00°C/min	Ar, 50,0 ml/min
25,0°C 10,0 min	Ar, 50,0 ml/min

Figure (90): DTA analysis of Mg-5Sn-1Ca alloy using stainless crucible.

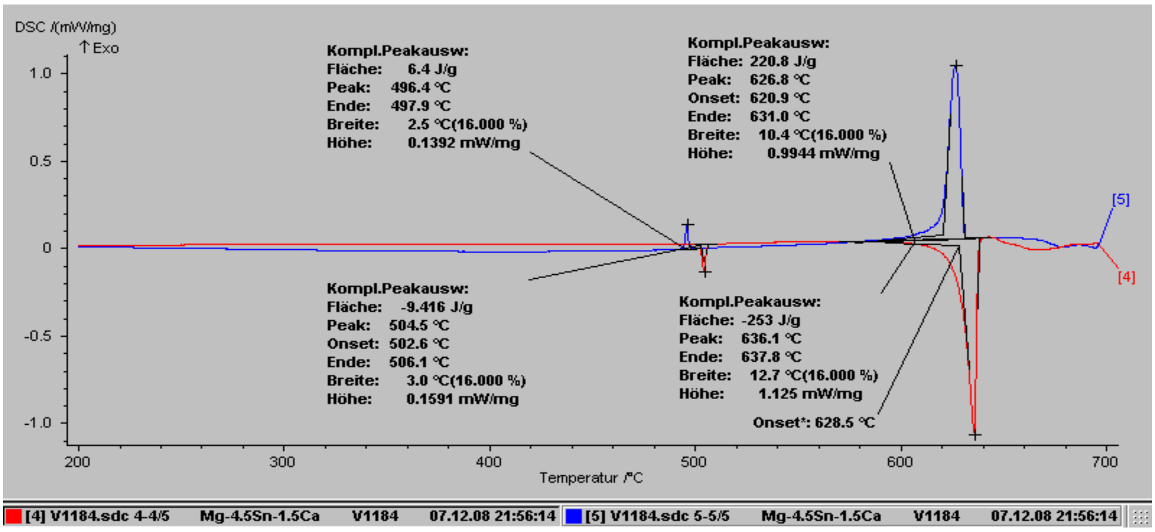

Figure (91): DSC analysis of Mg-3Sn-1Ca alloy using stainless crucible.

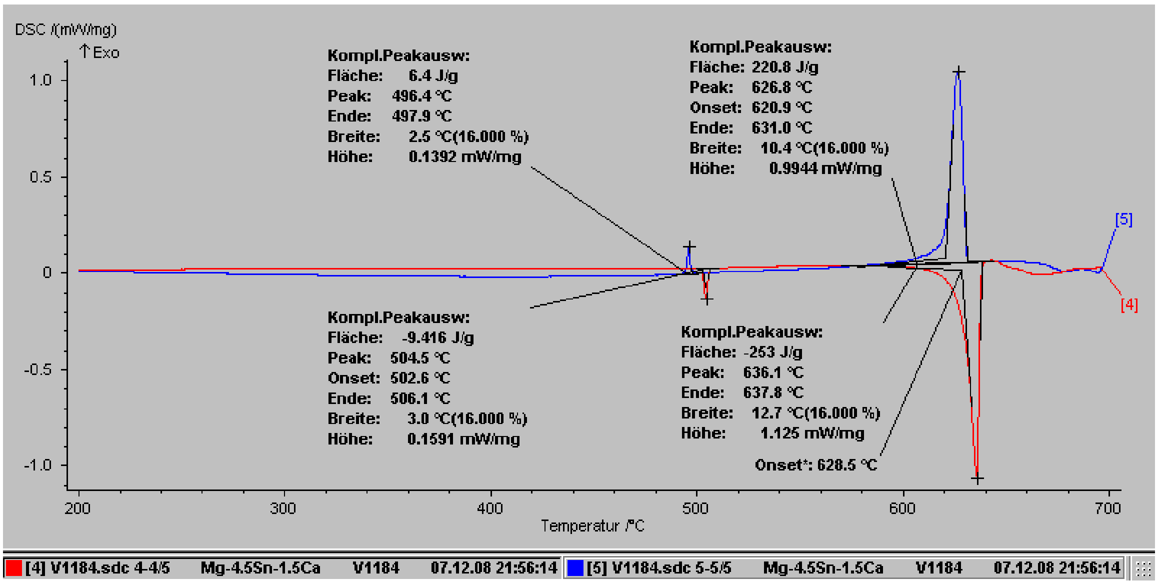

Figure (92): DSC analysis of Mg-4.5Sn-1.5Ca alloy using stainless crucible.

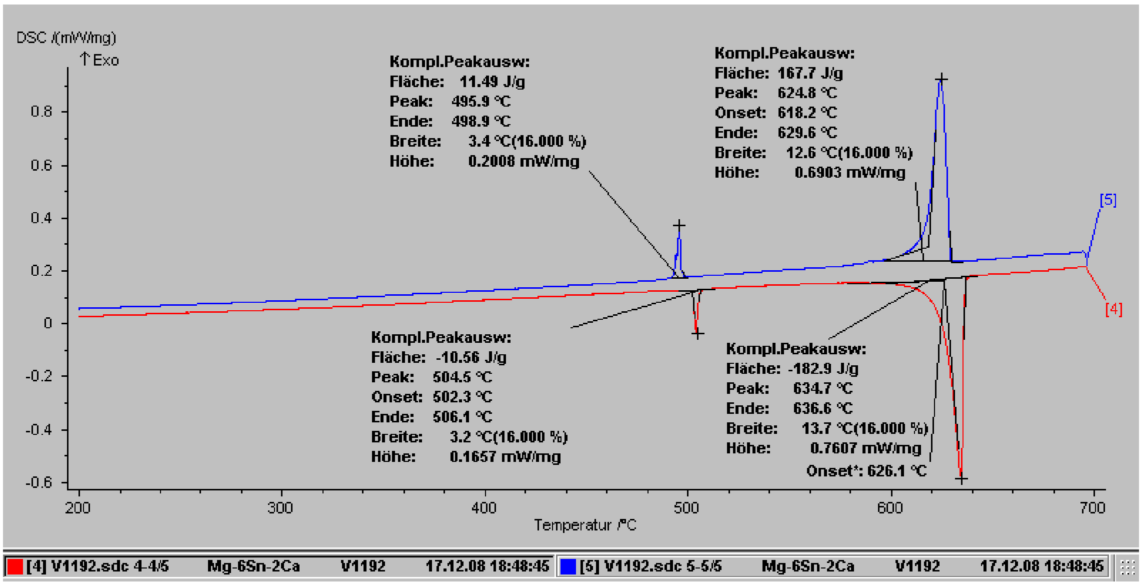

Figure (93): DSC analysis of Mg-6Sn-2Ca alloy using stainless crucible.

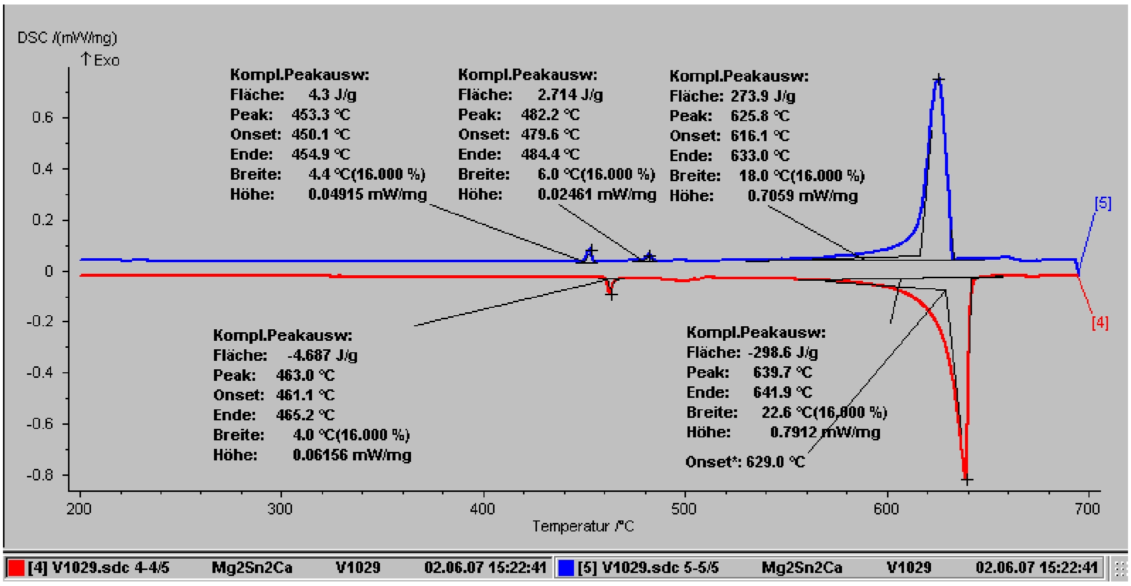

Figure (94): DSC analysis of Mg-2Sn-2Ca alloy using stainless crucible.

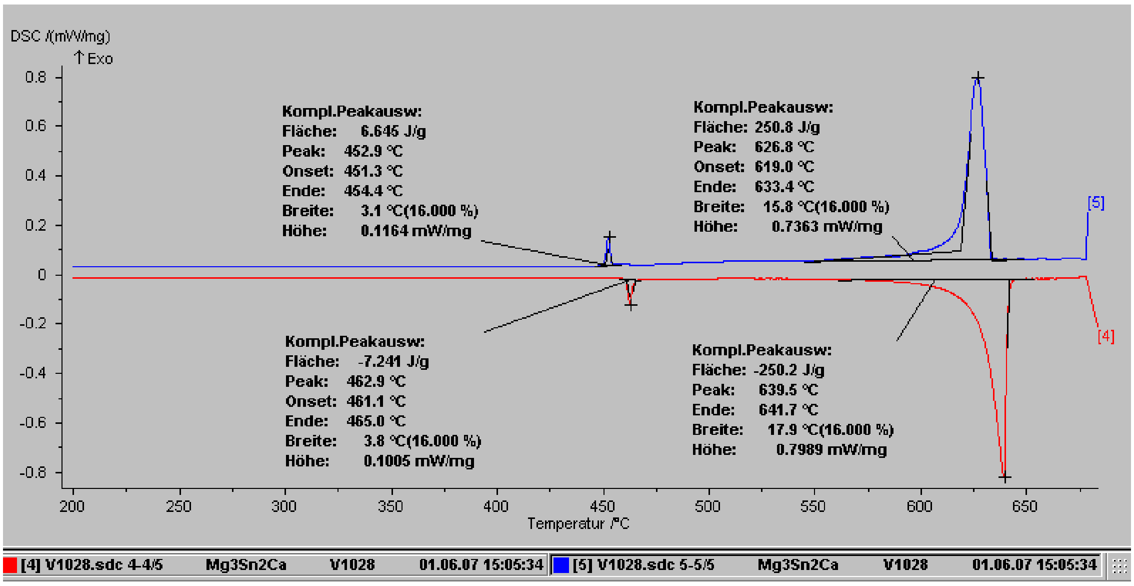

Figure (95): DSC analysis of Mg-3Sn-2Ca alloy using stainless crucible.

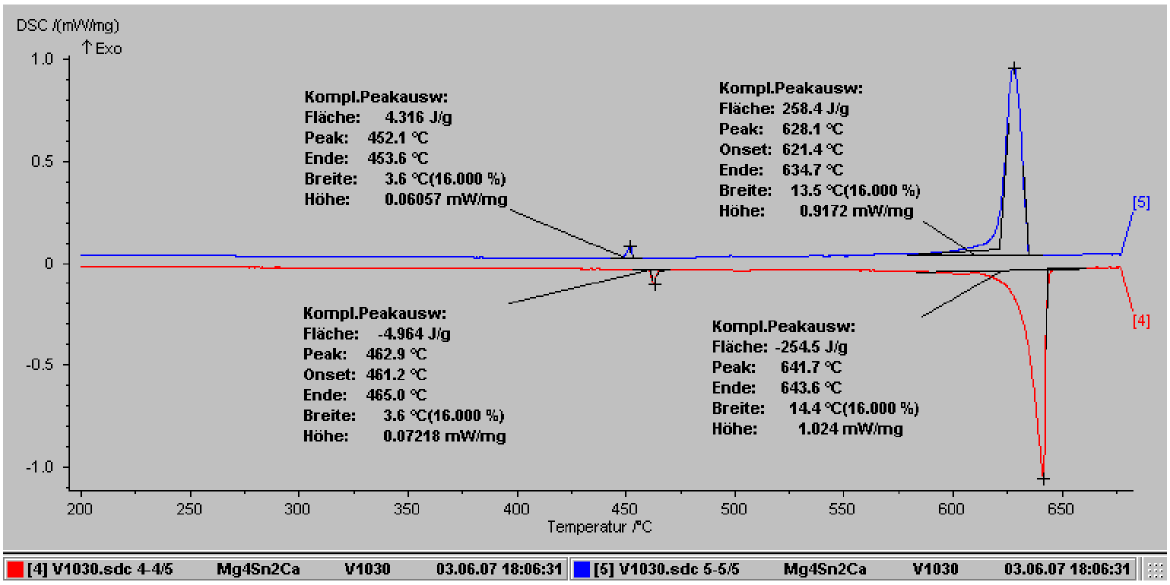

Figure (96): DSC analysis of Mg-4Sn-2Ca alloy using stainless crucible.

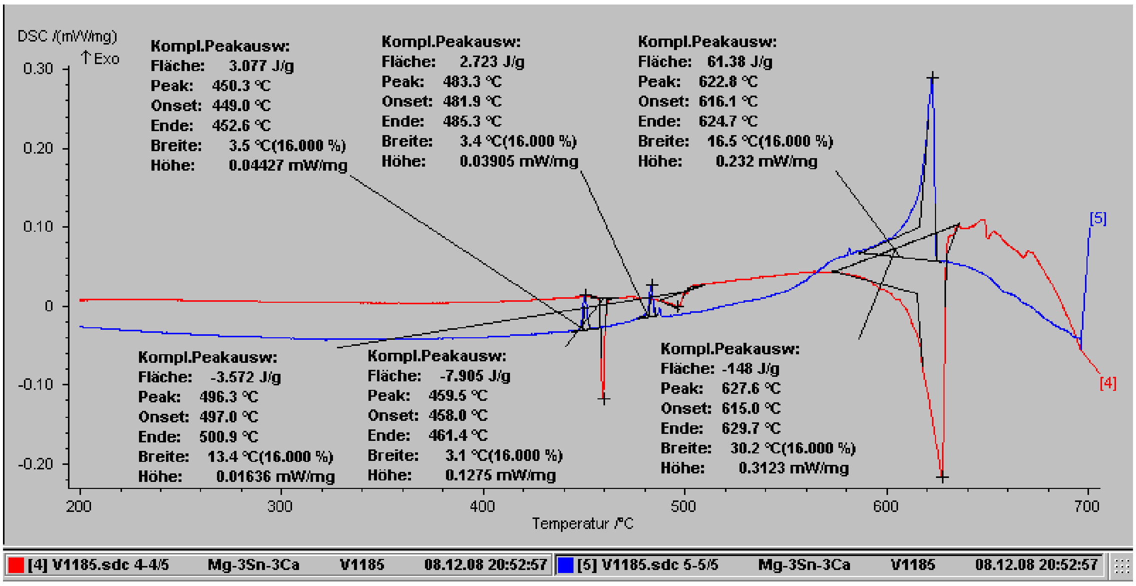

Figure (97): DSC analysis of Mg-3Sn-3Ca alloy using stainless crucible.

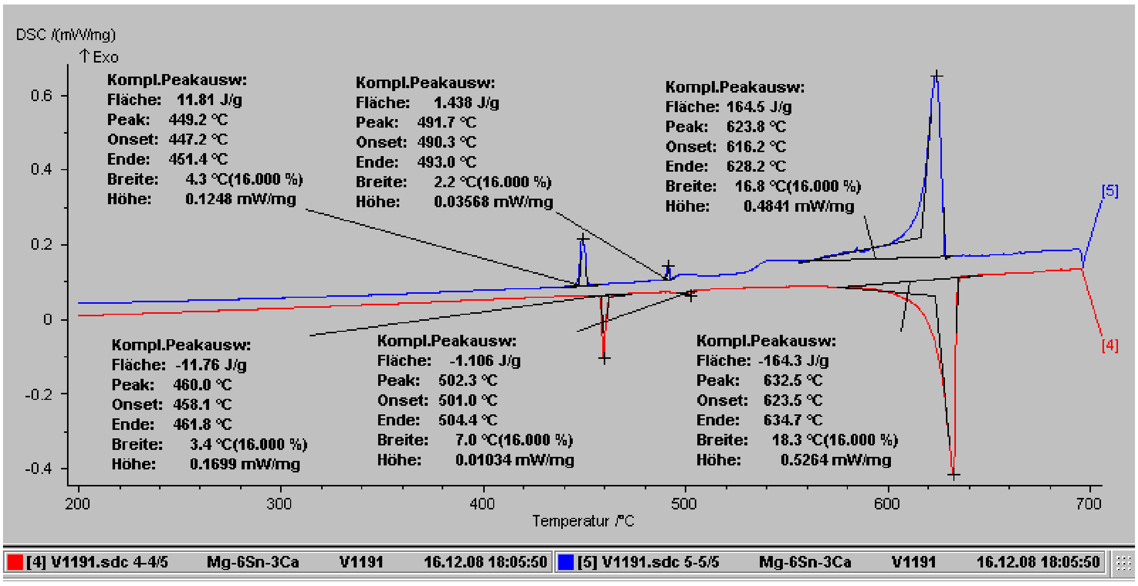

Figure (98): DSC analysis of Mg-6Sn-3Ca alloy using stainless crucible.

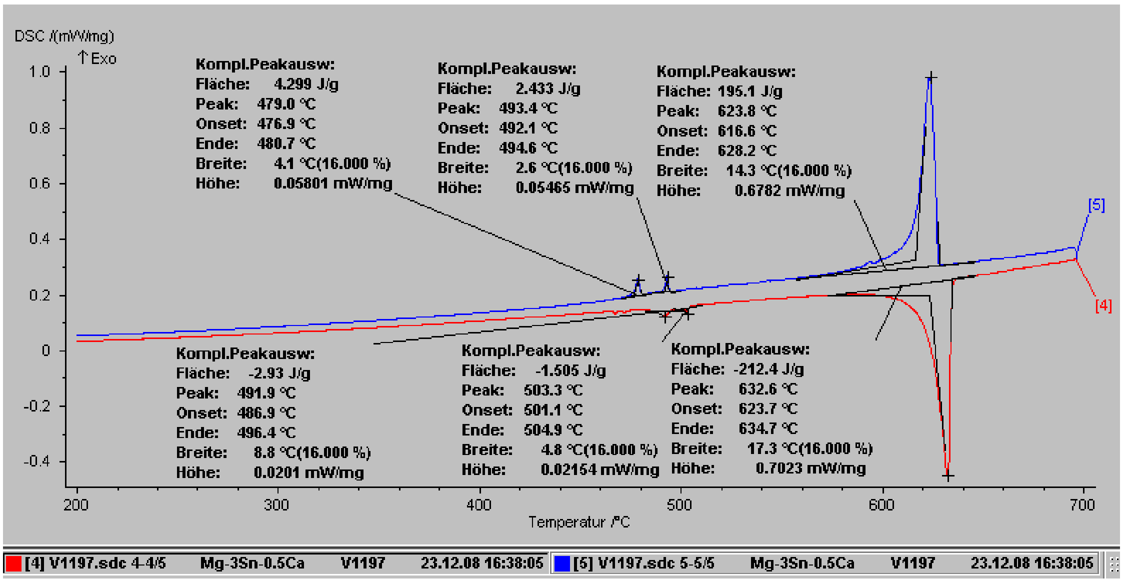

Figure (99): DSC analysis of Mg-3Sn-0.5Ca alloy using stainless crucible.

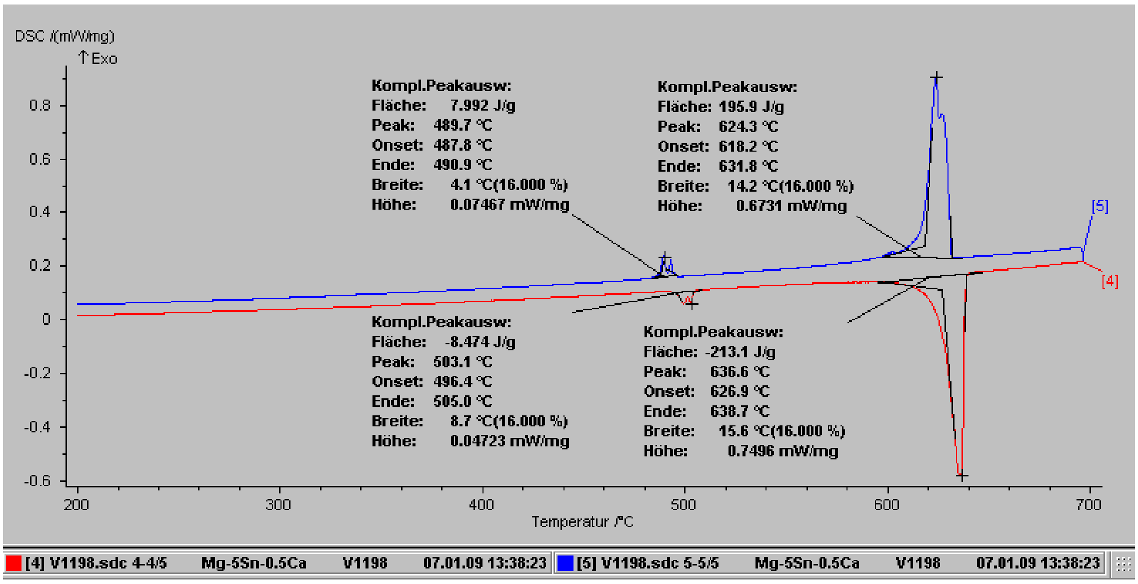

Figure (100): DSC analysis of Mg-5Sn-0.5Ca alloy using stainless crucible.

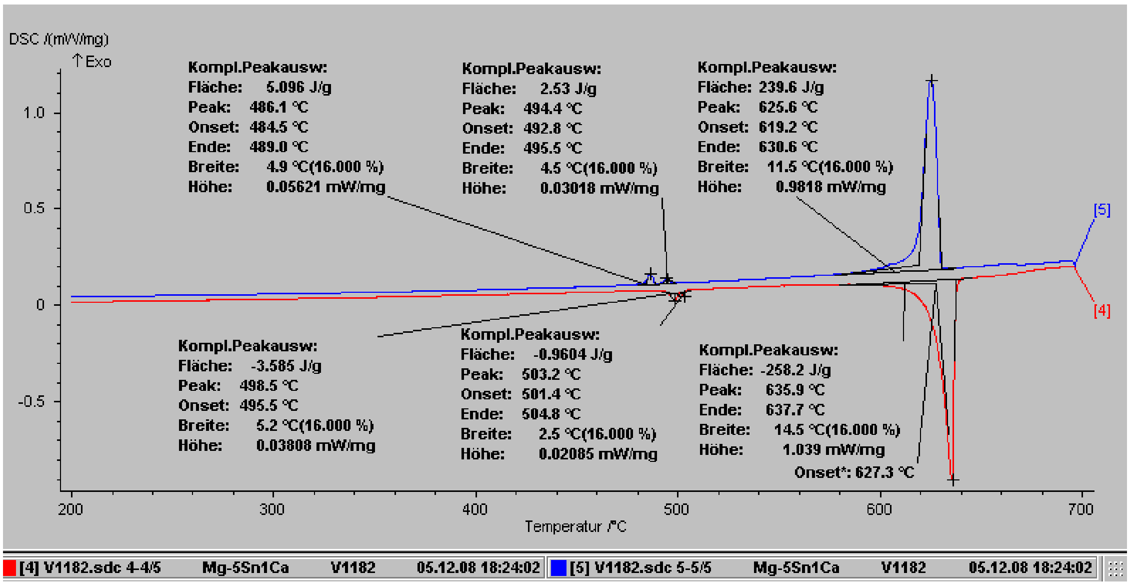

Figure (101): DSC analysis of Mg-5Sn-1Ca alloy using stainless crucible.

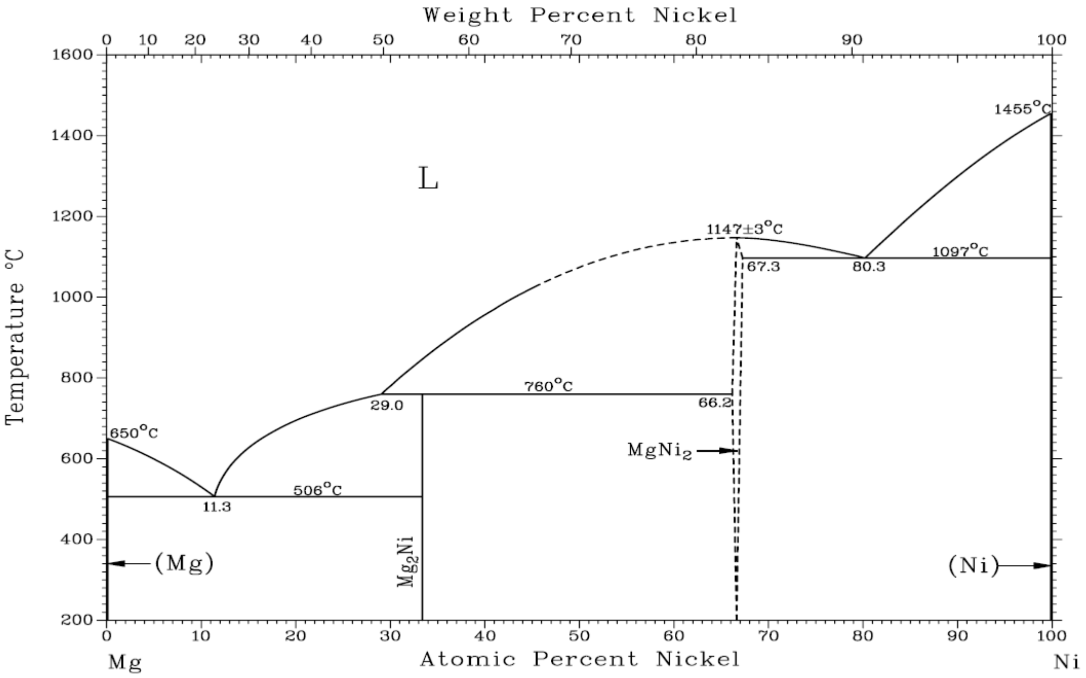

Figure (102): Mg-Ni phase diagram

8.2 Corrosion

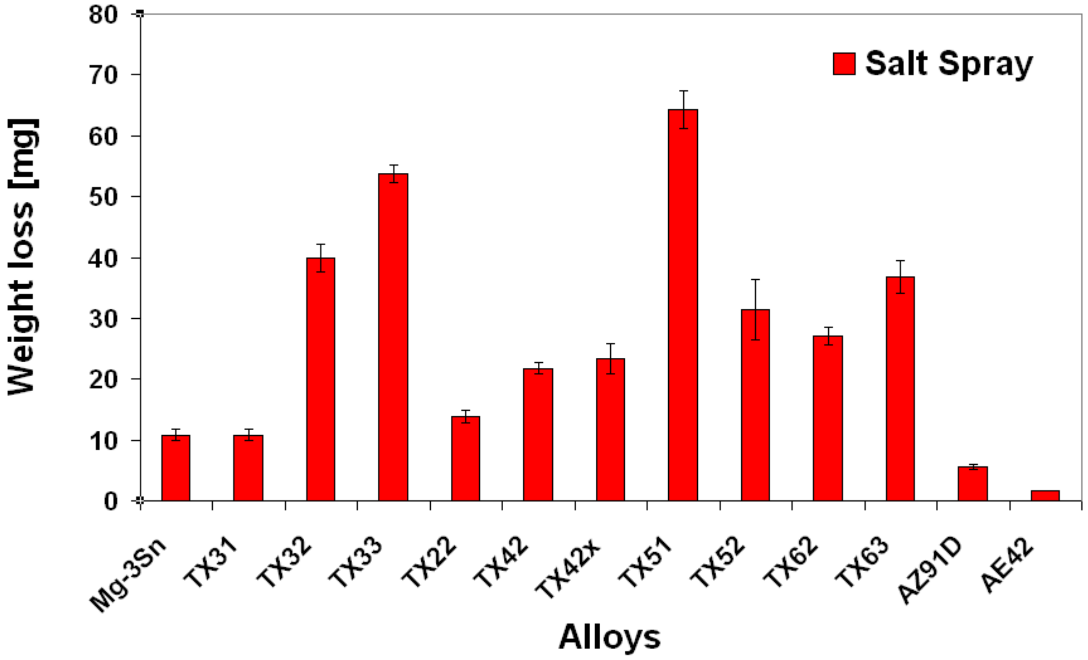

Figure (103): Influence of TX-alloys with proportions of Sn and Ca with a ratio of Sn:Ca 1:1 and 2:1 on the Weight loss.

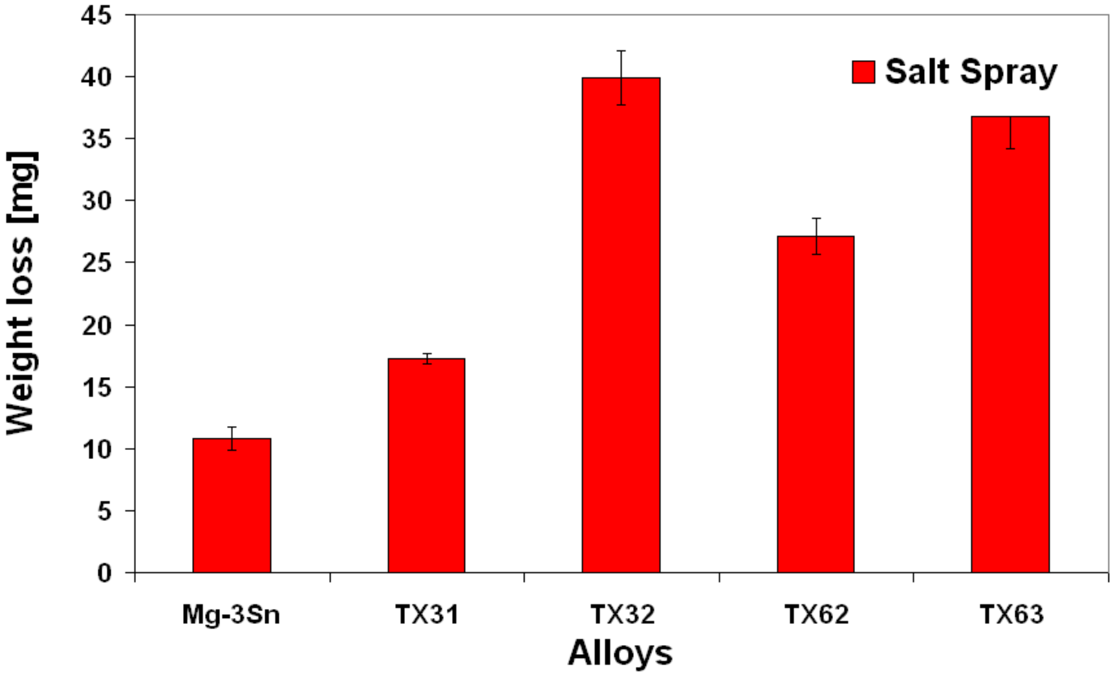

Figure (104): Influence of the amount of Ca on the Weight loss.

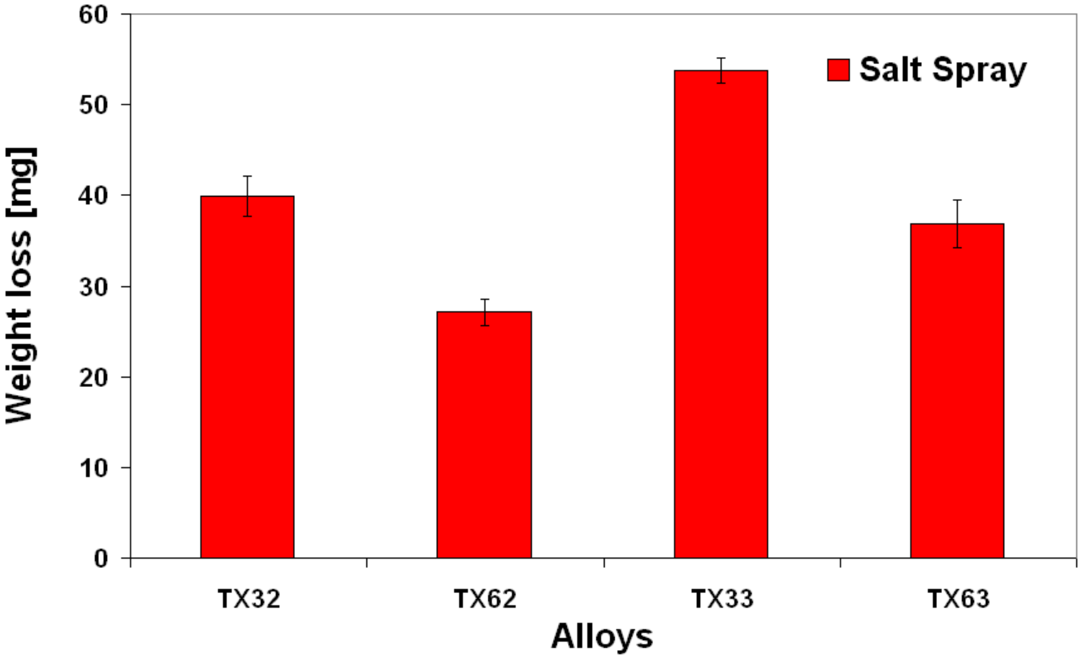

Figure (105): Weight loss and the influence of the amount of Sn on the measured corrosion rates.

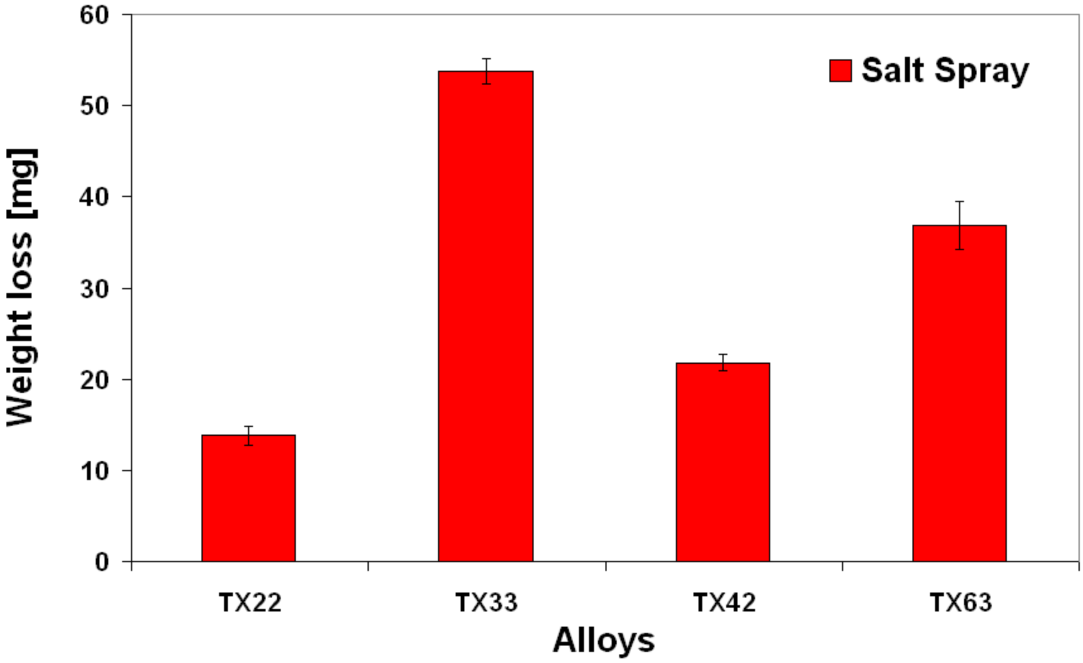

Figure (106): Influence of TX-alloys with proportions of Sn and Ca with a ratio of Sn:Ca 1:1 and 2:1 on the Weight loss.

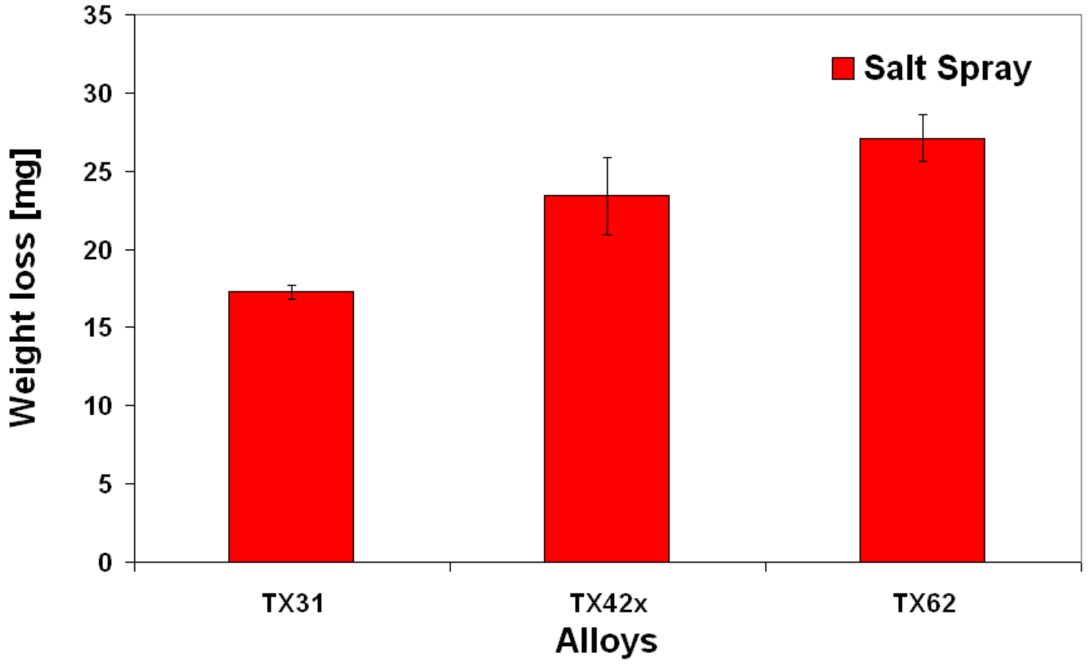

Figure (107): Influence of TX-alloys with same proportions of Sn and Ca with a ratio of Sn:Ca 3:1 on the Weight loss.

8.3 Mechanical properties (tensile and compression)

8.4 Hardness

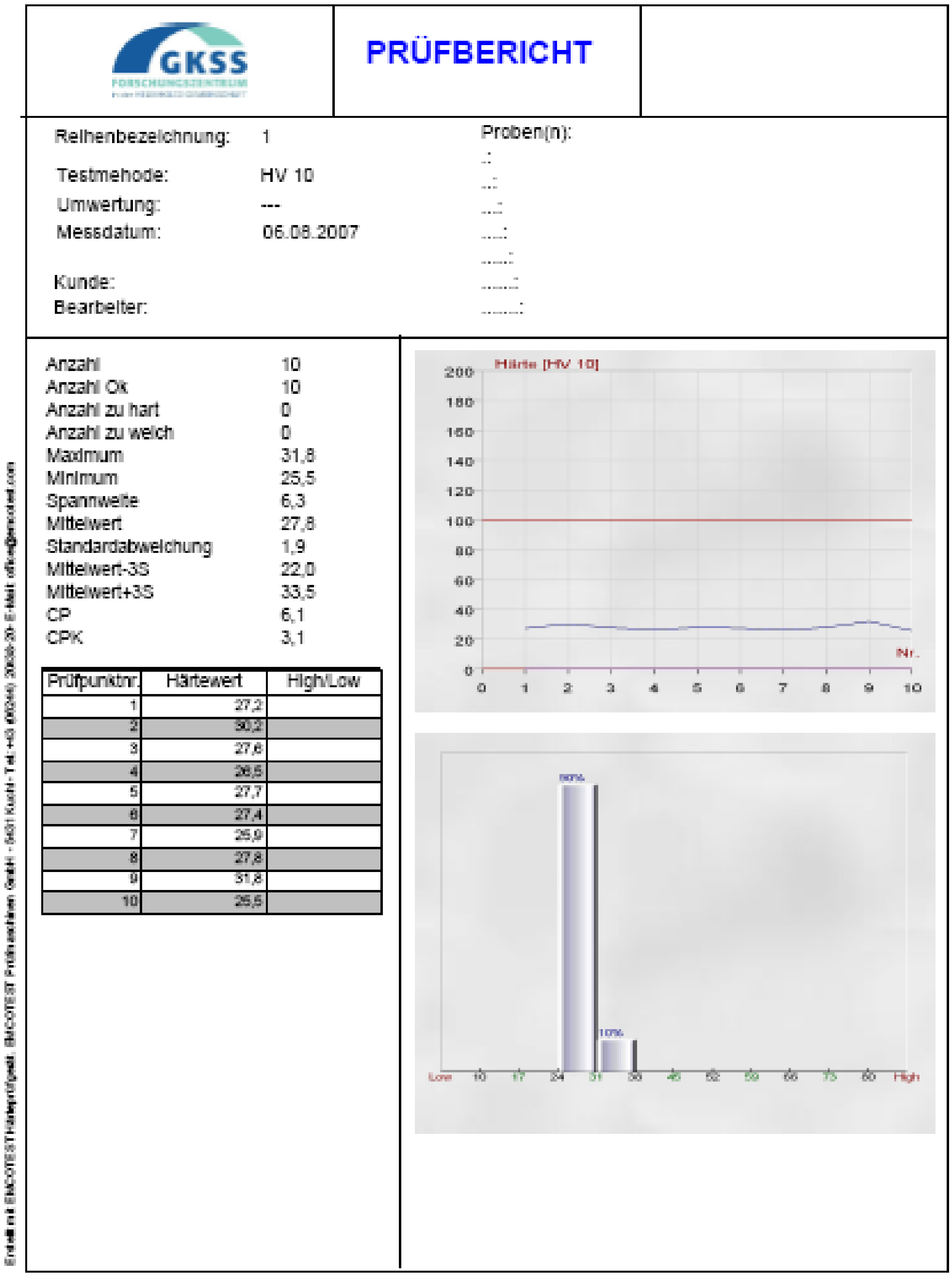

PRÜFBERICHT

Reihenbezeichnung: 1
Testmehode: HV 10
Umwertung: ---
Messdatum: 06.08.2007
Kunde:
Bearbeiter:

Proben(n):
.:
..:
...:
....:
.....:
......:
.......:

Anzahl	10
Anzahl Ok	10
Anzahl zu hart	0
Anzahl zu weich	0
Maximum	31,8
Minimum	25,5
Spannweite	6,3
Mittelwert	27,8
Standardabweichung	1,9
Mittelwert-3S	22,0
Mittelwert+3S	33,5
CP	6,1
CPK	3,1

Prüfpunktnr.	Härtewert	High/Low
1	27,2	
2	30,2	
3	27,6	
4	26,5	
5	27,7	
6	27,4	
7	25,9	
8	27,8	
9	31,8	
10	25,5	

Erstellt mit EMCOTEST Härteprüfgerät. EMCOTEST Prüfmaschinen GmbH - 5431 Kuchl - Tel: +43 (06244) 20038-20- E-Mail: office@emcotest.com

Figure (108): Vickers hardness of Mg-3Sn alloy.

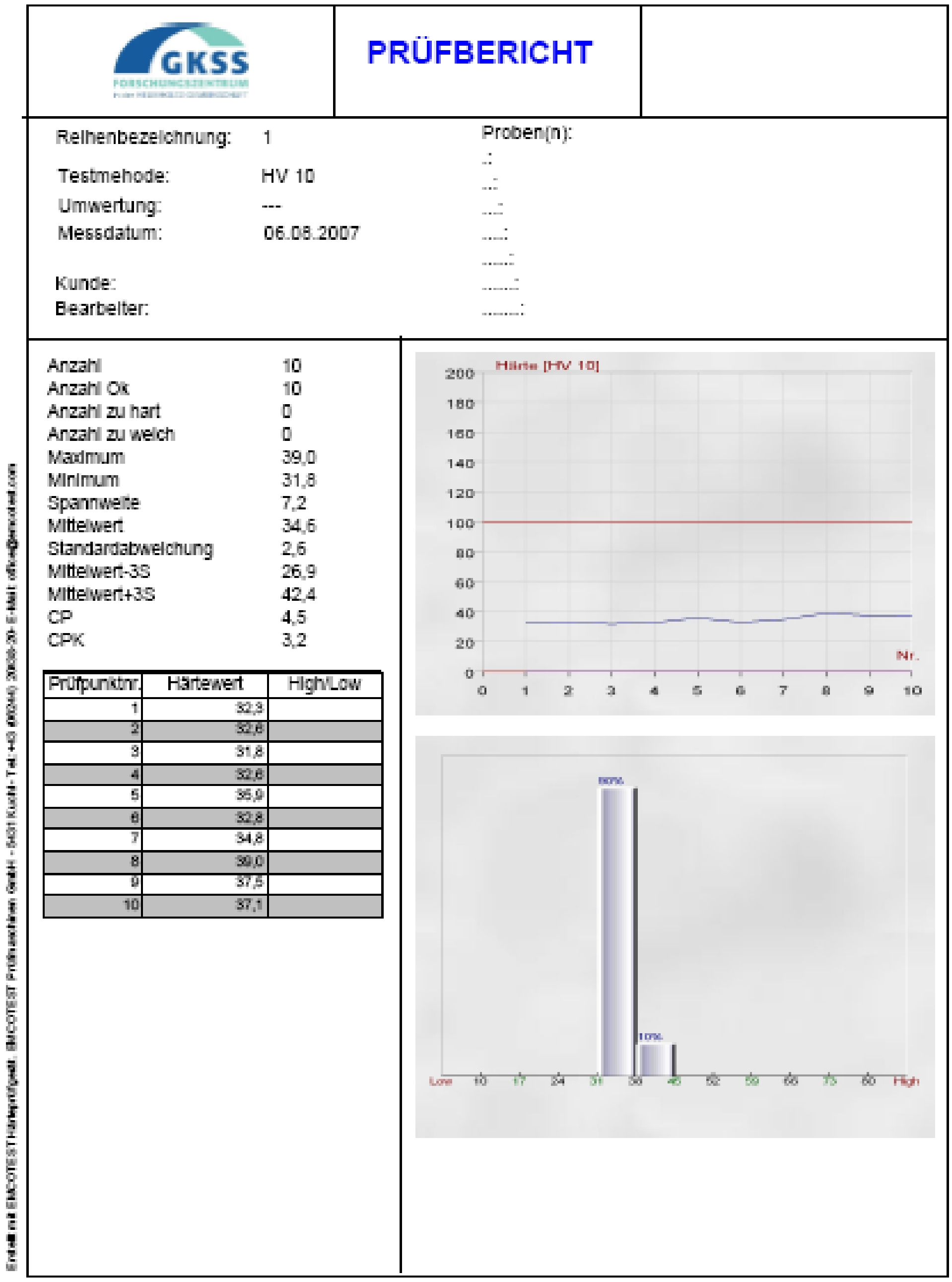

PRÜFBERICHT

Reihenbezeichnung:	1	Proben(n):
Testmehode:	HV 10	
Umwertung:	---	
Messdatum:	06.08.2007	
Kunde:		
Bearbeiter:		

Anzahl	10
Anzahl Ok	10
Anzahl zu hart	0
Anzahl zu weich	0
Maximum	39,0
Minimum	31,8
Spannweite	7,2
Mittelwert	34,6
Standardabweichung	2,6
Mittelwert-3S	26,9
Mittelwert+3S	42,4
CP	4,5
CPK	3,2

Prüfpunktnr.	Härtewert	High/Low
1	32,3	
2	32,6	
3	31,8	
4	32,6	
5	35,9	
6	32,8	
7	34,8	
8	39,0	
9	37,5	
10	37,1	

Erstellt mit EMCOTEST Härteprüfgerät, EMCOTEST Prüfmaschinen GmbH - 5431 Kuchl - Tel. +43 (6244) 20038-20 E-Mail: office@emcotest.com

Figure (109): Vickers hardness of TX31-alloy.

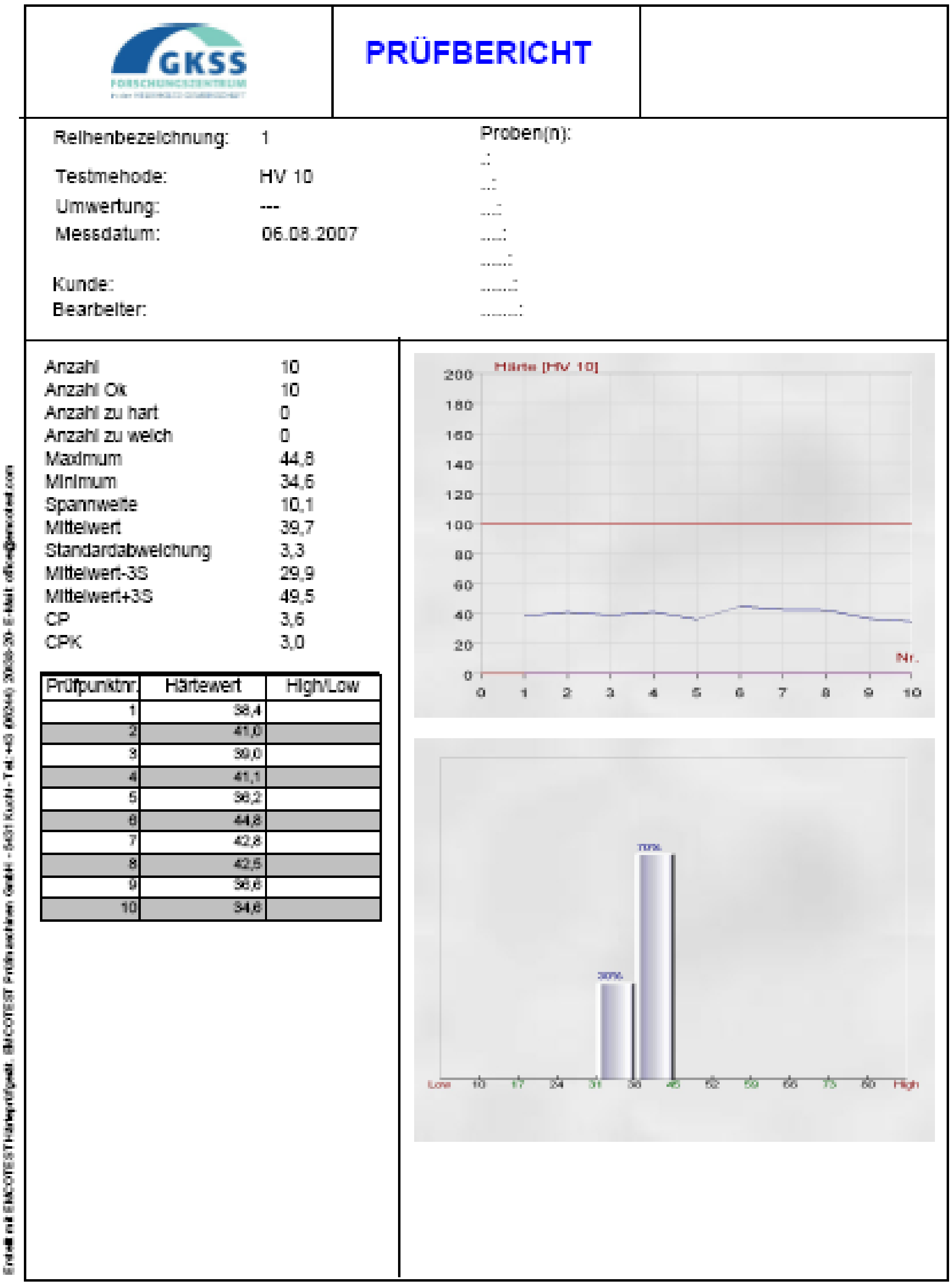

PRÜFBERICHT

Reihenbezeichnung: 1
Testmehode: HV 10
Umwertung: ---
Messdatum: 06.08.2007

Kunde:
Bearbeiter:

Proben(n):
.:
..:
...:
....:
.....:
......:
.......:

Anzahl	10
Anzahl Ok	10
Anzahl zu hart	0
Anzahl zu weich	0
Maximum	44,8
Minimum	34,6
Spannweite	10,1
Mittelwert	39,7
Standardabweichung	3,3
Mittelwert-3S	29,9
Mittelwert+3S	49,5
CP	3,6
CPK	3,0

Prüfpunktnr.	Härtewert	High/Low
1	38,4	
2	41,0	
3	39,0	
4	41,1	
5	36,2	
6	44,8	
7	42,8	
8	42,5	
9	36,6	
10	34,6	

Erstellt mit EMCOTEST Härteprüfgerät, EMCOTEST Prüfmaschinen GmbH - 5431 Kuchl - Tel: +43 (6244) 20038-20- E-Mail: office@emcotest.com

Figure (110): Vickers hardness of TX32-alloy.

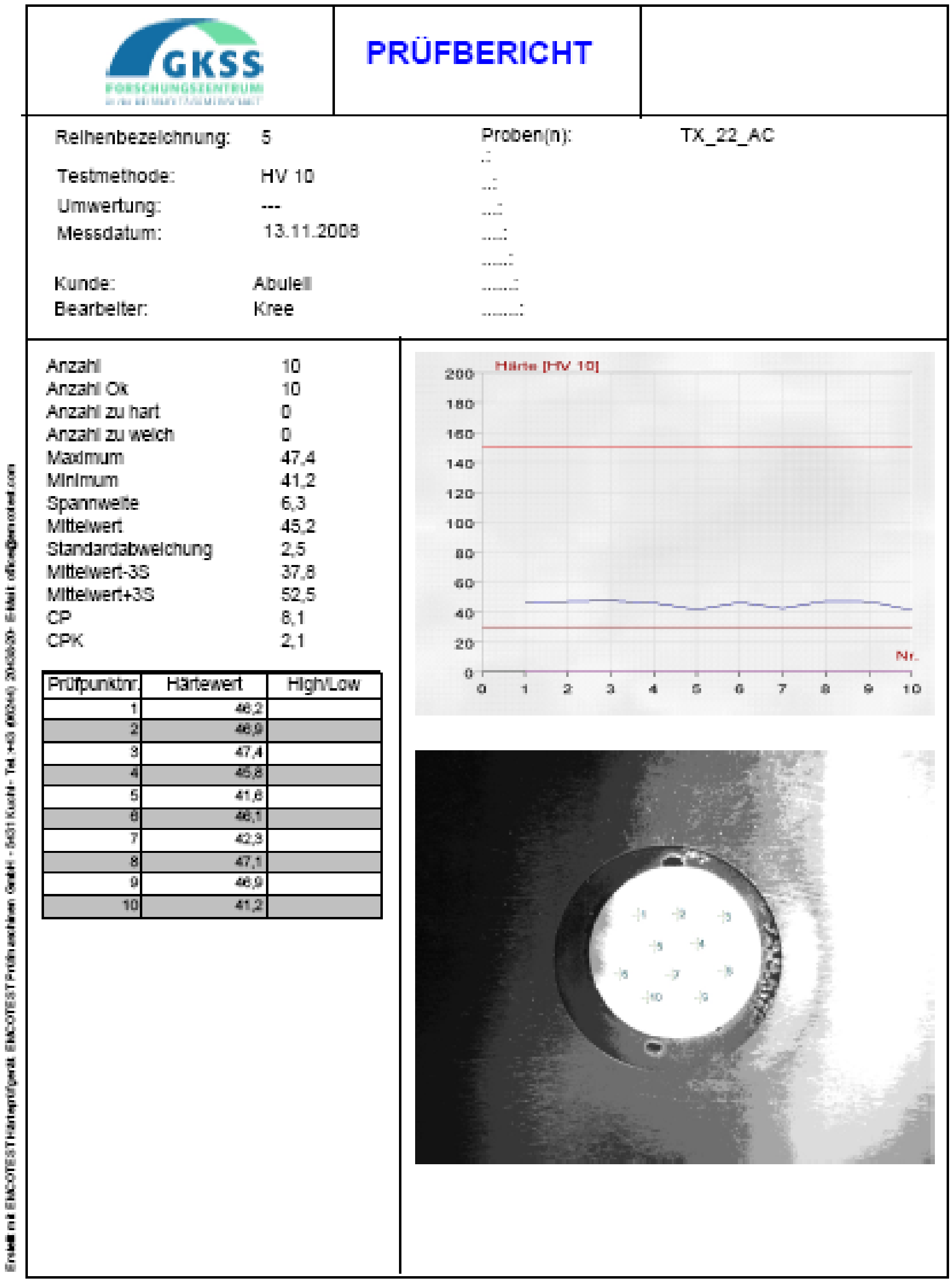

PRÜFBERICHT

Reihenbezeichnung:	5	Proben(n):	TX_22_AC
		.:	
Testmethode:	HV 10	..:	
Umwertung:	---	...:	
Messdatum:	13.11.2008	....:	
		.....:	
Kunde:	Abuleil	......:	
Bearbeiter:	Kree	.......:	

Anzahl	10
Anzahl Ok	10
Anzahl zu hart	0
Anzahl zu weich	0
Maximum	47,4
Minimum	41,2
Spannweite	6,3
Mittelwert	45,2
Standardabweichung	2,5
Mittelwert-3S	37,8
Mittelwert+3S	52,5
CP	6,1
CPK	2,1

Prüfpunktnr.	Härtewert	High/Low
1	46,2	
2	46,9	
3	47,4	
4	45,8	
5	41,6	
6	46,1	
7	42,3	
8	47,1	
9	46,9	
10	41,2	

Erstellt mit EMCOTEST Härteprüfgerät. EMCOTEST Prüfmaschinen GmbH - 5431 Kuchl - Tel. +43 (6244) 20438-0 - E-Mail: office@emcotest.com

Figure (111): Vickers hardness of TX22-alloy.

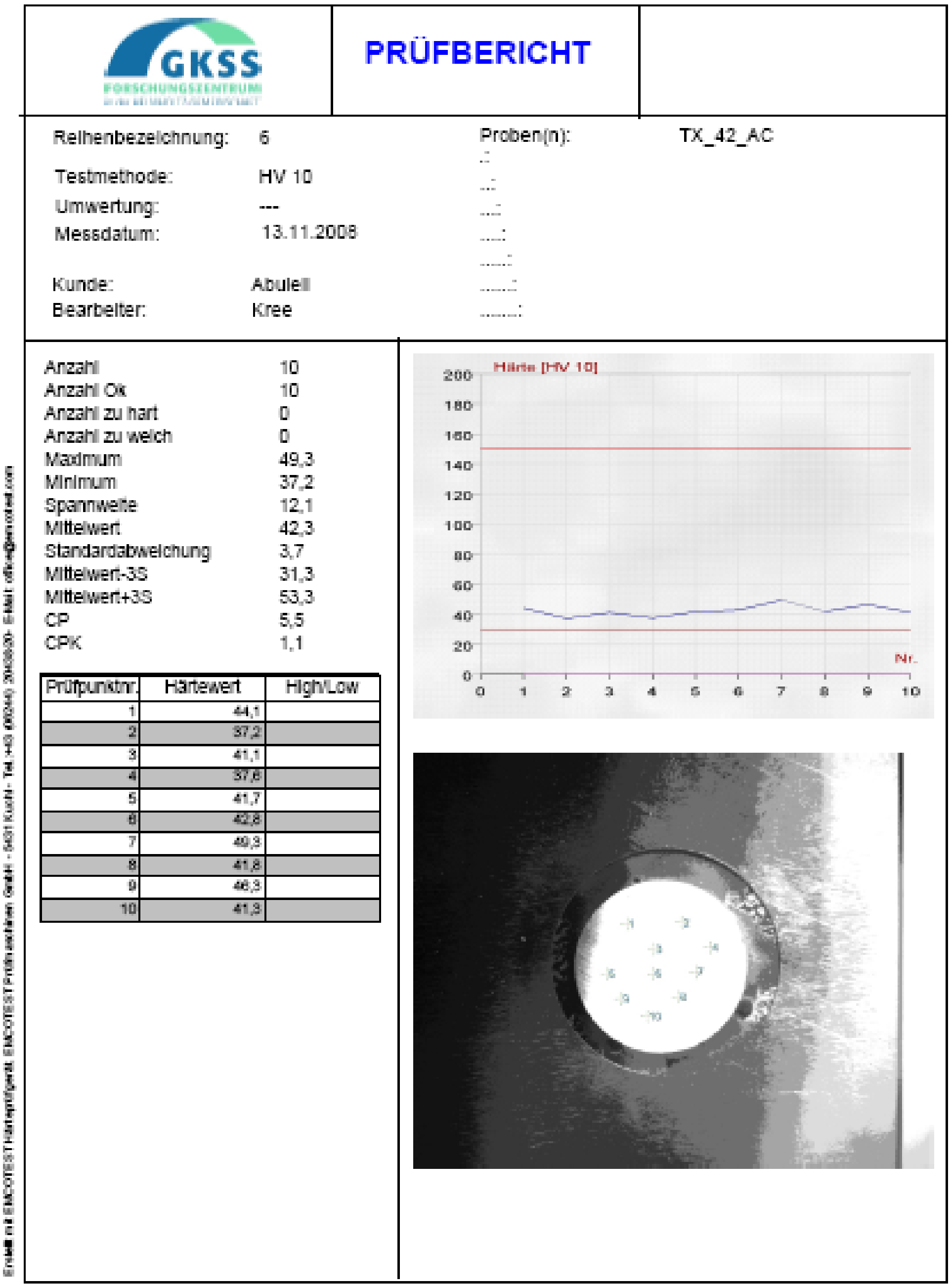

GKSS FORSCHUNGSZENTRUM

PRÜFBERICHT

Reihenbezeichnung:	6	Proben(n):	TX_42_AC
Testmethode:	HV 10	.:	
Umwertung:	---	..:	
Messdatum:	13.11.2008	...:	
		....:	
		.....:	
Kunde:	Abuleil	......:	
Bearbeiter:	Kree	.......:	

Anzahl	10
Anzahl Ok	10
Anzahl zu hart	0
Anzahl zu weich	0
Maximum	49,3
Minimum	37,2
Spannweite	12,1
Mittelwert	42,3
Standardabweichung	3,7
Mittelwert-3S	31,3
Mittelwert+3S	53,3
CP	5,5
CPK	1,1

Prüfpunktnr.	Härtewert	High/Low
1	44,1	
2	37,2	
3	41,1	
4	37,8	
5	41,7	
6	42,8	
7	49,3	
8	41,8	
9	46,3	
10	41,3	

Erstellt mit EMCOTEST Härteprüfgerät. EMCOTEST Prüfmaschinen GmbH - 5431 Kuchl - Tel. +43 (6244) 20438-20 - E-Mail: office@emcotest.com

Figure (112): Vickers hardness of TX42-alloy.

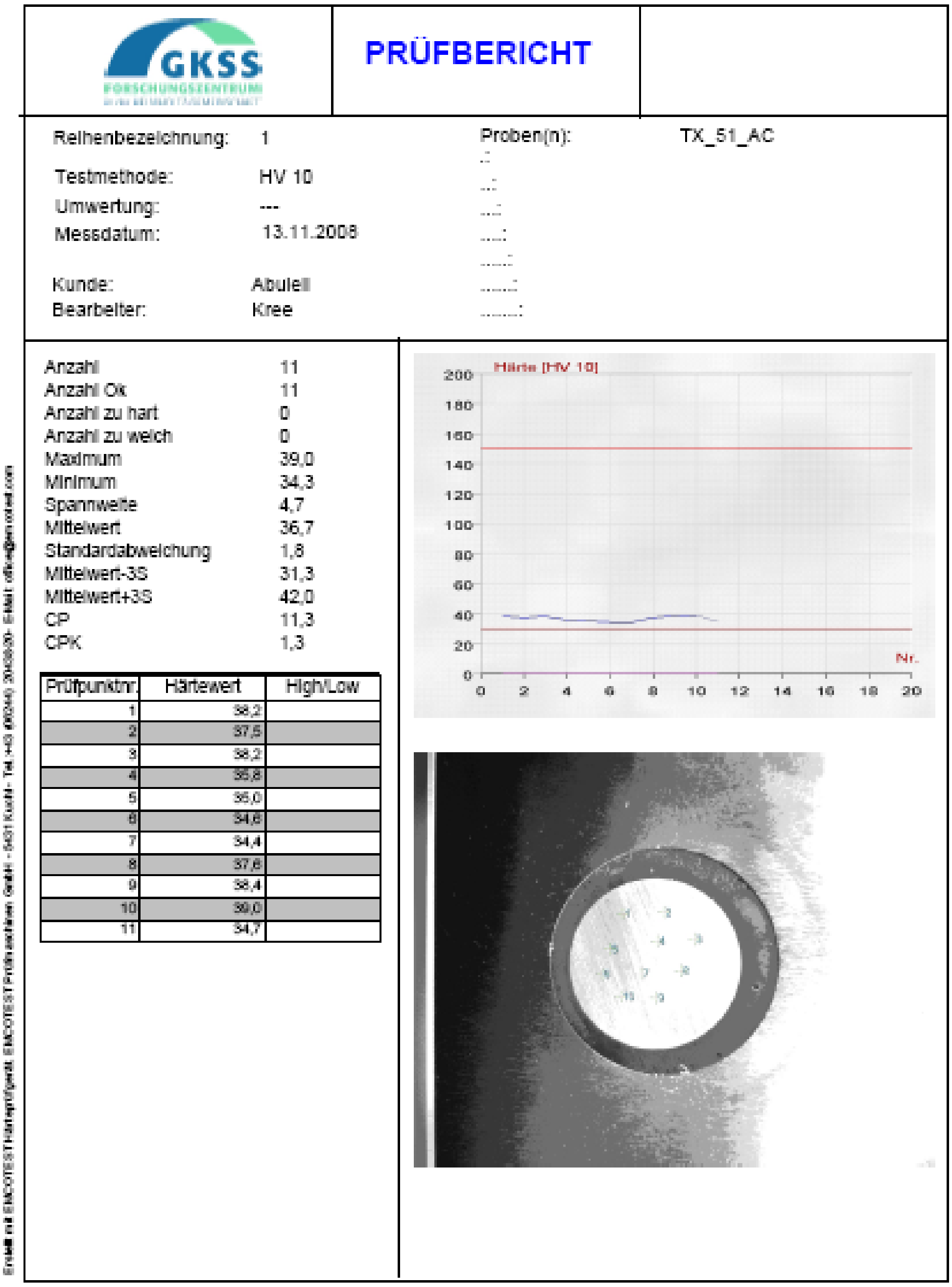

PRÜFBERICHT

Reihenbezeichnung:	1	Proben(n):	TX_51_AC
Testmethode:	HV 10		
Umwertung:	---		
Messdatum:	13.11.2008		
Kunde:	Abulell		
Bearbeiter:	Kree		

Anzahl	11
Anzahl Ok	11
Anzahl zu hart	0
Anzahl zu weich	0
Maximum	39,0
Minimum	34,3
Spannweite	4,7
Mittelwert	36,7
Standardabweichung	1,8
Mittelwert-3S	31,3
Mittelwert+3S	42,0
CP	11,3
CPK	1,3

Prüfpunktnr.	Härtewert	High/Low
1	38,2	
2	37,5	
3	38,2	
4	35,8	
5	36,0	
6	34,6	
7	34,4	
8	37,6	
9	38,4	
10	39,0	
11	34,7	

Figure (113): Vickers hardness of TX51-alloy.

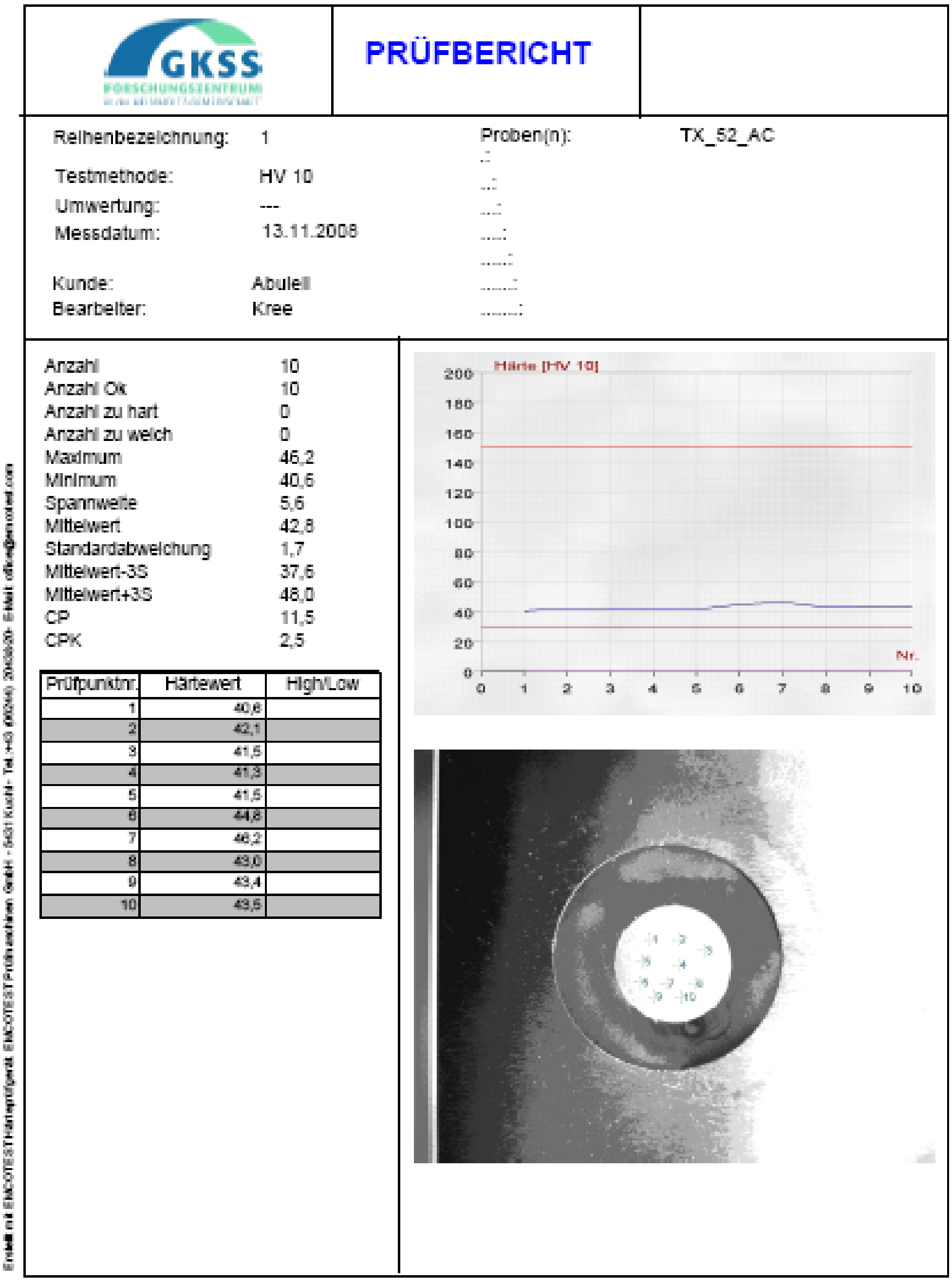

PRÜFBERICHT

Reihenbezeichnung:	1	Proben(n):	TX_52_AC
		.:	
Testmethode:	HV 10	..:	
Umwertung:	---	...:	
Messdatum:	13.11.2008	....:	
		.....:	
Kunde:	Abuleil	......:	
Bearbeiter:	Kree	.......:	

Anzahl	10
Anzahl Ok	10
Anzahl zu hart	0
Anzahl zu weich	0
Maximum	46,2
Minimum	40,6
Spannweite	5,6
Mittelwert	42,8
Standardabweichung	1,7
Mittelwert-3S	37,6
Mittelwert+3S	48,0
CP	11,5
CPK	2,5

Prüfpunktnr.	Härtewert	High/Low
1	40,6	
2	42,1	
3	41,5	
4	41,3	
5	41,5	
6	44,8	
7	46,2	
8	43,0	
9	43,4	
10	43,5	

Erstellt mit EMCOTEST Härteprüfgerät. EMCOTEST Prüfmaschinen GmbH - 5431 Kuchl - Tel. +43 (06244) 20438-20 - E-Mail: office@emcotest.com

Figure (114): Vickers hardness of TX52-alloy.

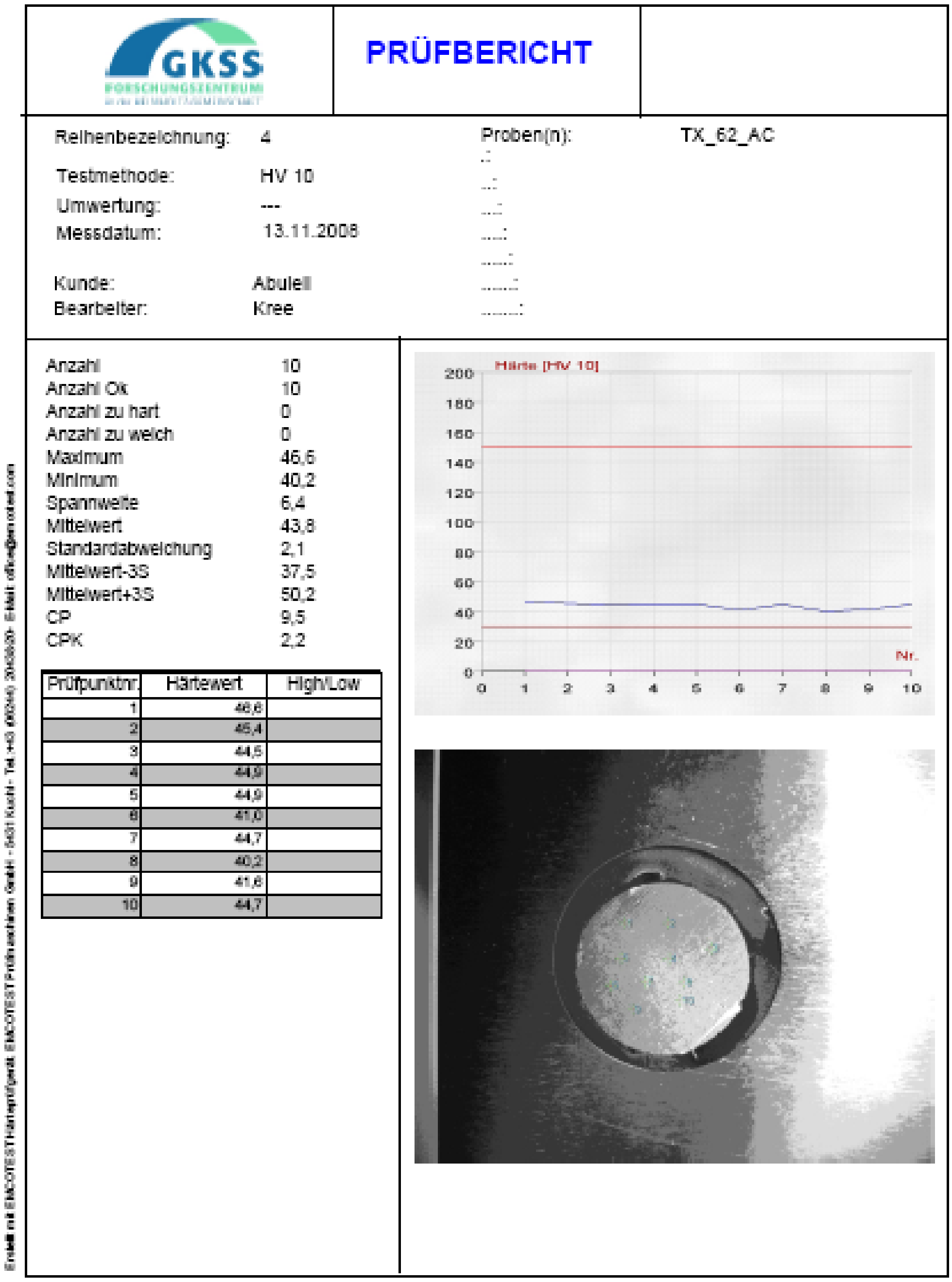

GKSS FORSCHUNGSZENTRUM

PRÜFBERICHT

Reihenbezeichnung:	4	Proben(n):	TX_62_AC
Testmethode:	HV 10		
Umwertung:	---		
Messdatum:	13.11.2008		
Kunde:	Abulell		
Bearbeiter:	Kree		

Anzahl	10
Anzahl Ok	10
Anzahl zu hart	0
Anzahl zu weich	0
Maximum	46,6
Minimum	40,2
Spannweite	6,4
Mittelwert	43,8
Standardabweichung	2,1
Mittelwert-3S	37,5
Mittelwert+3S	50,2
CP	9,5
CPK	2,2

Prüfpunktnr.	Härtewert	High/Low
1	46,6	
2	45,4	
3	44,5	
4	44,9	
5	44,9	
6	41,0	
7	44,7	
8	40,2	
9	41,6	
10	44,7	

Erstellt mit EMCOTEST Härteprüfgerät. EMCOTEST Prüfmaschinen GmbH - 5431 Kuchl - Tel. +43 (6244) 20438/20 - E-Mail: office@emcotest.com

Figure (115): Vickers hardness of TX62-alloy.

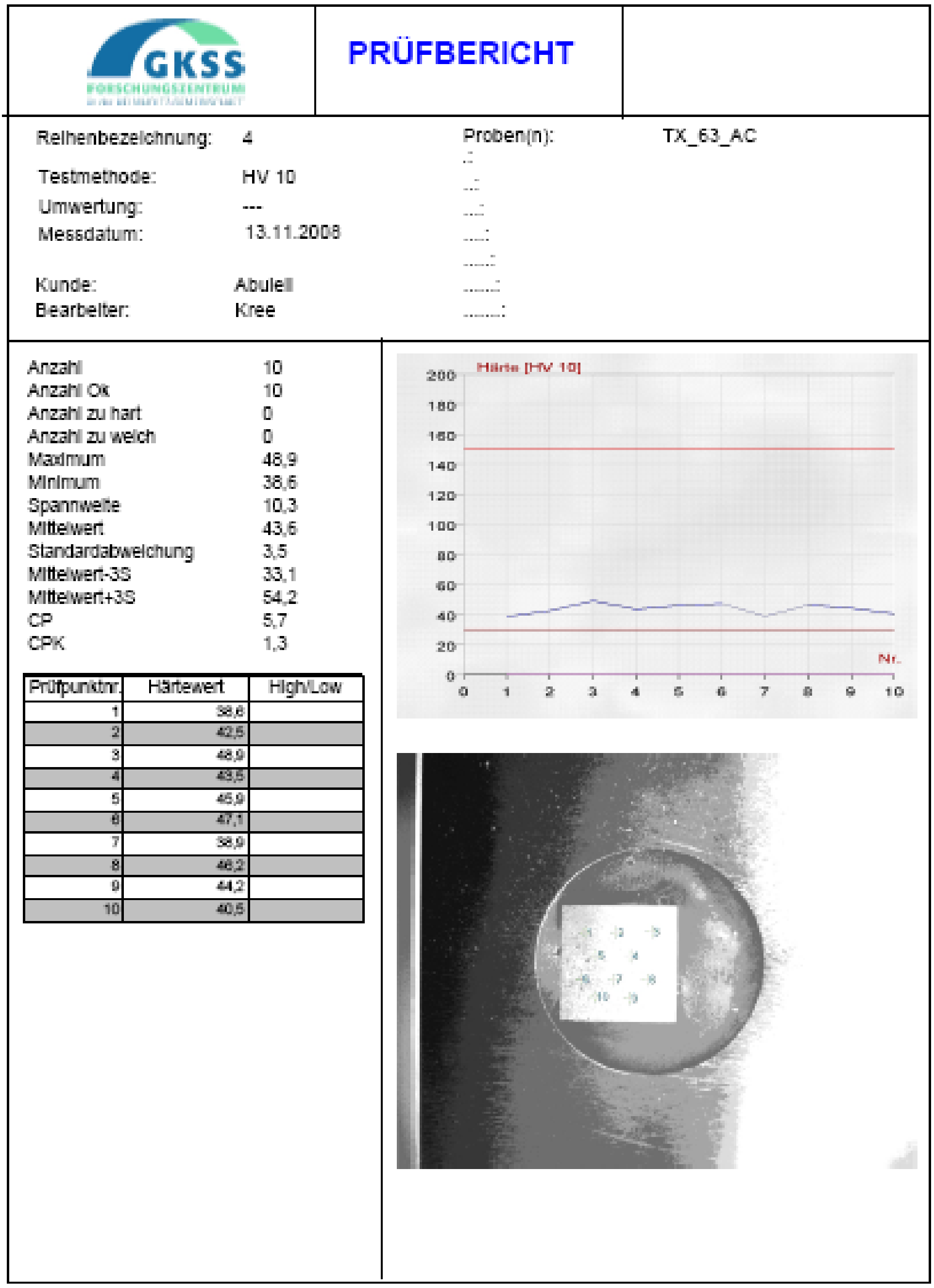

PRÜFBERICHT

Reihenbezeichnung: 4
Testmethode: HV 10
Umwertung: ---
Messdatum: 13.11.2008

Kunde: Abulell
Bearbeiter: Kree

Proben(n): TX_63_AC
.:
..:
...:
....:
.....:
......:
.......:

Anzahl	10
Anzahl Ok	10
Anzahl zu hart	0
Anzahl zu weich	0
Maximum	48,9
Minimum	38,6
Spannweite	10,3
Mittelwert	43,6
Standardabweichung	3,5
Mittelwert-3S	33,1
Mittelwert+3S	54,2
CP	5,7
CPK	1,3

Prüfpunktnr.	Härtewert	High/Low
1	38,6	
2	42,5	
3	48,9	
4	43,5	
5	45,9	
6	47,1	
7	38,9	
8	46,2	
9	44,2	
10	40,5	

Erstellt mit EMCOTEST Härteprüfgerät. EMCOTEST Prüfmaschinen GmbH - 5431 Kuchl - Tel +43 (06244) 20438-20 - E-Mail: office@emcotest.com

Figure (116): Vickers hardness of TX63-alloy.

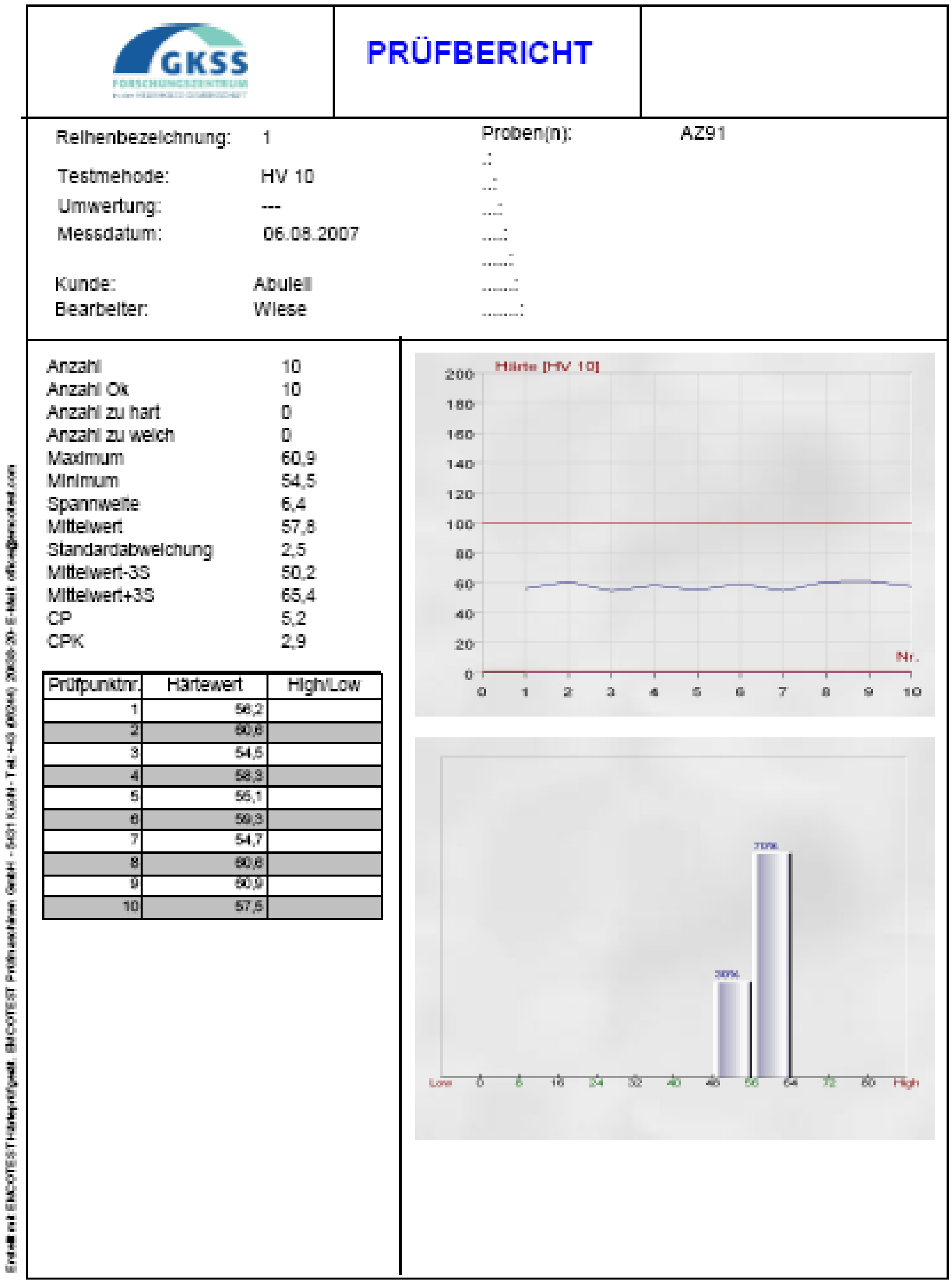

PRÜFBERICHT

Reihenbezeichnung:	1	Proben(n):	AZ91
Testmehode:	HV 10	.:	
Umwertung:	---	..:	
Messdatum:	06.08.2007	...:	
		....:	
Kunde:	Abuleil	.....:	
Bearbeiter:	Wiese	......:	

Anzahl	10
Anzahl Ok	10
Anzahl zu hart	0
Anzahl zu weich	0
Maximum	60,9
Minimum	54,5
Spannweite	6,4
Mittelwert	57,8
Standardabweichung	2,5
Mittelwert-3S	50,2
Mittelwert+3S	65,4
CP	5,2
CPK	2,9

Prüfpunktnr.	Härtewert	High/Low
1	56,2	
2	60,6	
3	54,5	
4	58,3	
5	55,1	
6	59,3	
7	54,7	
8	60,6	
9	60,9	
10	57,5	

Erstellt mit EMCOTEST Härteprüfgerät. EMCOTEST Prüfmaschinen GmbH - 5431 Kuchl - Tel. +43 (6244) 20038-20 E-Mail: office@emcotest.com

Figure (117): Vickers hardness of AZ91D-alloy.

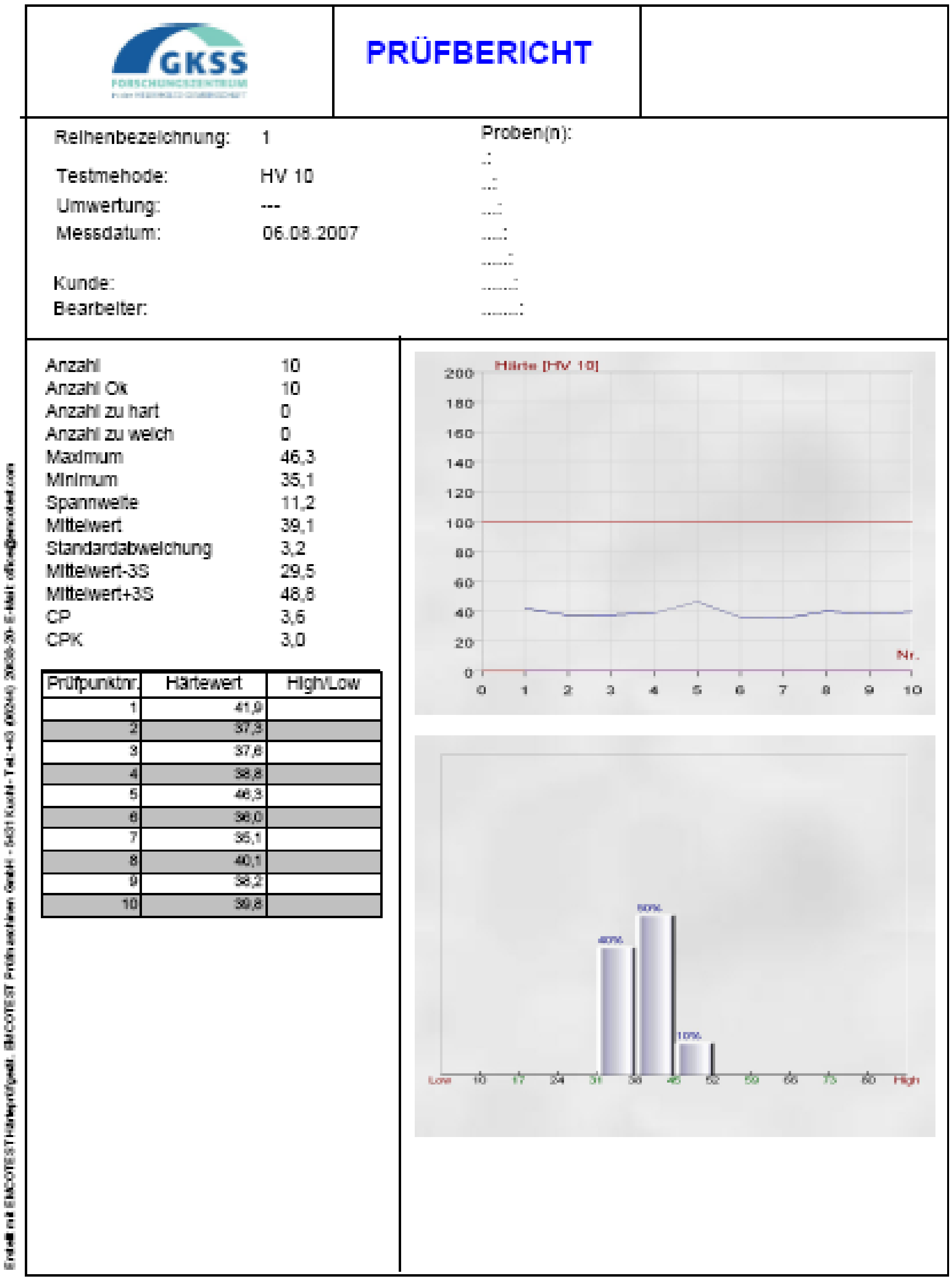

PRÜFBERICHT

Reihenbezeichnung: 1
Testmehode: HV 10
Umwertung: ---
Messdatum: 06.08.2007

Kunde:
Bearbeiter:

Proben(n):
.:
..:
...:
....:
.....:
......:
.......:

Anzahl	10
Anzahl Ok	10
Anzahl zu hart	0
Anzahl zu weich	0
Maximum	46,3
Minimum	35,1
Spannweite	11,2
Mittelwert	39,1
Standardabweichung	3,2
Mittelwert-3S	29,5
Mittelwert+3S	48,8
CP	3,6
CPK	3,0

Prüfpunktnr.	Härtewert	High/Low
1	41,9	
2	37,3	
3	37,8	
4	38,8	
5	46,3	
6	38,0	
7	35,1	
8	40,1	
9	38,2	
10	39,8	

Erstellt mit EMCOTEST Härteprüfgerät, EMCOTEST Prüfmaschinen GmbH - 5431 Kuchl - Tel: +43 (06244) 20038-20 - E-Mail: office@emcotest.com

Figure (118): Vickers hardness of AE42-alloy.

9 List of my Publications

Journal Papers

1 **T. Abu Leil,** K. P. Rao, N. Hort, C. Blawert, W. Dietzel, Y. Huang, K. U. Kainer, Microstructure and Corrosion behaviour of Mg-Sn-Ca alloys after extrusion, Transactions of Nonferrous Metals Society of China, Volume 19, Issue 1, 2009, p. 40.

2 Kozlov, M. Ohno, **T. Abu Leil**, N. Hort, K. U. Kainer and R. Schmid-Fetzer, Phase equilibria and Thermodynamics of the Mg-Sn-Ca system, Part 2: Experimental Investigation of ternary Mg-Sn-Ca phase equilibria and solidification microstructure, Intermetallics 16, 2008, p. 316.

3 H Y. Huang, H. Dieringa, N. Hort, **T. Abu Leil**, K. U. Kainer, Effects of segregation of primary alloying elements on the creep response in magnesium alloys, Scripta Materialia, Volume 58, Issue 10, 2008, p. 894.

4 Y. Huang, **T. Abu Leil**, N. Hort, K. U. Kainer and Yilin Liu, Effect of microstructural inhomogeneity on creep response of Mg-Sn alloys, Key Engineering Materials Volums 345-346, pp. 561.

5 **T. Abu Leil**, Y. Huang, H. Dieringa, N. Hort, K.U. Kainer, J. Buršík, Y. Jirásková and K.P. Rao, Effect of heat treatment on the microstructure and creep behavior of Mg-Sn-Ca alloys, Materials Science Forum Volums 546-549, pp. 69.

6 N. Hort, Y. Huang, **T. Abu Leil**, P. Maier and K. U. Kainer, Microstructural investigations of the Mg-Sn-xCa system, Advanced Engineering Materials, Volum 8, Issue 5, 2006, pp. 359.

Conference Papers

1 F. Elsayed, **T. Abu Leil**, A. Abd El-Aziz, K. Kainer, N. Hort, Investigations on Microstructure and Properties of Mg-Sn-Ca alloys with 3% Al additions, Magnesium Technology 2010, Editors: S. Agnew; E. Nyberg; W. Sillekens; N. Neelameggham, TMS 2010, Washington, USA.

2 **T. Abu Leil**, N. Hort, K. U. Kainer and K. P. Rao, Microstructure, corrosion and creep investigations on Mg-3Sn-3Ca and Mg-6Sn-3Ca alloys, Proceedings of the 8th International Conference on Magnesium Alloys and Their Applications, Editor: K. U. Kainer, Wiley-VCH, Weinheim, Germany, 2009, p. 52.

3 N. Hort, K. P. Rao, **T. Abu Leil**, H. Dieringa, V. Y. R. K. Prasad, K. U. Kainer, Creep and hot working behaviour of a new magnesium alloy Mg-

3Sn-2Ca, Magnesium Technology 2008, Editors: M. Pekguleryuz, R. Beals, E. Nyberg, TMS 2008, Louisiana, USA, p. 401.

4 K. U. Kainer, K. P. Rao, Y. Huang, **T. Abu Leil,** N. Hort, Properties and processing of new magnesium-tin-calcium Alloys for powertrain and hand tool applications, China Magnesium and Automotive 2007, Chongqing, China, 2007, p. 228.

5 **T. Abu Leil**, K. P. Rao N. Hort, Y. Huang, C. Blawert, H. Dieringa and K.U. Kainer, Microstructure, corrosion and creep of cast magnesium alloys Mg2Sn2Ca and Mg4Sn2Ca, in Magnesium Technology 2007, Editors: R.S. Beals, M.O. Pekguleryuz, R. Neelameggham, and A.A. Luo, TMS 2007, Florida, USA, p. 257.

6 **T. Abu Leil**, K. P. Rao, N. Hort, C. Blawert and K.U. Kainer, Corrosion behaviour and microstructure of a broad range of Mg-Sn-X alloys, Magnesium Technology 2006, Editors: A. Luo, N. R. Neelameggham, R. S. Beals, TMS 2006, San Antonio, Texas, USA, p. 281.

7 **T. Abu Leil,** K.P. Rao, N. Hort, H. Dieringa, C. Blawert, Y. Huang, K.U. Kainer, Development and Characterization of a Series of Mg-Sn-Ca alloys, Magnesium Technology in global age, Editors, M.O. Pekgueryuz and L.W. Mackenzie, CIM 2006, Montreal, Canada, p. 739.

8 J. Buršík, V. Buršíková, Y. Jirásková, **T. Abu Leil**, C. Blawert, W. Dietzel, N. Hort, K. U. Kainer, Microstructure and Micromechanical Properties of as-cast Mg-Sn-Ca and Mg-Sn-Mn Alloys, Proceedings of the 7th International Conference on Magnesium Alloys and Their Applications, Editor: K. U. Kainer, Wiley-VCH, Weinheim, Germany, 2006, p. 37.

9 J. Buršík, K. Zábranský, Y. Jirásková, V. Buršíková, **T. Abu Leil**, C. Blawert, Y. Huang, W. Dietzel, N. Hort, K. U. Kainer and K. P. Rao, Effect of Heat Treatment on the Microstructure, Microhardness and Corrosion Behavior of Cast Mg-3Sn-2Ca Alloy, Proceedings of the 7th International Conference on Magnesium Alloys and Their Applications, Editor: K. U. Kainer, Wiley-VCH, Weinheim, Germany, 2006, p. 49.

Conference Posters

1 **T. Abu Leil**, K.P. Rao, N. Hort, H. Dieringa, C. Blawert, Y. Huang and K.U. Kainer, Development and Characterization of a series of Mg-Sn-Ca alloys, Junior Euromat, Lausanne, Switzerland, 2006.

2 **T. Abu Leil**, N. Hort, C. Blawert, Y. Huang, H. Dieringa and K.U. Kainer, Untersuchungen zum Korrosions- und Kriechverhalten von Mg-Sn-Ca-Legierungen für den Hochtemperatureinsatz, DGM-Tag, Berlin, Germany, 2006.

3 Y. Huang, **T. Abu Leil**, N. Hort and K. U. Kainer, Effect of Alloy Composition on the Microstructure and Lattice Parameters in Mg-Sn Systems, Editor: A. Mortensen, EUROMAT 2005, Prague, Czech republic, 2005.

10 Curriculum vitae

Personal details

Name	Tarek Abu Leil
Date of birth	08/09/1973
Place of birth	Bethlehem
Nationality	Jordanian

Education

10/01-09/03	M.S. Degree in Mechanical Engineering	Faculty of Modern Technologies, Department of Mechanical Engineering, University of Kassel, Germany
04/95-09/01	B.S. Degree in Mechanical Engineering	Faculty of Power Engineering, Department of Mechanical Engineering, University of Kassel, Germany
09/93-01/95	Studienkolleg “College”	University Münster, Germany
09/90-06/91	The General Secondary Education Certificate	Alrasheddiya school, Jerusalem

Professional Experience

09/04-03/09	Researcher at MagIC-Magnesium Innovation Center, GKSS Research Center, Germany	
11/00-07/01	Project Assistant at Volkswagen AG, Germany	Design & development of an HVAC As a team member, participated in the design and development of a modern CO_2-Compressor for air-conditioning
01/03-08/03	Project Assistant at University Kassel, Germany	Development of new adhesive joints Participation in the development of new Adhesive Joints
11/97-02/98	Intern at Volkswagen, Germany	Quality analysis of automobile transmissions and engines

Other Activities

Award	DAAD Outstanding Student Award 2000, University of Kassel
Languages	Arabic, English and German
Since 01/00	Member of Association of German Engineers (VDI)
Since 02/08	Member of The Minerals, Metal & Materials Society (TMS)
06/01-08/04	Advisor for International Students, University of Kassel, Germany
06/05-06/06	PhD-Students Speaker, GKSS Research Center, Germany